DEPARTMENT OF CHEMISTRY
UNIVERSITY OF GLASGOW

ELECTRON OPTICAL STUDIES OF VANADIUM COMPOUNDS

by

AHMED LEGROURI

(Licencié ès–Sciences, Mohamed V Univ., Rabat)
(Docteur de 3°cycle, Inst. Natl. Polytech., Toulouse)

Thesis submitted for the degree of
DOCTOR OF PHILOSOPHY

October 1988

ProQuest LLC.
789 East Eisenhower Parkway
P.O. Box 1346
Ann Arbor, MI 48106 – 1346

To Fatna and Yassine.

CONTENTS

CHAPTER THREE:

VANADIUM PENTOXIDE– SUPPORTED RHODIUM CATALYST 117

ACKNOWLEDGEMENTS

I would like to express my special thanks to my supervisors, Dr. Thomas Baird and Dr. John Fryer, for all the advice and encouragement they have given me throughout the course of my research at Glasgow University.

Thanks are also due to my fellow workers in the Electron Microscopy Group for useful discussions, and in particular Davi Thom for his technical assistance and Lorraine Garrick for her meticulous proof reading of this thesis.

I am particularly indebted to Professor G. Webb and the members of the Surface Chemistry Group for their interest and collaboration in the catalysis part of this thesis.

Many other people contributed to this work and it will be difficult to thank every one individually, also I wish that they will find here the expression of my thanks.

This study was made possible by an award and a study leave granted to me by the British Council and the Cadi Ayyad University (Marrakech), respectively. I am therefore grateful to both organisations.

The staff members of the British Council, both in Morocco and in Britain, made my coming as well as my stay here enjoyable. Thanks to all of them, and in particular the Director in Rabat, Mr. J.W. Edmundson, and my program officer in Glasgow Miss Margaret Bennie.

Finally, I am grateful to the Dean of the Faculty of Science and my colleagues at the Chemistry Department, both of the Cadi Ayyad University in Marrakech, for enabling me to spend the few extra months, which were needed for the completion of this thesis, in Glasgow.

DECLARATION

This thesis is a record of the work carried out by the author in the Department of Chemistry at the University of Glasgow, under supervision of Dr T. Baird and Dr. J.R. Fryer.

No part of this work has been submitted in any previous application for a degree.

Some of the work described in this thesis has appeared in the following papers:

1— Legrouri, A. (1987). Electron optical studies of the formation of vanadium pentoxide catalyst. *Proc. 45th Ann. Meet. Electron Microsc. Soc. Am.*, (Bailey, G.W., Ed.). San Fransisco: S.F. Press, pp. 354—355.

2— Legrouri, A., Baird, T. & Fryer, J.R. (1987). Electron optical studies of vanadium pentoxide catalysts. *Electron Microsc. Anal.*, (Brown, L.M., Ed.). London: Inst. Phys., Conf. Ser. No. 90, pp. 31—34.

3— Legrouri, A., Baird, T. & Fryer, J.R. (1988). Electron optical studies of the thermal decomposition of ammonium metavanadate (NH_4VO_3), *React. Solids*, 5, 53—68.

4— Legrouri, A. (1988). Preparation and characterisation of vanadium pentoxide—supported rhodium catalyst. *Proc. 46th Ann. Meet. Electron Microsc. Soc. Am.*, (Bailey, G.W., Ed.), San Fransisco: S.F. Press, pp. 946—947

5— Legrouri, A., Baird, T. & Fryer, J.R. (1988). Rhodium—catalysed reduction of vanadium pentoxide. *EUREM 88, Proc. 9th Europ. Congr. Electron Microsc.*, (Goodhew, P.J. & Dickinson, H.G., Eds.). London: Inst. Phys., Conf. Ser. No. 93, pp. 289—290.

6— Legrouri, A., Baird, T. & Fryer, J.R. (1988). Electron optical studies of vanadium pentoxide—supported rhodium catalyst, in preparation.

SUMMARY

After an introductory chapter on the theory of electron microscopy, which was the predominant technique used in this study, the work described in this thesis was divided into two parts, namely, the thermal decomposition of ammonium metavanadate and the use of vanadium pentoxide as a support for rhodium catalyst.

The thermal decomposition of ammonium metavanadate, up to 400°C in air, was studied by thermogravimetry, differential thermal analysis, infrared spectroscopy and x—ray diffraction. The possible identities of the decomposition products are discussed. Complementary morphological and structural investigations were made by scanning and transmission electron microscopy. The parent material and its calcination products were found to be subject to radiation damage in the transmission electron microscope. High resolution lattice imaging, combined with the minimum dose technique, has allowed a correlation to be made with the structural features of AMV, intermediate products and final vanadium pentoxide material.

Prior to its use as a support for rhodium catalyst, the microstructure of vanadium pentoxide, produced from the thermal decomposition of ammonium metavanadate, was investigated by high resolution electron microscopy in correlation with scanning electron microscopy and gas adsorption measurements. Examination of ultrasonic dispersed crystals in the transmission electron microscope showed that some features could be mistaken for pores in these crystals. However, high resolution electron microscopy examination of crystals prepared, for this technique, by thin sectioning, provided no evidence of porosity, in agreement with krypton gas adsorption and scanning electron microscopy studies.

A catalyst was prepared by impregnation of vanadium pentoxide with a rhodium salt. The catalyst thus prepared was characterised by x—ray diffraction, infrared spectroscopy, temperature programmed

reduction, carbon monoxide chemisorption and electron optical methods. The reduction of the catalyst at different temperatures showed that the support, vanadium pentoxide, is reduced to lower oxides; this reduction being catalysed by the presence of metallic rhodium at its surface.

The catalyst action was studied in the hydrogenolysis of butane, reaction for which rhodium metal is known to be among the most active catalysts, using a continuous flow fixed bed apparatus at atmospheric pressure. For comparison, an alumina— supported rhodium catalyst was prepared and tested under the same conditions.

On both supports, rhodium proved to be active in the hydrogenolysis of butane, with better activity when it is supported on γ - alumina. Except at high conversion rates where the alumina— supported catalyst showed some multiple hydrogenolysis, only single hydrogenolysis, with better selectivity for central bond rupture, occurred with both catalysts.

CHAPTER ONE

ELECTRON MICROSCOPY

*** 1.1 ***

TRANSMISSION ELECTRON MICROSCOPY

1.1.1– INTRODUCTION

The idea of using electron beams for microscopy is often assumed to have been a logical consequence of the hypothesis of the wave nature of the electron due to de Broglie (1924) and its experimental confirmation (Davisson & Germer, 1927; Thomson & Reid, 1927). In fact the initial investigations of imaging by Knoll & Ruska (1932) were based on studies by Busch (1926, 1927) which treated electrons as classical charged particles. As Ruska (1980) makes clear, it was only later that the wave formulation was pointed out to them, opening up the prospect of attaining a very high resolution.

The transmission electron microscope (TEM) was developed in the 1930's and 40's (Ruska, 1934; von Borries & Ruska, 1939; Burton et al., 1939; Hillier & Vance, 1941; von Ardenne, 1944; Hillier & Ramberg, 1947), and has been commercially available since then. In the ensuing half century, it has developed far beyond the vision of its originators, Knoll and Ruska, in its physical and engineering aspects as well as its applications, which now reach into almost all scientific disciplines.

Modern day commercial electron microscopes, such as the JEOL JEM 1200EX at Glasgow University, are now achieving resolution of better than 0.3nm routinely. Higher accelerating voltage instruments, such as the Cambridge 600kV microscope (Cosslett et al., 1979), can approach atomic resolution, for suitable specimens, and have achieved lattice resolution of less than 0.1nm (Hall & Hines, 1970; Murata et al., 1976; Iijima, 1977; Fryer, 1983; Marks & Smith, 1983; Smith et al., 1983a, 1985) allowing better understanding of

material structure in many diverse fields (Hirsch et al., 1965; Murata et al., 1976; Fryer & Smith, 1984; Buseck, 1985).

The history of electron microscopy and diffraction has been well documented (Mulvey, 1967; Ruska, 1980; Goodman, 1981; Cosslett, 1981, 1987; Hawkes, 1985) and the optical theories and development of the instrument have been extensively reviewed (Zworykin et al., 1945; Hillier & Vance, 1945; Cosslett, 1951; Magnan, 1961; Hirsch et al., 1965; Hall, 1966; Grivet, 1972; Hawkes, 1972; Cowley, 1979; Geiss, 1979; Spence, 1980; Wischnitzer, 1981; Watt, 1985). Electron microscopy has also been the subject of several local and international conferences since 1949 (conferences).

1.1.2– PRINCIPLES OF THE ELECTRON MICROSCOPE

An electron microscope uses a series of magnetic lenses to focus an electron beam that is accelerated, by a high potential, through the specimen. Electrons are greatly influenced by the medium through which they pass and have almost no penetrating power. They can only travel for any reasonable distance in a vacuum. Accordingly, the pressure in the column must be maintained at 10^{-3}Pa or less and the specimen must be very thin.

The main features of a modern electron microscope are shown schematically in Fig. 1.1. An electrically heated cathode at selected negative potential emits electrons. A tungsten hairpin filament (Haine & Cosslett, 1961; Hall, 1966) is usually employed. However, better brightness can be obtained using a special pointed tungsten filament (Wolf & Joy, 1971) or from a lanthanum hexaboride cathode (Ahmed, 1971; Batson et al. 1976, Yonezawa et al., 1977); the use of a field emission gun (Crewe et al., 1968) as an alternative to electrical heating, derives similar benefits. The electrons are accelerated by the electrical potential difference between the filament and anode and are focussed, via a double condenser lens system with

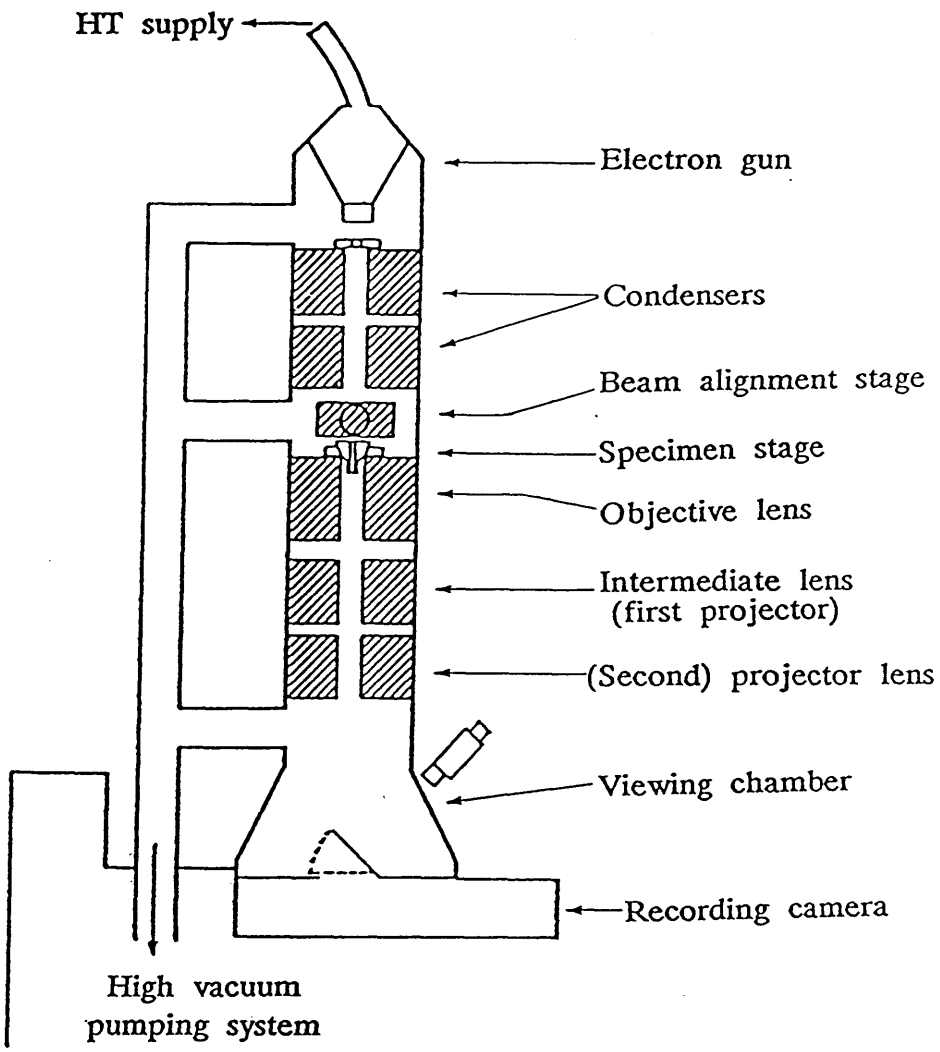

Fig. 1.1: Schematic diagram of high resolution transmission electron microscope.

field— limiting aperture, onto the specimen. An image, or diffraction pattern, from the specimen is obtained on a fluorescent screen via a three— or four— lens magnification system and can be recorded on a photographic plate. Image contrast may be enhanced by the use of an objective aperture, and the area for diffraction may be selected by a selected area aperture. The image is focussed with the objective lens and magnification is controlled by the excitation of the intermediate and/or diffraction lens.

In the case of the JEOL JEM 1200EX electron microscope used in this study, either a pointed tungsten filament or a lanthanum hexaboride cathode was used as source for electrons. The image forming lenses number six; namely, an objective lens, an objective mini— lens, three stage intermediate lens and a projection lens. Using this configuration the magnification may be altered from 50 to 1,000,000. The whole optical column is maintained at a vacuum of 10^{-5}Pa. This microscope has an accelerating voltage of 120kV and as such an electron beam wavelength of 0.003nm. This is considerably smaller than x— ray wavelength of 0.1 to 0.2nm and so electron microscopy, at first sight, should allow the direct imaging of atomic details. As will be seen later, however, the spherical and chromatic lens aberrations (and other aberrations) set a practical limit to the performance of the electron microscope. Nevertheless, in general the accuracy of operation and calibration of the instrument controls the quality of electron micrographs, and the precision with which they can be analysed quantitatively.

1.1.3— BEAM— SPECIMEN INTERACTION

The interaction of a high— energy electron beam with a solid specimen generates a variety of signals all of which yield information on the nature of the solid (Fig. 1.2). The events of interest to transmission electron microscopy, where very thin films of solid are

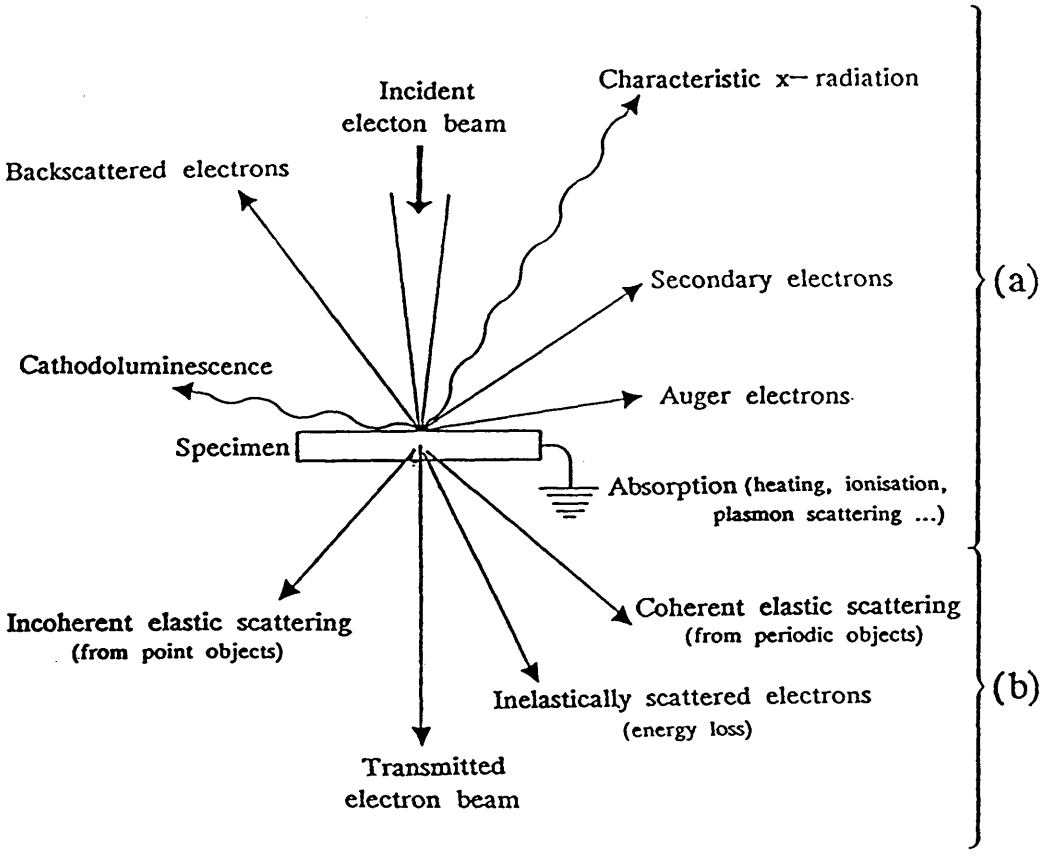

Fig. 1.2: Schematic representation of the wealth of information resulting from the interaction between the electron beam and the specimen in:

(a) scanning or analytical electron microscopy,

(b) conventional and scanning transmission electron microscopy.

studied, are indicated. When interacting with the atoms of a solid, impinging electrons may suffer two types of scattering processes:

(a) elastic scattering, due to interaction with the nuclei in the specimen — this does not involve transfer of energy to the atoms.

(b) inelastic scattering due to interaction with the orbital electrons in the specimen thus involving energy transfer and absorption.

Although TEM will make use of both elastically and inelastically scattered electrons, the major imaging techniques are based on the elastic processes, which deserves, consequently, a somewhat more detailed presentation (Hirsch et al, 1965; Humphreys, 1979) and are dealt with in the next paragraph.

The ratio of the directly transmitted electrons to that of elastically scattered is related to the contrast of images in TEM. Images of crystalline specimens are largely influenced by Bragg reflections. Inelastically scattered electrons may cause chromatic aberration in the image formation process. The absorbed energy i.e. the energy which scattered electrons have lost while passing through the specimen, results in excitation of the atoms and atomic nuclei in the specimen. This causes heating, magnetism, ionisation, etc. When an incident electron has high energy, part of the energy may sometimes give rise to radiation damage of the specimen by irreversibly ejecting the atoms from their positions elastically.

1.1.4– IMAGE FORMATION AND CONTRAST

The result of the interaction of the electron wave with the solid is to form, at the exit surface, a transmitted wave which may be interpreted as being the sum of an unscattered plus a set of scattered waves. The second step of the process is the propagation of this transmitted electron wave along the optic axis of the objective lens of the microscope.

Fig. 1.3 schematises the formation of an image by the objective

lens. The principle is the same as that of Abbe theory for gratings in light optics (Abbe, 1873). If the unscattered and the scattered beams can be made to recombine, so preserving their amplitudes and phases, then a lattice image of the planes which are diffracting may be resolved directly (phase contrast). Alternatively, amplitude contrast is obtained by deliberately excluding the diffracted beams from the imaging sequences by the use of suitably sized apertures, placed in the back–focal plane of the objective lens. Such an image is called a bright field image (Fig. 1.4.a). Alternatively, a dark field image can be obtained by excluding all beams except the particular diffracted beams of interest (Fig. 1.4.b).

The Abbe theory of imaging may be conveniently translated into mathematical form for thin specimens (less than 10nm), where only single scattering events occur (Cowley, 1975). This is termed kinematical conditions and the relative intensities of the scattered and transmitted beams can be calculated (Hirsch et al., 1965; Gevers, 1978). As indicated in Fig. 1.3, the distribution of the wave amplitude $A_f(u,v)$ in the back–focal plane (the diffraction pattern) is related to the amplitude $A_o(x,y)$ of the transmitted wave at the exit surface of the specimen (object plane) by a Fourier transform:

$$A_f(u,v) = F[A_o(x,y)]$$

where x,y and u,v are coordinates perpendicular to the optic axis in the object and back–focal plane, respectively.

The waves will then propagate from the back–focal plane to the image plane, where they interfere to give the amplitude distribution $A_i(x,y)$. This interference may be represented by a second Fourier transform:

$$A_i(x,y) = F[A_f(u,v)] = F\{F[A_o(x,y)]\}$$

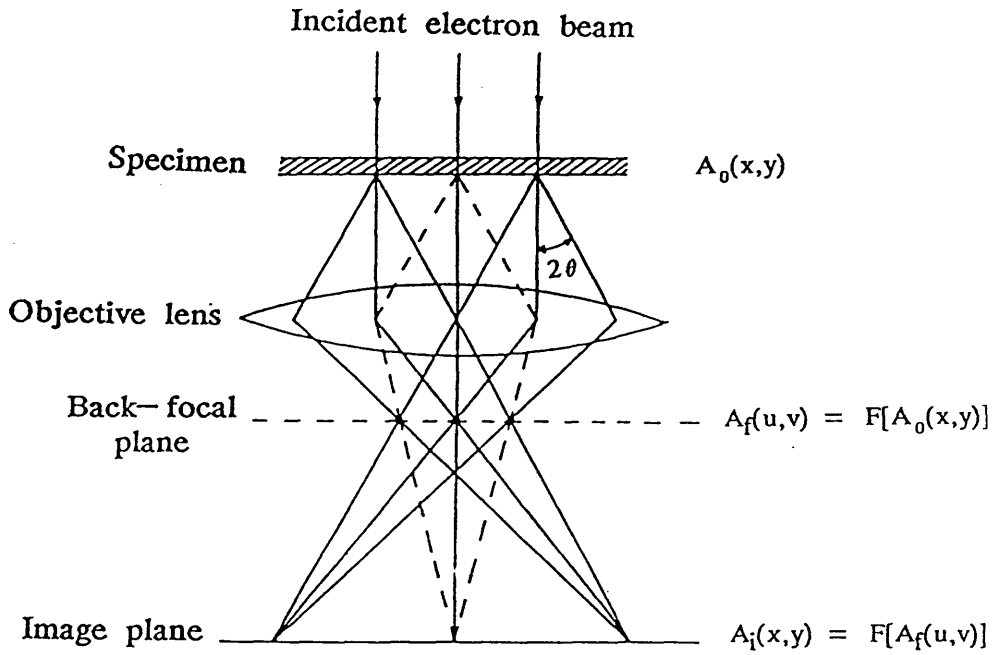

Fig. 1.3: Schematic diagram of the formation of an image by the objective lens in a TEM. The mathematical formulations of the wave amplitudes in various planes along the optic axis are indicated.

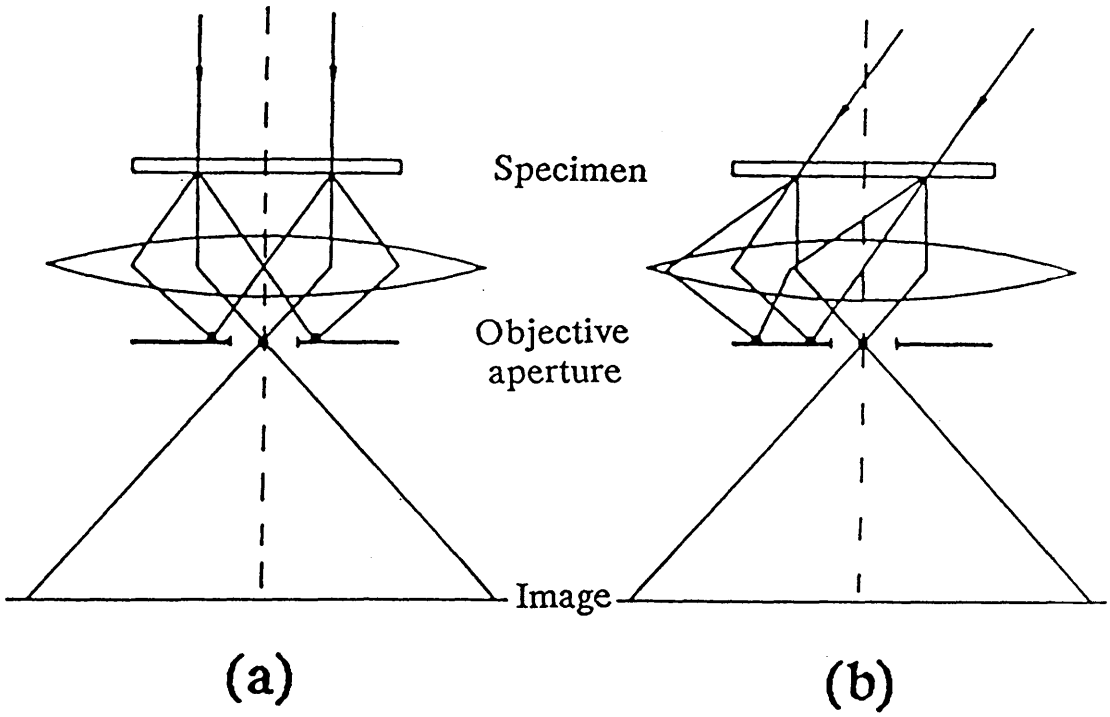

Fig. 1.4: Imaging modes in the TEM: (a) bright field, and (b) dark field.

This formulation expresses that the imaging process, i.e. the operation of obtaining the amplitude and phase distribution in the image given that in the object, can be regarded as two successive Fourier transforms:

$$\text{SPECIMEN} \xrightarrow[\text{transform}]{\text{Fourier}} \text{DIFFRACTION PATTERN} \xrightarrow[\text{F.T.}]{\text{inverse}} \text{IMAGE}$$

For a crystal at the exact Bragg orientation, the appearance of a sharp spot in the diffraction pattern reflects the periodic oscillation of the transmitted wave amplitude with a frequency 1/d. The oscillation reproduces the regular spacing of the set of diffracting planes. If both the unscattered wave and the diffracted wave are allowed to pass through the objective aperture, their interference in the image plane will bring about a periodic variation of the intensity in the form of fringes which may be interpreted as a magnified image of the lattice planes. This is the phase contrast effect, which governs the appearance of the image in the high resolution electron microscope (HREM).

The effect of insertion of an objective aperture in the back–focal plane is to remove some of the spatial frequencies. As a result, the amplitude distribution in the image is no longer an exact reproduction of the transmitted wave. If the specimen is limited to a point, its image will not be perfect point but a small disk (the Airy disk), of diameter D_A with:

$$D_A = 0.61(\lambda/\alpha_0)$$

where α_0 is the maximum scattering angle that is admitted through the objective aperture. D_A is the well–known resolution limit of any wave optical instrument in the absence of lens aberration.

As the electron wavelength is much less than interatomic distances, atomic details should be, in principle, clearly revealed.

Unfortunately, electron lenses are far from perfect. The main defect is spherical aberration C_S. Its geometric effect is that the scattered waves are focussed in slightly different image planes for different values of the scattering angle 2θ. It may be shown (Heidenreich, 1964) that this phenomenon is identical to the introduction of a phase delay:

$$\chi = -\pi C_S (2\theta)^4 / 2\lambda$$

to the waves scattered by an angle 2θ.

Another alteration of the phases of the waves must be considered. Indeed, if the focus of the objective is varied so that the image plane is shifted along the z axis by an amount ΔF (the defect of focus or defocus) from its former position, the distribution of the wave amplitude in this former image plane may be obtained by introducing a phase delay (Heidenreich, 1964):

$$\chi_F = \pi \Delta F (2\theta)^2 / \lambda$$

As $2\theta = \lambda/d$ (Bragg law), the total phase delay which is a rearrangement of Scherzer's expression (Scherzer, 1949) becomes:

$$\chi = \pi \lambda / d^2 (\Delta F - C_S \lambda^2 / 2d^2) \qquad (1)$$

If the unscattered and the scattered waves are out of phase, their interference in the image plane will not give a faithful image of the wave transmitted by the specimen. If this transmitted wave contains only one spatial frequency 1/d, it is possible, using equation (1), to adjust ΔF to compensate for the phase delay introduced by C_S. The spacing of the fringes, which are then obtained in the image plane, corresponds to the spacing of the lattice plane. The problem of imaging together several different spatial frequencies is

more complex. It may be demonstrated that these frequencies may be all faithfully reproduced on the image if sin $\chi = 1$ for all of them. Sin χ is called the phase contrast transfer function (PCTF) (Hanszen, 1971; Erickson, 1973).

Some examples of the variation of the PCTF as a function of the spatial frequency 1/d are shown on Fig. 1.5. One observes that there exists an optimum value of ΔF for which sin $\chi \cong 1$ within a fairly broad range of 1/d frequencies. This value is given by:

$$\Delta F = 1.19\sqrt{\lambda C_s}$$

and is called the Scherzer focus (Scherzer, 1949). It is around this defocus value that the most faithful image down to the smallest structural detail will be obtained. The objective lens may thus be considered as a "filter" which retains, for imaging, only the range of spatial frequencies within which sin $\chi \cong 1$.

The resolution limit D_{min} of the microscope is usually defined as the largest value of d for which sin $\chi = 0$ at the optimum defocus. Calculation (Eisenhandler & Siegel, 1966) gives:

$$D_{min} = 0.65 C_s^{1/4} \lambda^{3/4}$$

It follows that the improvement of resolving power requires reduction of C_s (i.e. a more perfect lens) and of λ (i.e. a higher operating voltage). However, in real life the performance of the microscope is determined by other complicating factors, such as the instabilities in the high-voltage supply and lens current (chromatic aberration) and the finite illumination source size (partial spatial coherence), which impose an 'envelope' function (Hanszen, 1971; Misell, 1973; Frank, 1973; Beorchia & Bonhomme, 1974) on the calculated transfer function, and ultimately sets a limit even to this resolution. Consequently, the PCTF has to be modified to allow for the effects

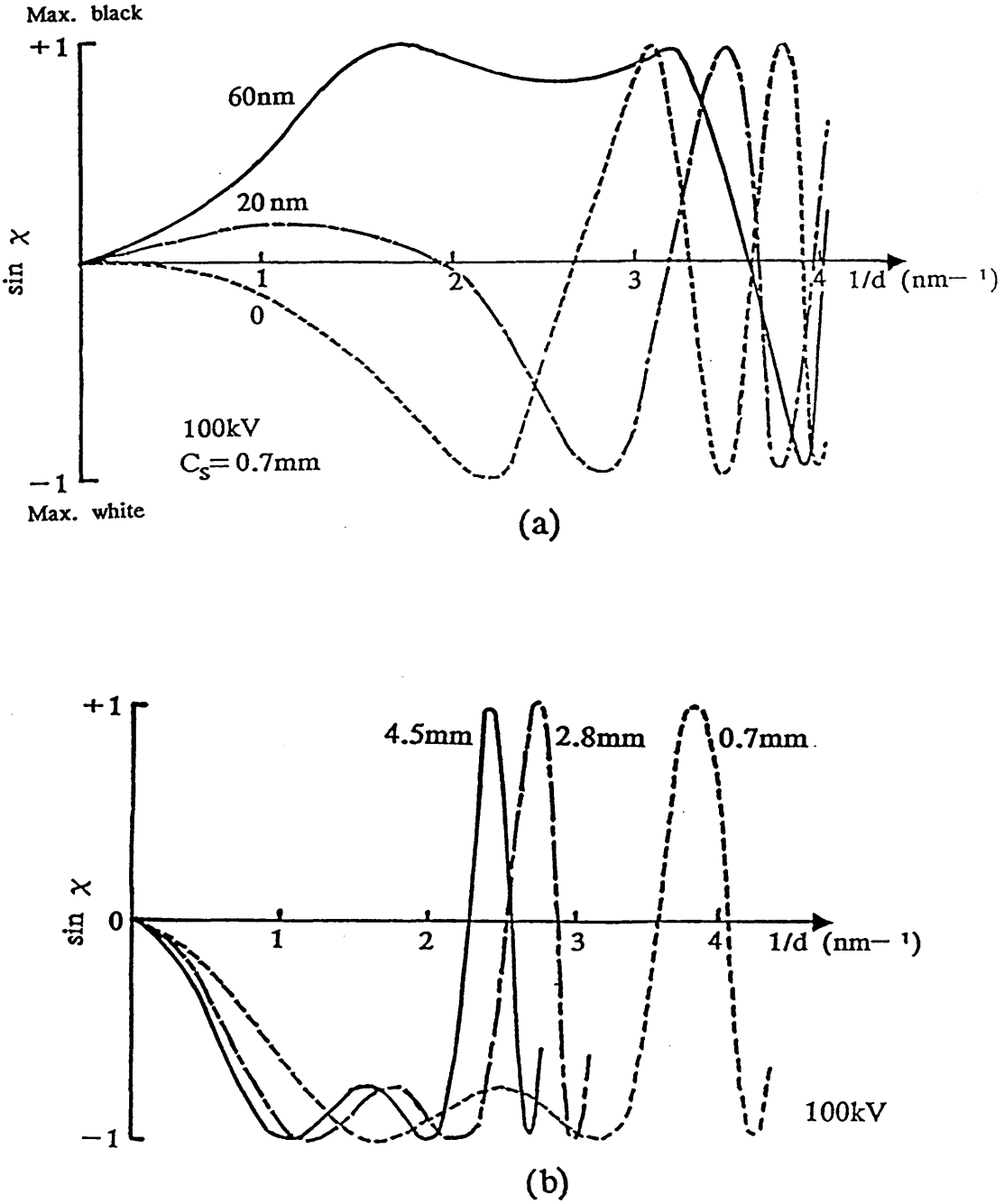

Fig. 1.5: A comparison of PCTF curves: (a) for a range of values of defocus ΔF = 0, 20 and 60nm underfocus, and (b) for various spherical aberration coefficients, C_s = 4.5, 2.8 and 0.7, under optimum defocus condition.

of chromatic aberration and partial coherence as shown below,

$$\sin \chi' = \sin \chi . E_\alpha . E_\varepsilon$$

where E_α is the envelope function representing damping of the PCTF due to partial coherence, and E_ε represents the PCTF modification due to chromatic aberration (Frank, 1973; Fejes, 1977).

Fig. 1.6 shows the same PCTF as in Fig. 1.5, this time incorporating the effects of partial coherence and chromatic aberration envelopes.

Furthermore, effects of multiple scattering of electrons within the sample become important in all but the thinest of crystals. The kinematical calculations lose their validity, and to obtain the exact amplitudes and phases of the scattered waves, the more rigorous dynamical treatment must be applied (Cowley & Moodie, 1957; Lynch & O'Keefee, 1972; Allpress et al., 1972; Goodman & Moodie, 1974; Cowley, 1975; Whelan, 1978).

In the type of 100kV microscope, used for the classical studies, the point resolution was of the order of 1nm (Hillier, 1946; Menter, 1956). Nowadays lenses and goniometer stages can be so constructed (Hawkes, 1980; Kuzuya et al., 1984) as to permit, firstly, a point resolution of 0.2nm (Harada & Watanabe, 1978; Hutchison, 1982) and, secondly, the facility of orienting the specimen so as to allow the imaging of essentially any particular projection of its structure. With such resolution, details of the projected surface atomic structures of certain materials can be assessed (Hutchison, 1978; Bovin et al., 1985; Bursill et al., 1985; Buseck, 1985; Hutchison & Briscoe, 1985; Smith, 1985, 1986; Iijima, 1986; Kang et al., 1987; White et al., 1987).

When microscopes are operated at their highest level of resolution, the object under investigation experiences intense electron irradiation. Problems do, therefore, arise because of specimen

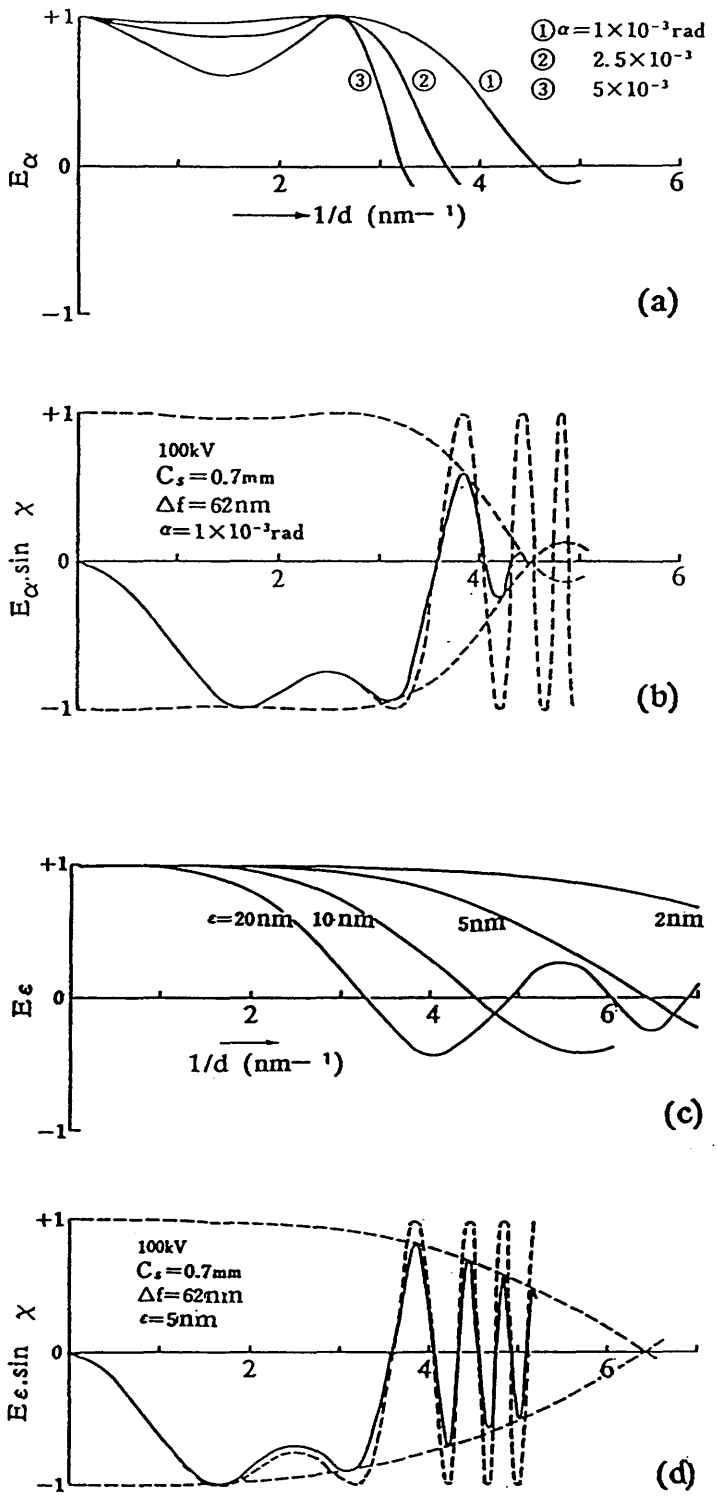

Fig. 1.6: (a) Envelope function E_α and (b) PCTF E_α.sin χ dumped for $\alpha = 10^{-3}$rad. (c) Envelope function E_ε and (d) PCTF E_ε.sin χ dumped for $\varepsilon = 5$nm.

damage, and sometimes it is not possible to fully utilise the resolution capabilities due to the beam sensitivity of the material.

1.1.5– CALIBRATION OF THE MICROSCOPE

Accuracy in calibration of the instrument for high resolution imaging or diffraction pattern is critically important for quantitative microscopy (Haine & Cosslett, 1961; Agar, 1965; Edington, 1974; Hines, 1984). There are two types of calibration:

(a) permanent calibration which is always obtained for a new microscope then checked periodically during its life, or if the instrument is modified. This calibration is normally adequate for most purposes.

(b) imaging system alignment which is a routine (regular) calibration and has to be performed each time one wants to use the microscope.

The following three factors are the most important in controlling image quality:

(a) alignment of the objective lens axis: misalignment of this lens seriously reduces the resolving power of the instrument because of increased spherical aberration, and sensitivity to chromatic aberration.

(b) adjustment of objective astigmatism: astigmatism arises from rotational variation in the focal length of the lens. A compensating field is applied to correct it. This is, conventionally, established when a symmetrical Fresnel fringe is obtained around a hole in a holey carbon support film or when the grain of a carbon support film appears symmetrical (Haine & Mulvey, 1954).

(c) illumination conditions: they influence the quality of both images and diffraction patterns. As the beam intensity increases the following effects occur:

(i) specimen contamination which consists largely of deposition

on the specimen of polymerised hydrocarbons present as residual gases inside the microscope (Hillier, 1948; Ennos, 1953; Fryer, 1979) or non—deposited species present that react with the specimen or adsorb on it (Hartman et al., 1974; Moodie & Warble, 1974).

(ii) local specimen heating increases, producing differential thermal expansion between specimen and support grid which causes more specimen drift.

(iii) electrical charging of the specimen may increase.

(iv) the coherence of the illumination is reduced.

All of these effects reduce resolution in the image. The first three factors above may be minimised by spreading the electron beam, but this reduces the coherence of the illumination and therefore the resolution of the image. Consequently, the choice of illumination conditions is a compromise. Thus the beam must be bright enough to keep exposure times less than about 5s to minimise loss in resolution from specimen drift.

1.1.6— RADIATION DAMAGE

Most materials undergo some form of alteration during examination in the electron microscope. To the extent that such alterations affect the integrity of the information sought from the specimen, they are referred to as 'radiation damage', but, when the effects prove incidental to this information, they are largely ignored.

Radiation damage frequently occurs in minerals and other inorganic materials (Burton et al., 1947; Hobbs, 1979, 1984, 1987; Csencsits & Gronsky, 1987; Dahmen et al., 1978; Sharma et al., 1987; Smith et al., 1987). As the present work is concerned with inorganic materials, it would be useful to consider here the various ways in which electron microscopical examination of the materials can be hampered by their radiation sensitivity and to mention some of

the methods employed to alleviate the problem. This project, however, whilst being directly affected by the problem of radiation sensitivity was, nevertheless, not concerned with a study of the processes involved. The purpose of this section is thus to provide an introduction to the problem of radiation damage.

The subject of radiation damage has been extensively studied by a large number of workers. The consequences and the precursor mechanisms of radiation damage and how they may best be avoided or minimised during examination have been addressed extensively (Burton et al., 1947; Glaeser, 1975; Jones, 1975; Makin, 1978; Fryer, 1979; Hobbs, 1979, 1984; Urban, 1979; Holland et al., 1983; Brown, 1987).

There are basically two avenues for electron beam damage in the TEM:

(a) "Knock–on" displacement from the bulk (McKinley & Feshbach, 1948; Seitz & Koehler, 1956) which involves the interaction of the incident electrons with cores of atoms in the specimen and occurs above critical energy thresholds.

(b) radiolytic mechanisms which involve the transfer of energy from the incident electrons to the electrons in the specimen leading to bond breakage and consequently to the possible alteration of the structure (Hobbs, 1987).

Many attempts have been made to minimise irradiation damage. Encapsulation of organic crystals by carbon films proved to be extremely successful (Fryer & Holland, 1984; Holland, 1984) and image intensifiers have been used to aid focus adjustment at low beam doses (Reynolds, 1968; English & Venables, 1971, 1972; Hart & Yoshiyama, 1975). A system that permits photography of beam sensitive specimens with a minimum dose in the high resolution region has been developed (Williams & Fisher, 1970; Fujiyoshi et al., 1980). This system was named the Minimum Dose System (MDS) and is compatible with the JEOL JEM 1200EX electron microscope used

in this study.

Fig. 1.7 shows the principle of operation of the MDS. Basically, the operation of this system consists of three modes: search, focus and photo. The condenser lens and deflector are designed to be automatically controlled in each mode as required. The specimen is thus subjected to electron beam exposure only for the duration of the photographic exposure.

The MDS has been used effectively in taking HREM photographs of beam sensitive specimens, without sacrificing the resolving power of the electron microscope (Fujiyoshi et al., 1980; Uyeda et al., 1980; Fryer, 1983).

The additional use of either nuclear track emulsion (Kuo & Glaeser, 1975) or x—ray films (Fryer, 1978) for image recording, have also been reported as providing further useful gains (Fryer et al., 1980).

1.1.7— OPTICAL DIFFRACTION ANALYSIS

Optical diffraction analysis is an extension of the Abbe—Porter treatment (Abbe, 1873; Porter, 1906). Following the appearance of the laser in 1960, diffraction became a practical vehicle for data—processing. Details of the method, with applications to microscopy, have been described by many authors (Thon & Siegel, 1970; Horne & Markham, 1973; Power & Pincus, 1974; Pincus, 1978).

The source of illumination is a laser which radiates a coherent monochromatic illumination. The input is a micrograph and the resulting optical diffraction pattern (ODP) is the two—dimensional Fourier transform of the input image. This transform is a graph of the distribution of orientations and spacings of the elements in the input.

The optical bench equipment used in this study is schematised in Fig. 1.8. The source of illumination is a helium—neon laser (Spectra

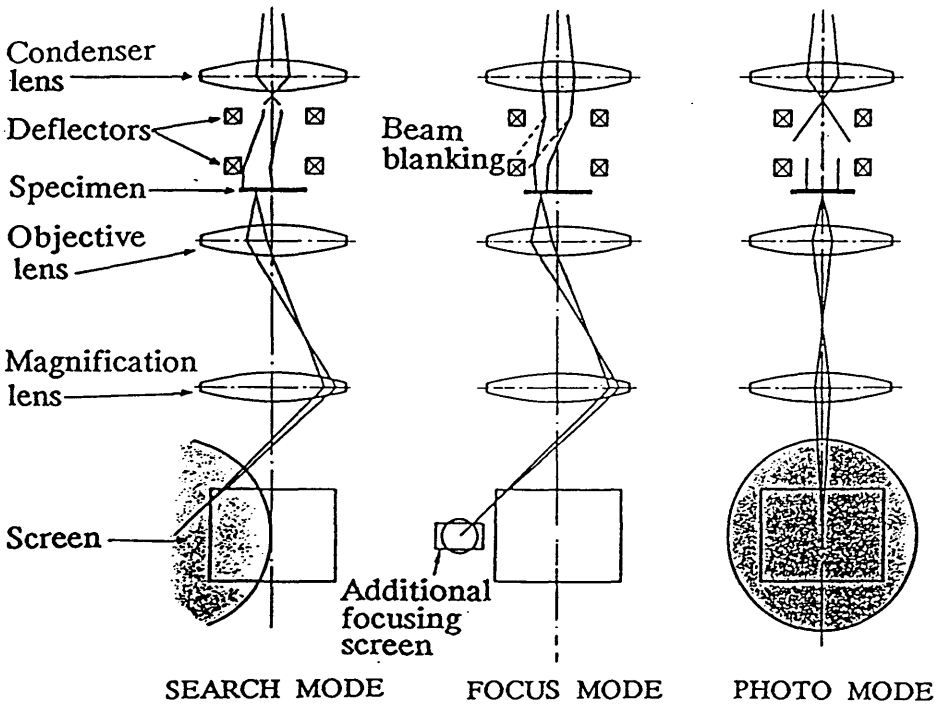

Fig. 1.7: Ray diagram of the minimum dose system.

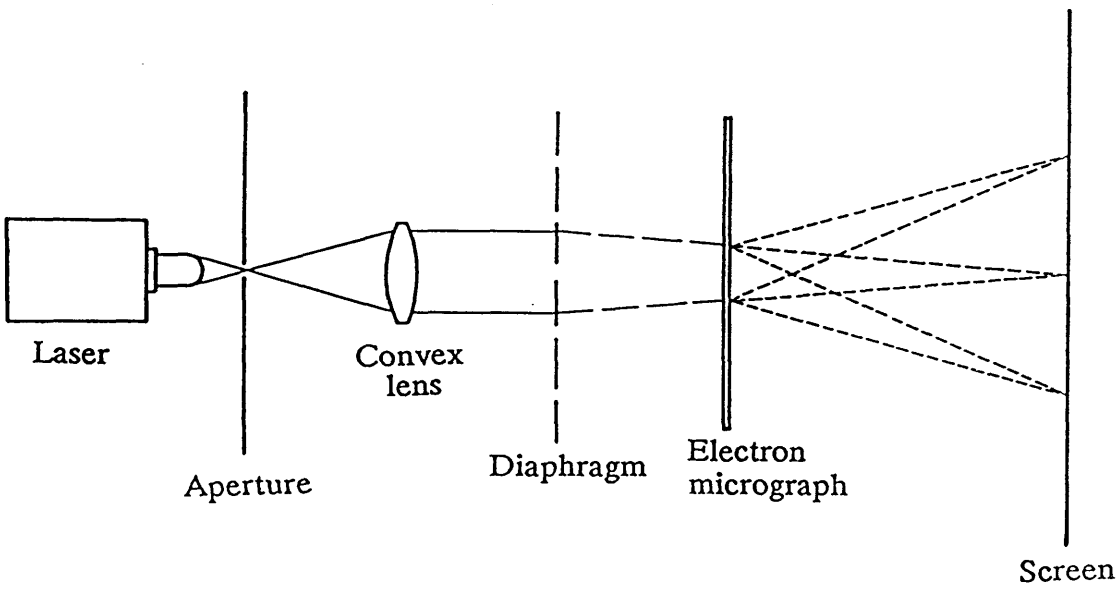

Fig. 1.8: Schematic diagram of bench-mounted optical diffractometer for the analysis of electron micrographs.

Physics, Model 132) in a Polaron optical diffractometer. The system can be used for several purposes. It is much easier to identify the separate periodicities, from the ODP of a micrograph containing overlapping periodic objects. Instrumental defects, such as astigmatism and specimen drift and instability, can be diagnosed and image filtering and reconstruction can be carried out although care must be taken to avoid artifacts (Fryer, 1979).

1.1.8– ELECTRON DIFFRACTION

Electron diffraction patterns (EDP) and microscope images are closely related by the fact that electrons scattered by a specimen provide EDP at the back–focal plane of the electron lens which are in turn Fourier–tansformed so as to form images. Thus the EDP and the intermediate image are always present in the microscope (Fig. 1.9), and the intermediate lens setting determines which is projected onto the image plane. Accordingly, the structure of the specimen can be examined by correlating the EDP and the microscope images. The intermediate lens can be focussed at the back–focal plane of the objective thereby allowing the EDP to be observed on the screen and photographed. If an aperture of diameter D is placed in the first intermediate image plane (Fig. 1.10), only electrons passing through an area D/M on the specimen can reach the final screen (M is the magnification of the objective). The apertures inserted in the plane can typically be as small as 20μm. With an objective magnification of 50 times, a selected area of only 0.4μm in diameter can be analysed. This is called selected area electron diffraction (SAED). The procedure for performing the SAED has been described by Agar (1960) and Phillips (1960), and it is based on the approach of Le Poole (1947).

The geometry of the diffraction (coherent scattering) by crystalline solids is essentially the same whatever the nature of the

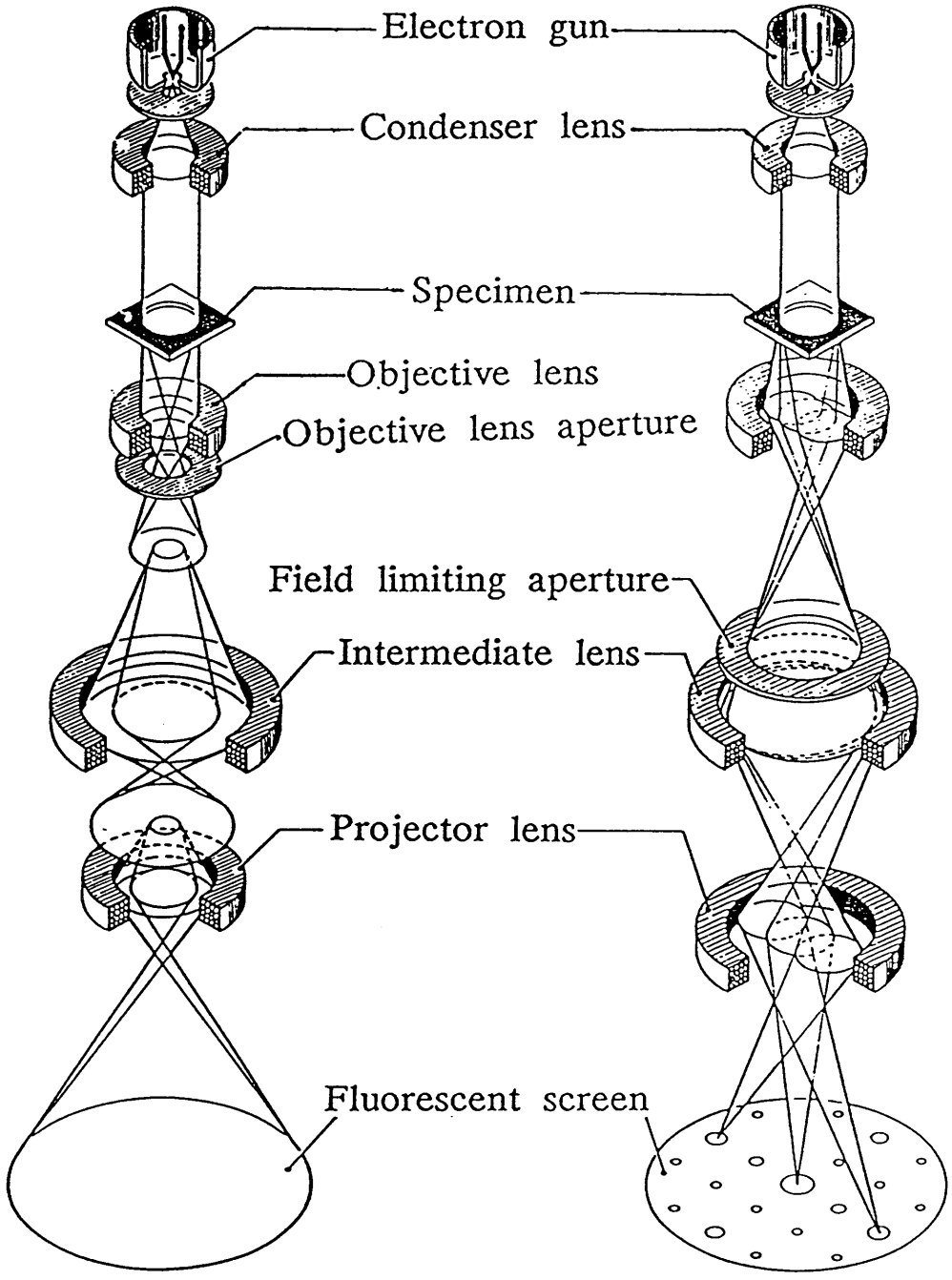

Fig. 1.9: Comparison between image and electron diffraction pattern formation in the transmission electron microscope.

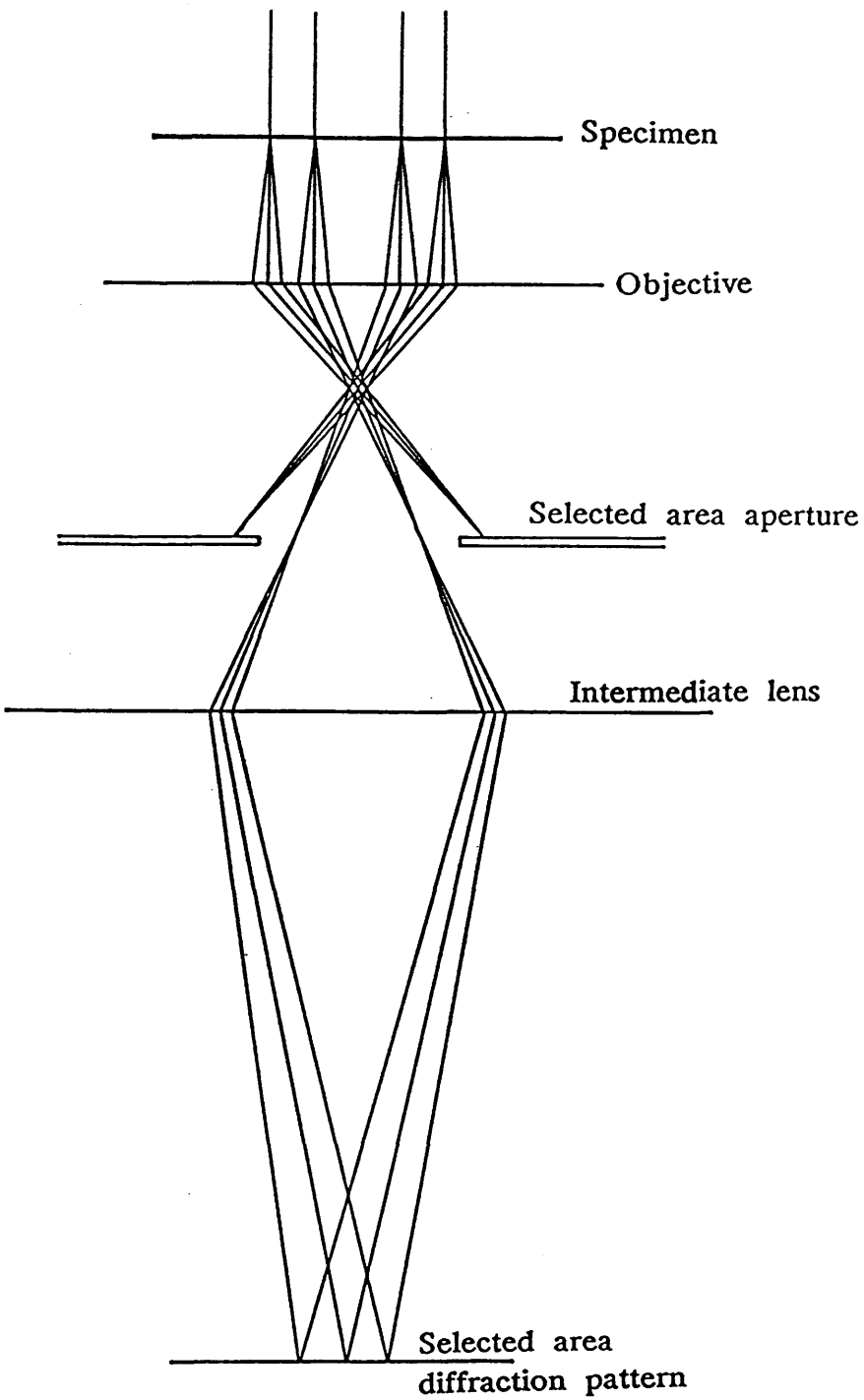

Fig. 1.10: The selected—area aperture ensures that only electrons coming from a chosen region in the specimen contribute to the electron diffraction pattern.

incident wave (electron, x—ray, neutron, etc...). Since the wavelength of an electron is very much shorter than that of x—ray radiation (for a 100keV electron beam, $\lambda = 0.0037$nm whilst for the x—ray K_α line of Copper $\lambda = 0.154$nm), the radius of the Ewald reflection sphere ($1/\lambda$) increases to the extent that it can be assumed that part of the sphere is a plane. Accordingly, by using a reciprocal lattice, a diffraction pattern can be analysed fairly simply.

The formation of the EDP is shown diagrammatically in Fig. 1.11 for a set of lattice planes, spacing d, at an angle θ to the electron beam. If R is the distance between the incident and the diffracted beam at the plane of the photographic plate and L the camera length, which is dependent upon the lens excitation, then:

$$R/L = \tan 2\theta$$

The Bragg law ($n\lambda = 2d \sin \theta$) for first order diffraction ($n=1$) can be applied. The value of θ is very small, as for 100keV electron wave: $\lambda = 0.0037\text{nm} \ll d$, and hence:

$$\tan 2\theta \cong 2\sin \theta \cong 2\theta$$

Therefore, by substitution:

$$R/L = 1/d \quad \underline{\text{or}} \quad Rd = \lambda L = K$$

where K is a constant for a particular set of operating conditions and is called the camera constant. L is the effective camera length, which is equivalent to the physical distance between the diffraction plane and the final image screen, given by:

$$L = f_0 M_1 M_2 M_3$$

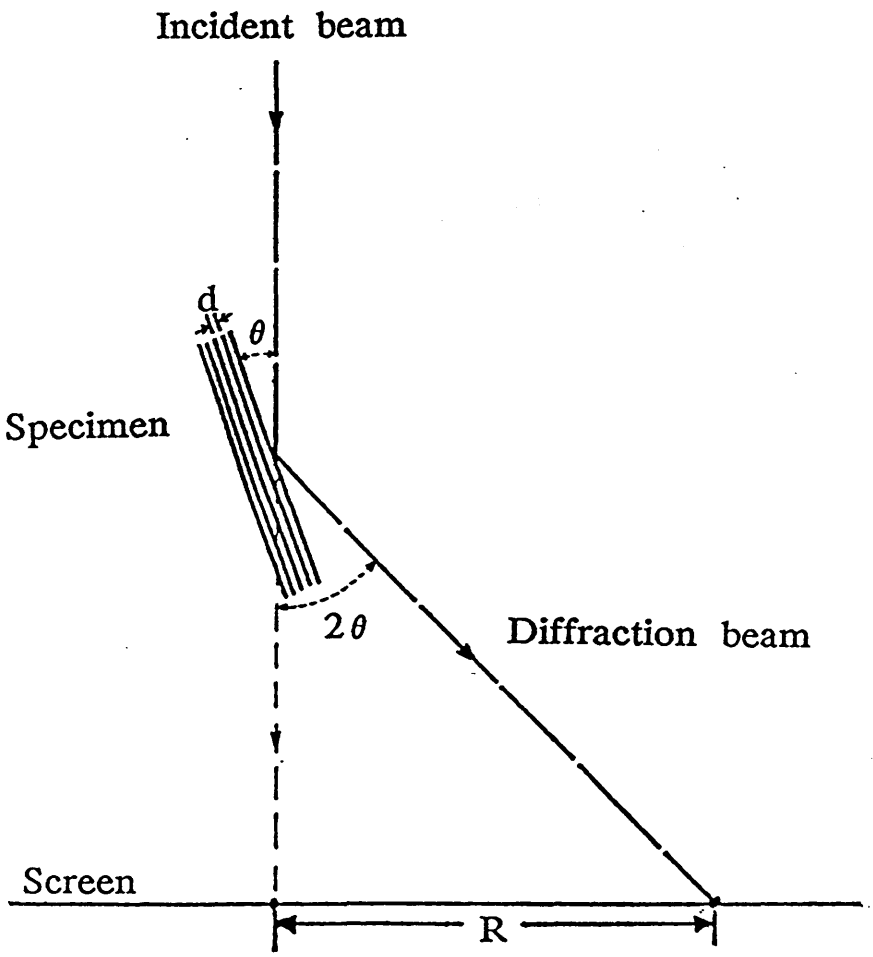

Fig. 1.11: The transmission electron microscope as a simple diffraction camera

where f_0 is the focal length of the objective lens and M_1, M_2 and M_3 are the magnifications of the intermediate and projector lenses.

In practice, a standard specimen of known diffraction spacings (e.g. graphite), is used so that K is obtained and the unknown is studied under the same microscope conditions. Thus:

$$d_{unknown} = K/R_{measured}$$

Generally, the identification of a substance from an electron diffraction pattern is accomplished by comparing electron diffraction data with the available x—ray diffraction data published by the Joint Committee on Powder Diffraction Standards (Philadelphia, USA). If many fine particles are within the area selected, the EDP obtained will be in form of rings, somewhat similar to those observed by x—ray powder diffraction; an individual small particle will give spot single crystal pattern. However, unlike x—ray diffraction where the crystal is rotated, the electron microscope specimen is stationary and therefore only lattice planes approximately parallel to the electron beam give reflections that can be recorded. Thus the relative intensities of the diffracted beam are often different, and in some cases forbidden reflections occur, caused by multiple scattering within the specimen. This restriction, however, can be used to determine the orientation of the specimen.

The EDP contains the structural data, periodicities and orientations for the plane projected normal to the electron beam. Formulae are available which allow calculation of interplanar spacings, angles between planes, zone axes and angles between zone axes for common crystal systems (Andrews et al., 1971; Beeston, 1972; Edington, 1975). Displacements and changes in intensities of specific reflections can provide information about changes within a specimen (Hirsch et al., 1965) and fading of a diffraction pattern under electron beam irradiation gives a correlation between the dimensions

of fine structure in a specimen and its radiation stability (Fryer, 1979).

1.1.9— SAMPLE PREPARATION

Most materials are initially in an unsuitable form for TEM examination and a number of standard procedures have been developed by which specimens may be prepared for examination (Keown, 1974).

In the course of this study, two techniques were used, namely, ultrasonic dispersion and ultra—thin sectioning. This section is concerned with the description of these two techniques.

1.1.9.a— Ultrasonic dispersion

An agate mortar and pestle were used to crush the solid powder before being transferred to a micro test tube containing water or ethanol and placed in an ultrasonic bath. A slurry of the solid/water mixture was then withdrawn from the test tube using a finely drawn Pasteur pipette and a drop placed on a standard 3mm copper grid which had previously been coated with a film of carbon. The grids were then allowed to dry at around 30°C, in a laboratory oven, before transfer to the microscope.

The thin carbon films were prepared by the Bradley process (Bradely, 1954) which is schematised in Fig. 1.12.a. Spectroscopically purified graphite was evaporated on to a cleaved mica substrate using the high vacuum evaporating system schematised in Fig. 1.12.b. The films were then floated off the mica onto distilled water and picked up on specimen grids.

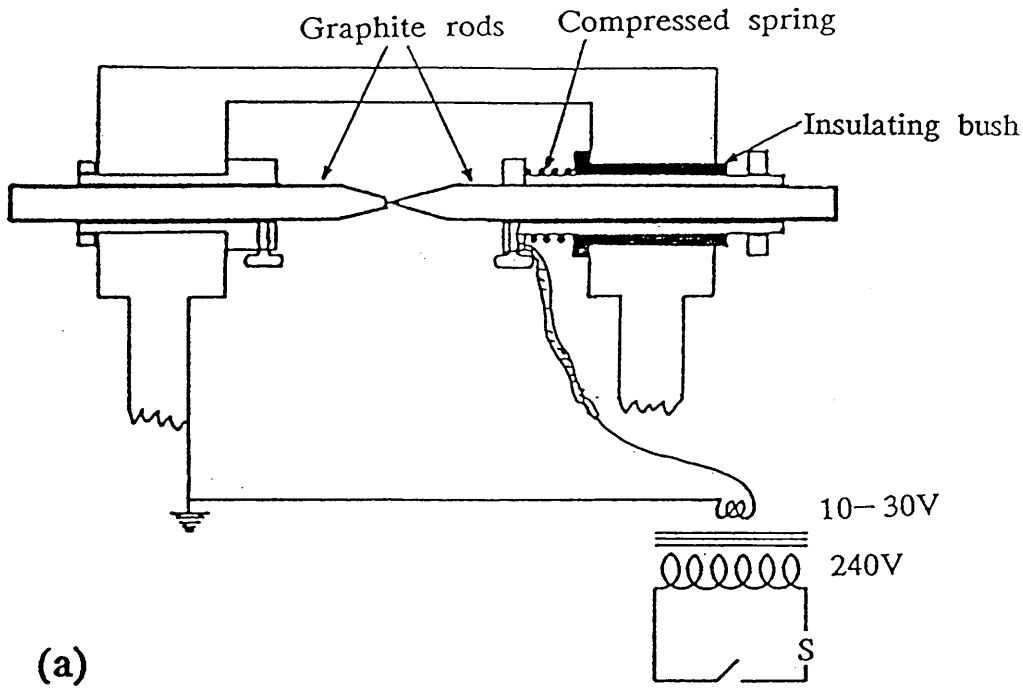

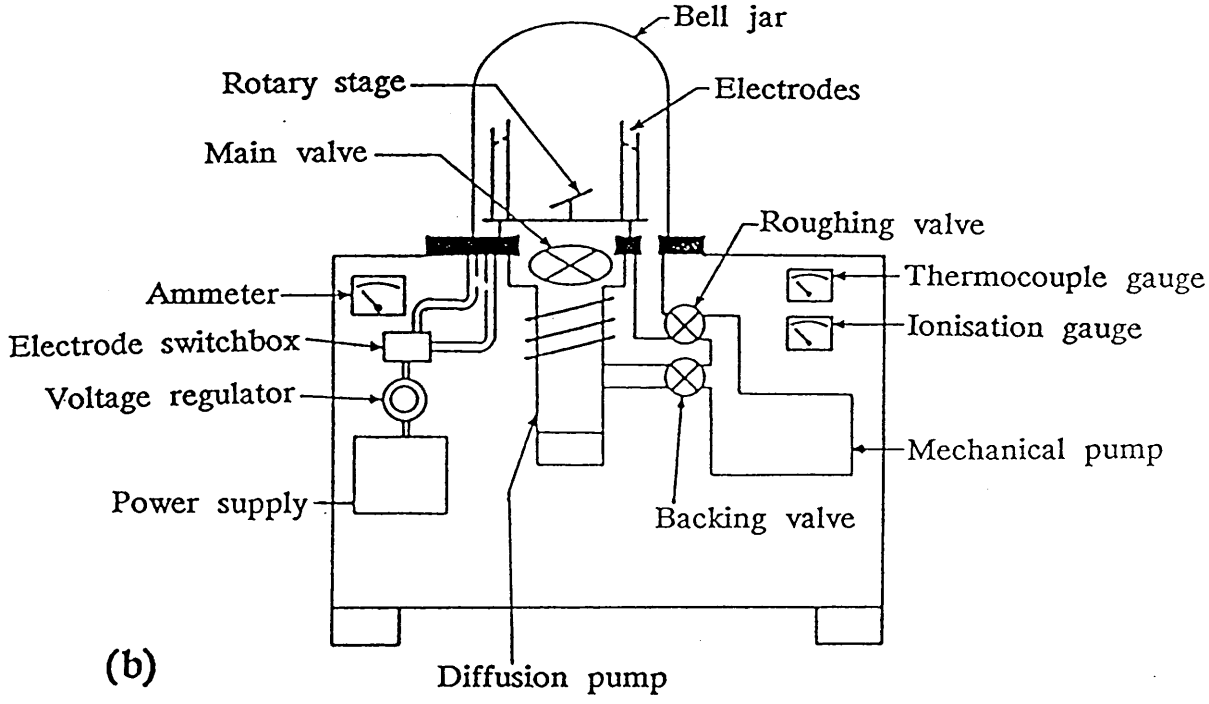

Fig. 1.12: (a) Practical source of evaporation of carbon by the Bradley process, and (b) a standard vacuum evaporator.

1.1.9.b— Ultra— thin sectioning

The procedure evolved in material ultra— thin sectioning, called also ultramicrotomy, has been detailed elsewhere (Reid, 1974; Watt, 1985) and is briefly introduced here.

Ultra— thin sections were prepared by embedding the crystals in Scandiplast metallurgical embedding resin, followed by sectioning, as shown diagrammatically in Fig. 1.13, on an ultramicrotome fitted with a diamond knife. The thin sections were then picked up on uncoated copper grids.

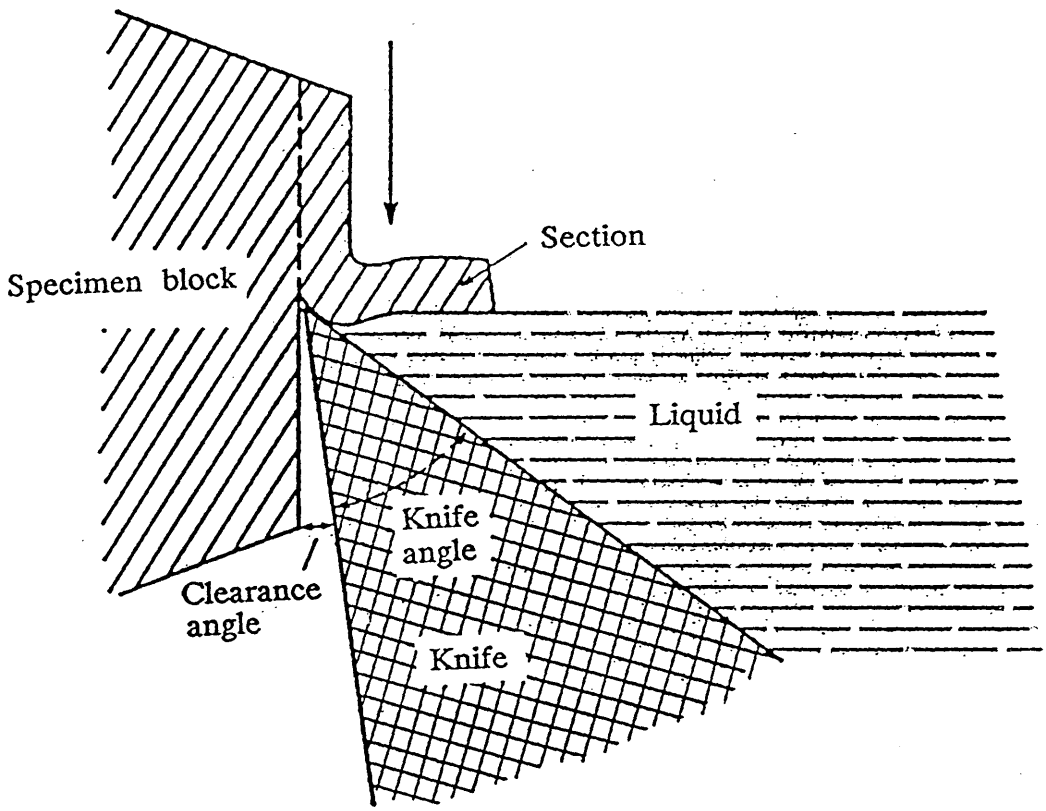

Fig. 1.13: Schematic cross-section of the process of ultrathin sectioning.

*** 1.2 ***

SCANNING ELECTRON MICROSCOPY

1.2.1— INTRODUCTION

The modern development of the scanning electron microscope (SEM) has been almost entirely due to the work started in Cambridge by McMullan (1953) and continued there under the direction of Professor Oatley (Oatley et al., 1965; Cosslett, 1967; Oatley, 1972). The instrument was improved and was commercially available a decade later. The reason for its popularity originally was the strikingly three—dimensional manner in which the surface of solid specimen could be imaged. However, now in addition to imaging, many other modes of operation are possible (Everhart, 1960; Wells, 1974; Heinrich, 1975; Reimer, 1976). These are illustrated diagrammatically in Fig. 1.2. Each one can be used, in conjunction with an appropriate detection system, to provide a particular information about the properties of a specimen.

This chapter considers the mode of operation which has been used in this study. This is the emissive mode which produces micrographs showing the topography or surface shape of the specimen.

1.2.2— PRINCIPLE OF THE INSTRUMENT

The principle of the SEM, used for examining a solid specimen in the emissive mode, is closely comparable to that of a closed—circuit TV system (Fig. 1.14).

In the TV camera, light from the objects forms an image on a special screen, and the signal from the screen depends on the image

intensity at the point being scanned. This signal is then used to modulate the brightness of a cathode—ray tube (CRT) display (van Essen, 1979).

In the SEM, the object is scanned with a fine probe of electrons and the electrons scattered back from the surface are collected and amplified to form the video signal. The emission varies from point to point on the specimen surface and so an image is obtained. The probe is typically a few hundreds of Angstrom units in diameter, and carries a current of between 10^{-10} and 10^{-12}A at a voltage of 2.5 to 50kV. The principle of the method is outlined in Fig. 1.15. The beam emerging from the triode electron gun (usually a tungsten filament) is focussed into a minute probe on the specimen by means of two or, as here, three magnetic electron lenses. It is then deflected in a regular raster by scanning coils situated before the final lens, which is fitted with a stigmator to allow correction of its astigmatism. The specimen surface is arranged at an angle to the beam axis, to ensure a high yield of scattered electrons into the collector. The collector consists of a scintillator, to which a bias voltage may be applied, connected by a light pipe to a photo—multiplier and a video amplifier. The output from the latter is used to modulate a CRT which is scanned synchronously with the scan of the probe on the specimen. For visual display a tube with a long—persistence screen must be used, operating at frame repetition frequency of the order of one per second owing to the weakness of the signal. The electron optical column and specimen chamber are evacuated to a high vacuum of less than 10^{-4}mbar by independent systems of rotary and oil diffusion pumps. For photographic recording, a short—persistence high—definition tube is used, the exposure being made in the form of a single frame scan over a time of 1 to 10 minutes. The magnification obtained is given by the ratio of the width of scan on the tube to the width of scan on the specimen, and is conveniently controlled by varying the latter, as

indicated in Fig. 1.15. The resolving power of the instrument (Simon, 1970) is governed by a number of factors: the shot noise in the electron image, the current density which can be focussed into the probe, the properties of the electron gun, the aberrations of the electron lenses and the properties of the collector system.

In the SEM used in this study, Philips SEM 501B, three magnetic lenses are used, which produce an electron probe of a minimum diameter of about 25nm. This microscope can be operated at an accelerating voltage of 1.8 to 30kV.

1.2.3– IMAGE FORMATION

The mechanism of contrast formation in the image is complicated, depending on the physical and electrical conditions over the surface and on whether the collector receives only the true secondary electrons (of low energy) or the reflected primary electrons (of high energy), or both (Pease, 1971; Everhart & Hayes, 1972). Normally the secondary electrons are much the more numerous and convey more information, but the reflected electrons give greater contrast.

Three factors chiefly determine the image contrast, their relative influence depending on the nature of the specimen examined:

(a) Surface topography: variation in the local angle presented by the surface to the incident beam profoundly affects the fraction of the electrons, primary and secondary, which is collected.

(b) Chemical constitution: The yield of secondary electrons depends on the secondary emission coefficient. For most materials, however, this coefficient differs very little from unity and only rarely does it contribute appreciably to contrast. The yield of reflected electrons, on the other hand, depends on the atomic number of the element encountered. The back scattering coefficient varies by a factor of about six over the periodic table, so that contrast differences will be

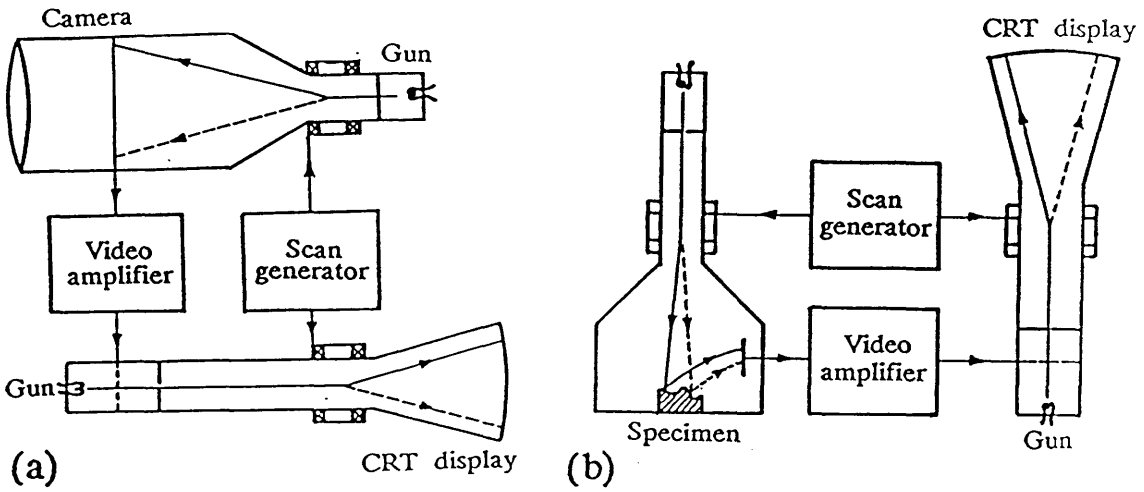

Fig. 1.14: Comparison between (a) a TV closed–circuit system and (b) a scanning electron microscope.

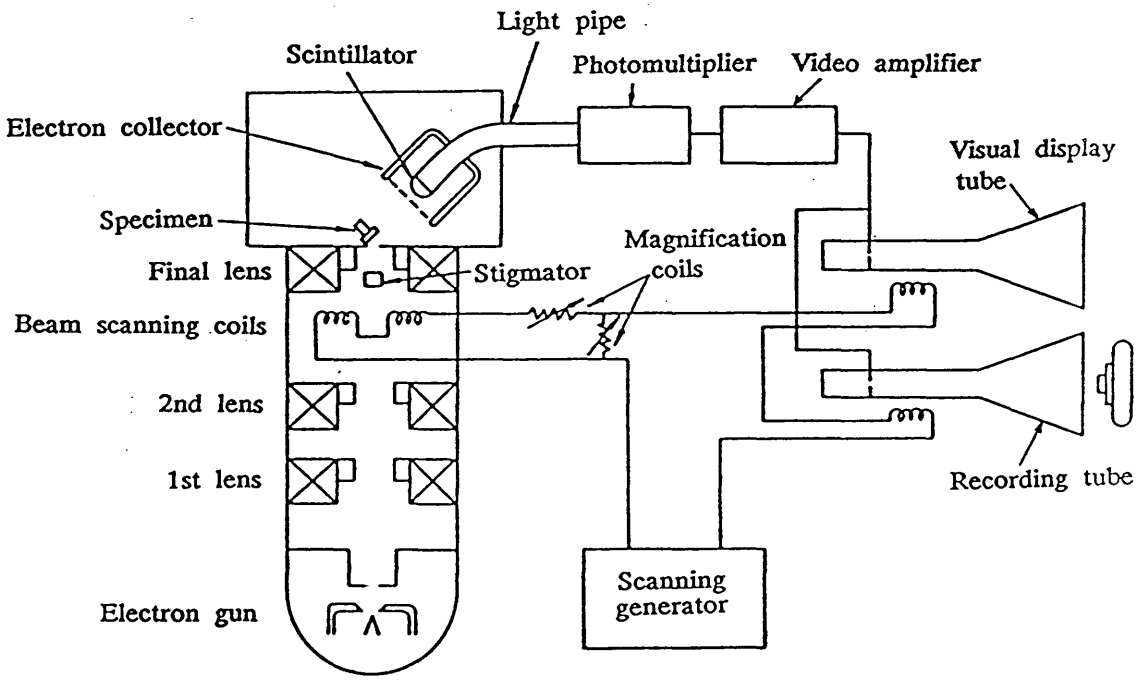

Fig. 1.15: Schematic diagram of the scanning electron microscope.

observable whenever the specimen surface contains elements of widely differing atomic number.

(c) Potential variations: since the secondary electrons leave the specimen with very low energies, their trajectories are strongly influenced by the local potential on the surface, so that the proportion reaching the collector will vary.

1.2.4— SPECIMEN PRAPARATION

Specimens for examination in the SEM were suitably mounted on aluminium stub spindles. The sample in the form of a dry powder was sprinkled onto the surface of a very thin adhesive layer, with either silver paste or carbon cement being used as the mounting medium. They were then coated, by vacuum deposition, with gold in a sputter coater to minimise the severe charging effects that proved to be characteristic of the materials examined. As well as providing a conducting film, the coating layer also performs the useful function of giving enhanced electron emission from the specimen surface.

All samples examined by SEM were pre—coated using an Emscan coater (Kent, U.K.) and run on a Philips SEM 500B microscope (Eindhoven, The Netherlands) operated at an accelerating voltage of 15—30kV, using a spot size of 100nm in diameter.

CHAPTER TWO

THERMAL DECOMPOSITION OF AMMONIUM METAVANADATE

*** 2.1 ***

INTRODUCTION

The oxides of vanadium, in particular vanadium pentoxide, have been studied extensively because of their interesting physical properties (Goodenough, 1971). Vanadium pentoxide is used in a variety of industrial processes because of its catalytic properties (Kosuge, 1967; Seone et al., 1980). Like other d–metal oxides, it is generally a good catalyst for oxidation and ammoxidation processes (Murakami, 1977; Andersson & Lundin, 1979, 1980; Dadyburjor et al., 1979; Andersson, 1981, 1982a; Gellings, 1985; Andersson et al., 1986).

The well–known industrial applications of sulphuric acid have made the oxidation of sulphur dioxide to sulphur trioxide a process of technological importance. A wealth of papers have been published on the vanadium pentoxide catalysed oxidation of sulphur dioxide. They cover basic research and also research applied in the sulphuric acid industry (Kenney, 1980; Urbanek & Trela, 1980).

Vanadium pentoxide is also used in the production of phthalic anhydride by the vapour–phase oxidation of ortho–xylene or naphthalene (Wainwright & Foster, 1979). Table 2.1 lists some of the important oxidation and ammoxidation reactions in which vanadium pentoxide is used.

2.1.1– PREPARATION OF VANADIUM PENTOXIDE

Vanadium (V) oxide can be obtained by burning finely divided vanadium metal in excess of oxygen, but contamination with lower oxides is then common and the main source of its production is the roasting of ammonium metavanadate (AMV) recovered from the

Table 2.1: Oxidation and ammoxidation processes using vanadium pentoxide— containing catalysts.

Reactants	Products	References
Oxidation		
anthracene	anthraquinone	Bhaskarannair et al., 1974 Giancard et al., 1976
benzene	maleic anhydride	Bielanski & Inglot, 1974, 1977
1— butene	maleic anhydride	Kerr, 1966 Stefani & Fontana, 1976
ethylbenzene	styrene	Christmann & Teel, 1974 Belomestnykh et al., 1976
ethylene	acetaldehyde	Evnin et al., 1973 Forni & Giraldi, 1976
ethylene	acetic acid	Seoane et al., 1980
methanol	formaldehyde	Sharma et al., 1980
naphtalene	naphthoquinone phthalic anhydride	D'Alessandro & Farkas, 1956 Pyatnitskii & Golodets, 1975
ortho— xylene	phthalic anhydride	Grabowski et al., 1975 Wainwright & Foster, 1979 Bond & Konig, 1982
propene	acrylic acid	BASF, 1968; Ono et al., 1972
toluene	phthalic anhydride	Martin et al., 1976
Ammoxidation		
3— picoline	nicotinotrile	Andersson & Lundin, 1979, 1980 Andersson, 1981
toluene	benzaldehyde	Murakami et al., 1981 Niwa & Murakami, 1982

hydrometallurgical treatment of some vanadium—containing ores (Morette, 1958).

Due to charge transfer, the oxide, prepared from purified AMV, is bright orange colour; but it may appear reddish—brown when prepared by thermal decomposition of commercial grade AMV in oxygen (Reuter & Jaskowski, 1967) or dark blue if it has not been prepared under fully oxidising conditions.

2.1.2— AIM OF THIS STUDY

The knowledge of the process of thermal decomposition of AMV is important in obtaining the oxide at a temperature at which no appreciable sintering occurs. The thermal decomposition of AMV is however not fully understood and literature reports are conflicting. It was therefore necessary to examine the decomposition process by characterising the intermediates formed during heating as well as the parent material and the final product. The process has been monitored by thermal analyses, infrared spectroscopy, x—ray powder diffraction, scanning electron microscopy and, predominantly, transmission electron microscopy. For the latter, high resolution imaging of the crystal lattices was combined with the minimum dose technique to correlate the structure of the parent AMV with the intermediate products and finally vanadium pentoxide.

2.1.3— THERMAL DECOMPOSITION

Application of the term thermal decomposition to a chemical process is, in general, intended to signify the breakdown of one or more constituents of the reactant into simpler atomic groupings by temperature increase (Galwey, 1975; Brown et al., 1980). In general usage, a more restricted meaning of the definition has become acceptable and is specifically applied to those processes in which

bond redistribution yields a solid residue of different chemical identity from that of the reactant. The thermal decomposition of a solid is, therefore, represented by:

$$A(s) \longrightarrow B(s) + C(g) \qquad (1)$$

where A is the reactant, B and C are the product or products and (s) and (g) specify the solid and gaseous phases, respectively. The stability of the compound obtained by this process, at a temperature T, is determined by:

$$\Delta G^0 = \Delta H^0 - T\Delta S^0$$

where ΔG^0 is the standard free energy change. ΔH^0 and ΔS^0 are the variation of standard enthalpy and entropy, respectively, and do not change much with temperature. Since ΔS^0 is positive for the process (1), ΔG^0 becomes more negative for the decomposition reaction by increase of the temperature. This is the driving force for the thermal decomposition.

One of the main distinguishing features of reactions involving solids is that the chemical transformation occurs within a restricted zone of the solid, characterised by locally enhanced reactivity. This mechanistic representation has been widely applied in interpretation of observations on solid state reactions and there is ample experimental evidence for its existence in most, but not all, systems.

In fact, the reactivity and chemical properties of solids are strongly influenced by the relative immobility of the constituent ions and molecules in the lattice of the reactant phase, and perhaps also in the product phase. Because nominally identical chemical groupings in a solid reactant may occupy different positions in the crystal structure, and because this structure may contain imperfections, it follows that the reactivity of such groups may vary with their

position in the solid. In regions of local distortion and at crystal surfaces, the forces of lattice stabilisation may be relatively diminished, with consequent increase in the probability of reaction. Thus, during rate processes in solids, it is often observed that there are localised regions or sites of preferred onset of reaction. These zones are often referred to as the reaction interface. Such initiation usually occurs at the surface, leading to the development of a zone of preferred chemical transformation, which thereafter progressively advances into adjoining volumes of unreacted material. The initial formation of particles of such a product phase, nucleation, is sometimes possible only at a restricted number of specific surface sites, but in other systems rapid formation of a coherent product layer occurs all over reactant surfaces. Once this product layer is formed there is growth in its volume through an advance at the interface of reactant–product contact.

The study of the thermal decomposition is intended to identify the sequence of steps by which a crystalline reactant is converted into products and also the parameters which control the reactivity of the participating species, including any intermediates formed.

2.1.4– DECOMPOSITION OF AMMONIUM OXO–SALTS

Ammonium oxo–salts resemble hydrates in several respects since, like water, the ammonia molecule may occupy a variety of bonding situations from which it may be removed unchanged. There is general agreement that, for most ammonium oxo–compounds, the first step is proton transfer (Brown et al., 1980). The consequent accumulation of protons in the neighbourhood of the oxygen network of oxyanions results in the elimination of water, accompanied by condensation (or continued condensation) of these anions.

Since the decomposition of many ammonium oxo–salts evolve ammonia and water simultaneously, or consecutively, in a 2:1 molar

ratio, it is often convenient to represent the formula of such salts in the form:

$$m(NH_4)_2O.n(\text{metal oxide}).xH_2O$$

where m,n and x are integers.

Determination of the influence of crystal structure and reactant environment on deammination and dehydration processes is complicated by the several solid phase transformations that are a characteristic feature of many ammonium salts. Sublimation and/or melting may also occur. Deammination and dehydration steps are generally reversible. At high temperatures, however, particularly in the presence of a radical oxide product or a strongly oxidising anion, some of the ammonia initially released may be oxidised (Park, 1972). The final composition of the volatile substances formed may thus be sensitive to the effective contact between gaseous and solid products during reaction. The thermal properties of these compounds have been predicted from the calculations of their enthalpies of formation (Luft, 1955; Shidlovskii, 1960).

Thermal analyses of 26 ammonium salts were reported by Erdey et al. (1964) and more references to ammonium salts are to be found in Duval's book (1953).

2.1.5– THERMAL DECOMPOSITION OF AMV

2.1.5.a– Preparation of AMV

This compound presents a particular interest since it can be precipitated from solutions containing vanadium, thus allowing titration of the latter as well as its purification and preparation of its derivatives.

In solution, an ortho– or pyro– vanadate undergoes a marked

hydrolysis represented by:

$$2VO_4^{3-} + H_2O \rightleftharpoons V_2O_7^{4-} + 2OH^-$$

$$V_2O_7^{4-} + H_2O \rightleftharpoons 2VO_3^- + 2OH^-$$

The equilibrium of the last reaction is displaced from left to right by diminishing the hydroxide ion concentration which can be done by addition of ammonium ions. Sefstrom (1831) found that AMV is deposited when solid ammonium chloride, more than sufficient for saturation, is placed in a solution of a vanadate. Gerland (1877) showed that if the solution was made alkaline with a potassium salt then the precipitated metavanadate is contaminated with the alkali; but with sodium salts, the precipitate was not affected.

Solutions of vanadic anhydride, neutralised by an excess of ammonia and to which an ammoniacal salt has been added, led also to AMV (Berzelius, 1832).

AMV has also been prepared by saturating an ammonia solution with moist vanadium pentoxide and crystallising the reaction product (Lachartre, 1924).

High purity AMV can be prepared by dissolving AMV in hot water, making the solution basic with ammonia and precipitating the AMV with saturated ammonium chloride solution. This operation should be repeated three times. The product obtained is finally dried in vacuum between 30 and 40°C (Morette, 1958).

The AMV crystals are colourless or pale yellow. Berzelius (1832) obtained yellow crystals, probably because they contained impurity of acidic vanadates.

2.1.5.b— Review of the literature

The overall reaction for the thermal decomposition of AMV is:

$$2NH_4VO_3 \longrightarrow V_2O_5 + 2NH_3 + H_2O \qquad (2)$$

This corresponds to a total loss of 22.2% from the original mass. The decomposition does not, however, occur in a single stage, but in several stages and there is little agreement on the intermediates formed. This disagreement stems from several factors. Firstly, the intermediates are very dependent upon the nature of the starting material; secondly, the conditions of temperature and surrounding atmosphere during the decomposition, and thirdly — under certain conditions — the ammonia formed may be oxidised or catalytically decomposed by the vanadium pentoxide formed, giving products other than those in reaction (2). Furthermore, Trau (1962) showed that the geometrical shape of the sample not only influences the character of the decomposition curve and the kinetic equation of the reaction, but can also be responsible for the appearance of new effects in the thermogravimetric traces under suitable conditions.

The early investigators thought that when the colourless crystals of AMV are heated in air, they lose ammonia and acquire a colour varying from lemon—yellow to reddish—brown (Berzelius, 1832; Roscoe, 1870; Norbald, 1875). Roscoe (1870) found that when heated in oxygen, the pentoxide alone remains as a residue, and if heated in a covered crucible, a mixture of vanadium nitride, dioxide, trioxide and one of the $V_2O_4.V_2O_5$ oxides is formed.

Lachartre (1924) studied the decomposition of AMV in vacuum. When heated to 210°C, the salt yields anhydrous ammonium trivanadate "$NH_4V_3O_8$", which is reduced at higher temperatures leading to a compound which is largely constituted of lower vanadium oxides.

Several investigators have used only the mass—loss during a particular stage to characterise the intermediates and have been misled into believing metavanadic acid (HVO_3) to be one of the products (Duval, 1953; Erdey et al., 1964). The same intermediate

has been described by Hakomori (1929) and Duval & Morette (1950) who believed that AMV loses its entire ammonia between 134 and 198°C (Hakomori, 1929) or 134 and 188°C (Duval & Morette, 1950) to give the metavanadic acid which is not stable and starts to dehydrate at 206°C to give vanadium pentoxide at 448°C. However, Tashiro (1931) reported 700°C as the lowest temperature for obtaining vanadium pentoxide whereas Kato et al. (1939) gave 650°C.

Sesbes (1955) postulated a stable intermediate of the composition $NH_3(V_2O_5)2H_2O$ between 280 and 320°C. This compound decomposed above 320°C and was entirely transformed to vanadium pentoxide at 460°C.

Taniguchi & Ingraham (1964) have pointed out that several possible reactions, leading to different intermediates, can give almost the same mass–losses and they suggested the use of the ratio of the amounts of ammonia and water evolved as the factor determining the stoichiometry. They suggested that the intermediate is ammonium hexavanadate (AHV) "$(NH_4)_2V_6O_{16}$".

Dubois & Breton (1938) obtained at 200°C AHV in air, which started to decompose at 275°C leading to vanadium pentoxide at 440°C. In addition, they obtained another intermediate corresponding to the formula:

$$(V_2O_5)_{8.3}(NH_4)_2O$$

Bhatnagar et al. (1972), on the basis of their nitrogen analysis of the intermediate, ruled out the formation of the metavanadic acid as an intermediate. However, it was difficult for them to choose between $NH_3(V_2O_5)2H_2O$, reported by Sesbes (1955), and AHV as suggested by Satava (1959) and Subba Rao & Mulay (1970). After x–ray diffraction and infrared spectroscopy analyses they were inclined to accept AHV as the intermediate compound.

Sas et al. (1978) concluded from their study that the

decomposition of AMV in air proceeds in two stages: between 160 and 230°C the AMV decomposes in air leading to AHV which gives vanadium pentoxide when it decomposes between 270 and 325°C.

Trau (1966), from the results of a thermogravimetric study in air, concluded that an intermediate corresponding to $(NH_4)_2V_4O_{11}$, ammonium bivanadate (ABV), is formed with a mass–loss of 11.1% at lower temperatures (below 180°C); this decomposes in turn, below 210°C to give the hexavanadate:

$$6NH_4VO_3 \longrightarrow (NH_4)_2V_4O_{11} + 2NH_3 + H_2O$$

$$3(NH_4)_2V_4O_{11} \longrightarrow 2(NH_4)_2V_6O_{16} + 2NH_3 + H_2O$$

Finally, above 300°C:

$$(NH_4)_2V_6O_{16} \longrightarrow 3V_2O_5 + 2NH_3 + H_2O$$

However, Lamure & Colin (1964) pointed out that the bivanadate is only formed with small sample masses, slow heating rates and removal of product gases.

Most of the studies of the thermal decomposition of AMV have been dynamic thermal analyses and little attempt has been made to obtain the detailed kinetic and mechanistic information. An exception to this is the work of Deaschanvres & Nouet (1967) arising out of their study of the preparation of oxygen bronzes of vanadium and ammonia (Deschanvres et al., 1965). Using mass spectrometric methods, they studied, over the temperature range 130–180°C, the kinetics of the first stage of the decomposition of AMV in vacuum, which corresponds to a loss of 14.8% of the original sample mass. The solid product has the empirical formulae of AHV sometimes represented as the trivanadate ($NH_4V_3O_8$).

Brown et al. (1974) determined the kinetic parameters and the

thermodynamic data of the various stages involved in the decomposition in various atmospheres and studied the mechanism of the decomposition (Brown et al., 1975).

When Selim et al. (1980) heated AMV in the presence of air, it gave rise to products almost identical with those obtained in vacuo by Brown et al. (1973) at temperatures lower than 350°C. Thus at 180 and 230°C the trivanadate, $3V_2O_5.O(NH_4)_2$, is obtained; which decomposes at 300°C to give the monohydrate vanadium pentoxide. At 350°C the vanadium pentoxide is produced with traces of the monohydrate. The latter disappears at higher temperatures, producing vanadium pentoxide with a well defined crystalline structure.

Although the bivanadate has been suggested as an intermediate, it has not been isolated. Hydrated forms of this compound have, however, been prepared as a precipitate obtained on boiling an aqueous AMV solution (Calvo, 1954) or by adding ethanol to the cooled solution after boiling and filtering (Lachartre, 1924). Attempts to obtain the anhydrous form were unsuccessful (Lamure & Colin, 1964), leading instead to the hexavanadate. Furthermore, studies of the phase diagram of the system $NH_3-V_2O_5-H_2O$ at 30°C (Kelmers, 1961a) and 25°C (Fedorov et al., 1967) indicated that the only stable solid phases were AMV, AHV and vanadium pentoxide. However, the hexavanadates have not the same composition; Kelmers obtained AHV with the composition $(NH_4)_2V_6O_{16}$, whereas the AHV described by Federov was $(NH_4)_2V_6O_{17}$. The difference in composition may be due either to the effect of temperature or to the use of different methods of analysing the solid phase. A number of other ammonium polyvanadates compounds have been reported in the literature. All of these appear to be unstable with respect to AHV or else do not exist at 25 or 30°C.

Although AHV has been proposed as a decomposition intermediate in most studies, there is some disagreement in the reported x-ray powder data for this intermediate (Tarama et al.,

1952; Satava, 1959; Kelmers, 1961b; Lamure & Colin, 1964; Taniguchi & Ingraham, 1964) which has also been prepared from acidified AMV solution (Beltran & Guillem, 1957; Kelmers 1961b).

Controversy over the nature of the final solid product of the decomposition of AMV has arisen largely from the differences in the prevailing conditions of temperature and surrounding atmosphere. Vanadium pentoxide is thought to be formed first, but if the gaseous products (ammonia and water) are allowed to accumulate, as when large quantities of sample are used, or in the presence of atmospheres of reducing agents, lower oxides may be formed (Sata et al., 1968; Sata & Ito, 1968).

2.1.6– DESCRIPTION OF THE STRUCTURES

2.1.6.a– Ammonium metavanadate

The structure of AMV, consisting of tetrahedral chains, was first proposed by Lukesh (1950) and later determined by Synecek & Hanic (1954). To confirm the dimensions of the tetrahedral chains for comparison with those found in potassium metavanadate, Evans (1960) refined the crystal structure of AMV by subjecting the data published by Synecek & Hanic (1954) to least square analysis.

This compound crystallises in an orthorhombic system. Lattice parameters and space group are given in table 2.2, according to different authors who studied this structure.

The tetrahedral chains in AMV are constituted from distorted tetrahedra of oxygen atoms about vanadium, linked by their corners and extending in the a– direction (Fig. 2.1.a). The apices of the tetrahedra in any one chain point in the same direction while the apices of the tetrahedra in adjacent chains along the b– direction point in opposite direction (Fig. 2.1.b).

There are two types of vanadium– oxygen (V– O) bonds in the

Table 2.2: Space group and lattice parameters for ammonium metavanadate.

Space group	a (nm)	b (nm)	c (nm)	References
Pbc or Pbcm	0.496	1.182	0.563	Lukesh, 1950
Pbcm	0.492	1.182	0.585	Synecek & Hanic, 1954
Pmab	0.5827	1.179	0.4902	Evans, 1960

tetrahedral chains. The V—O distance for the two oxygen atoms which are involved in linking the tetrahedra together is 0.181nm, while for the two oxygen atoms which are not shared the V—O distance is 0.166nm. The V—O—V angle is 145°.

The ammonium ions are irregularly surrounded by ten oxygen atoms at distances varying from 0.285 to 0.340nm (Fig. 2.1.c). Seven vanadium to oxygen vectors are shown, while three more with the magnitudes of A, B and C have been omitted. Corresponding sets of oxygen atoms have been labelled 1, 2 and 3. There are clearly several alternative hydrogen bonded configurations of the ammonium ion.

2.1.6.b— Ammonium hexavanadate

Kelmers (1961b) found that AHV as well as rubidium and cesium hexavanadates were all isostructural with the monoclinic potassium hexavanadate as it was described by Block (1960) and are all formed in a similar manner and have similar properties. The crystal structures of both potassium and cesium hexavanadates have been refined by Evans & Block (1966) who presented a better description of the structure. That of AHV has, however, not been refined probably because of the difficulty in obtaining single crystals from this compound. Since AHV is isostructural with both potassium and cesium hexavanadates and because the size of ammonium ion lies between those of potassium and cesium ions, the description of potassium and cesium hexavanadate structure can be applied to that of AHV.

AHV has a layer structure, based on that of potassium hexavanadate. In this structure, the vanadium atoms are in a square—pyramidal coordination with oxygen atoms, with a sixth oxygen atom weakly coordinated through the base of the pyramid. This coordination is similar to that found in several other

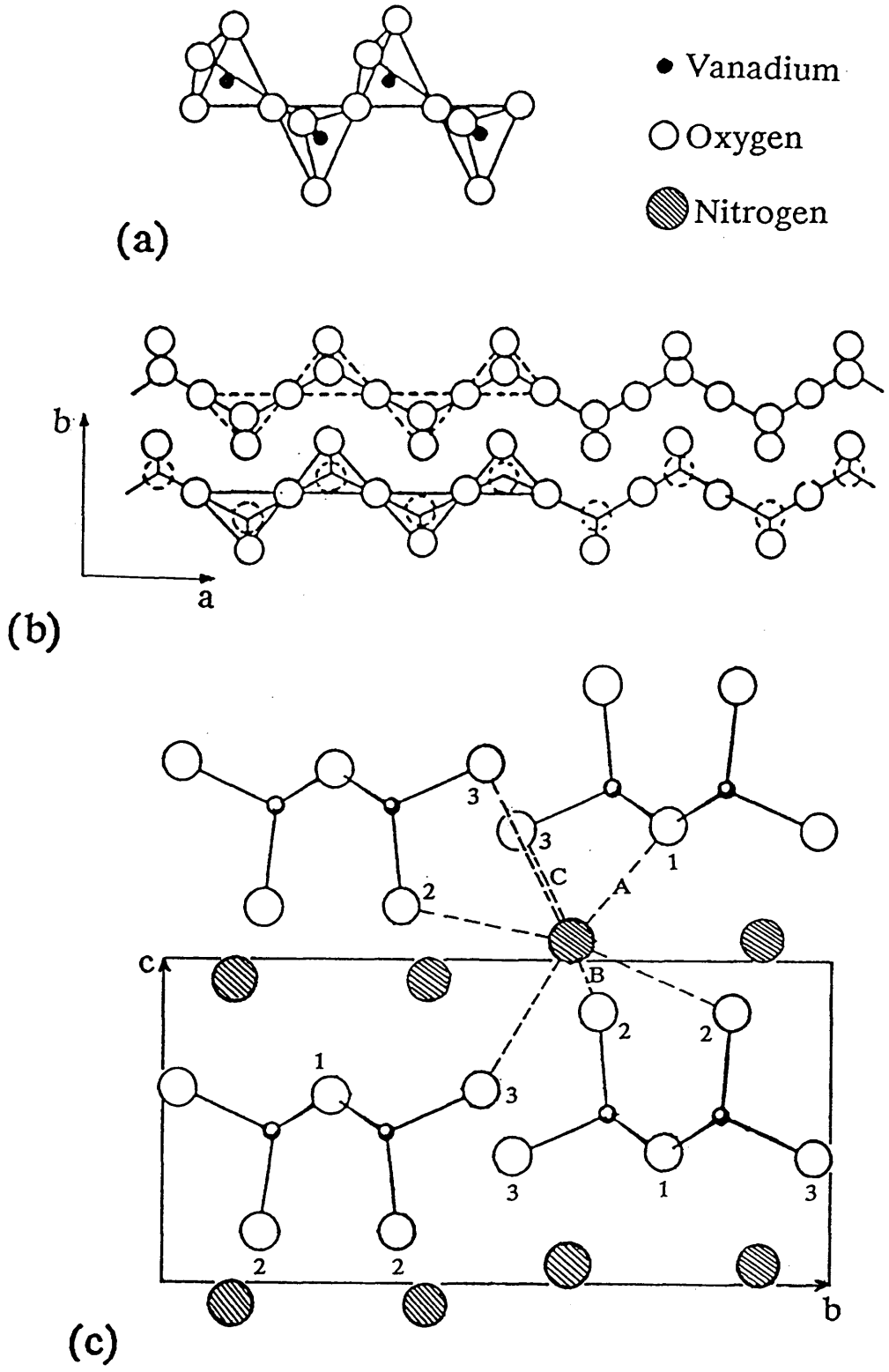

Fig. 2.1: Aspects of AMV structure: (a) linking of the distorted VO_4 tetrahedra; (b) arrangement of neighbouring chains; (c) the environment of an ammonium ion viewed in the a— direction

oxovanadate compounds, for example vanadium pentoxide (Bachmann et al., 1961) and lithium hexavanadate (Wadsley, 1957). One V—O distance (bond type A), in the VO_5 unit, is always considerably shorter than the other four (bond type B) which usually lie very nearly in a plane perpendicular to the short V—O bond. This configuration is illustrated in Fig. 2.2.a. In the square pyramid, the short V—O bond is so outstanding that Hanic (1958) has suggested that the diatomic group should be regarded as a discrete VO^{3+} ion. Evans & Mrose (1958) have suggested that this bond is practically a pure double bond and that the four basal ligands each represent the three—quarters bond of vanadium (V) or one—half bond for vanadium (IV).

Each two square pyramids share a base edge to form V_2O_8 units, which are slightly distorted from the ideal form illustrated in Fig. 2.2.b, with their apices directed opposite to each other. These double groups are joined into zig—zag chains along the b—axis by sharing corners through oxygen atoms (O_2), and these chains are linked into sheets by V—O groups represented by V_1 and O_1 as shown in the projection of the structure along the b axis illustrated in Fig. 2.2.c. The V_1-O_1 distance is somewhat shorter than the apical V—O distance V_2-O_2, while the opposite V—O distances (V_1-O_2 and V_2-O_4) through the pyramidal base are correspondingly longer and shorter. This group appears to be a characteristic feature of many oxyvanadium (V) structures. It can be clearly discerned in potassium, cesium (Evans & Block, 1966) and lithium (Wadsley, 1957) hexavanadates, vanadium pentoxide (Bachmann et al., 1961) and $Na_3V_6O_{15}$ (Wadsley, 1955).

The ammonium ions would occupy positions between the layers, in irregular 12—fold coordination with neighbouring oxygen atoms.

In potassium hexavanadate the potassium—oxygen distances vary from 0.270 to 0.355nm, and in cesium hexavanadate the cesium—oxygen distances vary from 0.299 to 0.368nm. Similar values would

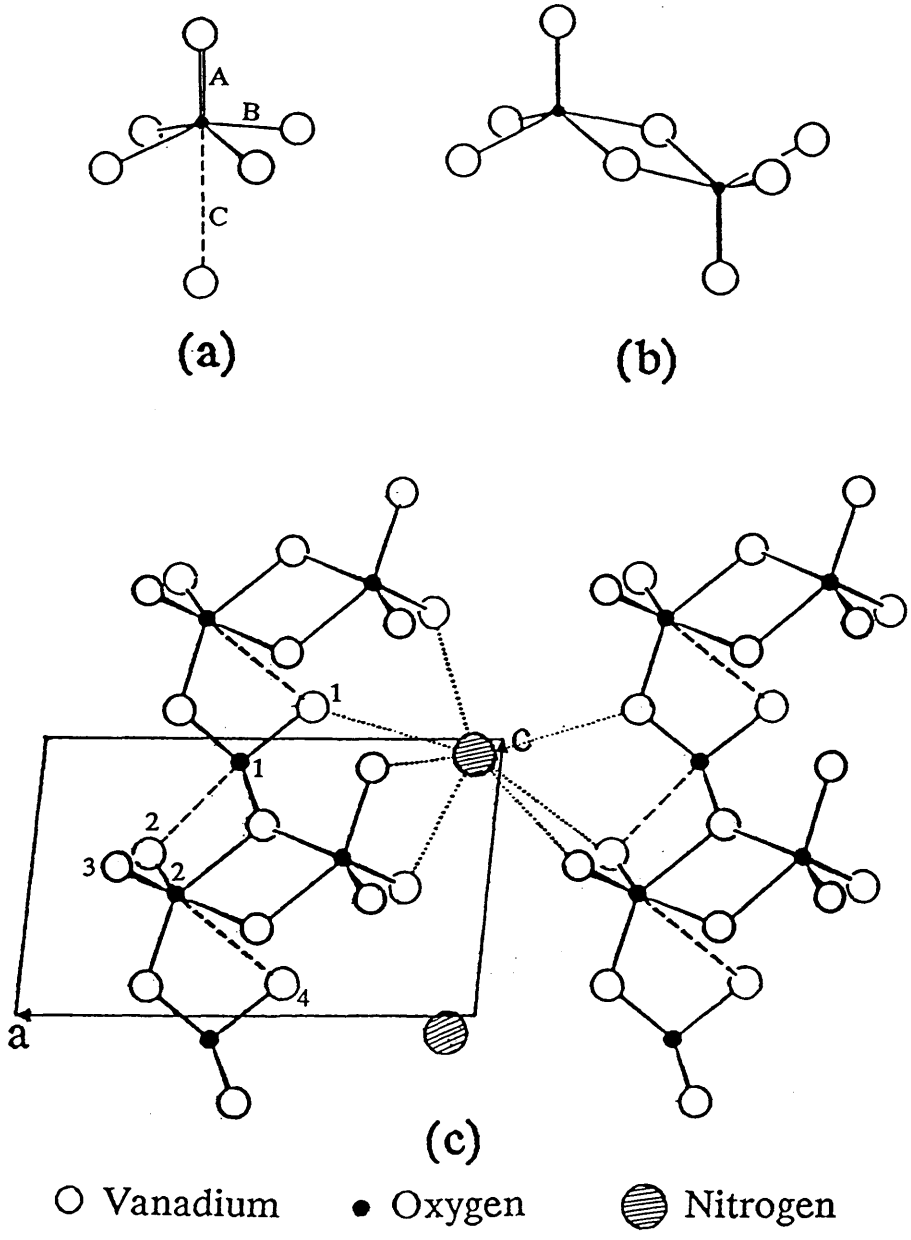

Fig. 2.2: (a) Square pyramid coordination of oxygen atoms around vanadium in hexavanadates; (b) double V_3O_8 groups found in cesium hexavanadate; (c) projection of the structure of cesium hexavanadate, which is isostructural to AHV, along the b– axix.

be expected for AHV since the radius of ammonium ion is somewhere between those of cesium and potassium ions. The marked increase in the average cation—oxygen distances, in going from potassium to cesium hexavanadates, corresponds to the increase in the crystallographic a-axis, as pointed out by Kelmers (1961b) (Fig. 2.3). It is also apparent from Kelmers' observations, that sodium and lithium analogues cannot be prepared. The special layer structure found for the hexavanadates probably requires the presence of relatively large interlayer cations to be stable. The space group is $P2_1/m$ and the system is monoclinic with the lattice parameters, given by Evans & Block (1966) and based on powder data published by Kelmers (1961b) being a = 0.7881nm, b = 0.8423nm, c = 0.5005nm and β = 96°28'.

Levanto (1969) deduced from the powder diffraction data the lattice parameters: a = 0.787nm, b = 0.843nm, c = 0.501nm and β = 96°45'.

2.1.6.c— Vanadium pentoxide

The first investigation of the orthorhombic structure of vanadium pentoxide was performed by Ketelaar (1936). This author interpreted the structure in terms of chains of deformed tetrahedra of oxygen atoms around vanadium atoms, sharing corners and extending parallel to [001] direction, and cross—linked by additional corner sharing along [001] direction to form two—dimensional nets. In the tetrahedron, vanadium—oxygen distances are ranging from 0.157 to 0.183nm. Ketelaar does, however, point out that the inclusion of an oxygen atom in an adjacent cell and at the slightly greater distance of 0.202nm from vanadium, would increase the coordination of vanadium to the five—fold. Machatschki (1936), on morphological grounds, contends that Ketelaar's structure should be considered solely in terms of single chains of tetrahedra parallel to [001] linked

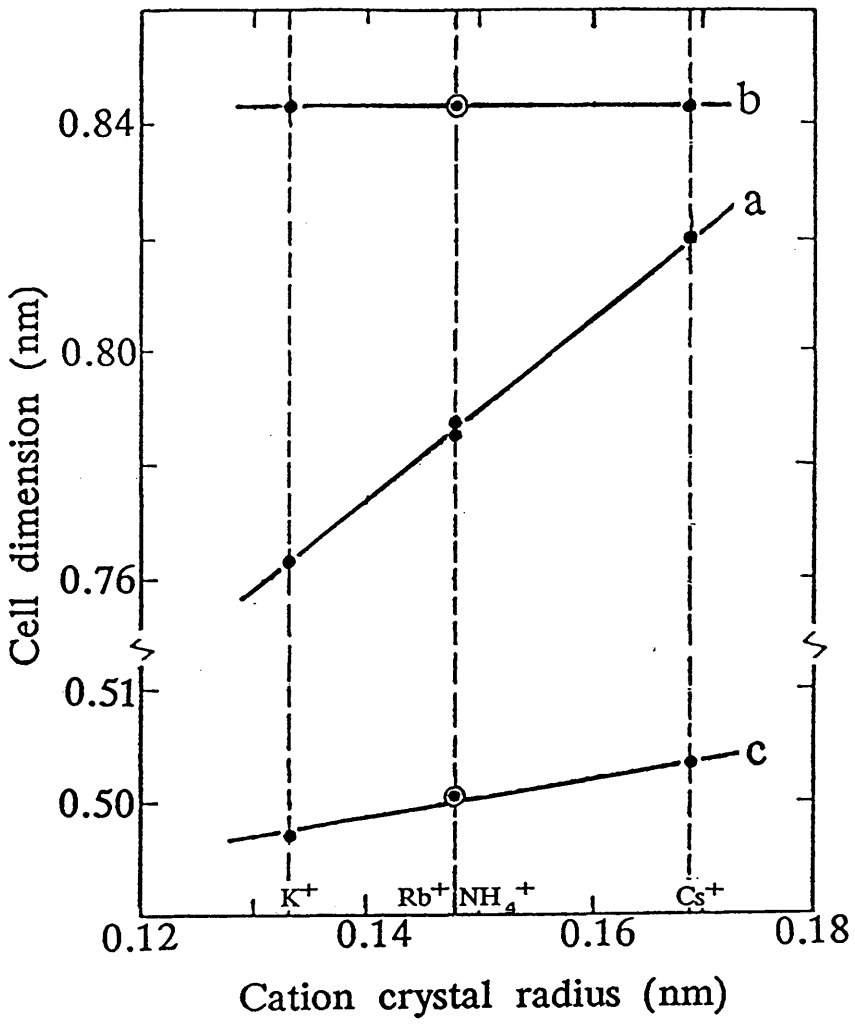

Fig. 2.3: Variation of cell dimensions with radii for potassium, rubidium, ammonium and cesium hexavanadates.

laterally along [100] by oxygen bridges.

Dissatisfied by some aspects of the crystal structure, especially with the very short distance (0.214nm) between certain pairs of oxygen atoms in the structure proposed by Ketelaar, Bystrom et al. (1950) have proposed in this orthorhombic network a new structural description based on trigonal bipyramids sharing edges and corners, making vanadium pentoxide sheets. They included in these coordination polyhedra the oxygen atom at 0.202nm from vanadium which has been rejected by Ketelaar but is only 0.188nm from vanadium in their structure; and they retain another oxygen atom at 0.183nm from vanadium in Ketelaar structure but which is 0.202nm from vanadium in their own. Thus they consider the oxygen atoms to be five—fold coordinated in vanadium pentoxide with V—O distances ranging from 0.154 to 0.202nm. Bystrom et al. also draw attention to the fact that very distorted octahedral coordination could be achieved by the inclusion of a sixth oxygen atom at the much greater V—O distance of 0.281nm, but this could imply stronger bonds between successive V—O layers along [010] than would be expected from the perfect {010} cleavage. They described the structure of vanadium pentoxide, more conveniently, as composed of double, or zig—zag, chains of trigonal bipyramids sharing edges along [001] and cross—linked along [100] through shared corners.

Magneli & Blomberg (1951) claim good agreement with vanadium and oxygen parameters of Bystrom et al. (1950) and the Natl. Bur. Stand. (1958) gives cell parameters in which b and c axes are permuted.

Later Bachmann et al. (1961) confirmed the work of Bystrom et al. without any significant discrepancies. The structure, according to them, is built up from distorted trigonal bipyramidal coordination polyhedra of oxygen atoms around vanadium, which share edges to form zig—zag double chains along [001] and are cross—linked along [100] through shared corners, thus forming sheets in the (010) plane.

In the course of the investigations carried out by Enjalbert & Galy (1986), by insertion of molecular complexes into the slabs of vanadium pentoxide, structural information based on accurate data collection and full matrix least squares refinement was used to render more precise the network coordination mode of vanadium atoms.

The bond lengths and angles determined by these authors agree well with the earlier structural determinations (Bystrom et al., 1950; Bachmann et al., 1961). Compared with these fundamental models, however, the oxygenated coordination polyhedron around vanadium atoms should be described, according to Enjalbert & Galy, in terms of a square instead of a trigonal pyramid as indicated by the previous authors. Thus the structure of vanadium pentoxide possesses layers built up of VO_5 square pyramids. These square pyramids are linked through a base corner to form V_2O_8 units which are linked through a third base corner into chains in the a-direction and into layers parallel to (001) plane through the remaining base corner (Fig. 2.4). The details of the association of coordination polyhedra around vanadium atoms are shown in the lower part of Fig. 2.4. In the c direction, the vanadium pentoxide sheets are held together via weak V—O interactions ($V-O_6$). The weak V—O bonds, with a distance of 0.2791 nm, cannot be treated as a real bond. They are not drawn in Fig. 2.5, representing a projection of this structure onto the (010) plane, in order to show more clearly that the cleavage occurs perpendicular to the c axis.

Fig 2.6 represents a projection of the orthorhombic structure of vanadium pentoxide onto the (001) plane.

The cell parameters and space group given by the different authors, who studied vanadium pentoxide structure, are listed in table 2.3.

In this study, the notation adopted by Enjalbert & Galy (1986) for vanadium pentoxide lattice parameters was used. In this notation

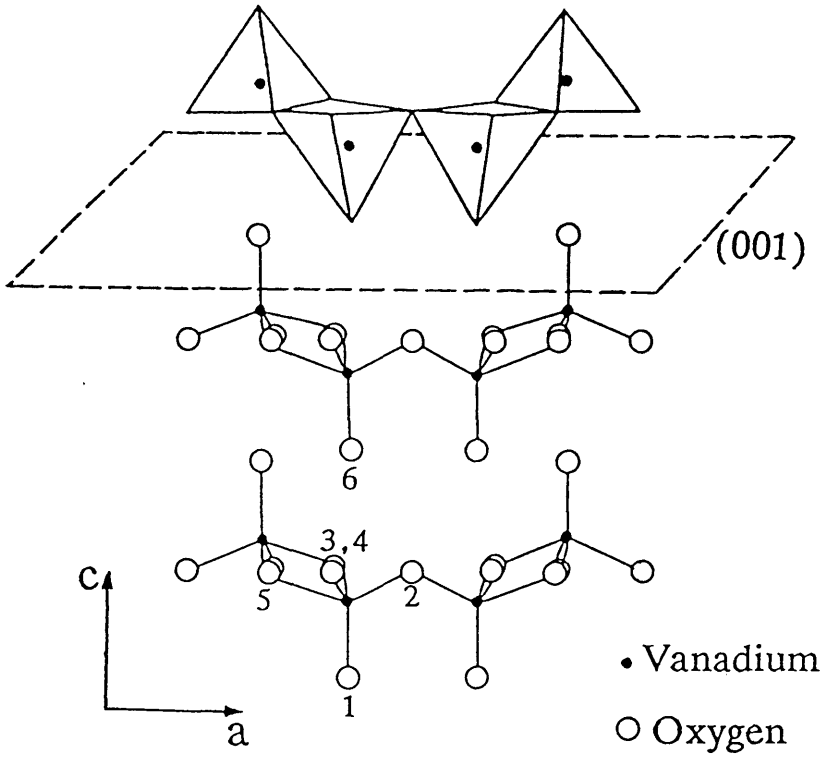

Fig. 2.4: Crystal structure of vanadium pentoxide projected onto (010) plane. The top row shows the linking of square pyramids. The six–fold coordination of vanadium by oxygen atoms, labelled 1 to 6, is also shown.

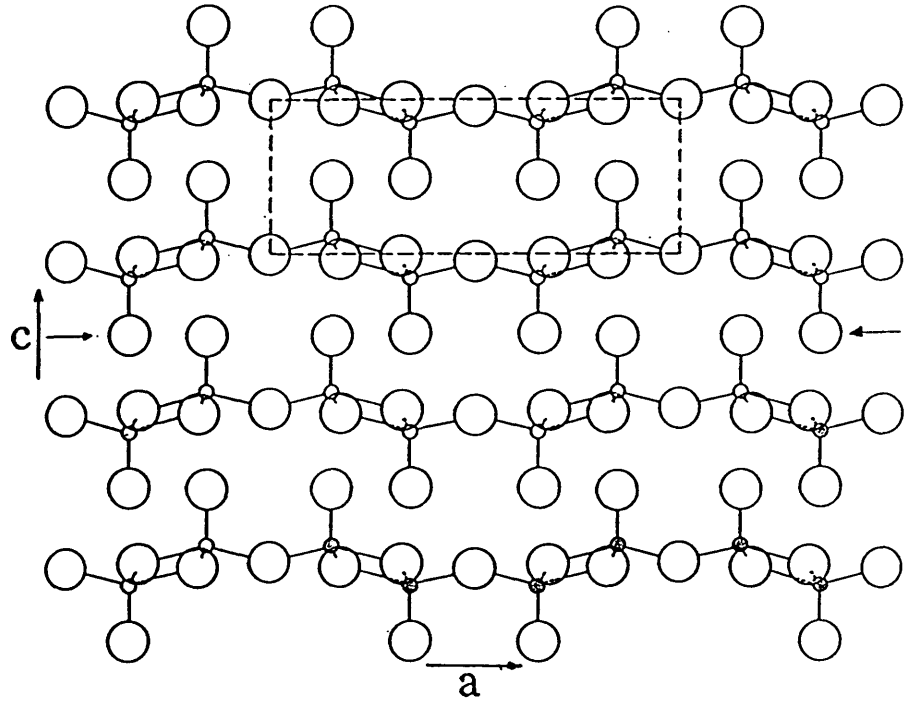

Fig. 2.5: Projection of vanadium pentoxide structure onto the (010) plane.

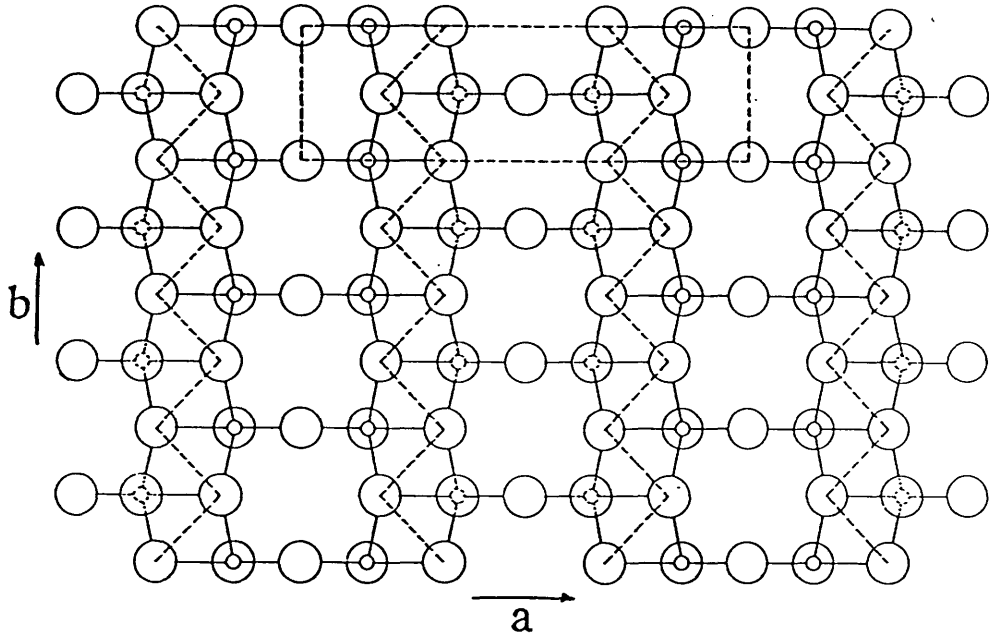

Fig. 2.6: Projection of vanadium pentoxide structure onto the (001) plane.

Table 2.3: Crystallographic data for vanadium pentoxide as given by different authors.

Space group	a (nm)	b (nm)	c (nm)	References
$Pmn2_1$	1.148	0.436	0.355	Ketelaar, 1936
Pmnm	1.1519	0.4373	0.3564	Bystrom et al., 1950
	1.1505	0.4373	0.3564	Magneli & Blomberg, 1951
Pmmn	1.151	0.3559	0.4371	Nat. Bur. Stand., 1958
Pmnm	1.1510	0.4369	0.3563	Bachmann et al., 1961
Pmmn	1.1512	0.3564	0.4368	Enjalbert & Galy, 1986

the b and c axes are permuted in comparison with the nowadays less–common notation of Bachmann et al. (1961).

*** 2.2 ***

EXPERIMENTAL

2.2.1– MATERIALS

2.2.1.a– Ammonium metavanadate

The AMV powder used was of 99.99% purity (Aldrich Chemical Co., Milwaukee, USA). Its analytical data, according to Aldrich, are given in table 2.4.

2.2.1.b– Air

Industrial grade air supplied by B.O.C. Ltd. (Brentford, U.K.) was used as the carrier gas. Its purity was 99.99%.

2.2.2– SAMPLE PREPARATION

Samples were prepared at selected temperatures for subsequent study consequently to the thermogravimetric results. The AMV was heated in a stream of air (50ml/min) for two hours at temperatures of 140, 190, 230, 320 and 400°C. The furnace employed was a Baird and Tatlock (London, U.K.) M193 laboratory tubular furnace. Small silica glass boats, containing AMV samples, were inserted into a silica glass tube of 42mm internal diameter. The furnace temperature was monitored by means of a tungsten/tungsten– rhenium thermocouple positioned inside the silica glass tube.

Table 2.4: Analytical information on the gold label ammonium metavanadate of Aldrich Chemical Co.

Appearance: Pale yellow crystalline powder and chunks

Purity: 99.99%

Elemental analysis	Vanadium	43.3%
Trace analysis (ICP)	Element	ppm
	Silicon	55
	Iron	25
	Titanium	25
	Magnesium	0.4

2.2.3– THERMOGRAVIMETRY

The instrument used for this study was a du Pont (Wilmington, USA) 990 analyser combined with a du Pont 951 thermogravimetric unit. The samples were suspended in platinum boats. A stream of air, at a flow rate of 50 ml/min, was passed over the material as it was heated. The samples were analysed in the temperature range of room to 800°C, using a heating rate of 5°C/min. The temperature was measured using a chromium/aluminium thermocouple.

2.2.4– DIFFERENTIAL THERMAL ANALYSIS

Differential thermal analysis (DTA) on powder samples were performed with a Shimadzu (Kyoto, Japan) 30–H unit. The curves were recorded over a range of temperature up to 500°C at a heating rate of 5°C/min in a dynamic atmosphere of air (50 ml/min) using small portions of test samples (10–20mg). Highly sintered alumina (α–Al_2O_3) was used as a reference material.

2.2.5– X–RAY DIFFRACTION

The x–ray diffraction (XRD) equipment used was a Philips diffractometer (Eindhoven, The Netherlands), which consisted of an x–ray generator and a diffractometer unit. The powdered samples were mounted on adhesive tape, rolled into a cylinder and placed in the XRD equipment. They were rotated through angles of 3–70° (two theta values) whilst being exposed to copper K_α radiation (λ = 0.154178nm) at 40 kV and 20mA. The resulting XRD patterns were recorded on a chart recorder operating at 400 counts per second. The lattice spacings were subsequently calculated using the Bragg equation:

$$2d \sin \theta = \lambda$$

2.2.6– INFRARED SPECTROSCOPY

The infrared (IR) absorption spectra reported in this study were registered on Perkin Elmer 580–B spectrophotometer (Beaconsfield, U.K.), equipped with a model PE–3500 data station. Samples were examined in the solid state in the form of thin discs containing approximately 2mg of sample and 300mg of spectroscopic potassium bromide (BDH Chemicals Ltd., Poole, U.K.). Spectra were recorded in the range 4000 to 250cm^{-1}. However, some of the spectral presentations do not include all of this range, as no information of importance in the work was to be found therein.

*** 2.3 ***

RESULTS AND DISCUSSION

2.3.1— THERMOGRAVIMETRY

The TG curve for AMV (Fig. 2.7) showed an overall weight loss of 22.5% at ca. 320°C occurring in three overlapping stages with maximum rate losses at 190, 230 and 280°C. The commencement of mass loss was observed at 150°C. The first distinct step which occurs between 150 and 190°C involves a weight loss of ca. 11.5% and is consistent with the evolution of ammonia and water via the reaction:

$$4NH_4VO_3 \longrightarrow (NH_4)_2V_4O_{11} + 2NH_3 + H_2O$$

(Theoretical weight loss, 11.10%). The second step, where a 15.7% weight loss is noted, takes place between 190 and 230°C and can be assigned to the formation of AHV following the reaction:

$$3(NH_4)_2V_4O_{11} \longrightarrow 2(NH_4)_2V_6O_{16} + 2NH_3 + H_2O$$

(theoretical weight loss, 14.83%). The third and final step brings the weight loss up to 22.5% and can be unambiguously assigned to the formation of vanadium pentoxide at 320°C (theoretical weight loss, 22.23%).

$$(NH_4)_2V_6O_{16} \longrightarrow 3V_2O_5 + 2NH_3 + H_2O$$

The TG results thus suggest a largely complete transformation of

AMV to vanadium pentoxide by 320°C via the formation of thermally unstable intermediates. On the basis of relevant gravimetric calculations that are a near fit to the observed mass losses, the intermediates may be identified as ABV and AHV. The total mass losses, temperature ranges and the empirical formulae of the products of each stage are given in table 2.5.

This result is in agreement with some earlier work (Dubois & Breton, 1938; Trau, 1962; Lamure & Colin, 1964; Brown & Stewart, 1970). Selim et al. (1980) derived also similar results, with the distinction that the monohydrate form of vanadium pentoxide was obtained prior to the anhydrous form. However, some authors (Taniguchi & Ingraham, 1964; Deschanvres & Nouet, 1967; Sas et al., 1978) obtained only one intermediate product corresponding to the second stage of the decomposition reaction, leading to AHV.

Consequent to TG results, samples were prepared at selected temperatures for subsequent study by other physicochemical techniques. The weight of each sample was monitored initially and after its calcination for two hours in a stream of air. The mass losses are given in table 2.6 for each sample.

2.3.2– DIFFERENTIAL THERMAL ANALYSIS

The DTA curve of AMV (Fig. 2.8) indicated the presence of a large endothermic peak centred at 200°C with a shoulder on a side centred at 230°C, and an exothermic peak centred at 290°C.

The large endothermic peak encompasses the loss of ammonia and water in the decomposition processes leading to ABV and AHV, respectively, as observed in the TG trace.

The exothermic peak is probably a combination of two processes: the removal of ammonia and water (endothermic) and a more pronounced exothermic effect due to crystal lattice rearrangement to form vanadium pentoxide.

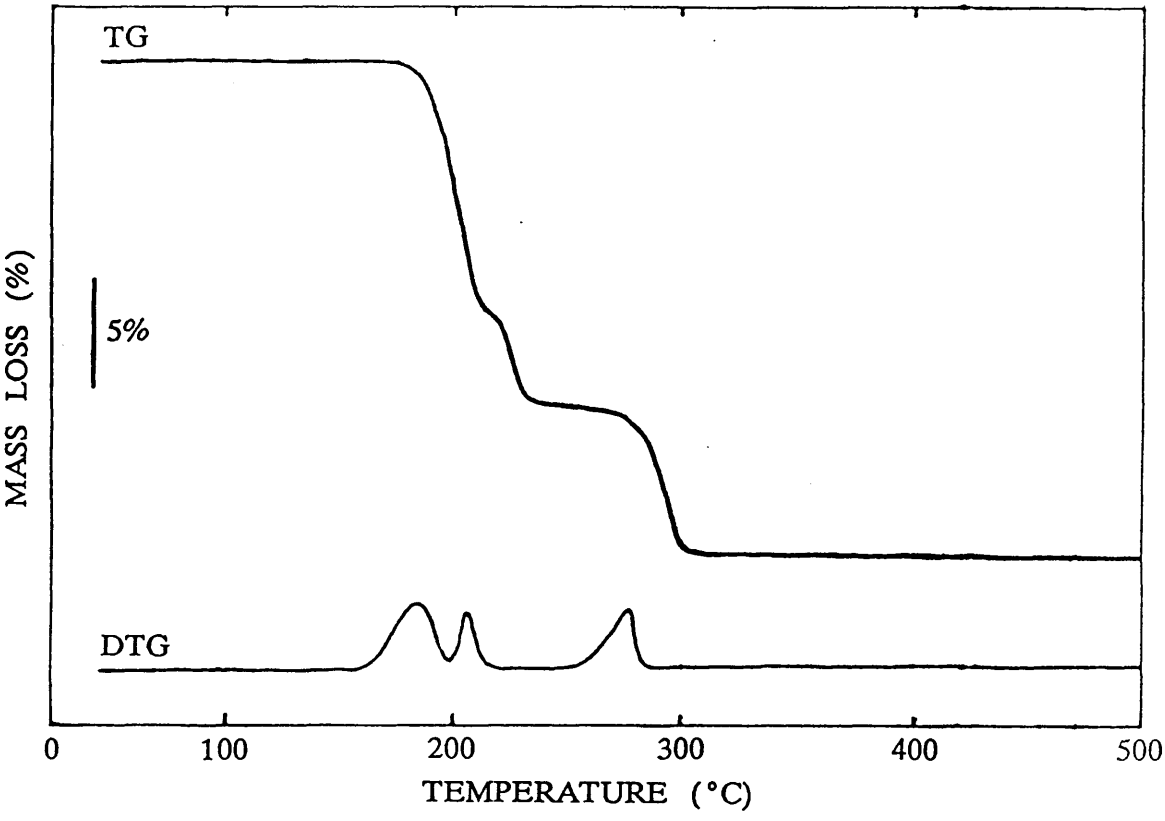

Fig. 2.7: Normal and differencial TG curves for AMV

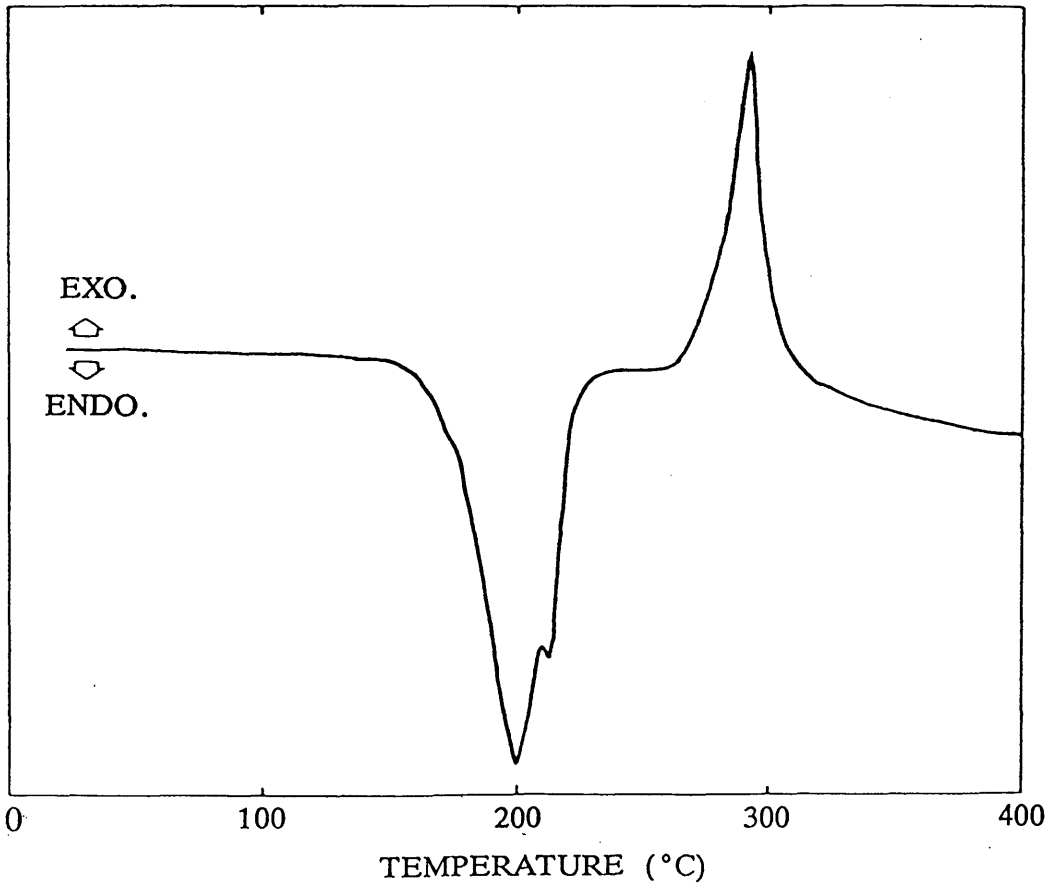

Fig. 2.8: DTA curve for AMV

Table 2.5: Consecutive stages of the thermal decomposition of AMV.

Stage	Temperature range (° C)	Exp. total mass loss (%)	Theoretical mass loss (%)	Reaction
1	140–190	11.5	11.10	$4AMV \rightarrow ABV + 2NH_3 + H_2O$
2	190–230	15.7	14.83	$3ABV \rightarrow 2AHV + 2NH_3 + H_2O$
3	230–320	22.5	22.23	$AHV \rightarrow 3V_2O_5 + 2NH_3 + H_2O$

* $AMV = NH_4VO_3$; $ABV = (NH_4)_2V_4O_{11}$; $AHV = (NH_4)_2V_6O_{16}$.

Table 2.6: Mass losses registered during preparation of the samples at different temperatures.

Temperature (°C)	Mass loss (%)	Formula
140	2.8	NH_4VO_3
175	14.0	$(NH_4)_2V_6O_{16}$
190	14.9	$(NH_4)_2V_6O_{16}$
230	15.5	$(NH_4)_2V_6O_{16}$
320	22.1	V_2O_5
400	22.1	V_2O_5

An exothermic peak has been found by Taniguchi & Ingraham (1964), in the DTA curves of AMV, at 375°C in nitrogen and at 325°C in oxygen which they ascribed to the catalytic decomposition of ammonia on the surface of freshly formed vanadium pentoxide. This possibility has not been rejected in the present studies. A similar reaction has been proved by mass spectrometric gas product determination in the decomposition of ammonium dichromate (Park, 1972) which showed the formation of nitrogen, diammonium oxide and water through the oxidation of ammonia nearby freshly generated chromium trioxide surfaces. In addition, it is well known that vanadium pentoxide catalysts are very active in the oxidation of ammonia (Germain & Perez, 1972).

2.3.3– X–RAY DIFFRACTION

XRD data from the powder samples calcined at the selected temperatures of 140, 190, 230, 320 and 400°C, with subsequent cooling to room temperature before examination, were recorded.

2.3.3.a– AMV and the sample heated at 140°C

The XRD trace of the 140°C sample corresponds to that of AMV. Typical x–ray data are presented in table 2.7. The observed d–spacings were compared with the calculated values obtained from structure determinations published by other workers or data available in the literature (Lukesh, 1950; Synecek & Hanic, 1954; Evans, 1960).

2.3.3.b– Samples obtained at 190 and 230°C

The XRD patterns from the samples heated at 190 and 230°C were almost indistinguishable from each other and yielded interplanar

spacings that were in good agreement with those measured by Kelmers (1961b) and Levanto (1969) for AHV, prepared in both cases from acidified metavanadate solutions (Table 2.8); but different from the values given by Satava (1959) and Taniguchi & Ingraham (1964) for the same compound prepared by thermal decomposition of AMV.

2.3.3.c— Samples obtained at 320 and 400°C

The samples calcined at 320 and 400°C exhibited d values in agreement with those of pure vanadium pentoxide when compared with the d values given in the literature (Ketelaar, 1936; Bystrom et al., 1950; Magneli & Blomberg, 1951; Bachmann et al., 1961; Natl. Bur. Stand., 1958; Enjalbert & Galy, 1986). The interplanar spacings measured from our spectra are listed in table 2.9, and are compared to the values determined by the Natl. Bur. Stand. (1958).

2.3.4— INFRARED SPECTROSCOPY

IR absorption spectra were recorded on AMV samples that had been heated to various selected temperatures to gain further information about the resultant chemical changes. The various spectra given by the different samples are illustrated in Fig. 2.9.

2.3.4.a— AMV and the sample heated at 140°C

The starting material and the sample obtained at 140°C gave absorptions corresponding to pure AMV. The spectrum obtained is similar to the spectra published by other authors (Miller & Wilkins, 1952; Frederickson & Hausen, 1963) except for details and positions of maxima.

The theoretical treatment of the vibrations of the metavanadate

Table 2.7: X— ray diffraction data for ammonium metavanadate

AMV d (nm)	140°C d (nm)	Evans (1961)		
		d (nm)	I/I_0	hkl
0.5902	0.5887	0.589	55	020
0.4898	0.4880	0.490	80	001
0.4143	0.4133	0.414	100	120
0.3763	0.3762	0.3769	30	021
0.3163	0.3162	0.3165	85	121
0.2912	0.2910	0.2914	55	200
0.2713	0.2713	0.2714	18	131
0.2629	0.2629	0.2629	30	140
0.2447		0.2453	25	002,211

Table 2.8: Comparison between the d— values measured and those determined by Levanto (1969) for AHV.

190°C d (nm)	230°C d (nm)	Levanto (1969)		
		d (nm)	I/I_0	hkl
	0.8498	0.866	20	010
0.7837	0.7844	0.783	100	100
0.5735	0.5746	0.574	50	110
0.3909	0.3917	0.391	100	200
0.3545	0.3548	0.355	100	210
		0.326	12	201
0.3214	0.3211	0.322	12	021
0.2901	0.2900	0.2915	12	201
		0.2870	20	220
		0.2604	12	300
0.2211	0.2211	0.2213	16	112
0.2023	0.2022	0.2025	10	231

Table 2.9: Lattice values measured for the 320 and 400°C samples compared to those given in the literature.

This work	Natl. Bur. Stand. (1958)		
d (nm)	d (nm)	I/I_0	hkl
0.5761	0.576	40	200
0.4381	0.438	100	001
0.4093	0.409	35	101
0.3409	0.340	90	110
0.2884	0.288	65	400
0.2767	0.276	35	011
0.2690	0.2687	16	111
0.2614	0.2610	40	310
0.2187	0.2185	18	002
0.2150	0.2147	12	102
0.1996	0.1992	18	411
0.1920	0.1919	25	600
0.1901	0.1900	18	302
0.1866	0.1864	14	012
0.1759	0.1757	30	601
	0.1740	14	402
0.1650	0.1648	12	021
0.1566	0.15764	10	611
	0.15640	12	412
0.1516	0.15149	18	321
	0.15124	12	420
0.1493	0.14925	18	710

chains $(VO_3)_n^{n-}$ can be done in the same manner as the corresponding silicate chains (Lazarev, 1972). These chains can be considered as V_2O_6- chain segments, taking into account the fact that the end groups of the segments are VO_2-, instead of VO_3-, groups.

The AMV IR- absorption spectrum has three characteristic bands, at 850, 890 and 940cm^{-1}. These vibrations are characteristic of infinite chains of tetrahedra and have been found in the IR spectra of potassium, rubidium, cesium and thallium metavanadates with slight shifts (Botto et al., 1976). The band at 935 and 928cm^{-1} can be assigned to the symmetric stretching of the shorter unshared vanadium- oxygen (V- O) bonds at the end of the chains, while the bands at 896 and 916cm^{-1} correspond to the asymmetric stretching of these bonds.

The vibrations at 853 and 504 cm^{-1} correspond to the asymmetric and symmetric vibrations of the V- O- V units along the chains, respectively. The deformation of the VO_2 units shows up in the IR spectrum at 366cm^{-1} while the VO_2- rocking bands appear below 377cm^{-1} and can be assigned to the vibrations which are parallel to the axis of the V- O- V chains.

The strong and broad band, maximised at 684cm^{-1}, can be treated, as in chromium trioxide (CrO_3) (Mattes, 1971), as a combination of inner and outer vibrations of the V- O- V chains.

The ammonium ion has two main IR active fundamental frequencies at 3200 and 1400cm^{-1} corresponding to nitrogen- hydrogen (N- H) bond stretch and ion deformation, respectively. Other bands at 2800 and 2960cm^{-1} are also attributable to this ion (Miller & Wilkins, 1952).

2.3.4.b- Samples obtained at 190 and 230°C

The AMV samples calcined at 190 and 230°C gave very similar

spectra to each other in which the two fundamental frequencies of the ammonium ion still persisted. The spectrum in Fig. 2.9 illustrates the IR absorption pattern for the two samples. It corresponds to that of AHV (Frederickson & Hausen, 1963; Zurkova & Ulicka, 1985).

The bands at 1000 and 970cm^{-1} are attributable to the stretching of the double V=O bonds while that at 740cm^{-1} is due to the V−O−V chains.

These vibrations occur in most hexavanadates (Frederickson & Hausen, 1963) in two distinct regions 950 to 1000 and 720 to 760cm^{-1}. They are due to the fact that, in the coordination polyhedron of oxygen atoms around the vanadium atom, there is one short V−O bond (Wadsley, 1955) with the remaining V−O bonds being appreciably longer and more variable.

2.3.4.c− Samples obtained at 320 and 400°C

The samples obtained at 320 and 400°C gave indistinguishable IR data consistent with vanadium pentoxide formation at these temperatures (Frederickson & Hausen, 1963; Kera & Herota, 1969; Fabbri & Baraldi, 1972; Gilson et al., 1973; Clauws & Vennik, 1976; Abello et al., 1983; Clauws et al., 1985). In particular, absorptions corresponding to the ammonium ion are now absent.

The bands with their relative attributions have extensively been discussed by many authors (Clauws & Vennik, 1976; Abello et al., 1983; Clauws et al., 1985) who have reported the IR spectrum of vanadium pentoxide powder in potassium bromide and studied the IR and Raman spectra of its single crystal. Most of the authors agreed that the absorption bands at 1020 and 995cm^{-1} are attributable to the stretching vibration of unshared V=O bonds. The assignments of the IR bands present in our spectrum (Fig. 2.9) are given in table 2.10.

Crystalline vanadium pentoxide has given rise to numerous

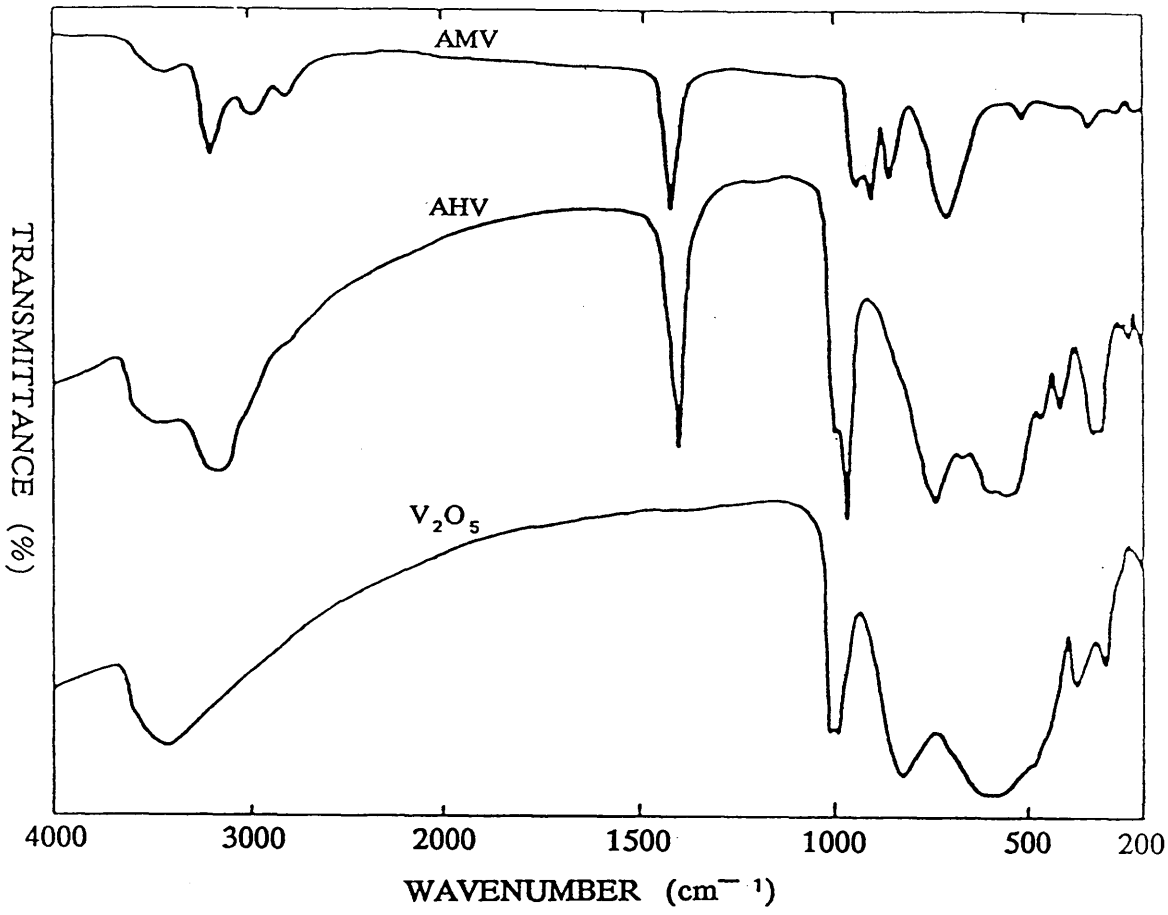

Fig. 2.9: IR spectra for AMV at different stages of decomposition.

Table 2.10: Assignment of IR spectroscopic absorption bands in the vanadium pentoxide spectrum.

Wavenumber (cm^{-1})	Assignment	Description
1023	V=O	stretching
982	V=O	stretching
813	V–O–V	stretching
605	OV_3	stretching
472	OV_3	stretching + deformation
370	V=O	deformation
294	V–O–V	deformation
262	OV_3	deformation
217	V=O	deformation

studies. In three—dimensional oxides it is difficult to isolate very individualised groups of atoms. However, in the vanadium pentoxide structure one can recognise different basic units.

Gilson et al. (1973) have analysed their data in terms of $(V_2O_4)_n$ chains (Fig. 2.10), that they considered as self—contained units and assigned doublets observed in their spectrum to these chains, these vibrations being coupled into pairs in the unit cell via the doubly linked bridging oxygen atoms. However this description is not very convenient for the full description of the vibrations of the crystal as far as the shared oxygen atom is considered separately. Moreover, usually the dominant characteristics of the spectra are associated with the strongest bonds in the structure, in other terms it seems rather more logical to consider $(V_2O_5)_n$ chains connected to each other via the longest d_4 bonds of. 0.202nm (Fig. 2.10). This model has been used by Abello et al. (1983).

According to this model one predicts that modes of each individual (V_2O_5) chain are coupled through the long d_4 bonds into doublets. They considered both the external motions of one V_2O_5 unit (considered as an isolated pseudo molecule) and the internal modes of V_2O_5 units which are described in terms of V—O stretching and bending vibrations. However, they emphasise that this description is somewhat arbitrary and that some coupling between these two types of motion exist.

There is a good agreement between frequencies measured in both works (Gilson et al., 1973; Abello et al., 1983). Three frequency ranges characteristic of different types of bonding can be identified:

(a) The vibrations associated with $V{=}O_A$ bonds are very pure, and observed at about $1000cm^{-1}$ for stretching modes and at 155—$346cm^{-1}$ for bending modes.

(b) The vibrations characteristic of the bridging oxygen atoms are pure, and located at about 830, 450 and $200cm^{-1}$. The asymmetric

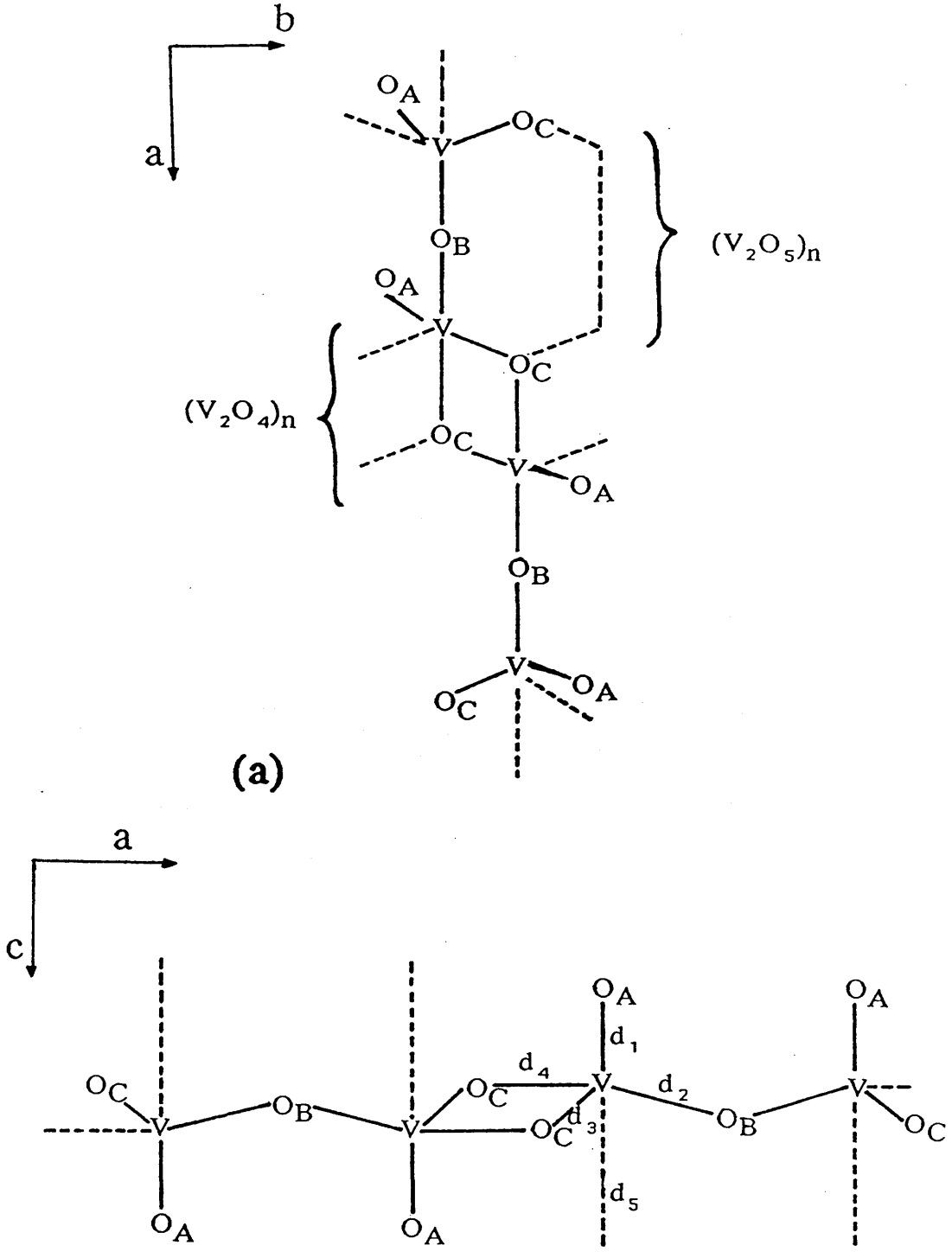

Fig. 2.10: Unit cell representation of vanadium pentoxide: (a) projection onto the (001) plane, with the two possible chain models, $(V_2O_5)_n$ and $(V_2O_4)_n$. (b) Projection onto (010) plane, $d_1 = 0.158$, $d_2 = 0.177$, $d_3 = 0.188$, $d_4 = 0.202$ and $d_5 = 0.278$nm.

stretching vibration for $V-O_B-V$ units is placed at about $550cm^{-1}$ and involves mainly the displacement of vanadium atoms.

(c) Finally the modes at about $700cm^{-1}$, at 535, $487-480cm^{-1}$ and at $316-387cm^{-1}$ correspond to stretching and bending modes of VO_C bonds respectively.

Most of the low frequency modes can be described in terms of external modes of V_2O_5 units.

2.3.5– AMMONIUM BIVANADATE

Although ABV formation was inferred from the thermal analysis results at 190°C, it has not been detected as a stable intermediate, on cooling to room temperature, in the present XRD and IR studies. Present efforts to prepare it at lower temperature (175°C) and shorter calcination times have been unsuccessful and gave only AHV product, contrary to the expectations of Selim et al. (1980).

Hydrated forms of this compound have, however, been obtained. The tetrahydrated form, $ABV.4H_2O$, was precipitated from boiling solutions of AMV (Calvo, 1954). The trihydrate form of ABV has also been prepared from boiled acidified metavanadate solution (Lachartre, 1924). When maintained under dry vacuum, the trihydrate slowly loses two molecules of water at room temperature. Removal of the third water molecule, which begins at 50°C, is also accompanied by loss of ammonia and leads directly to AHV (Dubois & Breton, 1938; Lamure & Colin, 1964).

Furthermore, the phase diagram of the system $NH_3-V_2O_5-H_2O$ indicates that the only stable phases at 25°C (Fedorov et al., 1967) and 30°C (Kelmers, 1961a) are AMV, AHV and vanadium pentoxide.

2.3.6– SCANNING ELECTRON MICROSCOPY

The morphological features of the parent AMV and the samples obtained from its calcination at different temperatures were investigated by examination in the scanning electron microscope.

The original AMV and the 140°C sample (Fig. 2.11.a) consisted mainly of fairly well formed crystallites with smooth surfaces and sharp edges, some intergrowth and attachment, but very little irregular material.

The stable AHV intermediate of the decomposition of the original AMV which is present at 190 and 230°C has crystallites which are very similar in size to those of original AMV, but they are less formed, with smooth faces and rounded edges and corners (Fig. 2.11.b).

It is shown from Fig. 2.11.c that the final product obtained at 320 and 400°C, vanadium pentoxide, contains particles of varying sizes which have essentially no surface cracks or porosity. Because of their layered structure, vanadium pentoxide crystals are most clearly broken parallel to the (001) plane. Thus, the two samples contain well–developed plate–like grains in which the predominant face corresponds to a (001) plane.

This SEM study revealed morphological similarities between all these specimens. A wide size range of well–formed crystals with smooth surfaces and sharp edges are observed in all three products. These morphological similarities suggest that no recrystallisation process has occurred during the thermal decomposition of AMV.

2.3.7– TRANSMISSION ELECTRON MICROSCOPY

High resolution TEM imaging in conjunction with electron diffraction technique was used as a tool for structure determination. It was possible to view changes in the lattice structure of AMV both

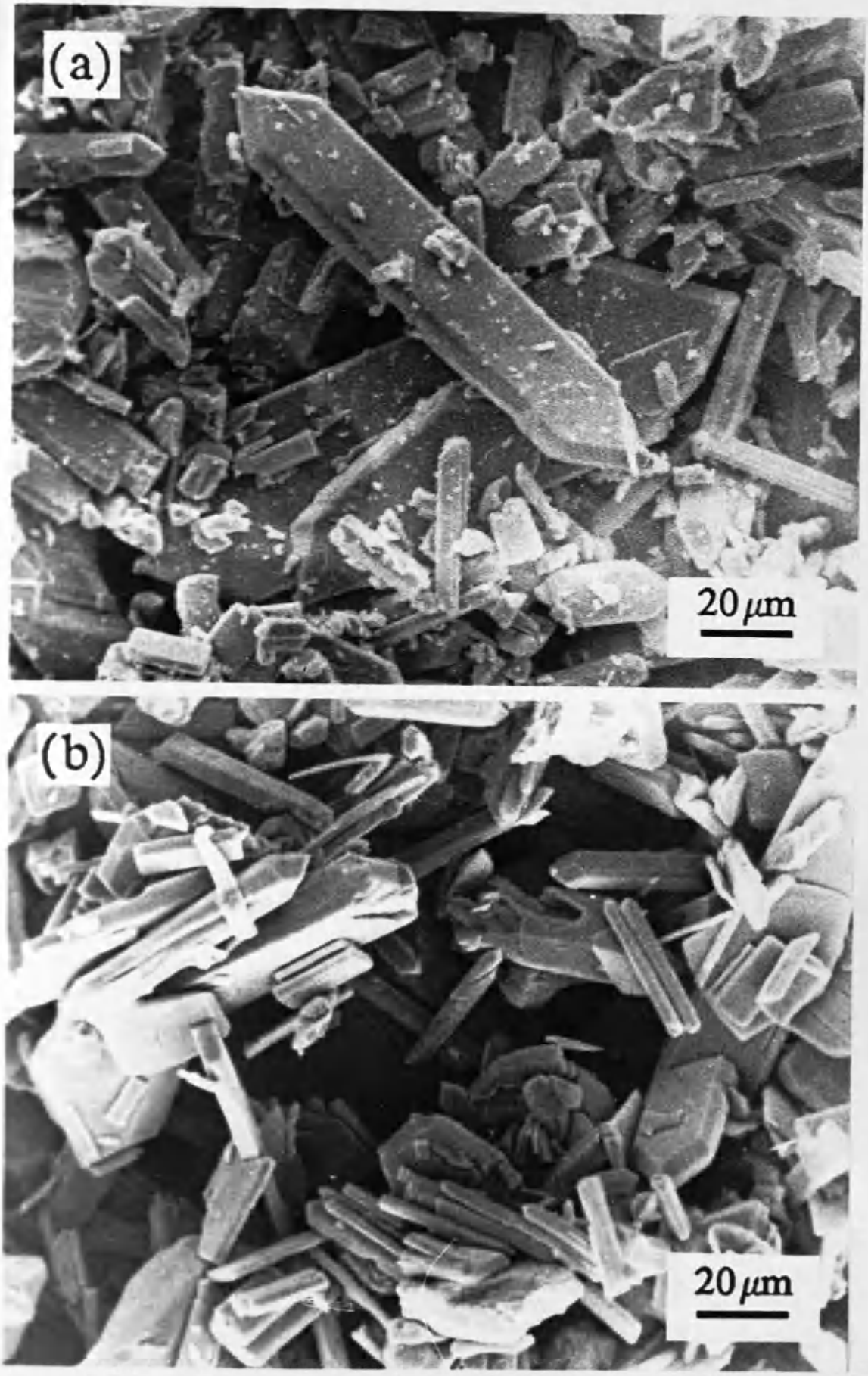
(a)
20 μm
(b)
20 μm

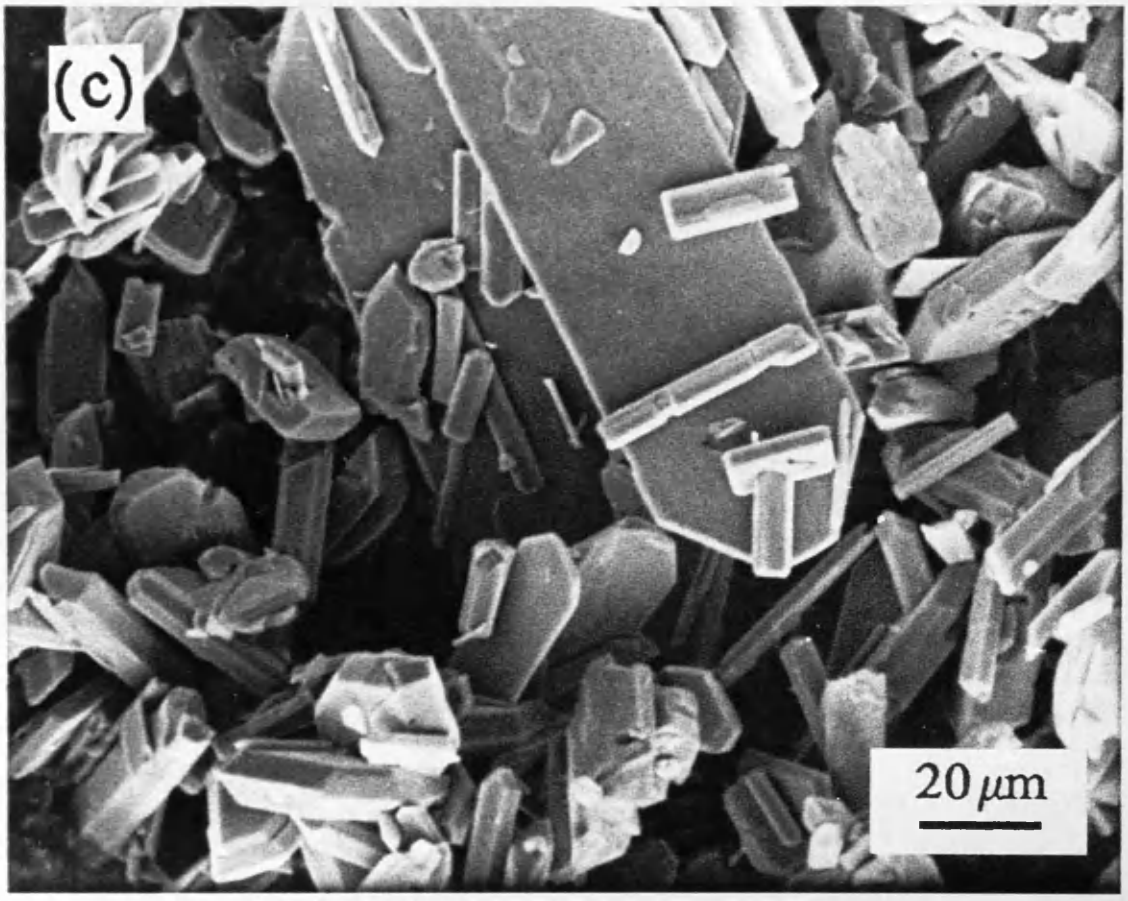

Fig. 2.11: SEM photographs of AMV at different stages of the thermal decomposition: (a) AMV, (b) AHV and (c) vanadium pentoxide.

fresh and after calcination at different temperatures.

No particular differences between the various samples were observed on low magnification micrographs. The particles were of various shapes and sizes.

2.3.7.a— AMV and the sample obtained at 140°C

The preparation of the samples from AMV and the 140°C sample for TEM examination by dispersion in water has failed due to the solubility of AMV in this medium. It has been reported that the solubility of AMV, relatively to 100cc of water, was 0.518g at 15°C (Lachartre, 1924; Weast, 1987) and 1.04g at 32°C (Lachartre, 1924). Therefore ethanol was used as dispersion medium owing to the lower dissolution of AMV in it (Lachartre, 1924).

Electron diffraction patterns (EDP) of crystals from both samples (Fig. 2.12) were in the form of textural patterns indicating the orientation of these crystals. The d—spacings measured from the EDP are closely related to those XRD data obtained for AMV and the 140°C samples.

Selected area electron diffraction (SAED) pattern of a single crystal (Fig. 2.13) in which the electron beam is perpendicular to the (001) plane, of the orthorhombic structure of the crystal, consisted of many spots which could be indexed in accord with the orthorhombic unit cell. The diffraction spots corresponding to the lattice planes (020) and (120), which have spacings of 0.589 and 0.414nm, respectively, are at an angle of 45°. Those corresponding to the planes (200) and (140) with lattice spacings of 0.2914 and 0.2629nm, respectively, are at an angle of 63°. The two angle values are consistent with the values of 45.3° and 63.2°, respectively, which were calculated using the formula (Andrews et al., 1971):

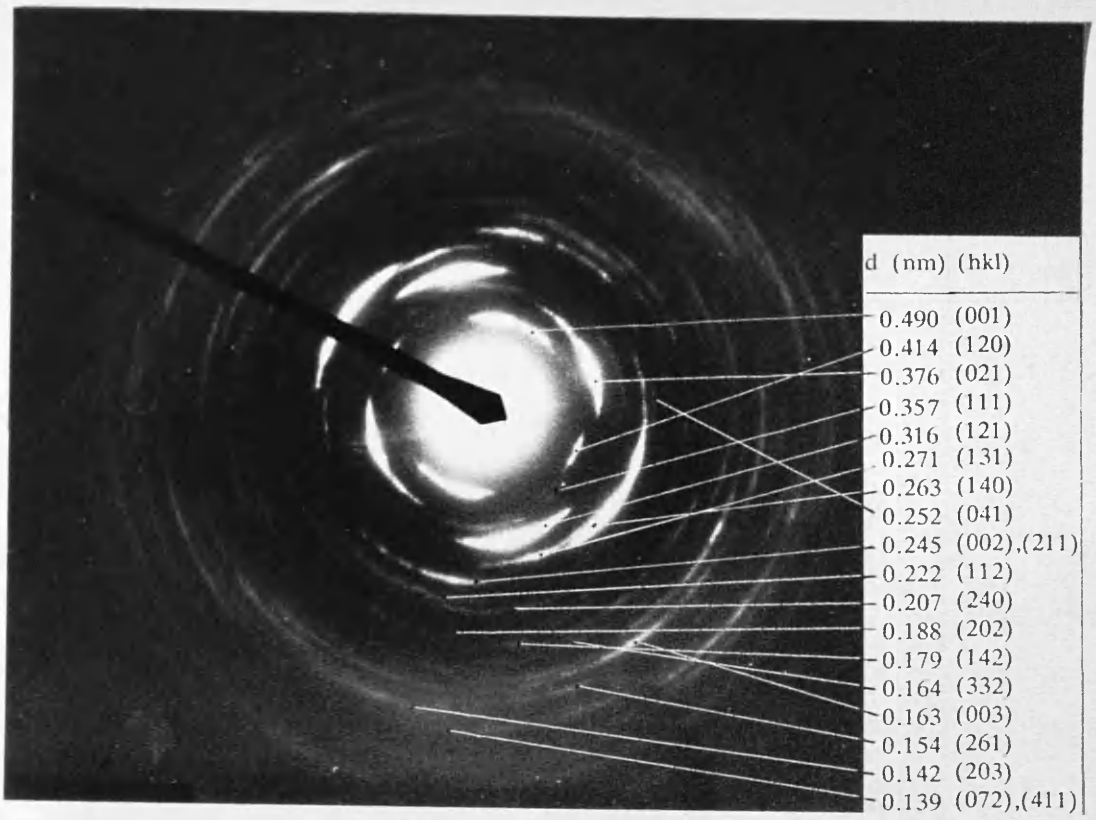

Fig. 2.12: EDP corresponding to AMV crystals.

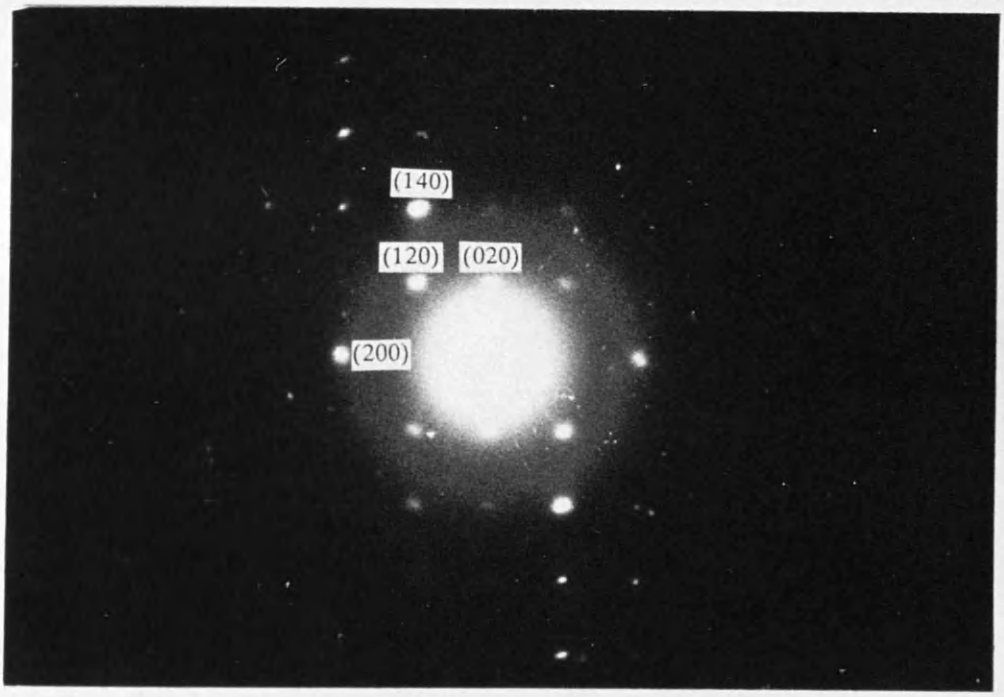

Fig. 2.13: SAED pattern of an AMVsingle crystal.

$$\cos\phi = \frac{\frac{1}{a^2}h_1h_2 + \frac{1}{b^2}k_1k_2 + \frac{1}{c^2}l_1l_2}{\left\{\left(\frac{1}{a^2}h_1^2 + \frac{1}{b^2}k_1^2 + \frac{1}{c^2}l_1^2\right)\left(\frac{1}{a^2}h_2^2 + \frac{1}{b^2}k_2^2 + \frac{1}{c^2}l_2^2\right)\right\}^{1/2}}$$

where Φ is the angle between the planes $(h_1k_1l_1)$ and $(h_2k_2l_2)$.

The parent AMV and its calcination product at 140°C proved to be subject to rapid beam radiation damage in the electron microscope. Electron diffraction spots disappeared after a few seconds of normal irradiation. The minimum dose technique was therefore applied for high resolution imaging of these two compounds. Lattice images corresponding to AMV spacings were, subsequently, successfully obtained from both the parent and 140°C samples.

The lattice fringes with spacings of 0.490nm and 0.414nm, shown in Fig. 2.14, correspond to the (001) and (120) planes of the orthorhombic structure of AMV, respectively.

The small crystal represented in Fig. 2.15.a is oriented with the (100) plane parallel to the substrate. The lattice fringes present in this micrograph have spacings of 0.453 and 0.589nm representing the (011) and (020) planes, respectively. The two sets of planes are shown on the projection of the AMV structure, onto the (100) plane, in terms of atomic arrangement inside the crystal (Fig. 1.15.b).

In addition, some crystals in both the parent and 140°C sample showed lattice spacings of 0.77nm (Fig. 2.16) which do not correspond to any of the AMV lattice spacings. It is feasible that such crystals have undergone thermal decomposition, under the electron beam, leading to AHV which has a (100) interplanar spacing close to 0.77nm (0.783nm).

2.3.7.b— Samples obtained at 190 and 230°C

The samples obtained at 190 and 230°C were also beam sensitive, but less so than AMV. When specimens were irradiated by

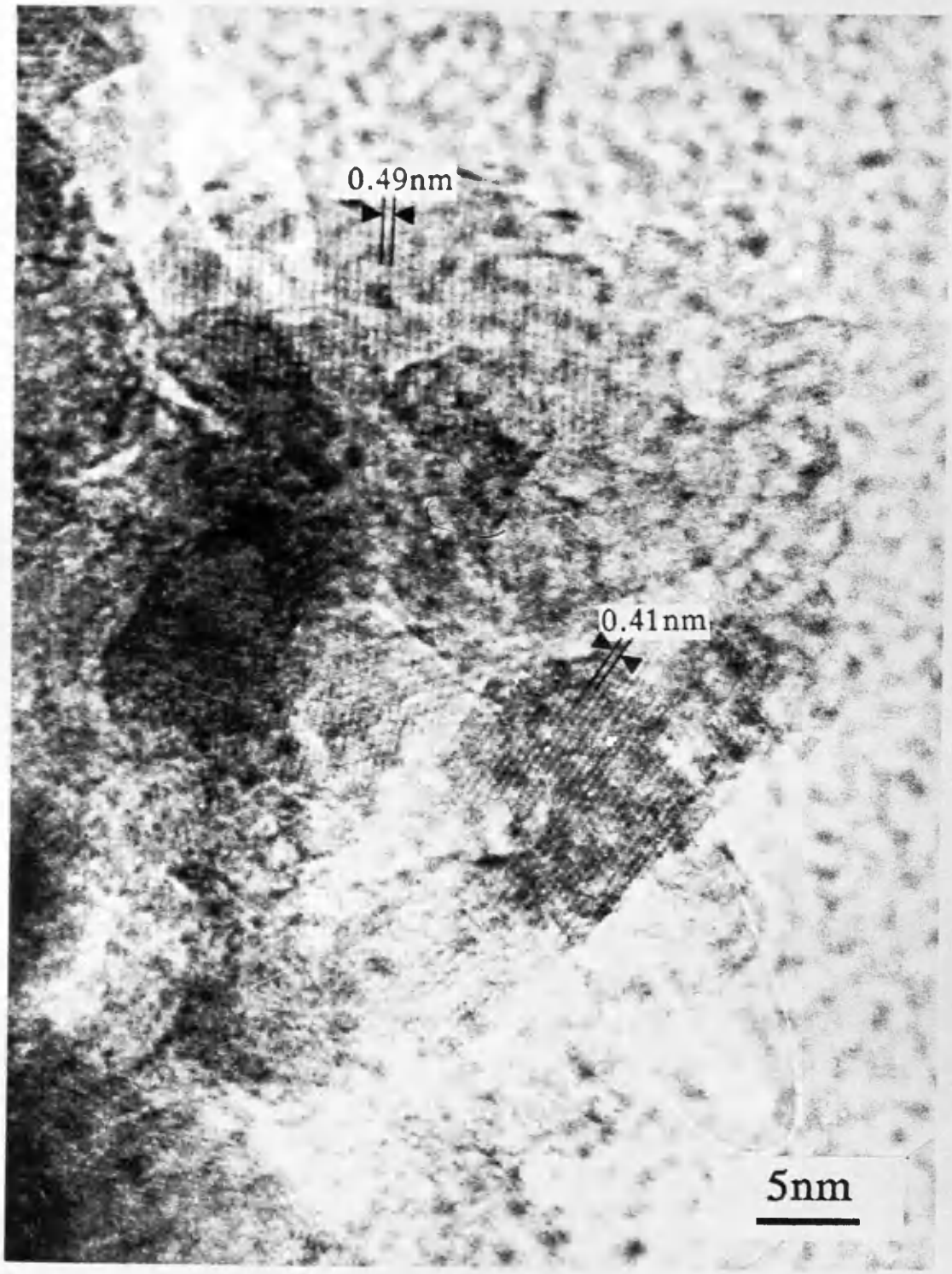

Fig. 2.14: HREM lattice image of AMV crystals.

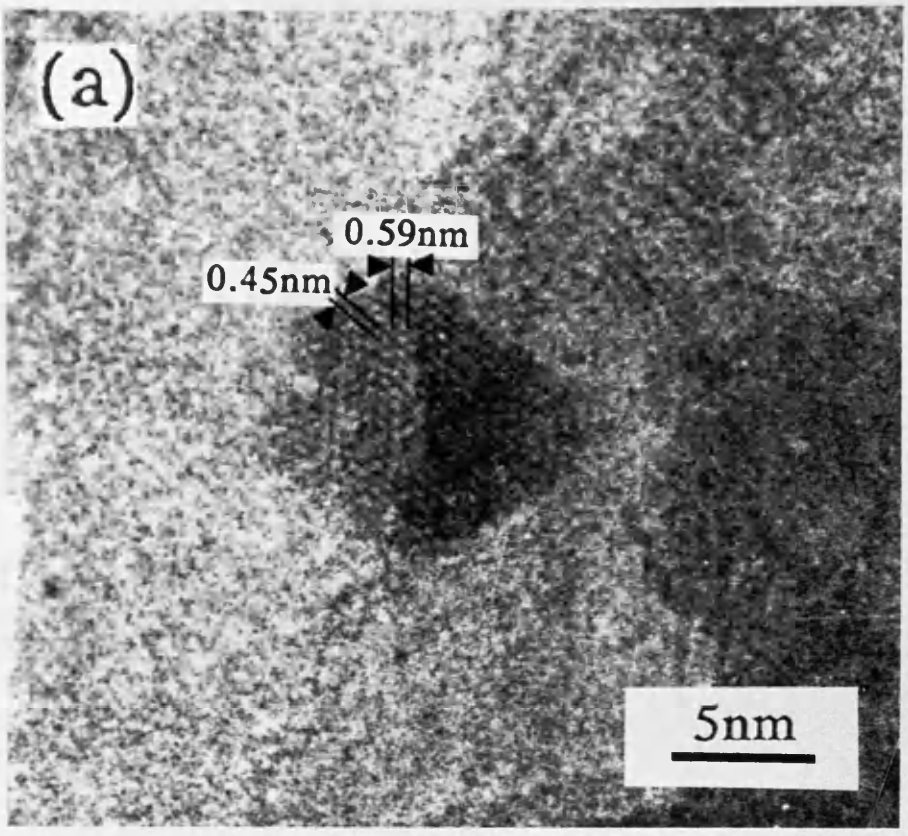

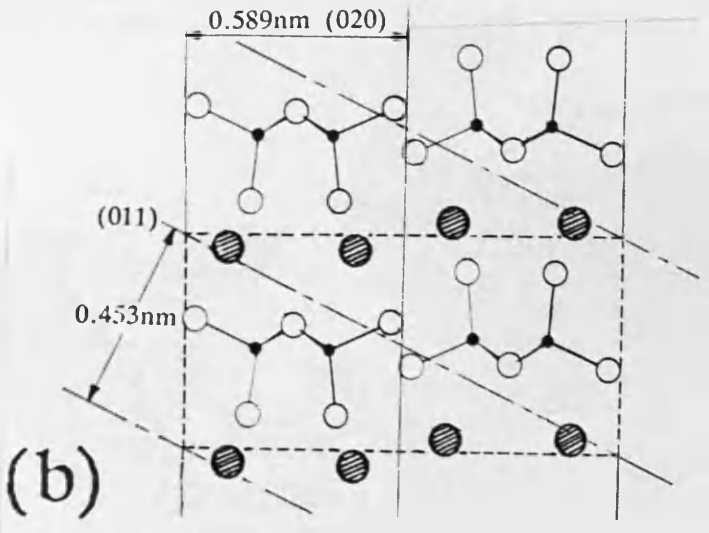

Fig. 2.15: (a) HREM lattice image of an AMV single crystal. (b) The two sets of lattice fringes are shown on the projection of the AMV structure onto the (100) plane.

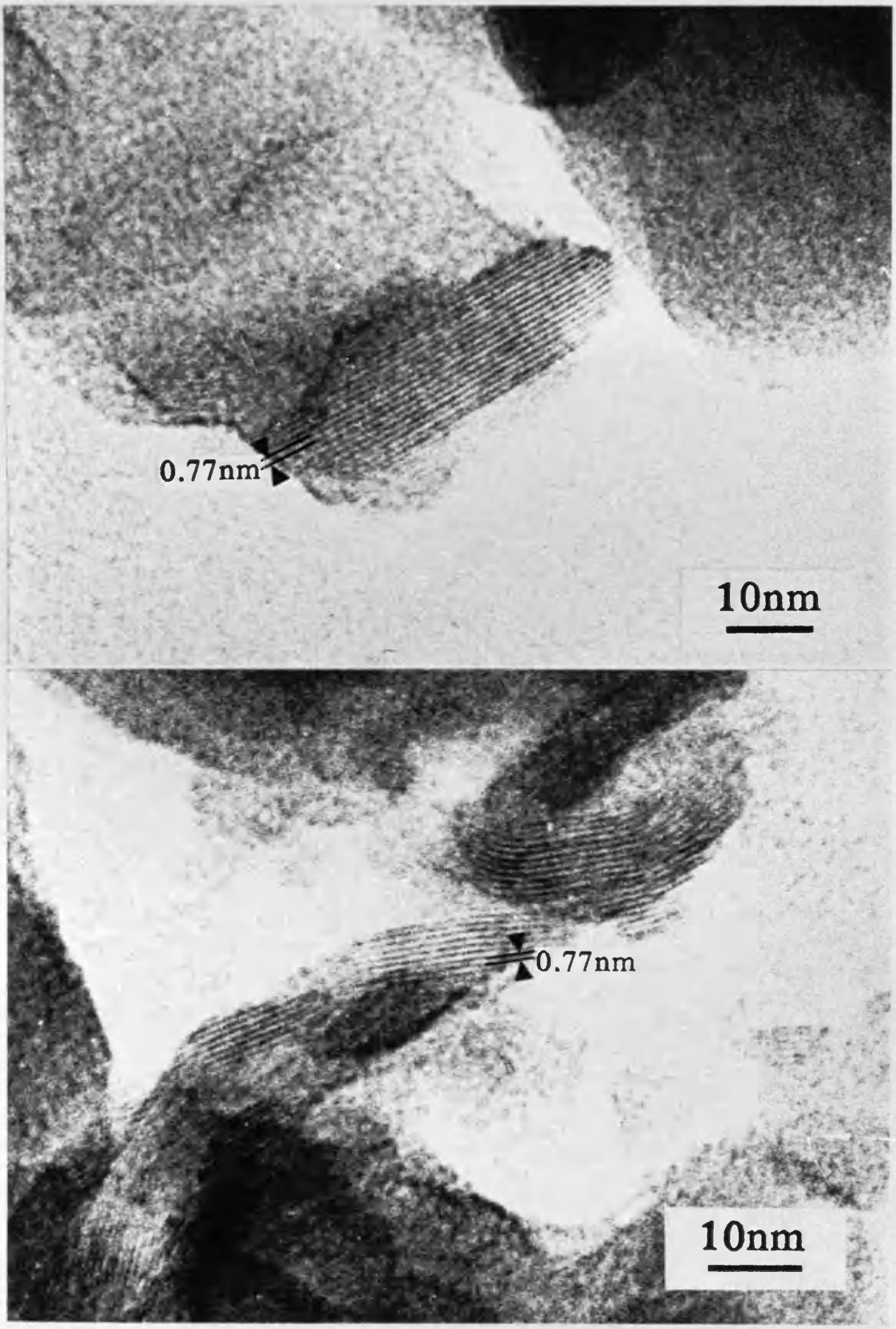

Fig. 2.16: Crystals showing lattice fringes which do not correspond to AMV.

an electron beam of higher intensity, beam damaged regions appeared preferentially at thin parts of the specimen (Fig. 2.17). This phenomenon has been observed by Horiuchi et al. (1975) in a vanadium oxide (V_6O_{13}). They considered these regions to be the sites where the reduction of the oxide by the carbon support film begins.

Electron diffraction patterns of crystals from the two samples contained spotty rings (Fig. 2.18), which could be indexed in agreement with the monoclinic structure of AHV.

SAED patterns of single crystals in which the electron beam was perpendicular to (100) and (010) planes are given in Fig. 2.19. The spots observed in both patterns give a good fit with the crystalline orientation of the crystallographic planes in the monoclinic structure when the corresponding d−spacings and angles between them were measured.

In addition, lattice spacings corresponding to AHV were commonly observed in the present studies. The lattice fringes, shown in Fig. 2.20, with spacings of 0.866, 0.783 and 0.574nm correspond to (010), (100) and (110) planes in AHV structure, respectively.

Close examination of the micrograph in Fig. 2.21.a with the laser diffractometer showed that the cross lattices, present in the micrograph, have lattice spacings of 0.78nm (100), 0.44nm (101) and 0.33nm (201) at angles of 52° and 35° between (100) and (101) on one hand and (100) and (201) on the other, respectively, in accord with the monoclinic structure of AHV. The calculated values for these angles, using the following formula (Andrews et al., 1971):

$$\cos\phi = \frac{\frac{1}{a^2}h_1h_2 + \frac{1}{b^2}k_1k_2\sin^2\beta + \frac{1}{c^2}l_1l_2 - \frac{1}{ac}(l_1h_2 + l_2h_1)\cos\beta}{\left\{\left(\frac{1}{a^2}h_1^2 + \frac{1}{b^2}k_1^2\sin^2\beta + \frac{1}{c^2}l_1^2 - \frac{2h_1l_1}{ac}\cos\beta\right) \times \left(\frac{1}{a^2}h_2^2 + \frac{1}{b^2}k_2^2\sin^2\beta + \frac{1}{c^2}l_2^2 - \frac{2h_2l_2}{ac}\cos\beta\right)\right\}^{1/2}}$$

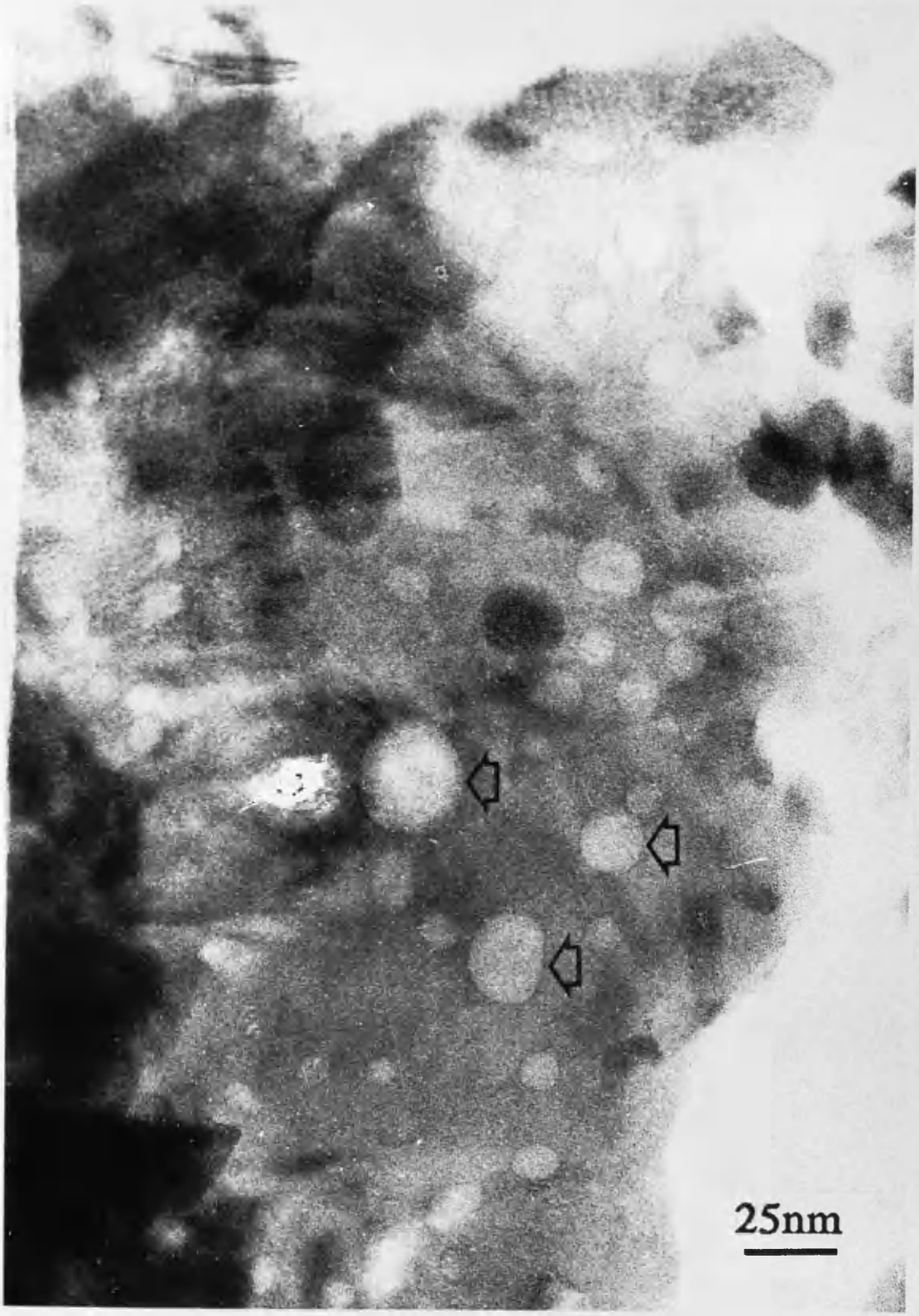

Fig. 2.17: TEM micrograph of AHV crystals showing regions which have been damaged by the electron beam (arrows).

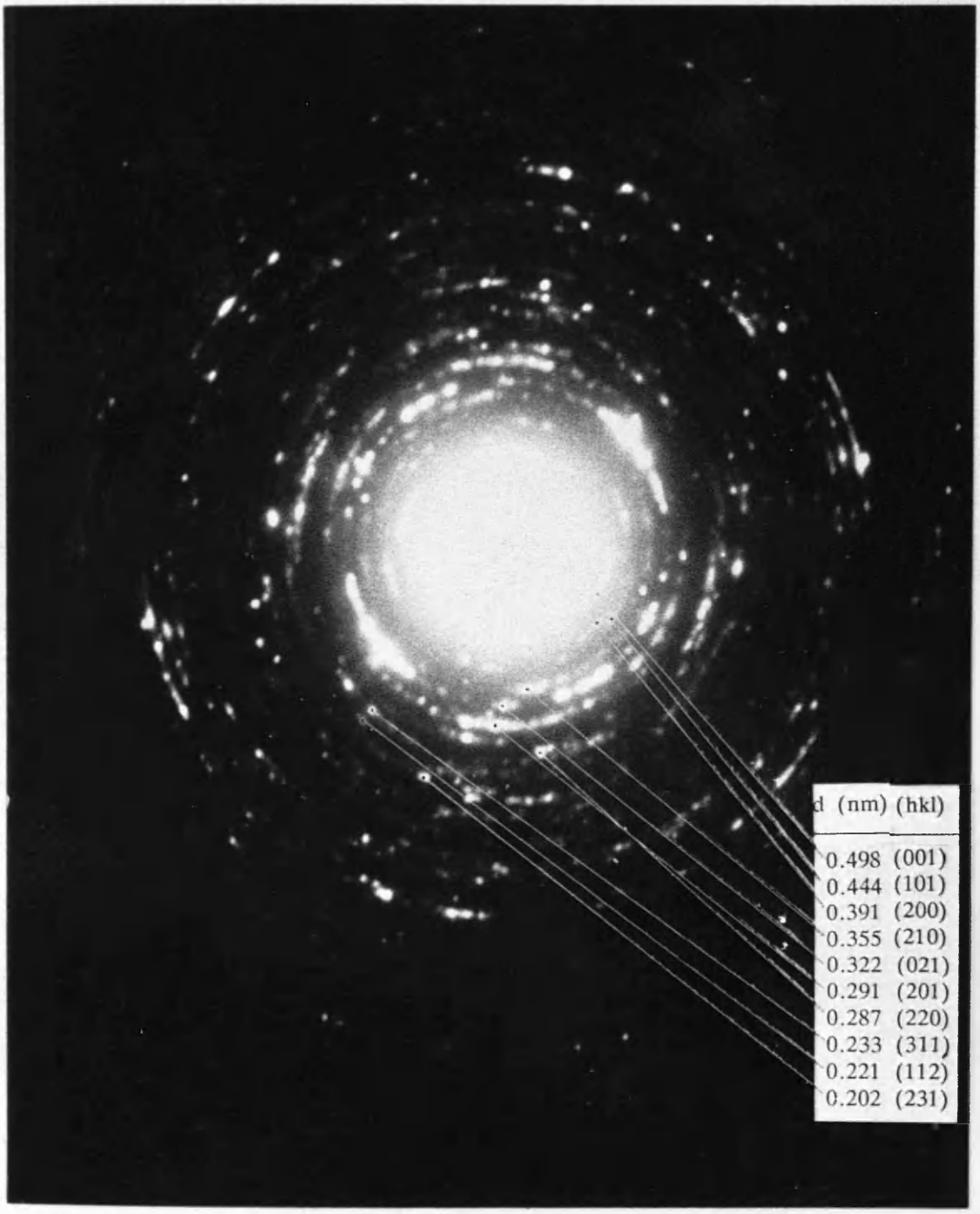

Fig. 2.18: EDP corresponding to AHV crystals.

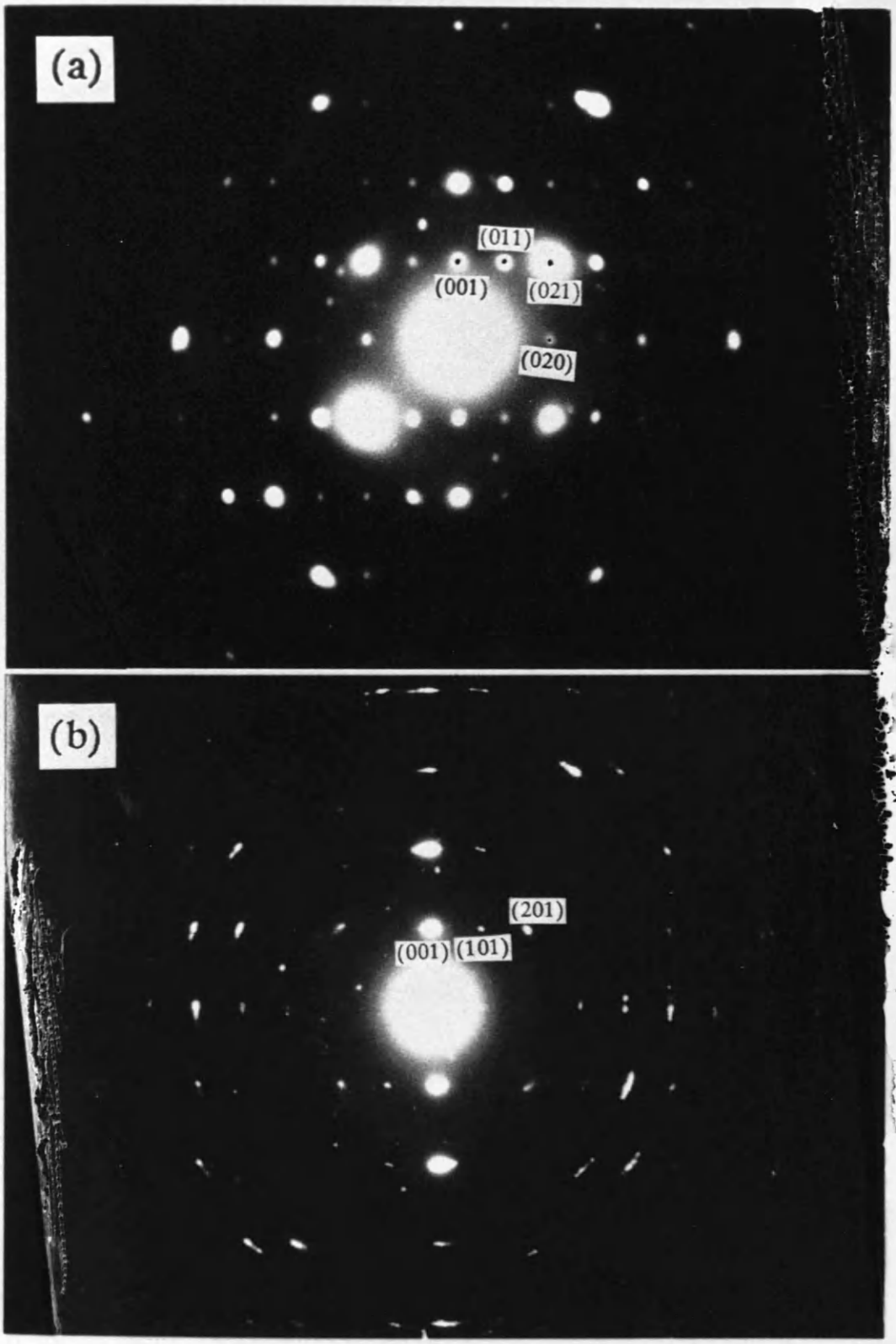

Fig. 2.19: SAED patterns of AHV single crystals in which the electron beam is perpendicular to (a) (100) and (b) (010) planes.

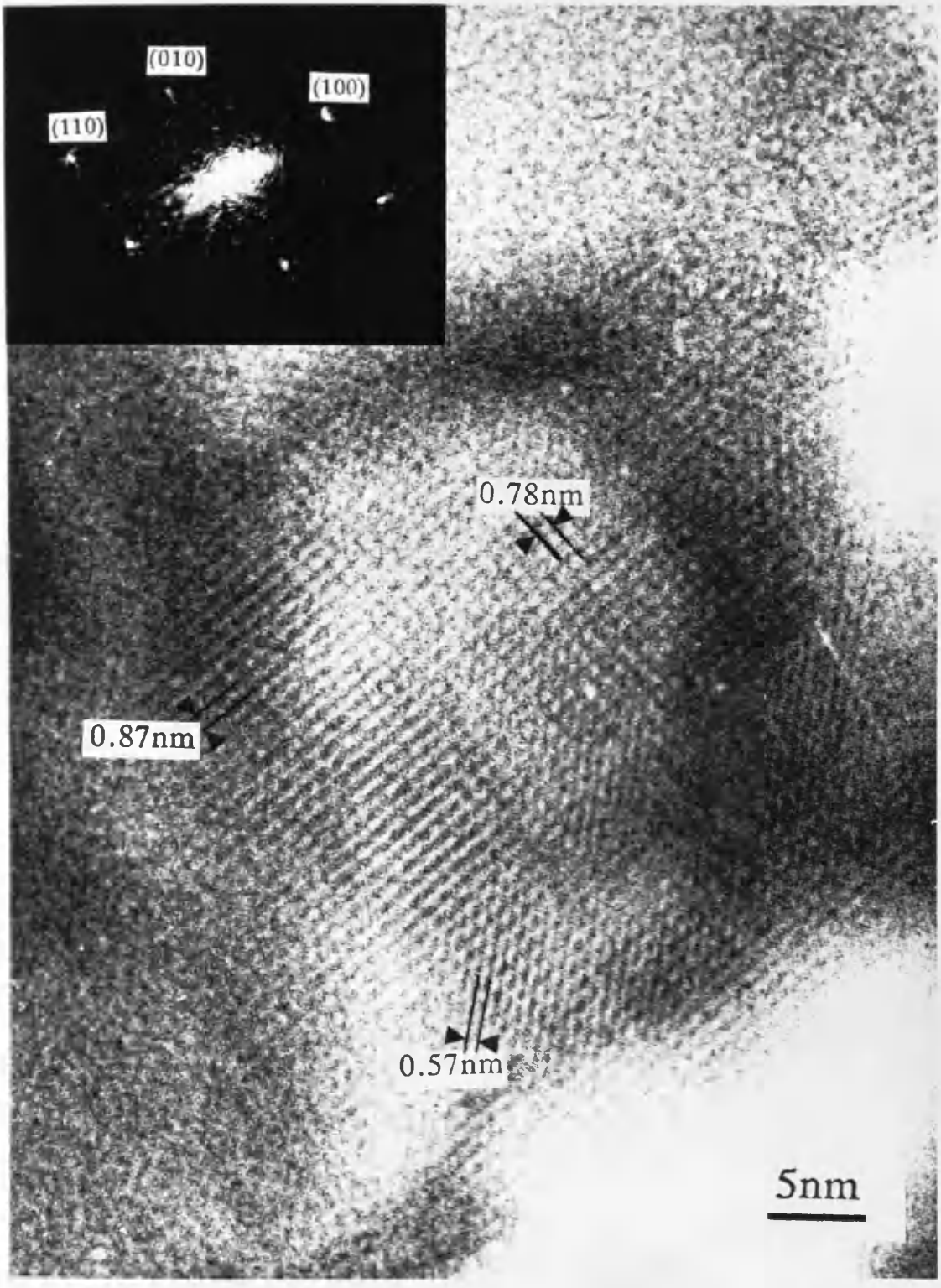

Fig. 2.20: HREM lattice image in which the electron beam is perpendicular to the (001) plane in the AHV structure, and the corresponding ODP.

which gives the angle Φ between two lattice planes $(h_1k_1l_1)$ and $(h_2k_2l_2)$ for the monoclinic system, are 52.8° and 35.5°. The correlation between the three sets of lattice fringes, present in the HREM micrograph, and the atomic arrangement inside the crystal is illustrated in the projection of the monoclinic structure of AHV onto the (010) plane (Fig. 2.21.b).

In addition to AHV lattice spacings, some crystals manifested 0.68nm lattices (Fig. 2.22) which do not correspond to any of the AHV spacings or to other known vanadium compounds listed in the x—ray powder diffraction file index.

The electron micrograph in Fig. 2.23 shows radiation damage initiated at what appears to be a dislocation. This phenomenon is not unexpected since, like any other defect, a dislocation is generally considered to be a high energy site and consequently a very reactive site.

2.3.7.c— Samples obtained at 320 and 400°C

The sample preparation at 320 and 400°C exhibited similar characteristics to each other in the electron microscope. The two samples were less beam sensitive than either AMV or AHV.

Structure determination for these samples by electron diffraction gave spotty rings (Fig. 2.24) which yielded d values in agreement with those identified for these samples by XRD and given in the literature for vanadium pentoxide compound. However, the most intense peak present in the XRD pattern, 0.438nm (001), was absent from our EDP. This is due to the orientation of vanadium pentoxide crystallites.

In fact, most of the vanadium pentoxide crystals present at 320 and 400°C preferentially exposed (001) plane, resulting from the lamellar structure of these crystals which are prone to easy cleavage along the (001) planes. The SEM examination of the same samples

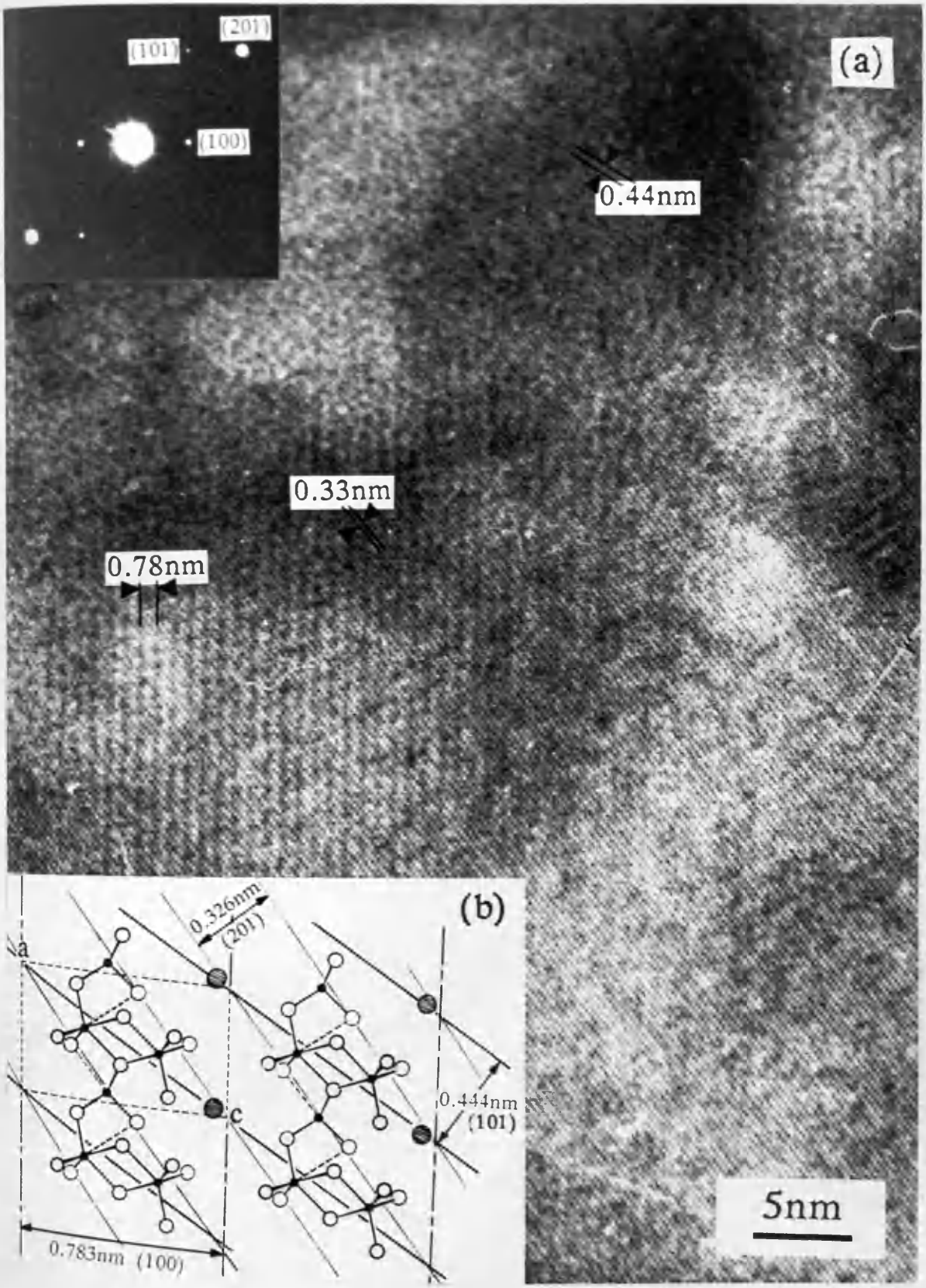

Fig. 2.21: (a) HREM lattice image of AHV with the corresponding ODP, and (b) the projection of the AHV structure onto the (010) plane in which the three sets of lattice fringes observed are represented.

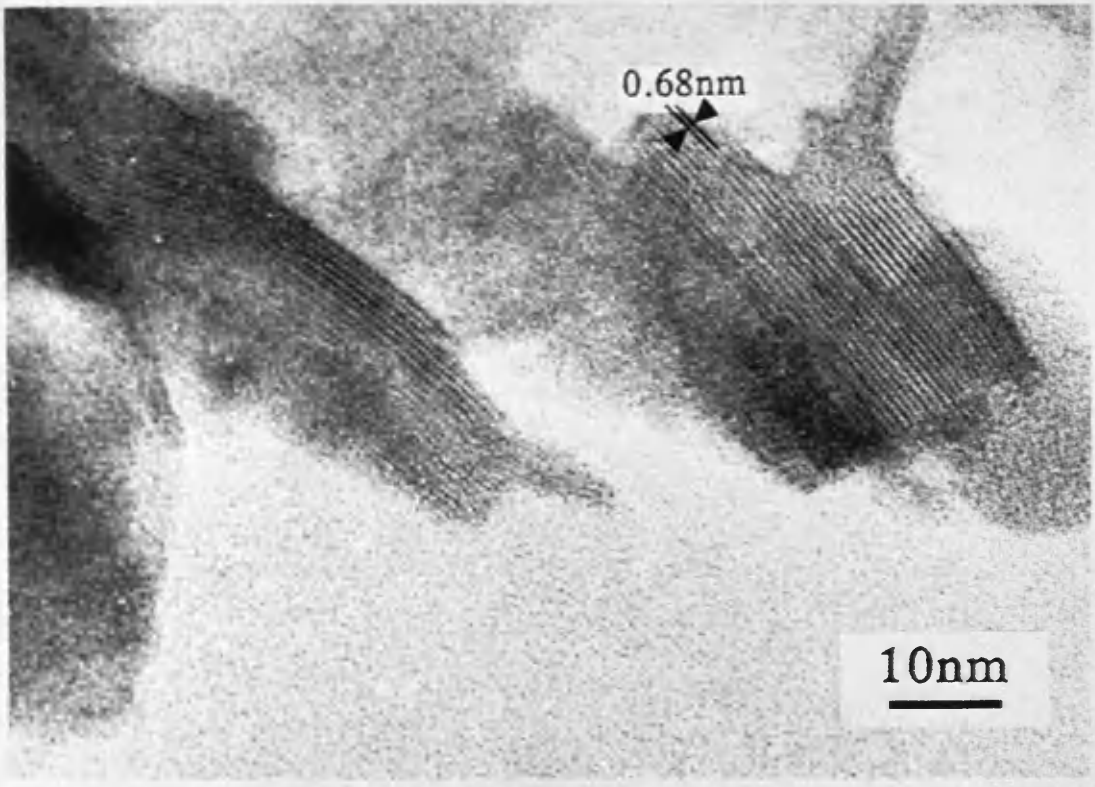

Fig. 2.22: TEM micrograph showing crystals with lattice fringes which do not correspond to AHV.

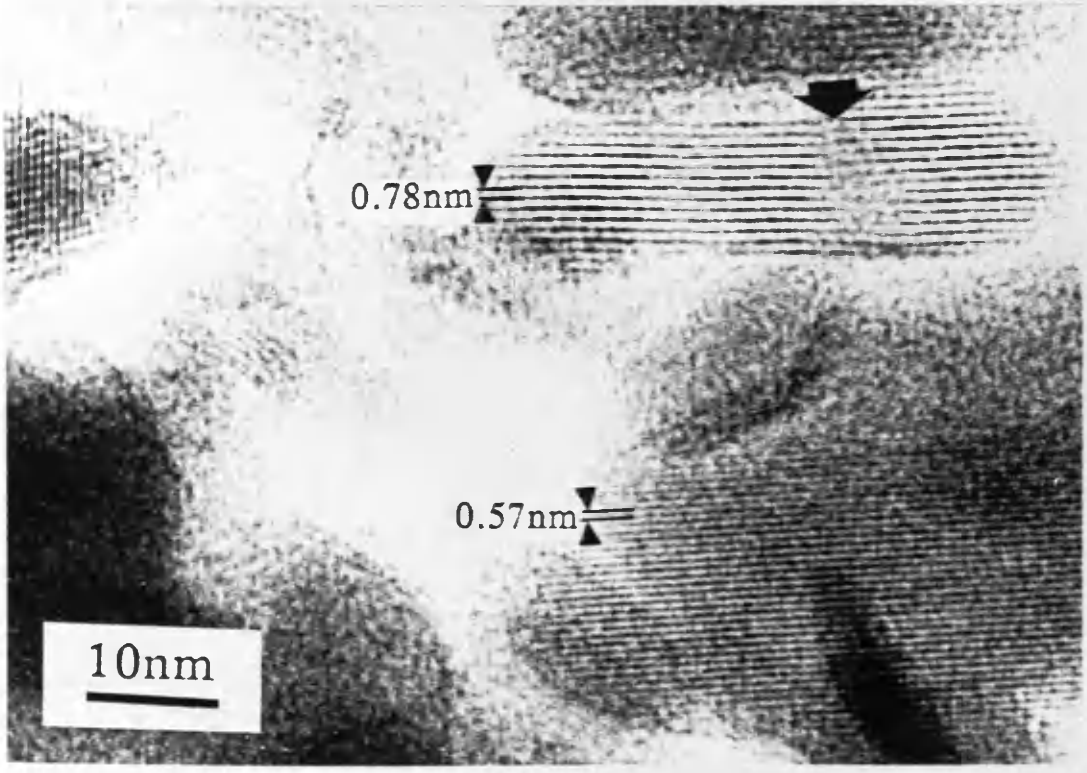

Fig. 2.23: HREM micrograph showing AHV lattice fringes and radiation damage starting at a dislocation (arrow).

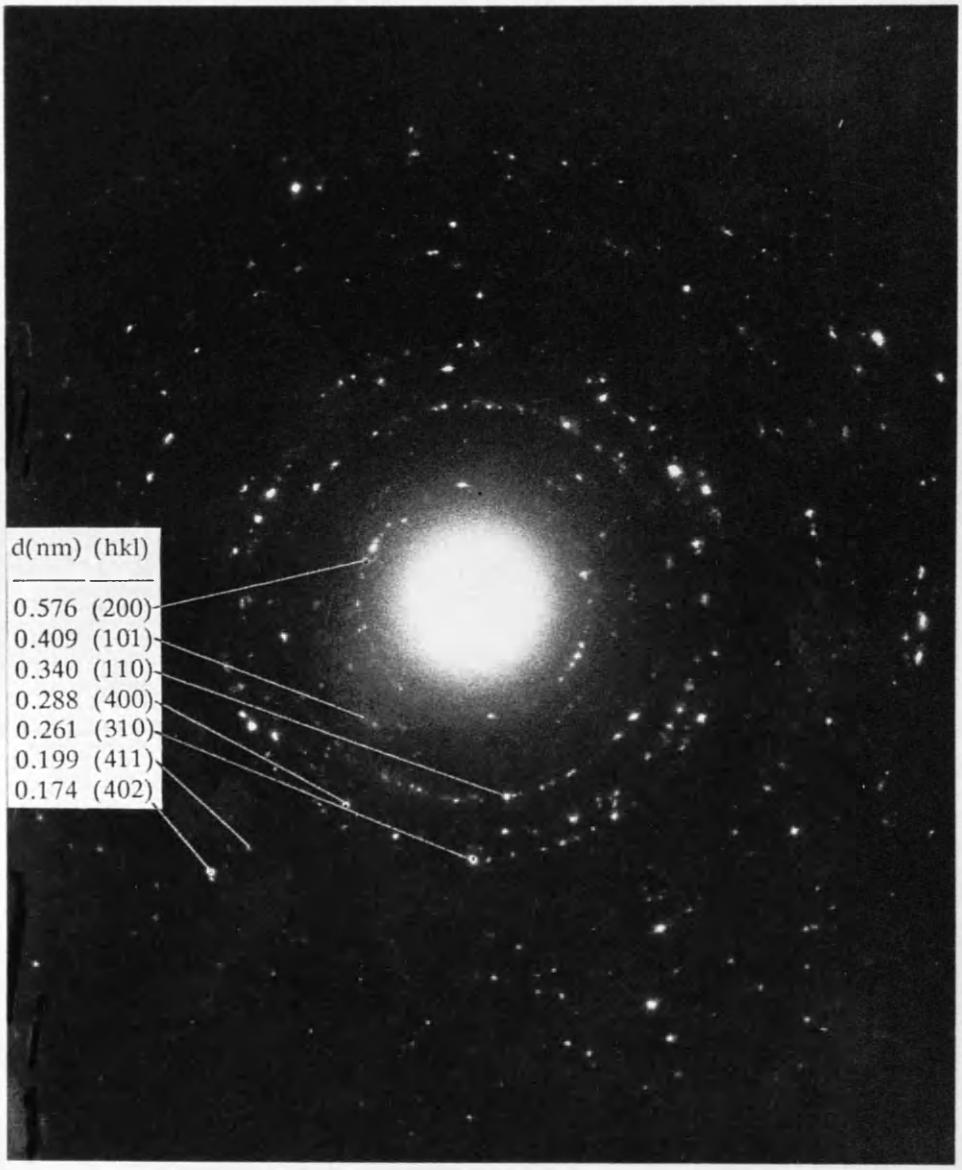

Fig. 2.24: EDP corresponding to vanadium pentoxide.

revealed the existence of large (001) faces. This result has been evident from the SAED patterns of single crystals (Fig. 2.25) as well as their HREM examination.

Fig. 2.26.a is a typical HREM image of vanadium pentoxide crystals. The cross lattices present with spacings of 0.576nm and 0.34nm correspond to (200) and (110) planes in the orthorhombic structure of vanadium pentoxide, respectively. The two sets of planes are in accord with the orthorhombic structure of vanadium pentoxide when the angle between them is measured. They are shown in the projection of the structure of vanadium pentoxide, onto the (001) plane, in terms of atomic arrangement inside the crystal (Fig. 2.26.b).

Some crystals, from the samples obtained at 320 and 400°C, have exposed the (010) plane as shown in Fig. 2.27.a. The lattice fringes present in the micrograph with spacings of 0.576nm and 0.414nm correspond to (200) and (101) planes in the orthorhombic structure of vanadium pentoxide, respectively. These two planes are represented in the projection of the structure onto the (010) plane (Fig. 2.27.b).

No lattice spacing corresponding to the exposure of the (100) plane have been found in the course of this study. Furthermore, as indicated earlier, the (001) plane which gives the most intense peak in the XRD pattern of vanadium pentoxide was absent in our electron diffraction patterns even in polycrystalline regions.

Catalytic activity and selectivity are due largely to the species present at the surface of the catalyst, thus the orientation of the latter is very important. The V=O bonds on the surface of vanadium pentoxide perform an important role as the adsorption and also reaction sites for many reactions such as oxidation (Tarama et al., 1965; Kera et al., 1967) and ammoxidation (Andersson, 1985). It has been concluded from organic compound adsorption studies on vanadium pentoxide that the (001) planes contain the vanadyl bonds,

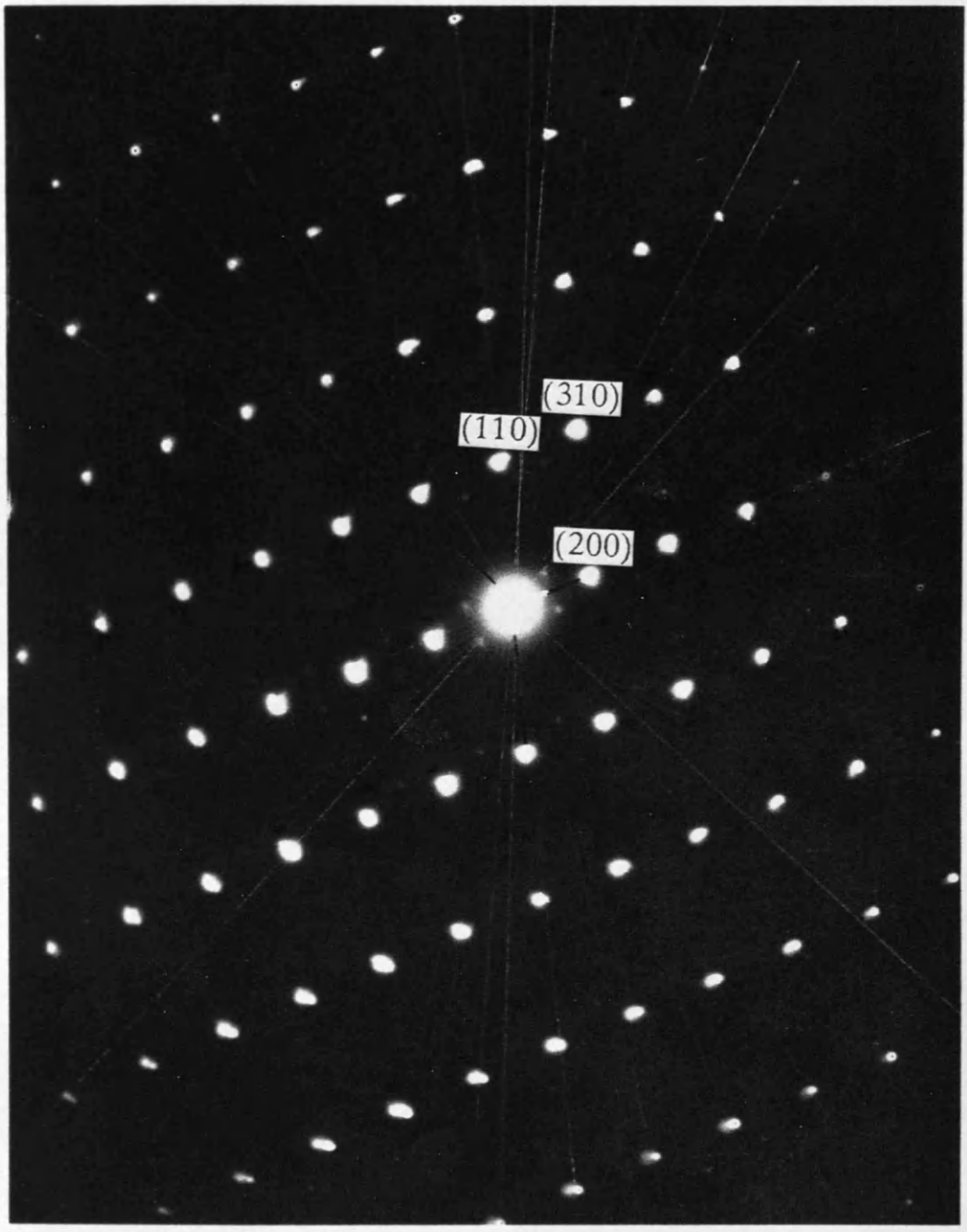

Fig. 2.25: Typical SAED pattern of a vanadium pentoxide single crystal with the electron beam perpendicular to the (001) plane.

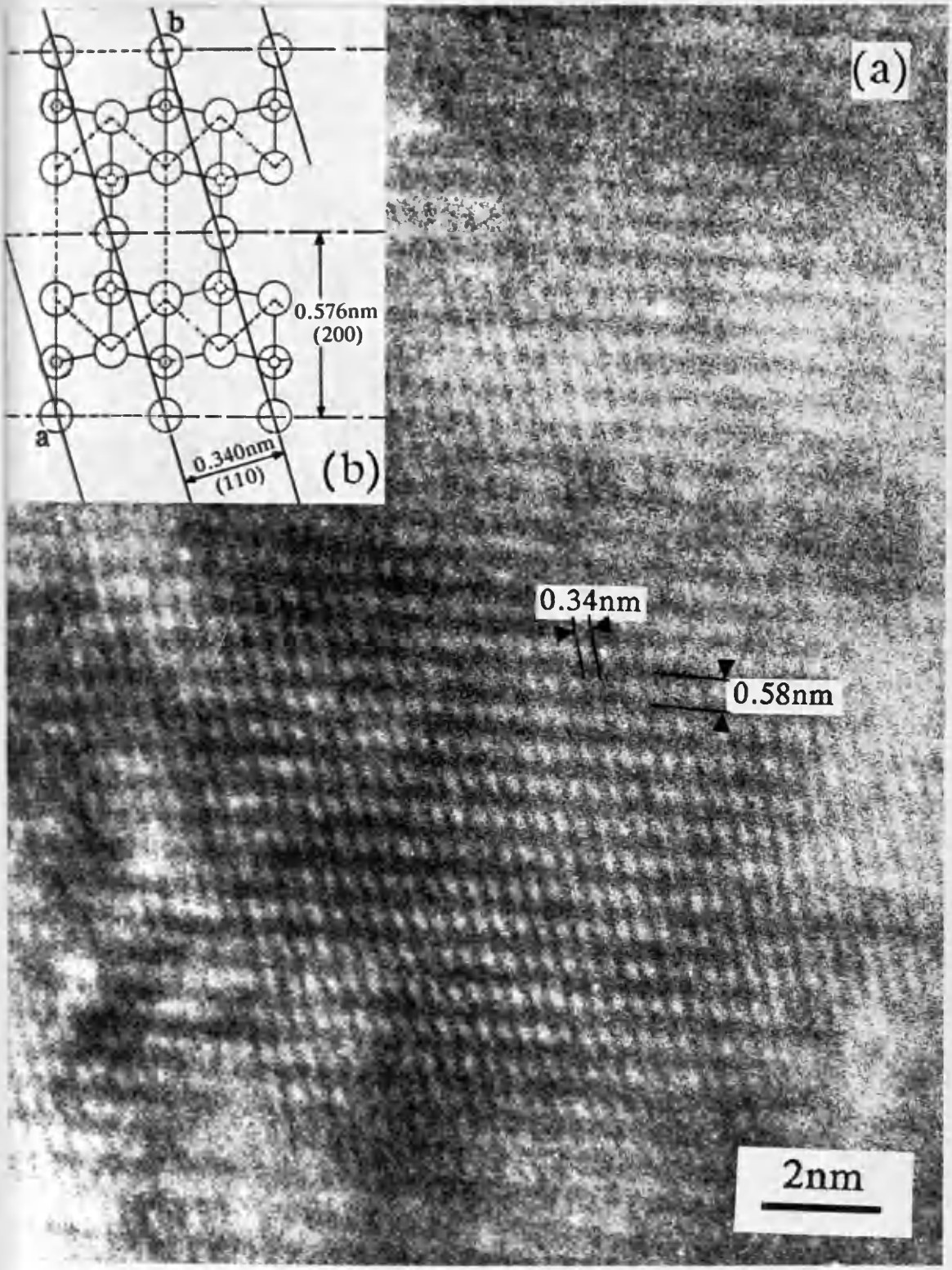

Fig. 2.26: (a) HREM image of vanadium pentoxide crystal exposing the (001) plane; (b) lattice structure of standard crystal as a projection onto (001) plane.

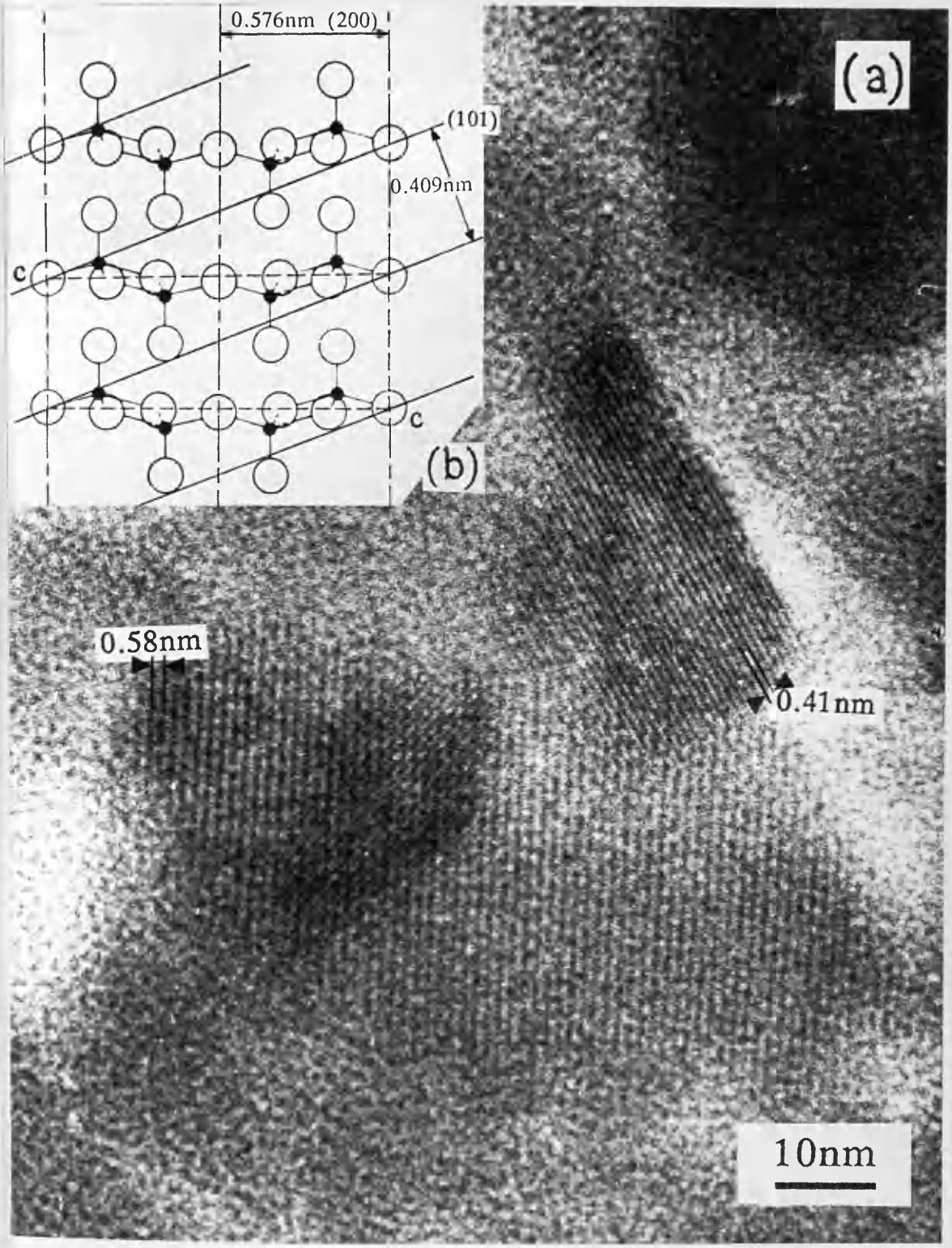

Fig. 2.27: (a) HREM micrograph of vanadium pentoxide crystals exposing the (010) plane with (b) a projection of the structure onto this plane.

while preferentially reduced vanadium ions can be found on the (100) planes (Miyamoto et al., 1981, 1983; Andersson, 1982b), and it has been shown that the (001) surface containing V=O groups exhibits higher activity in oxidation than the (010) faces (Mori et al. 1985).

Furthermore, there is experimental evidence for the vanadium oxide V_6O_{13} being more active than vanadium pentoxide in oxidation and ammoxidation reactions (Shaprinskaya et al., 1970; Gasior et al., 1979), the rationale being that the (001) planes of vanadium pentoxide expose only about a half as can the (010) planes in V_6O_{13} of V=O bonds (Andersson & Lundin, 1979). It was found also that the selectivity for the formation of phthalic anhydride in the oxidation of ortho-xylene could be correlated to the frequency of the (001) planes (Gasior & Machej, 1983).

Some electron beam damage has, however, been observed with these samples as shown for example in Fig. 2.28.b, compared with the initial image (Fig. 2.28.a). This damage was usually observed after the time necessary to take an initial EDP and a through-focus series of HREM images. Typically this was a period of about 5 to 15min. Initial EDP were typical vanadium pentoxide single crystal patterns and initial images showed corresponding lattice fringes. Subsequently, the image degraded, with disappearance of detail and simultaneous appearance in various regions of the crystal of domains mainly without a discernible structure. In other instances these small regions contained groups of parallel fringes of 0.62nm, without discernible structure in many cases.

Fig. 2.29 shows a series of SAED patterns from a vanadium pentoxide specimen recorded initially and at different times after irradiation. After few minutes of exposure to the electron beam, an extra array of spots were visible (Fig. 2.29.b) which were absent from the initial SAED in Fig. 2.29.a and which appear to have a well-defined orientational relationship with the vanadium pentoxide spots. On longer or very intense exposure to the electron beam, a

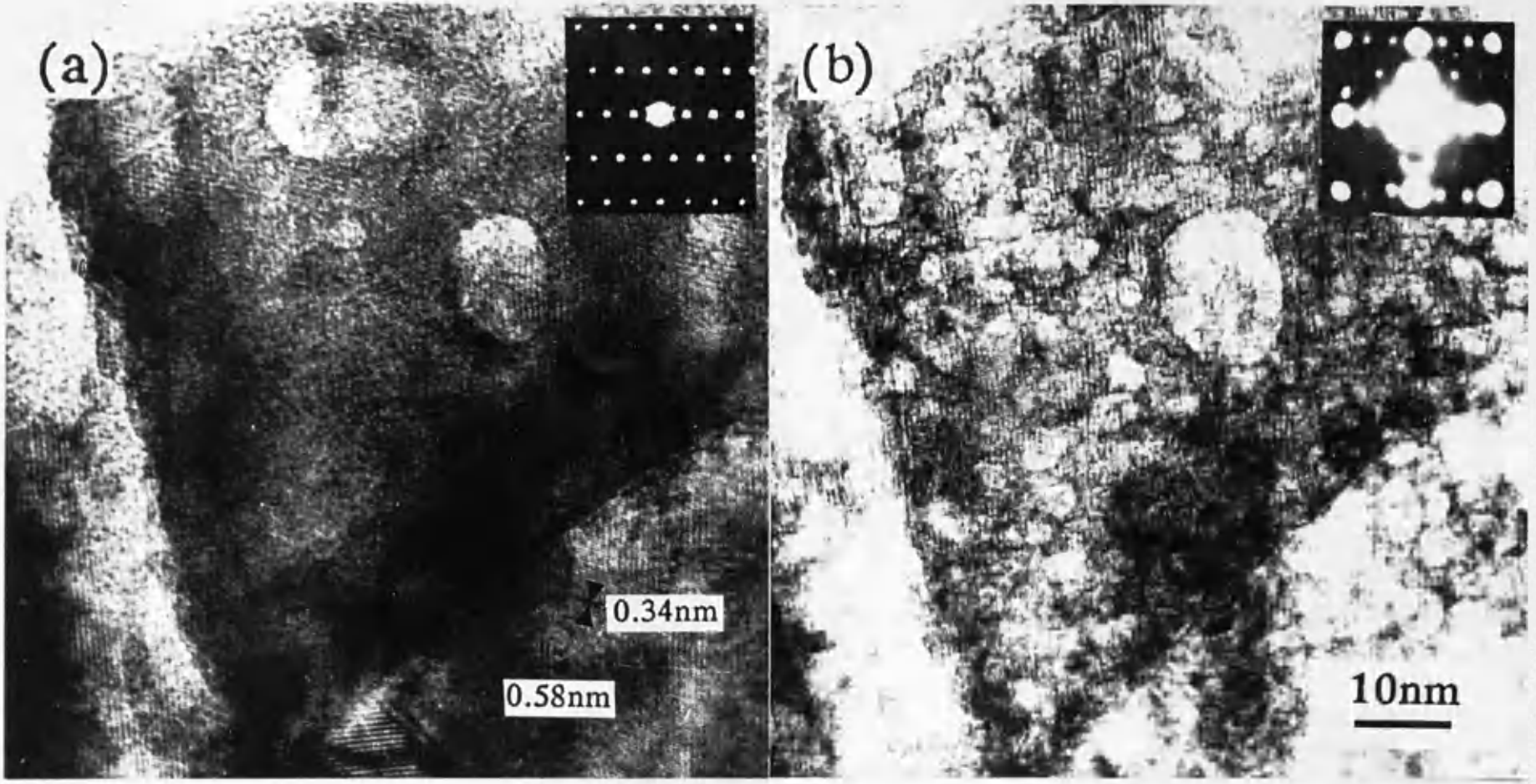

Fig. 2.28: HREM micrographs of vanadium pentoxide crystals with the corresponding SAED patterns: (a) initially, and (b) after irradiation with the electron beam.

new pattern appeared and became more intense.

The orthorhombic dimensions from the initial vanadium pentoxide SAED pattern (Fig. 2.29.a) provided a reference calibration for accurate measurement of the extra spots in Fig. 2.29.b and c. These d—spacings calculated from the SAED pattern spots correspond to 0.204 and 0.144nm. Reference to the x—ray powder diffraction file index revealed a considerable number of lower valence vanadium oxides, such as V_4O_5, V_6O_{13}, V_8O_{15} and VO_2, which have comparatively large unit cell dimensions and predominant lattice spacings in the range 0.33 to 0.36nm. Only vanadium metal, which has a body—centred cubic structure with a cell dimension: a = 0.3027nm, and the vanadium monoxide would seem to be a serious candidates for the modified surface layer, and an approximately 4% distortion would be required in the case of vanadium metal.

As many other monoxides of the transition metals, the vanadium monoxide has a sodium chloride type structure. It is, furthermore, stable over a wide range of non—stoichiometry (VO_x) which extends from x = 0.8 to x = 1.27 (Schonberg, 1954; Westman & Nordmark, 1960; Banus & Reed, 1970; Anderson, 1974). The cell parameter value varies from 0.402 to 0.414nm. This is due to the fact that the vanadium monoxide contains defects on three sites: anion vacancies, metal vacancies and interstitials as well as displacements of metal atoms near oxygen vacancies (Kofstad, 1972; Gjonnes, 1976).

A similar finding has been reported by Smith et al. (1987). They attributed their SAED pattern, which is similar to ours, to the non—stoichiometric vanadium monoxide $VO_{0.9}$ which has a lattice parameter a = 0.412nm.

2.3.8— THE DECOMPOSITION MECHANISM

The detailed mechanism for the evolution of ammonia and

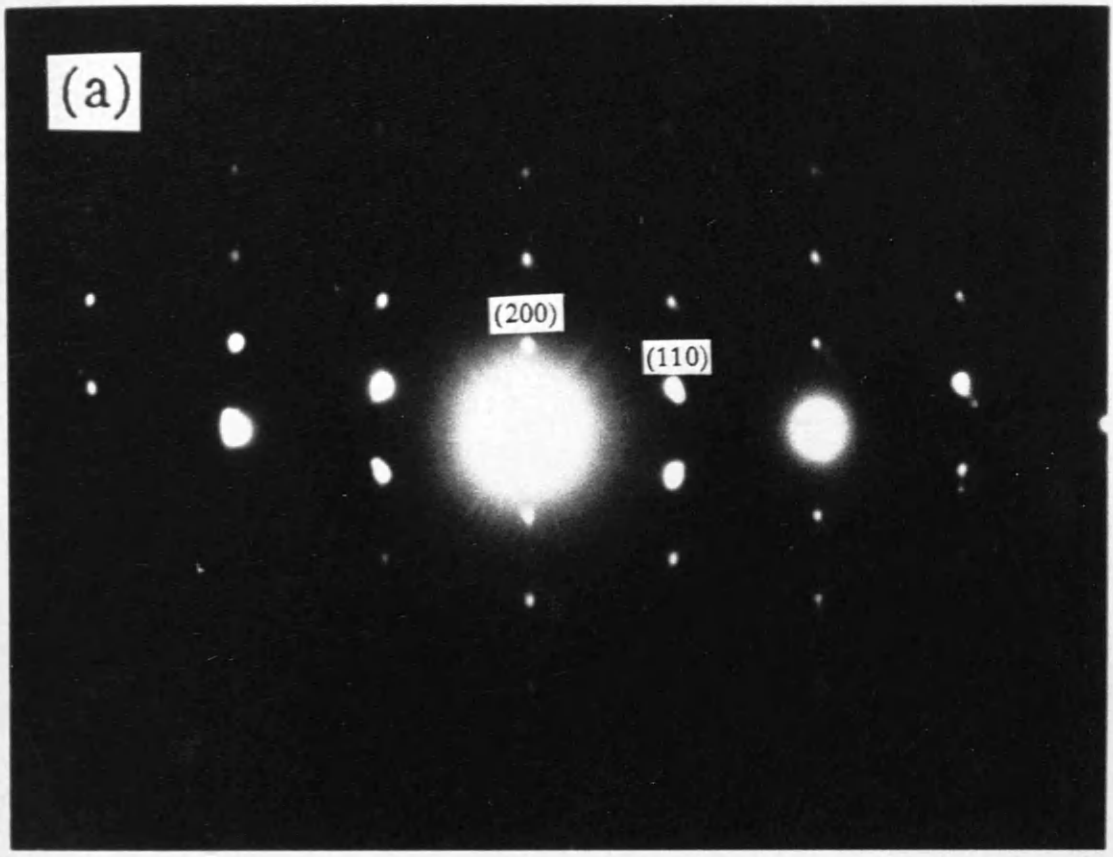
(a)
(200)
(110)

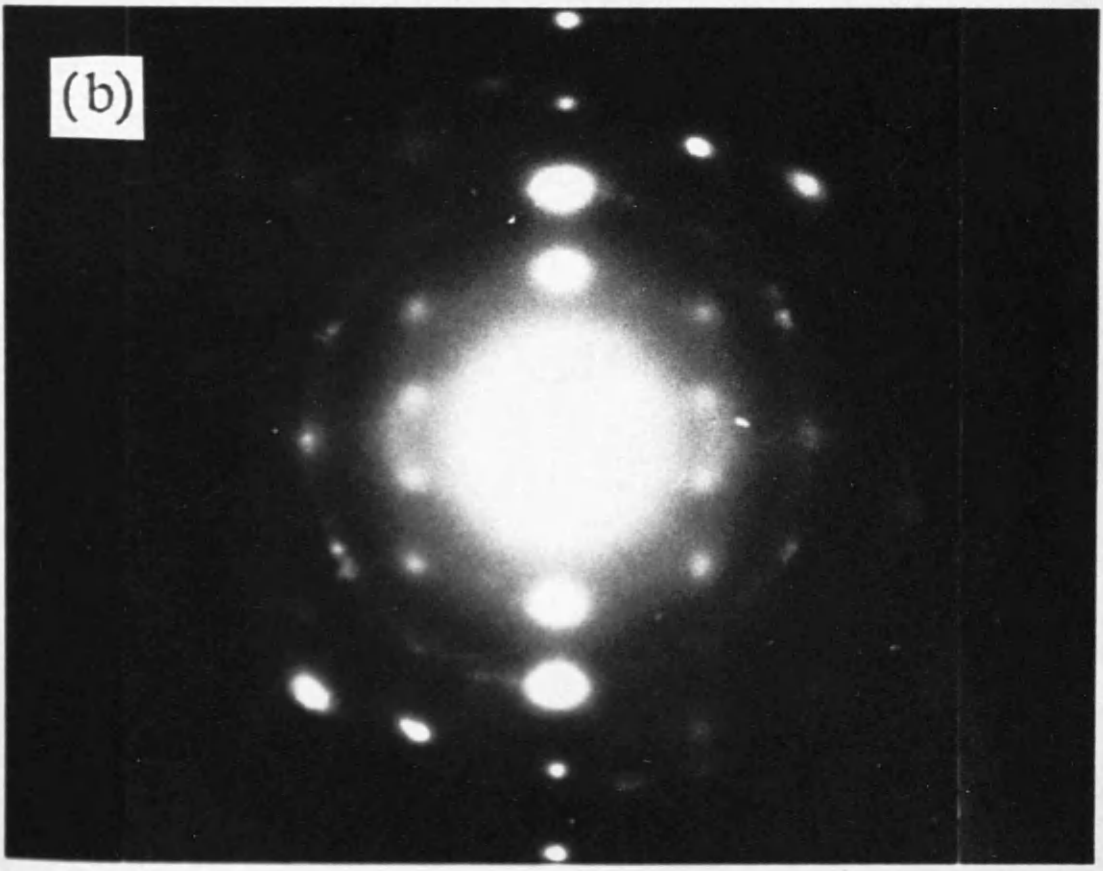
(b)

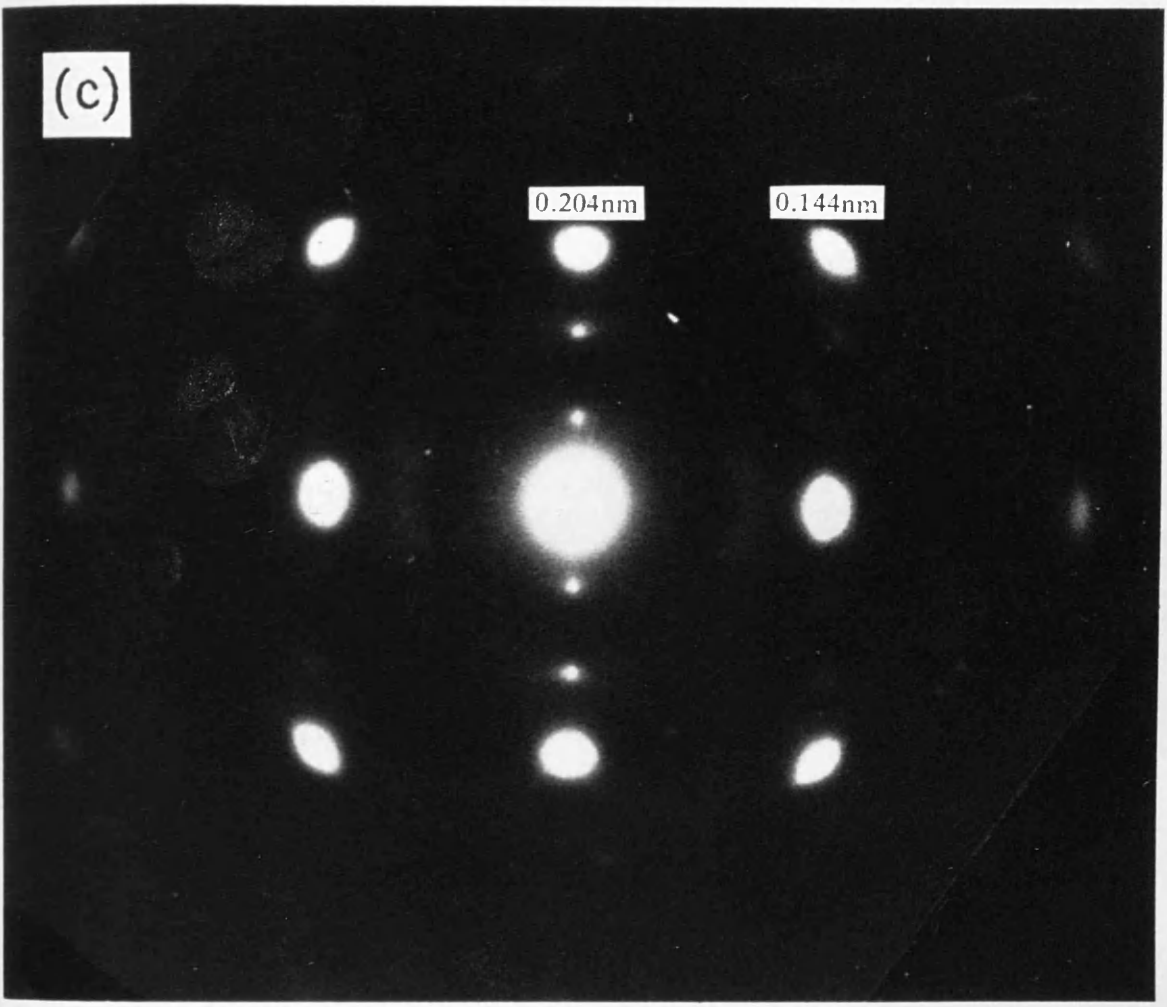

Fig. 2.29: Series of SAED patterns from a vanadium pentoxide specimen recorded (a) initially, and (b) and (c) at different times after exposure to the electron beam.

water, throughout the decomposition of AMV, may be expected to be rather similar to that proposed for the thermal decomposition of ammonium—exchanged zeolites (Rabo et al., 1961; Uytterhoeven et al., 1965; Kerr, 1969; Bolton & Lanewala, 1970), for which similar steps have been shown to be readily reversible (Bolton & Lanewala, 1970) as in the case for the AMV decomposition (Brown et al., 1973).

The concept of the decomposition mechanism envisaged the thermal decomposition of ammonium—exchanged zeolites to proceed through an intermediate hydrogen species formed by the evolution of ammonia (Rabo et al., 1961; Uytterhoeven et al., 1965). Doubts about the existence of a hydrogen intermediate containing free protons have been allayed by proposing the reaction of these protons with lattice oxygens to form hydroxyl groups (Uytterhoeven et al, 1965). This have been confirmed by the appearance of bands in the IR spectrum which correspond to hydroxyl stretching frequencies (Angell & Schaffer, 1965). However, this form was considered unstable at elevated temperatures and converted to the dehydroxylated form by the liberation of water. The same reaction has also been observed for ammonium mordenite (Benesi, 1967).

2.3.8.a— Decomposition of AMV to AHV

The application of the same mechanism to the first step in the thermal decomposition of AMV leading to AHV would involve the breaking of the distorted tetrahedral VO_4 chains of AMV into discrete units. The stoichiometry of the reaction of AMV decomposition to AHV,

$$6NH_4VO_3 \longrightarrow (NH_4)_2V_6O_{16} + 2NH_3 + H_2O$$

requires that these units should be based on a ratio of three

vanadium to eight oxygen atoms. By assuming that the fracture of the VO_4 chains is a cooperative process yielding identical V_3O_8 units, if the positions of fracture in AMV are chosen to allow the formation of AHV with the minimum of atomic movement, the situation illustrated in Fig. 2.30.b is obtained. This situation is derived directly from Fig. 2.30.a, with the omission of two molecules of ammonia and one of water for every three 'molecules' of AMV, as is appropriate for the decomposition. The tetrahedral chains in AMV break at the points marked with arrows in Fig. 2.30.a on removal of oxygen atoms as water.

The chemistry of the decomposition of AMV, following that of ammonium–exchanged zeolites (Bolton & Lanewala, 1970), may be represented by the following equation:

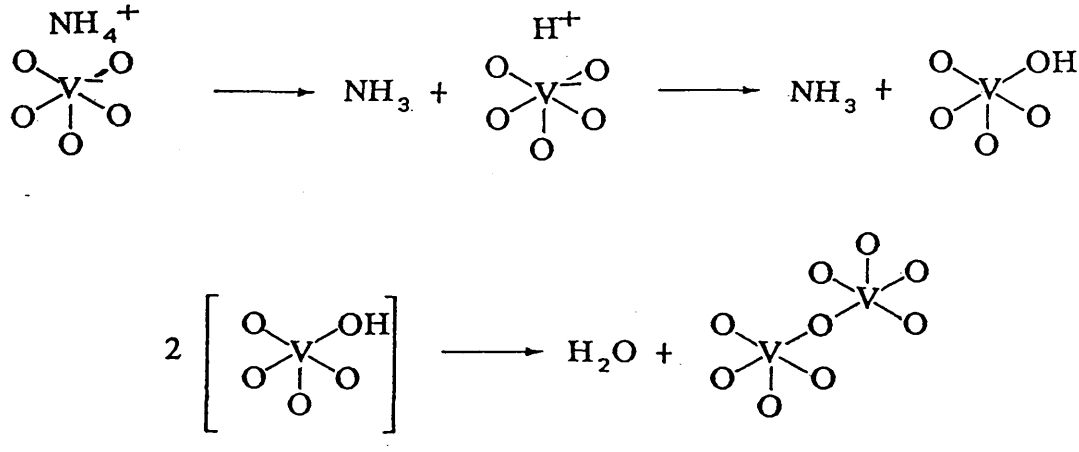

Each of the V_3O_8 units formed may be considered to rotate, about an axis joining the two terminal vanadium atoms, away from the direction in which the apices of the tetrahedra point, through 135 or 45° alternately (Fig. 2.30.c). This process is accompanied by a contraction in the b and c directions of AMV, resulting in the orientation of these units shown in Fig. 2.31.a. These units then cross–link to form the AHV structure (Fig. 2.31.b). It should be noted that the structures have been slightly distorted in drawing to emphasise the perspective.

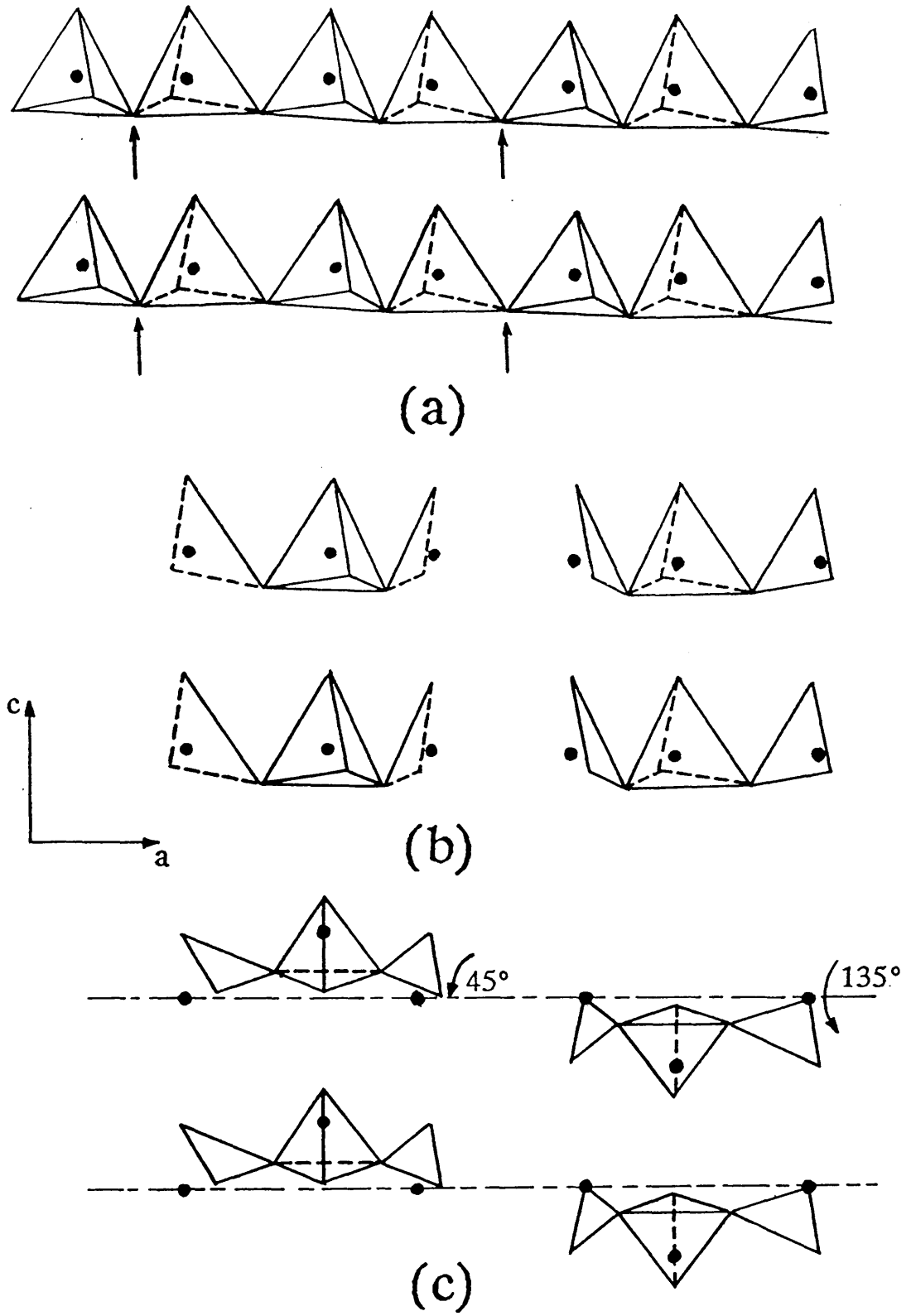

Fig. 2.30: (a) Distorted tetrahedral VO_4 chains of AMV; (b) formation of V_3O_8 units by rupture of the chains during the decomposition of AMV; (c) the two orientations of the V_3O_8 units after rotation about the axis joining the two terminal vanadium atoms and contraction in the b and c directions of AMV.

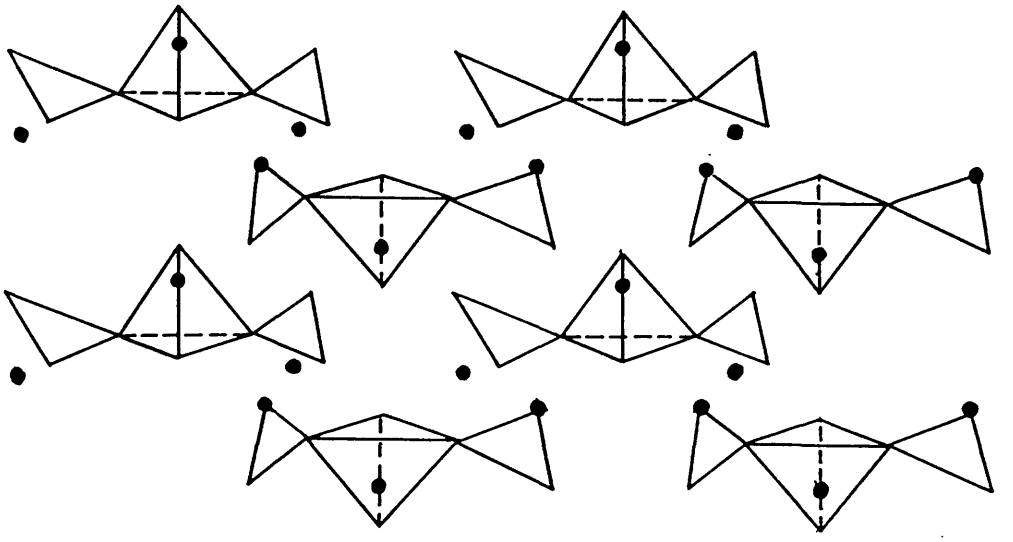

(a)

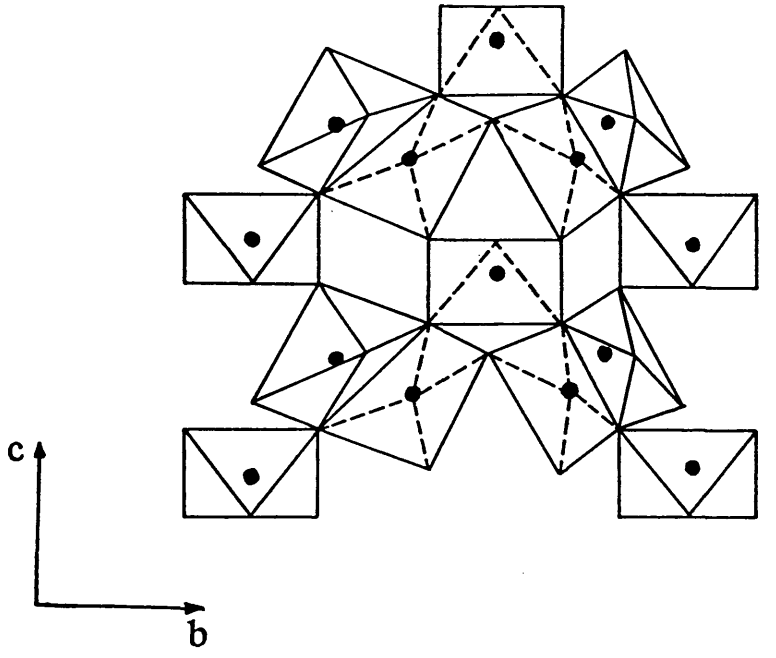

(b)

Fig. 2.31: (a) V_3O_8 unit arrangement after rotation and contraction, but prior to cross–linking to form the AHV; (b) representation of AHV structure in terms of linked square pyramids.

The isolation of the ABV intermediate under certain conditions suggests that scission of the V—O chains in AMV into discrete units is largely complete in these conditions before cross—linking, to AHV, occurs. Then, at the higher temperatures needed for the decomposition of ABV, the movements required for the cross—linking to AHV will be facilitated.

A chain scission process, as suggested, into ideally $V_3O_8^-$ units will, undoubtedly, lead to some disordered regions. These will be minimised if conditions allow a certain degree of reversibility of the decomposition process e.g., if the gaseous products are not rapidly removed. Brown & Stewart (1970) found that the intermediate AHV formed during the thermal decomposition in vacuum has a less ordered structure than that of AHV obtained at atmospheric pressure.

2.3.8.b— Decomposition of AHV to vanadium pentoxide

In the structure of AHV, the vanadium atoms are in square—pyramidal coordination with oxygen atoms, with a sixth oxygen atom weakly coordinated through the base of the pyramid (Evans & Block, 1966). This coordination is similar to that found in several other oxovanadates and vanadium pentoxide (Bachmann & Barnes, 1961). Accordingly, the basic V—O network in vanadium pentoxide is very similar to that in AHV.

The decomposition of AHV according to the reaction:

$$(NH_4)_2V_6O_{16} \longrightarrow 3V_2O_5 + 2NH_3 + H_2O$$

would involve removal of one of the 16 oxygen atoms from an AHV unit, as water, together with the ammonia molecules. This must involve rearrangement of the square pyramids so that edges rather than corners are shared. Neighbouring square pyramids with shared corners in AHV are in the correct orientation for edge sharing as in

vanadium pentoxide.

The V—O network in AHV is obviously not very regular since the various AHV reactants, prepared under different conditions, showed differing degrees of order (Brown & Stewart, 1970). As the distribution of ammonium ions can also be considerably asymmetrical, the removal of oxygen from AHV will almost certainly not be regular. This is borne out by the uncertainty in the uniformity of the structure of vanadium pentoxide catalysts, prepared by the decomposition methods. It has emerged from many discussions (Simard et al., 1955; Patrina & Ioffe, 1964; Gillis, 1964; Bhattacharyya & Mahanti, 1971) that vanadium pentoxide catalyst is a non stoichiometric oxide having a certain degree of anion deficiency. Furthermore, an increased crystallinity of the vanadium pentoxide was observed when AMV was decomposed in oxidising atmospheres (Brown & Stewart, 1970), where the special effect of oxygen exchange with the vanadium pentoxide lattice has been discussed (Brown et al., 1974).

CHAPTER THREE

VANADIUM PENTOXIDE– SUPPORTED RHODIUM CATALYST

*** 3.1 ***

INTRODUCTION

3.1.1— SUPPORTED METAL CATALYSTS

Supported metal catalysts are widely employed in the chemical industry with diverse applications such as petroleum refining, gas purification and the treatment of vehicle exhaust emission. Their importance stems from the possibility of their preparation with the metal in a high state of dispersion, with the support providing a structural framework for the active metal. In this form, the metal is present at the surface of the carrier in the form of small crystallites which are separated.

Consequently, the metal is more resistant to sintering and poisoning than unsupported metal powders or films. This produces a highly efficient catalyst with maximum specific metal surface area, and improves the thermal stability and therefore the life of the catalyst significantly. In addition, this may result in more selective catalysts depending whether or not the reaction is structure sensitive.

The literature on supported–metal catalysts is voluminous and reviews summarising the subject or particular aspects such as preparation procedures and characterisation have appeared (Anderson, 1975; Burton & Garten, 1977; Sinfelt & Cusumano, 1977; Dowden, 1978; Thomas & Lambert, 1980; Acres et al., 1981; Moss, 1981).

The efficient dispersion of the active phase (metal) over the support surface is the main aim of a successful preparation. Supported– metal catalysts may be prepared by three distinct methods: deposition, coprecipitation and impregnation. The direct deposition of the metal from the vapour phase onto the support has

been used in the laboratory to prepare model catalysts especially for electron microscopy studies (Baker et al., 1979; Ruckenstein & Chu, 1979; White, 1982). The impregnation method is probably the most common method used. It is generally a multiple process consisting of the distribution of a precursor compound (for example a metal salt) over the support surface followed by drying of the catalyst and transformation of the precursor compound into the active metallic phase by reduction.

Catalyst characterisation plays an important role in the design of the catalyst and is performed with the aim to find a link between catalyst performance and the catalyst structure and electronic properties.

A variety of physical methods, such as electron microscopy, XRD line broadening and low angle x—ray scattering can be employed in the determination of the size of metal crystallites (Delannay, 1984).

Another important feature in the study of supported—metal catalysts is the determination of the surface area of the metal. The most effective method of obtaining this surface area is by gas chemisorption. In this method it is clearly necessary to choose a gas which adsorbs selectively on the metal rather than on the support. The selective gas chemisorption of hydrogen and carbon monoxide has been used by many investigators.

The traditional view was that the support was an inert carrier of the active component with no chemical carrier—metal interaction. However, in recent literature on supported metal catalysts, new concepts regarding the influence of the support on metal particles have emerged. These concepts suggest that when the metal is supported on certain oxides, the support exerts a major influence on the behaviour of the metal. Some of the contributing factors to this influence, amongst the supports available for use, are the great variations in their surface area, porosity and surface chemical

reactivity (Bond & Burch, 1983). The first manifestation of an influence of the support on the metal is thus through the average size and size distribution of the metallic particles.

Accordingly, support materials were classified into four distinct classes (Foger, 1984):

(a) Inert supports, like silica, supplying high surface area for dispersion of active component.

(b) catalytically active supports, like aluminas, silica– aluminas, zeolites, etc.

(c) supports influencing active component by strong interaction, like partially reducible oxides, titania, niobium pentoxide, vanadium pentoxide, etc.

(c) structural supports, which are of increased importance for exhaust gas purification (monoliths).

3.1.2– METAL-SUPPORT INTERACTION

The industrial importance of metal catalysts supported on partially reducible oxides, like vanadium pentoxide, titania and niobium oxide, has stimulated considerable interest during the last few years (Imelik et al., 1982). These supports are known to influence the active component by strong interaction (Foger, 1984).

The metal– support interaction effect is defined as a direct influence of the support on the chemisorption and catalytic properties of the metal phase either by stabilising unusual metal particle structures, by changing the electronic properties due to electron transfer processes between the metal particles and the support, or chemical bonding – compound formation– between metal and support (Foger, 1984).

Metals interact only weakly with non– reducible carriers such as alumina, silica, magnesia, zirconia, unless these are reduced at extremely high temperatures, (Anderson, 1975).

However, metal particles inside zeolite channels (Gallezot, 1979) or supported on reducible oxides like titania and reduced at high temperatures (Tauster et al., 1978) exhibit strongly modified properties caused by support effects.

Over the past decade those aspects have attracted considerable interest. Bond (1982) has pointed out the diverse nature of support effects, and suggested a classification of metal–support interactions according to their strength into three categories:

(a) weak metal–support interactions, e.g., non–reducible carriers.

(b) medium metal–support interactions, as found with metal particles in zeolites.

(c) strong metal–support interactions (SMSI), for metals on certain reducible oxides after high temperature reduction treatment.

3.1.2.a– Strong metal–support interaction

The term initially introduced by Tauster et al. (1978) to interpret the suppression of the normal ability of group VIII noble metals supported on titania to adsorb hydrogen and carbon monoxide when reduced at 500°C, is now widely used to explain the modification of the chemisorption and reaction properties of supported metals caused by exposure to hydrogen at high temperatures.

It has been shown that the high temperature reduction of titania supported noble metals which results in a SMSI not only leads to the loss of the metal capacity for hydrogen chemisorption but also results in the suppression of the metal activity for hydrogenation and hydrogenolysis reactions. However, the SMSI is partially or totally destroyed when the catalysts are reoxidised either at room temperature or at 300–500°C (Meriaudeau et al., 1982).

Supports which are claimed to form strong interactions with metals include reducible oxides such as titania, niobium pentoxide, tantalum pentoxide, vanadium trioxide (Tauster & Fung, 1978) and

non reducible oxides such as alumina, silica and magnesia.

Studies of these oxides have shown that these oxides present common defect states (Ti^{3+}, V^{2+}, Ta^{2-4+}, Nb^{2-4+}) which are created upon hydrogen reduction at elevated temperatures (Sexton et al., 1982) and this partial reduction is catalysed by the presence of groups VIII metals due to spillover phenomena (DeCanio et al., 1983).

The SMSI effect was attributed by many authors to a transfer of electrons from partially reduced support to the metal particles (Chen & White, 1982; Ellestad & Naccache, 1981; Hermann et al., 1982; Meriaudeau et al., 1982). This transfer results in 'electron rich' metal particles, which have been identified from negative shifts of core level metal peaks in x—ray photoelectron spectra of SMSI catalysts (Bahl et al., 1980; Kao et al., 1980; Chien et al., 1982; Fung, 1982).

Many theories have been suggested to explain the SMSI. They can be divided into two types: electronic and geometric. SMSI effects on reducible oxides (n—type semi—conductors) originate from the transfer of electrons from the support to the metal leading to negative charged metal particles, while in non—reducible oxides (non—conducting oxides) these effects are due to the formation of intermetallic compounds between support and metal atoms (Foger, 1984).

3.1.3— CATALYSED REDUCTION OF OXIDE SUPPORTS BY THE SUPPORTED METALS

One of the symptoms to the close interaction between metal and support in supported metal catalysts is the phenomenon of hydrogen spillover. Hydrogen atoms formed by dissociation of molecular hydrogen on the metal may easily migrate to the catalyst support which has hydrogen acceptor sites, participate in chemical reactions

on the support and chemically reduce it. This process was first detected by Khoobiar (1964) and has been reviewed by Sermon & Bond (1973).

It is well established that certain metal oxides are reduced more readily by hydrogen when precious metals are present. Small quantities of the metal catalysts (0.1—1%), particularly palladium and platinum, were capable of substantially lowering the temperature of reduction of tungsten trioxide, molybdenum trioxide, uranium trioxide and vanadium pentoxide (Sancier, 1971; Il'Chenko, 1972; Bond et al., 1973).

Some practical considerations such as the use of some of the oxides as catalyst supports and the need for a better understanding of interactions occurring in supported metal catalysts motivated the study of the catalysed reduction of metal oxides by a support.

An important characteristic feature of these systems is that the metal, under the conditions of the reaction, does not form chemical compounds or solid solutions with the original oxide or the products of its reduction (Il'Chenko, 1972). The thermodynamic characteristics of the original oxide remain unchanged when the metal is added. It was proved experimentally by study of the adsorption—chemical equilibria that the energies of the bonds formed by oxygen with pure vanadium pentoxide and with vanadium pentoxide containing 0.1% per weight of platinum are identical (Stukanovskaya et al., 1968; Il'Chenko et al., 1970).

Thus the metallic additive, without influencing the thermodynamics of the reduction, increases its rate considerably, that is it catalyses the reduction. These reactions can be considered in some respects to be similar to gaseous—catalytic reduction processes. On the other hand, these reactions are heterogeneous topochemical reactions, in which one solid substance, the original oxide, is converted into another lower oxide or metal.

Many of the regular features formulated for the metal catalysed

reduction of certain oxides by hydrogen may also be applicable to their reduction by reducing agents other than hydrogen.

3.1.3.a– Metal–catalysed reduction of vanadium pentoxide

Roiter & Yuza (1962) found that the rate of reduction of vanadium pentoxide by hydrogen was increased considerably after the vanadium pentoxide had been melted in a platinum crucible. The catalytic action of very small quantities of platinum on the reduction of vanadium pentoxide was first established by Il'Chenko & Yuza (1966), who made a detailed study of the influence of various factors on the kinetics of this reaction. The platinum was introduced into the specimen by impregnation with its concentration varying from 0.0005 to 0.5 weight percent, relative to the original oxide. According to these authors, the reduction takes place in three macro–stages:

$$3V_2O_5 + 2H_2 \longrightarrow V_6O_{13} + 2H_2O$$

$$V_6O_{13} + H_2 \longrightarrow 3V_2O_4 + H_2O$$

$$V_2O_4 + H_2 \longrightarrow V_2O_3 + H_2O$$

The addition of platinum increases the rates of all three macro–stages, but the catalytic action of platinum is greater at low degrees of reduction.

Batley et al. (1974) found that a surface coating of 0.5 weight % platinum on vanadium pentoxide significantly lowered the reduction temperature, of 486°C, by nearly 300°C. They state that a mixture of vanadium pentoxide and 5% platinum supported on silica reduces slowly at 350°C.

However, Bond & Tripathi (1976), who studied this system by

TG and DTA, have reported that the onset of reduction by hydrogen is brought down from 387°C to about 127°C when 5% platinum supported on silica is added to vanadium pentoxide. They also stated that the catalysed reduction proceeds by way of V_2O_4 leading to vanadium trioxide.

The rate of the reduction of vanadium pentoxide by carbon monoxide increases sharply by addition of small quantities of palladium. Pure vanadium pentoxide begins to be reduced at 575°C, whereas the starting temperature for the reduction of a mixture of vanadium pentoxide and 0.1% palladium supported on barium sulphate ($Pd/BaSO_4$) is 25°C (Stukanovskaya et al., 1970).

It was also found that when palladium is added to vanadium pentoxide the reducibility of this oxide by ethylene (Blejean et al., 1970; Seoane et al., 1980) and by ortho–xylene (Blejean et al., 1970) is enhanced.

3.1.4– CHARACTERISATION OF SUPPORTED–METAL CATALYSTS BY TRANSMISSION ELECTRON MICROSCOPY

The main technique used in the course of this study, to characterise the vanadium pentoxide–supported rhodium catalyst prior to its use in the butane hydrogenolysis reaction, was transmission electron microscopy. This section describes the possibilities of this technique and the information which can be deduced after analysis of the specimens.

The instrumentation and theory of electron microscopy has been the subject of the first chapter of this thesis.

The technique offers a unique opportunity to observe, measure, size and analyse supported metal particles. It provides thus particle size, size distribution and metal dispersion data (Prestridge & Yates, 1971; Nakamura et al., 1975) for comparison with other techniques

such as chemisorption and XRD measurements which are essentially averaged data. In addition, particle shape and internal structure can be examined as well as the spatial distribution of the particles throughout the support (Yacaman & Ocana, 1977; Marks & Howie, 1979; Yang et al., 1979).

Several reviews have been the subject of the use of electron microscopy in supported metal catalyst characterisation (Howie, 1980; Poppa & Heinemann, 1980; Baird, 1982, 1984; Yacaman, 1984; Sanders, 1985; Matyi et al., 1987).

The data obtained by electron microscopy examination of supported metal catalysts are based on three implicit assumptions (Flynn et al., 1974), namely:

(a) the size of a metal particle is equal to the size of its image recorded after correction for magnification,

(b) detection of a particle at a given size implies that all particles of that size and all larger particles are being detected,

(c) image contrast of the metal particles is distinguishable from contrast arising from the support material.

However, the attainment of meaningful data from electron micrographs is not always straightforward. Many problems have been generally recognised when using TEM for quantitative measurements, e.g., lack of contrast, electron beam effects, crystallite agglomeration, selection of a diameter when examining irregularly shaped crystallites and representative sampling.

The visibility of very small metal particles and their apparent size are strongly affected by support microcrystallinity (Millward, 1980), orientation of particles and imaging conditions (Flynn et al., 1974). Many attempts have been made to sort out contrast effects from small metal particles experimentally and theoretically and tried to elucidate scattering mechanisms (Freeman et al., 1977; Howie, 1980; Baird, 1982).

The main scattering mechanism for small crystals is Bragg

reflection which depends strongly on the orientation of the specimen and this may lead to misinterpretation of the true particle morphology (Flynn et al., 1974). This generally makes amplitude or diffraction contrast the dominating effect for particle sizes above 3nm (Treacy & Howie, 1980). The amplitude contrast arises because electrons are scattered outside the objective aperture and are lost to the usual bright field image which consequently appears dark in the scattering region (Hirsch et al., 1965).

For sufficiently small particles, of 1.5nm in diameter or less, phase contrast mechanism dominates over diffraction contrast. Detection of these particles is therefore very sensitive to the defocus of the objective lens (Treacy & Howie, 1980).

The general consensus of the published work seems to be that bright field techniques are increasingly unreliable for particle sizes below 2nm (Foger, 1984). However, other contrast methods, such as hollow–cone dark field (Zenith et al., 1980) and other dark field methods where the contrast from the support is decreased and the Z–contrast technique (Treacy et al., 1978) where scattering is proportional to the atomic number, are useful for extremely small particles.

Image intensity varies with defocus and so detection of small particles depends on their elevation. Specimen thickness should be therefore kept to a minimum (Oikawa et al., 1970). It is however possible in some cases to remove the metal particles from the support by ultrasonic treatment (Baird, 1982) or dissolution of the support, but such treatments destroy other valuable information like spatial distributions of metal particles and metal–support interaction.

Another problem is the acquisition of statistically significant data. This can only be done if several thousand particles are counted and measured, a task which is generally very tedious.

Apart from particle size determinations electron microscopy is increasingly applied to study metal particle morphology, such as

crystal shape, crystal habit and defect structure, (Smith et al., 1983b) as well as metal—support interactions (Baker et al., 1979).

New opportunities to obtain direct structural information of small metal particles opened up with the development of scanning transmission electron microscopes (Crewe et al., 1975).

3.1.5— CATALYTIC HYDROGENOLYSIS

The catalytic hydrogenolysis reactions involve the rupture of carbon—carbon bonds and the formation of carbon—hydrogen bonds via interaction with hydrogen. These reactions which are exothermic and catalysed by various transition metals have been extensively investigated.

3.1.5.a— Classification of metal catalysts

According to their behaviour, the metals appear to fall into two categories:

— First, those leading to single hydrogenolysis with marked preference for cleavage of the terminal carbon—carbon bond of an alkane chain, such as platinum and palladium, at least below 350°C (Sinfelt, 1970, 1973; Anderson, 1973; Maurel & Leclercq, 1971; Matsumoto et al., 1970, 1971), which are also the least active metals.

— Second, those leading to multiple hydrogenolysis caused by the cleavage of several carbon—carbon bonds with almost equal ease before desorption of the species formed. In this second category are all the other group VIII metals (Maurel & Leclercq, 1971; Scott & Phillips, 1980), molybdenum (Leclercq et al., 1984) and rhenium (Leclercq et al., 1979).

Rhodium and iridium can be classified into both categories since at low temperature, below 200°C, they lead mainly to single

hydrogenolysis (Maurel & Leclercq, 1971; Paal & Tetenyi, 1977), while at higher temperature multiple hydrogenolysis occurs (Maurel & Leclercq, 1971).

3.1.5.b— Hydrogenolysis on rhodium

Rhodium is one of the most active of group VIII elements for hydrogenolysis of hydrocarbons (Logan & Kemball, 1960; Boudart & Ptak, 1970; Sinfelt, 1970; Bond, 1975). Sinfelt (1970) reported the following sequence of activities of the metals over the temperature range, 200–300°C:

$$Os > Ru > Ni > Rh > Ir > Re > Co > Fe > Cu > Pd = Pt$$

When selectivity in single hydrogenolysis is considered, the various metals also behave very differently: some are non–selective, i.e., they can break all the bonds in a given hydrocarbon at similar rates, such as platinum (Matsumoto et al., 1970, 1971) or ruthenium (Kempling & Anderson, 1972; Machiels & Anderson, 1979), while others lead to selective demethylation, such as nickel and cobalt (Kochloefl & Bazant, 1968; Kikuchi & Morita, 1969; Matsumoto et al., 1970, 1971), and finally some metals preferentially break internal carbon–carbon bonds, exemplified by rhodium and iridium deposited on supports (Bernard et al., 1977; Foger & Anderson, 1979; Yao & Shelef, 1979).

It must be pointed out here that for rhodium, the state of the catalyst seems to have great importance, since metal powders of rhodium catalyse preferentially terminal bond splitting (Carter et al., 1971; Paal & Tetenyi, 1979) while it is clear that when rhodium is supported the selectivity is completely different. It is therefore interesting to try to understand the reasons for such differences in the selectivities of various metals in the hydrogenolysis of alkanes.

3.1.5.c— Hydrogenolysis of saturated hydrocarbons

The hydrogenolysis of saturated hydrocarbons over metal catalysts has been widely studied. Most of the studies have been conducted with ethane (Cimino et al., 1954; Sinfelt & Yates, 1967), but recently a number of articles have been published dealing with hydrogenolysis of larger alkanes. The most studied metals are those of group VIII (Sinfelt & Yates, 1967; Paal & Tetenyi, 1979).

For most metals, the order in hydrocarbon for ethane hydrogenolysis on different metals is reported to be about unity, but the order in hydrogen varied with the metal used to catalyse the reaction as did the apparent activation energy.

Many kinetic results concerning the hydrogenolysis of ethane on different noble metals have been explained in terms of a mechanism proposed by Cimino et al. (1954), and later modified by Sinfelt (Sinfelt & Taylor, 1968, Sinfelt, 1972).

The scheme involves reversible dissociative adsorption of ethane to form an unsaturated surface species, and the rate limiting step is the irreversible rupture of the carbon—carbon bond. The monocarbon fragments then hydrogenate and desorb as methane. According to this scheme, the adsorbed ethane loses most of its hydrogen on many metals; this explains the large negative hydrogen exponents. This scheme can be translated into equations as follows:

$$C_2H_6 \rightleftharpoons C_2H_x(ads) + aH_2$$

$$C_2H_x + H_2 \longrightarrow CH_y(ads) + CH_z(ads)$$

$$CH_y + CH_z + H_2 \longrightarrow 2CH_4$$

The symbol (ads) refers to adsorbed, and the quantity a is equal to $(6-x)/2$.

In an alternative scheme, proposed by Boudart (1969), the reaction is considered to be a two step irreversible sequence on a non–uniform surface.

The studies of alkanes larger than ethane show, in many cases, the same characteristics described previously for ethane hydrogenolysis, except that their hydrogenolysis occurs generally with lower activation energy values (Kempling & Anderson, 1970, 1972; Sinfelt, 1970, 1973; Machiels & Anderson, 1979; Dalmon & Martin, 1980) and the same basic mechanism appears to be operative which can be represented by the following scheme:

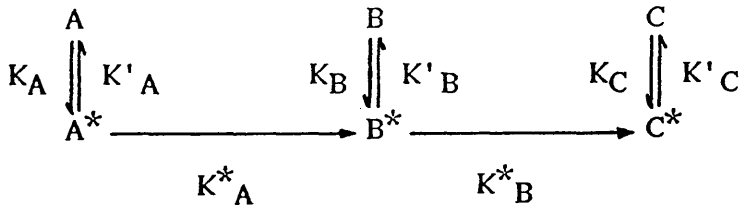

The reactant A is reversibly adsorbed producing the species A^* which are highly dehydrogenated. A^* could be desorbed to give again A, or could be split to give the species B^* which can also desorb producing the product B in the gas phase or can be split further to produce the adsorbed species C^*. The extent to which B is produced depends on the ratio of the desorption rate constants K'_B and the splitting rate constant K^*_B. If the desorption rate of B^* is small compared to its rate of splitting, the product C should be principally formed, producing multiple hydrogenolysis. Multiple hydrogenolysis increases with conversion and with temperature.

The distribution of products in the hydrogenolysis of alkanes depends on the structure of the metallic surface. In this sense, hydrogenolysis of hydrocarbons larger than propane could be used to characterise the catalyst surface (Guczi et al., 1979).

3.1.5.d— Hydrogenolysis of n—butane

There are numerous papers concerning the hydrogenolysis of n—butane on different metals and alloy catalysts. This reaction produces methane, ethane and propane; isobutane may also be formed. Many treatments of the n—butane reaction (Dowie et al., 1972; Leclercq et al., 1979; Dalmon & Martin, 1980; Tri et al., 1981; Wong et al., 1981) employ a kinetic formalism based only on the cleavage of terminal and central bonds, following the reactions:

$$C_4H_{10} + H_2 \longrightarrow CH_4 + C_3H_8$$

$$C_4H_{10} + H_2 \longrightarrow 2C_2H_6$$

A more constructive approach, which avoids the assumptions made in the procedure just described, has been adopted by Kempling & Anderson (1972). They developed a comprehensive framework which permits a deeper insight into the effects of catalyst structure and composition as well as reaction conditions on the reaction mechanism. This reaction network, which has been used by many investigators (Bond & Yide, 1984; Bond et al., 1986), can be represented by this scheme:

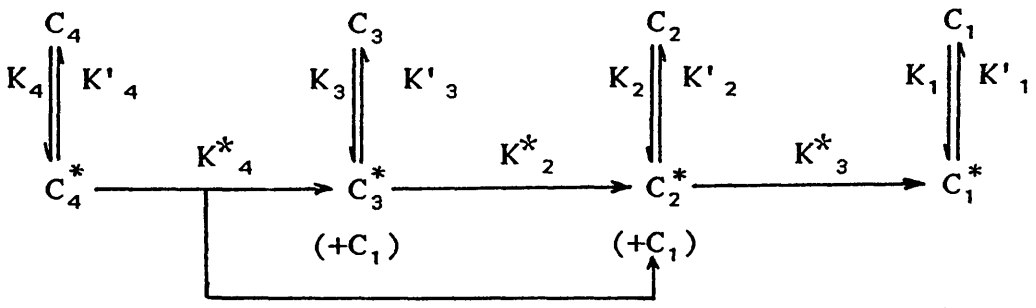

C^*_i (i = 1 to 4) represent the adsorbed species, containing i carbon atoms, which are in adsorption—desorption equilibrium with the gas

phase species C_i. These equilibria are combined with the carbon—carbon bond cleavage steps. The extension in which the individual compounds are produced depends on butane conversion at a given temperature and hydrogen:butane ratio. The product distribution depends on the catalyst used, e.g., Kempling & Anderson (1972), butane hydrogenolysis could be explained by a similar mechanism as that proposed by Cimino et al. (1954) for ethane hydrogenolysis.

3.1.6— AIM OF THIS STUDY

This part of the thesis reports on the study of the physicochemical and catalytic properties of metallic rhodium supported on vanadium pentoxide (Rh/V_2O_5).

The first step was the study of the internal structure of the support which is vanadium pentoxide prepared by thermal decomposition of AMV in air as explained in the first part of this thesis. Electron optical techniques were used for this investigation in conjunction with gas adsorption methods. In addition, a comparison was also made between two different ways of preparing specimens for HREM examination, namely, ultrasonic dispersion in water and ultrathin sectioning.

The support thus characterised was loaded with rhodium by impregnation with a rhodium chloride solution followed by drying and reduction in hydrogen. The catalyst prepared was then characterised by XRD, IR, temperature programmed reduction, carbon monoxide chemisorption and electron optical methods.

The same techniques were used to study the reduction of the support at different temperatures. This reduction was observed to be catalysed by the presence of rhodium at the surface of vanadium pentoxide.

The mechanism of the catalyst action was studied in the

hydrogenolysis of butane, reaction for which rhodium metal is known to be among the most active catalysts, using a continuous flow fixed–bed apparatus at atmospheric pressure. For comparison an alumina supported rhodium catalyst was prepared by the same method and tested in the hydrogenolysis of butane under the same conditions.

*** 3.2 ***

EXPERIMENTAL

3.2.1– MATERIALS

3.2.1.a– Vanadium pentoxide

The vanadium pentoxide used in this study was prepared, as explained in the second chapter of this thesis, by calcination of high purity AMV at 400°C for two hours under a stream of air (50ml/min).

3.2.1.b– Alumina

Aluminium oxide C (γ-alumina) powder was supplied by Degussa Geschaftsbereich Pigmente (Frankfurt, W. Germany) and was specified by the manufacturers as 99.99% pure. Its surface area measured by nitrogen gas adsorption (B.E.T.) was 140m^2/g.

3.2.1.c– Rhodium chloride

Rhodium chloride was in the form $RhCl_3.xH_2O$ and was supplied by Johnson Matthey Chemicals Ltd. (Hertfordshire, U.K.). It was specified as 99.99% pure.

3.2.1.d– Gases

All gas cylinders were supplied by British Oxygen Company Ltd. (Guildford, U.K.). All the gases were used directly from the cylinder

without further purification.

The gas butane used in the hydrogenolysis reaction was Grade N 2.0 (pure), which was specified by the manufacturers as being 99.4% pure. The impurities indicated by B.O.C. were: isobutane 0.3%, isopentane 0.2% and n—pentane 0.1%.

Hydrogen was used for the reduction of the catalyst and was mixed with butane for the hydrogenolysis experiments. It was specified as 99.9% pure.

Helium was used as a carrier gas for operation of the gas chromatograph and in carbon monoxide chemisorption experiments. Its stated purity was 99.9%.

The 6% hydrogen—94% nitrogen mixture used for temperature programmed reduction experiments was specified by the manufacturers as being 99.98% pure.

A mixture of 10% carbon monoxide—90% helium was used for the carbon monoxide chemisorption experiments. The manufacturers' stated purity for the mixture was 99.9%.

3.2.2— CATALYST PREPARATION

The catalysts were prepared by placing the appropriate support in an evaporating dish. Enough distilled water was added to wet the support thoroughly. The required volume of rhodium chloride solution was then added to give the desired percentage by weight of rhodium. The mixture was then stirred over a hot plate until most of the water had been evaporated off. The evaporating dish was then placed in an air oven, heated at 100°C, until the powder was completely dry. The dry sample was crushed and stored in a sample bottle until required.

3.2.3– TEMPERATURE PROGRAMMED REDUCTION

The temperature programmed reduction (TPR) technique is used to characterise catalysts by monitoring their reducibility. The catalyst is submitted to a programmed temperature rise, while a reducing gas mixture, usually, hydrogen diluted in some inert gas, is flowed over it. The rate of reduction is continuously measured by monitoring the composition of the reducing gas at the outlet of the reactor.

Using the system shown in Fig. 3.1, the reduction profile of each catalyst can be obtained. The catalyst was placed on a quartz sinter situated in the centre of a quartz reaction tube which was surrounded by a cylindrical electrical furnace. The temperature of the furnace was controlled by a linear temperature programmer (Stanton Redcroft, Model LVP/CA 40/R). A chromel/alumel thermocouple was placed in contact with the catalyst tube inside the furnace and the temperature recorded on a chart recorder.

Using the temperature programmes, the catalyst was heated linearly at a rate of 5°C/min, to a maximum temperature of 700°C. Any change in hydrogen concentration, which occurs as the catalyst is being heated, is monitored by the thermal conductivity detector. The signal is amplified and plotted against temperature on a chart recorder. The temperature is measured using a thermocouple attached to the wall of the reaction vessel.

The gas mixture used was 6% hydrogen– 94% nitrogen, with a flow rate of 20ml/min. The reduction profiles obtained in this way show the change in hydrogen concentration as a peak plotted on the chart recorder. Typical reduction profiles consist of a series of peaks with maxima at different temperatures, which correspond to different stages of reduction of the metal salt and sometimes of the support.

3.2.4— CARBON MONOXIDE CHEMISORPTION

The technique of carbon monoxide chemisorption gives valuable information regarding the surface area and dispersion of the catalyst.

Carbon monoxide chemisorption experiments were carried out in the pulse flow system shown in Fig. 3.2. This system consists of a helium carrier gas with a flow rate of 20ml/min which passes through a series of traps and one side of the thermal conductivity detector before entering a gas sampling valve. The gas sampling valve consists of two sample loops which are alternately filled with the mixture, 10% carbon monoxide—90% helium, and swept out with the helium carrier gas by turning a tap. In this way a pulse of carbon monoxide is admitted into the carrier gas. The combined eluant gas is monitored using thermal conductivity detector.

For calibration purposes, it is possible to direct the carbon monoxide/helium stream, via a by—pass, around the catalyst reaction vessel. In this way comparisons can be made between a peak corresponding to a full pulse, and a pulse of carbon monoxide which has passed over the catalyst, and which therefore corresponds to a volume of carbon monoxide less than than that of full pulse since some carbon monoxide has been chemisorbed by the catalyst.

3.2.5— PREPARATION OF REDUCED SAMPLES

Reduced samples of the vanadium pentoxide—supported rhodium catalyst were prepared at selected temperatures for subsequent study by XRD, IR, SEM and TEM. The catalyst was heated in a stream of hydrogen (50ml/min) for two hours at temperatures of 250, 450 and 600°C. The furnace employed was a Baird and Tatlock (London, U.K.) M193 laboratory tubular furnace. Small silica glass boats containing the samples were inserted into a silica glass tube. The temperature of the furnace was monitored by means of a tungsten/

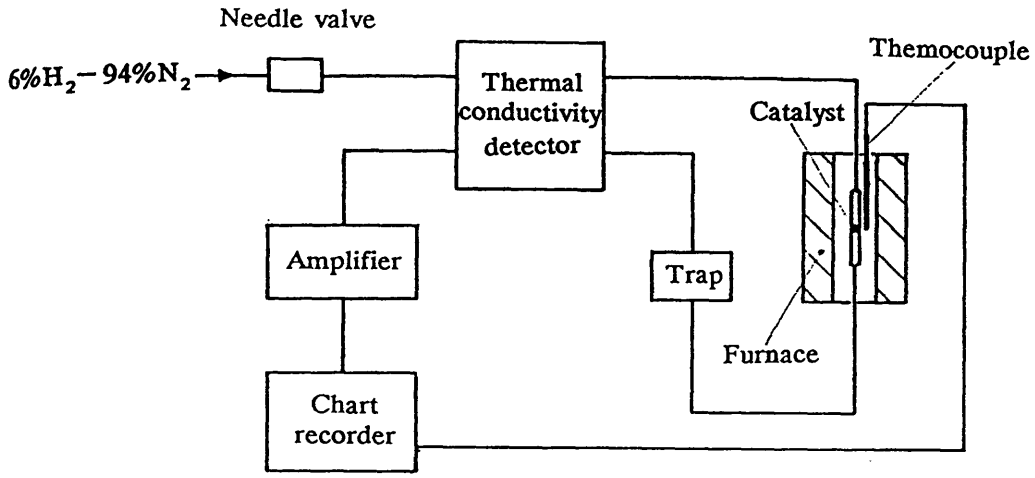

Fig. 3.1:Diagram of the apparatus used for TPR.

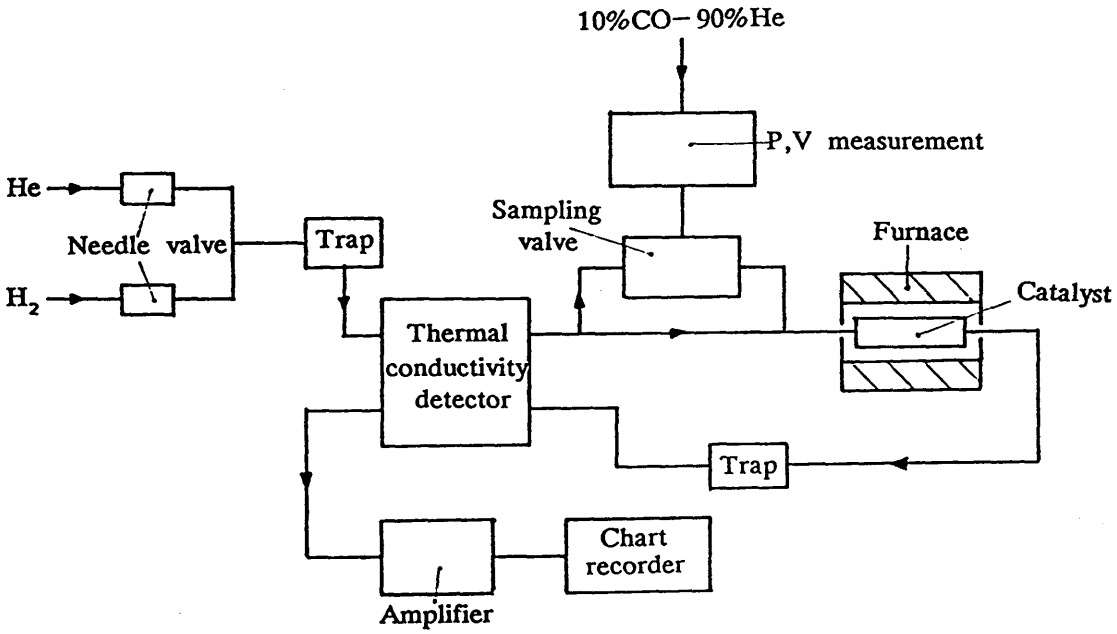

Fig. 3.2: Diagram of the system used for carbon monoxide chemisorption.

tungsten— rhenium thermocouple positioned inside the tube.

3.2.6— BUTANE HYDROGENOLYSIS

3.2.6.a— Apparatus

The catalytic studies of butane hydrogenolysis were performed in a stainless steel continuous flow system at atmospheric pressure. The apparatus is shown schematically in Fig. 3.3. It consists basically of lines of gases which are controlled before being mixed and passed through a small tube reactor R. The gas flows were measured using a soap bubble flowmeter. The temperature in the reactor was automatically regulated to ±1 °C. The analysis of the component gases was carried out by on— line gas chromatography. Gas samples were taken at the outlet of the reactor with the sample valve D.

3.2.6.b— Gas chromatography system

Resolution of reactant and product reaction mixtures was achieved using a 10m long, 3.2mm (1/8in) external diameter stainless steel column packed with a 33.3% in weight dispersion of dimethyl sulpholane (Chromatography Services Ltd., Hoylake, U.K.) fluid supported on 30— 60 mesh fire— brick, NAW chromosorb P. (Perkin Elmer, Beaconsfield, U.K.).

Chromatography was carried out using a Pye Unicam (Cambridge, U.K.) gas chromatograph fitted with a thermal conductivity detector. Helium was used as a carrier gas. The flowing gas was passed through one arm of the thermal conductivity cell then through the chromatography column and finally through the other arm of the thermal conductivity cell.

The gas samples were injected into the gas chromatograph using a sample valve and analyses were carried out under the following

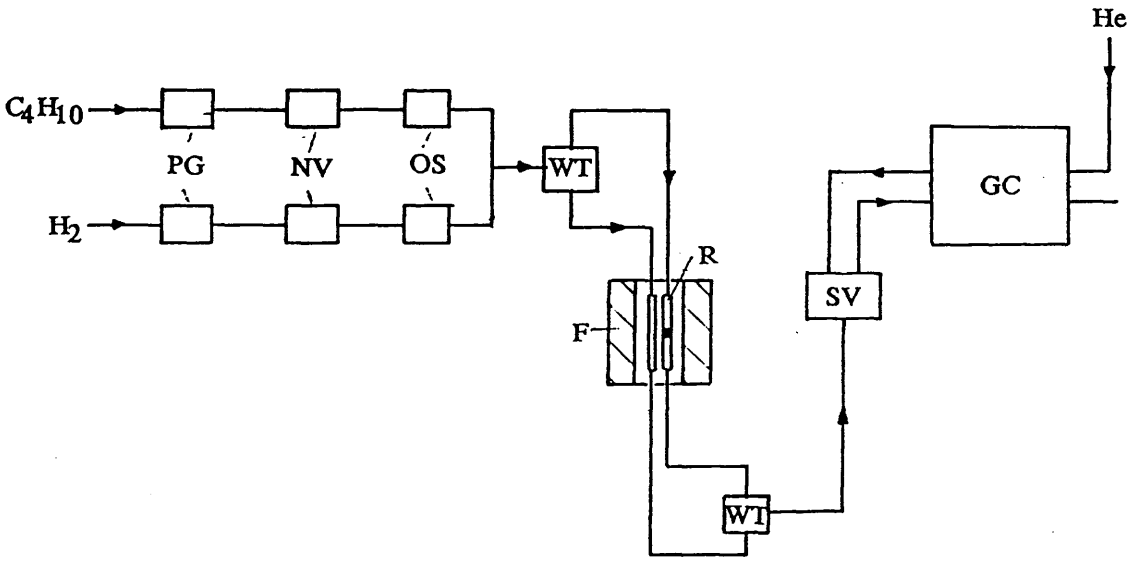

F: furnace
R: reactor
SV: sampling valve
GC: gas chromatograph

PG: pressure gauge
NV: needle valve
OS: on–off switch
WT: two way tap

Fig. 3.3: Schematic diagram of the equipment used for butane hydrogenolysis.

conditions:

Temperature of column: 30°C

Temperature of detector: 100°C

Helium flow rate: 20ml/min

Fig. 3.4 is the chromatogram of an injection of a typical mixture after hydrogenolysis of butane at atmospheric pressure.

3.2.6.c— Calibration of the chromatograph

Before the start of the hydrogenolysis of butane it was necessary to calibrate the gas chromatograph. Several binary mixtures of hydrogen—alkane with different proportions of alkane in each mixture were injected into the chromatograph under the conditions of the analysis. The partial pressures of the alkane, which was determined from both its flow rate and that of hydrogen, were plotted against the area of the peaks obtained in the chromatogram. In this way, the response coefficient for each alkane was obtained from the slope of each graph.

3.2.6.d— Experimental procedure

All the experiments, which will be described in this thesis, were carried out at atmospheric pressure. The weighed catalyst sample (usually 300mg) was placed on a piece of glass—wool in the tube reactor. For each experiment, the catalyst was reduced overnight in situ at 250°C in flowing hydrogen (16 hours approximately). It was then cooled, or heated, under hydrogen, to the desired temperature at which it had to be tested in the butane hydrogenolysis reaction.

The molar fraction of butane and hydrogen were 0.143 and 0.857, respectively. The standard flow rate of butane was 0.36 l/h (1.75×10^{-3} mol/h).

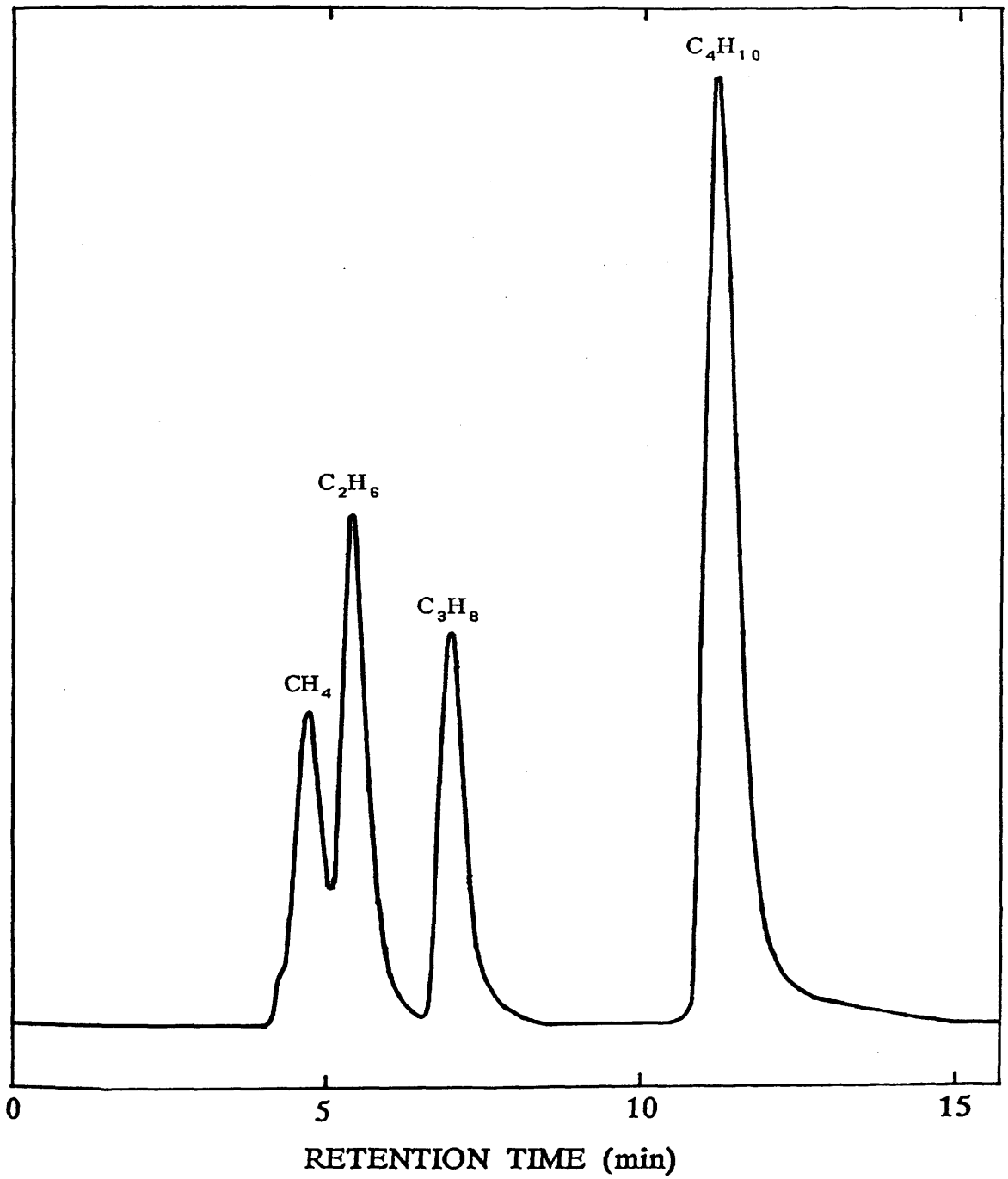

Fig. 3.4: Typical chromatogram of a gas mixture after hydrogenolysis of butane.

3.2.7— METHOD OF CALCULATION

Hydrogenolysis of butane produces a mixture of three reaction products and non—reacted butane, giving four peaks in the gas chromatographic analysis. Using the response coefficients of the four gases, it is possible to determine the partial pressure of each gas given the area of the corresponding peak. The molar percentage C_j of any component is then given by the equation:

$$C_j = 100.p_j \; / \sum_{i=1}^{4} p_i$$

The formalism of Kempling & Anderson (1972) was used for the determination of the conversion rate of butane as well as the selectivities for the three reaction products, namely, methane, ethane and propane.

3.2.7.a— Butane conversion

The percentage conversion of butane, τ is calculated from the composition of the gas mixture by the equation:

$$\tau = 100.A \; / \; (A + C_4)$$

A being the moles of butane transformed to produce C_1, C_2 and C_3 moles of methane, ethane and propane, respectively. It is calculated from the equation:

$$A = (C_1 + 2C_2 + 3C_3) \; / \; 4$$

3.2.7.b— Selectivity

The selectivity for a reaction product is defined as the number of moles of that product divided by the moles of butane transformed. For a reaction product i, it is given by the equation:

$$S_i = C_i / A$$

3.2.7.c— Reaction rate

The rate of the butane hydrogenolysis reaction was commonly expressed as the moles of butane transformed per hour and per gram of metal catalyst (rhodium). It has been calculated using the equation:

$$r = \tau.F / 2400.w.100$$

where F is the flow of butane in cm^3/hour and w is the weight of the metal after reduction. The constant 2400 was considered the molar volume of a gas at the room conditions in which the experiments were performed.

3.2.7.d— Rate of rupture of internal and terminal bonds

It is possible to determine the initial rates of the rupture of one or the other of butane bonds using the method described by Leclercq (1976). This author has shown that ethane hydrogenolysis was far more slower than that of propane and has thus considered that the only secondary important reaction was the hydrogenolysis of propane formed initially and was limited to the following scheme:

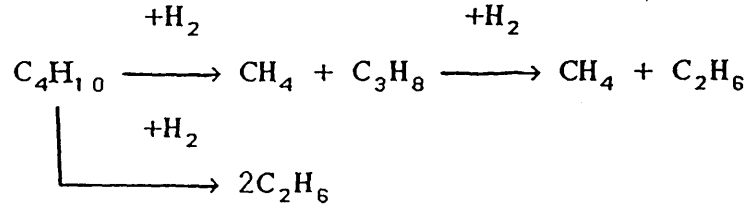

The values of C_1, C_2 and C_3 could be calculated after a correction due to the secondary hydrogenolysis of propane. If x is the quantity of propane hydrogenolysed into methane and ethane:

$$\underset{x/3}{C_3H_8} + H_2 \rightarrow \underset{2x/3}{C_2H_6} + \underset{x}{CH_4}$$

the conversion rates become:

$$C'_3 = C_3 + x$$

$$C'_2 = C_2 - 2x/3$$

$$C'_1 = C_1 - x/3$$

x can be calculated by considering the ratio $\alpha = C_3/C_1$ being equal to three and consequently the values of C'_1, C'_2 and C'_3 can be deduced:

$$C'_3 = 0.5(C_3 + 3C_1)$$

$$C'_2 = C_2 - C_1 + C_3/3$$

$$C'_1 = C_1/2 + C_3/6$$

The initial selectivities for the rupture of terminal (S_{ter}) and internal (S_{int}) butane bonds are given by the expressions:

$$S_{ter} = (C'_3 + 0.75C_3)/C$$

$$S_{int} = C'_2/C$$

or also:

$$S_{ter} = (2C_1 + 2C_3/3)/C$$

$$S_{int} = (C_2 - C_1 + C_3/3)/C$$

The rate of hydrogenolysis of the terminal bond is given by:

$$r_{ter} = r.S_{ter}$$

and for the central bond by:

$$r_{int} = r.S_{int}$$

3.2.7.e— Activation energy

Since the selectivity S_i was defined as moles of product i formed per mole of butane reacted and the rate of butane hydrogenolysis r as the number of moles of butane reacted per hour and per gram of rhodium, then the rate of formation of an individual product i, r_i, can be calculated from:

$$r_i = S_i.r$$

The temperature dependence of r and r_i is given by the Arrhenius equation:

$$r = A \exp(-E / RT)$$

$$r_i = A_i \exp(-E_i / RT)$$

where A and A_i are the corresponding frequency factors, E and A_i are the activation energy for butane removal and for the formation of product i respectively.

Plotting the Neperean logarithm of the rate against 1/T permits the calculation of the activation energy in each case.

During this study, the calculations were made with the aid of a program in BASIC language run on an Olivetti Personal Computer (Ivrea, Italy).

*** 3.3 ***

RESULTS AND DISCUSSION

3.3.1— INTERNAL STRUCTURE OF VANADIUM PENTOXIDE

As mentioned earlier, in section three of the second chapter, vanadium pentoxide crystals prepared by ultrasonic dispersion, as manifested by TEM examination, exposed mostly and preferentially the (001) surface planes. However, when the crystals were exposed for a long period to the electron beam, some new features appeared as a result of beam damage (Fig. 3.5). These features, together with thickness variations, could be mistaken for pores in the crystals.

Examination of thin sectioned crystals in the electron microscope revealed that these crystals had fragmented during thin sectioning (Fig. 3.6). When the sectioning was parallel to the (010) plane, the crystals cleaved parallel to the (001) plane (Fig. 3.7.a), due to the presence of the weak vanadium—oxygen bonds in the (010) planes of vanadium pentoxide. However, when the crystals were oriented otherwise, relative to the diamond knife, random fragmentation was obtained as shown in Fig. 3.7.b and it can be seen from the EDP that the crystals lie randomly in many different orientations.

When the cutting angle was perpendicular to the c—axis, a good cross—section could be obtained with very well resolved lattice fringes showing that the crystals break down parallel to the (001) plane resulting from the lamellar structure of vanadium pentoxide. High magnification images from this region (Fig. 3.8) showed lattice images corresponding to the (101) plane in vanadium pentoxide.

Unlike the crystals dispersed ultrasonically, where misinterpretation of the images could arise, the HREM images

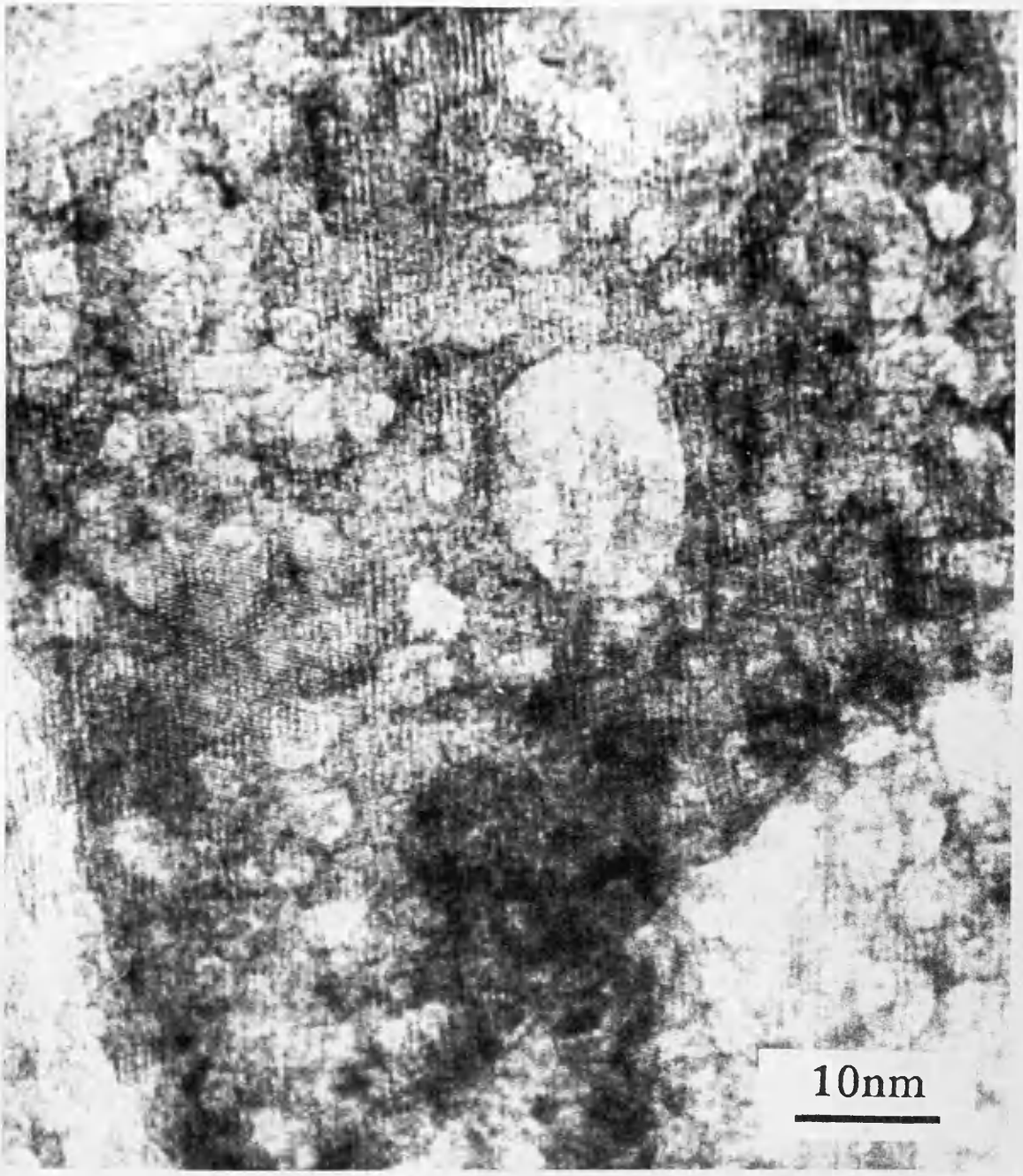

Fig. 3.5: Pore–like features induced by electron beam radiation damage in vanadium pentoxide crystals prepared by ultrasonic dispersion for TEM examination.

Fig. 3.6: Crystal fragmentation during thin sectioning with an ultramicrotome.

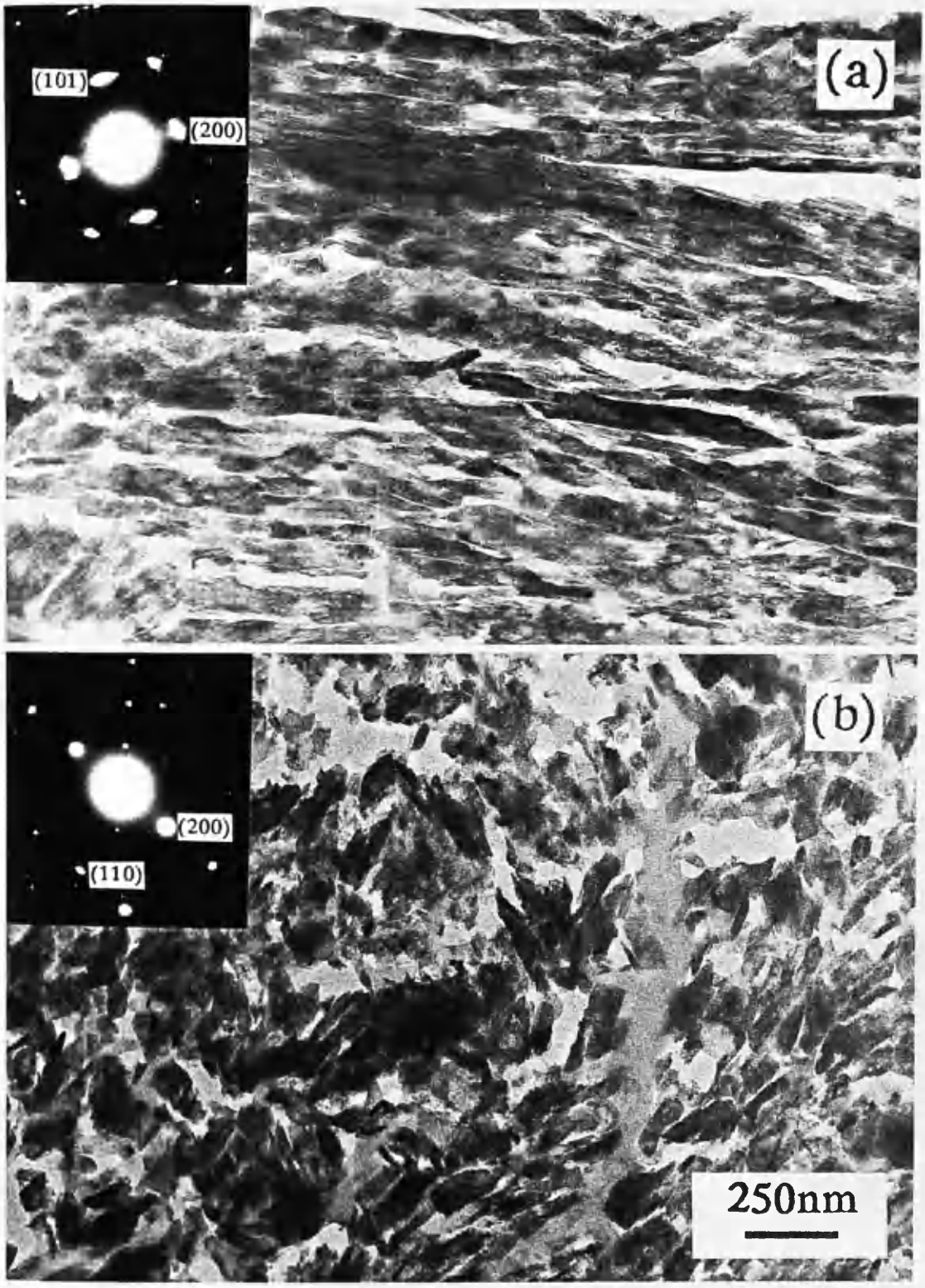

Fig. 3.7: Cleaved vanadium pentoxide crystals with relative SAED patterns: (a) the cleavage is parallel to the (010) plane, (b) a random cleavage.

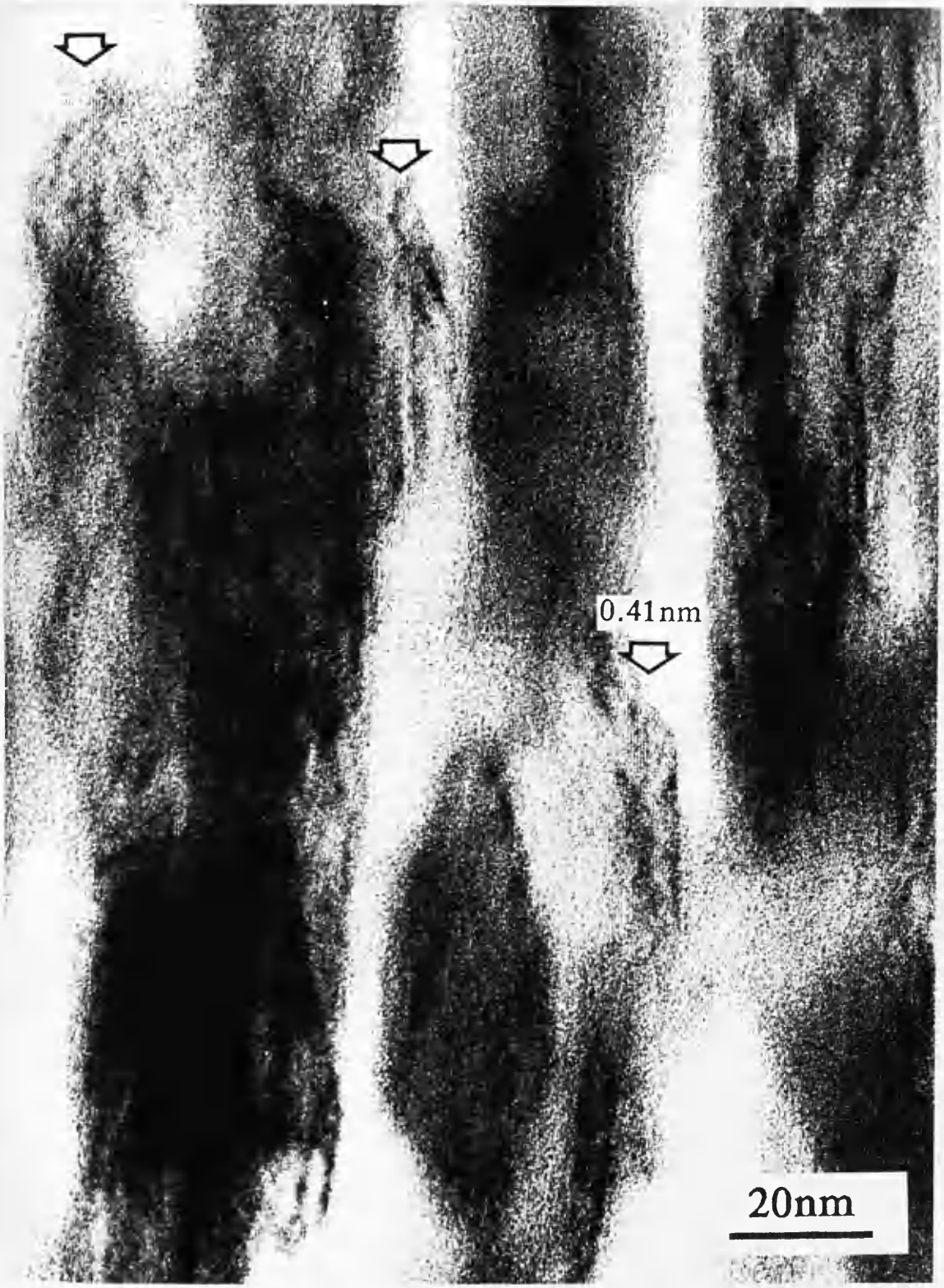

Fig. 3.8: High magnification micrograph, from the region shown in Fig. 3.7.a, showing lattice fringes corresponding to (101) plane in vanadium pentoxide (arrows).

obtained from thin sectioned material showed extensive crystalline regions in which the structural integrity of the crystals remained intact and no evidence of porosity was noticeable (Fig. 3.9). This result is in good agreement with our porosity measurements, evaluated from krypton gas adsorption data and confirms that vanadium pentoxide crystals are non— porous with a very low surface area measured to be $6m^2/g$. This value is comparable to those given in the literature for the same compound (Brown et al., 1974). SEM examination likewise indicated that the crystals had smooth surfaces (Fig. 3.10) and that macro— and meso— pores and cracks were absent.

The same results were found by Galbraith et al. (1979) when they studied β— iron(III) hydroxide oxide (β— FeOOH). They concluded from their studies that the 'mottling' observed by Watson et al. (1962) and attributed by them to 3nm pores in the crystals, was simply due to electron beam radiation damage.

It also appears from our study that the thin sectioned crystals were more stable, in the electron microscope, than those prepared from ultrasonic dispersion. This increase of stability might be due to increased thickness and/or encapsulation by embedding medium (Holland et al, 1983).

3.3.2— CATALYST CHARACTERISATION

The catalyst prepared was a 1% in weight rhodium supported on vanadium pentoxide. When dried in the oven this catalyst exhibited an IR spectrum and an XRD pattern both corresponding to vanadium pentoxide crystals.

3.3.2.a— Temperature programmed reduction

The reduction profiles of both the rhodium supported catalyst

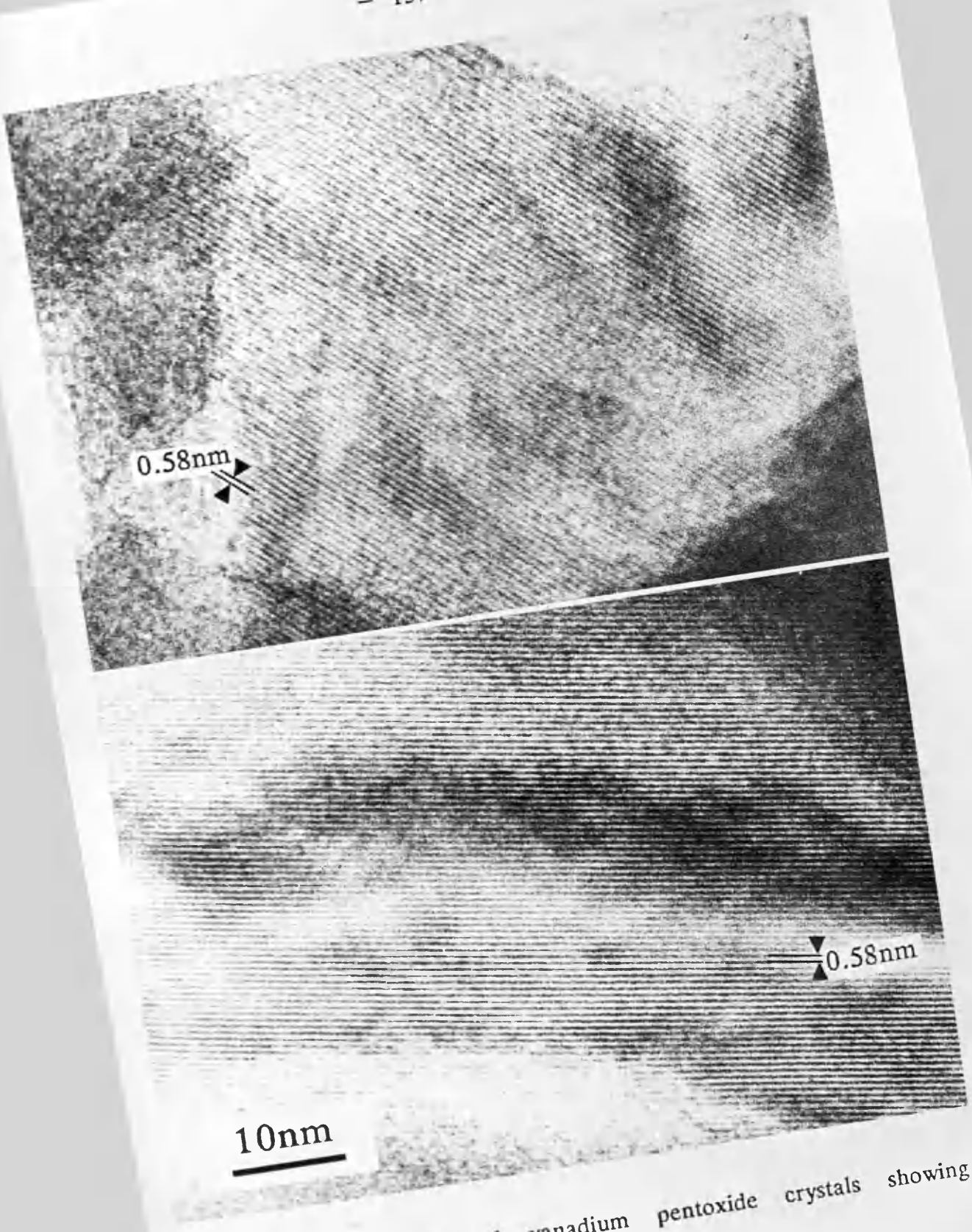

Fig. 3.9: Thin sectioned vanadium pentoxide crystals showing structural integrity.

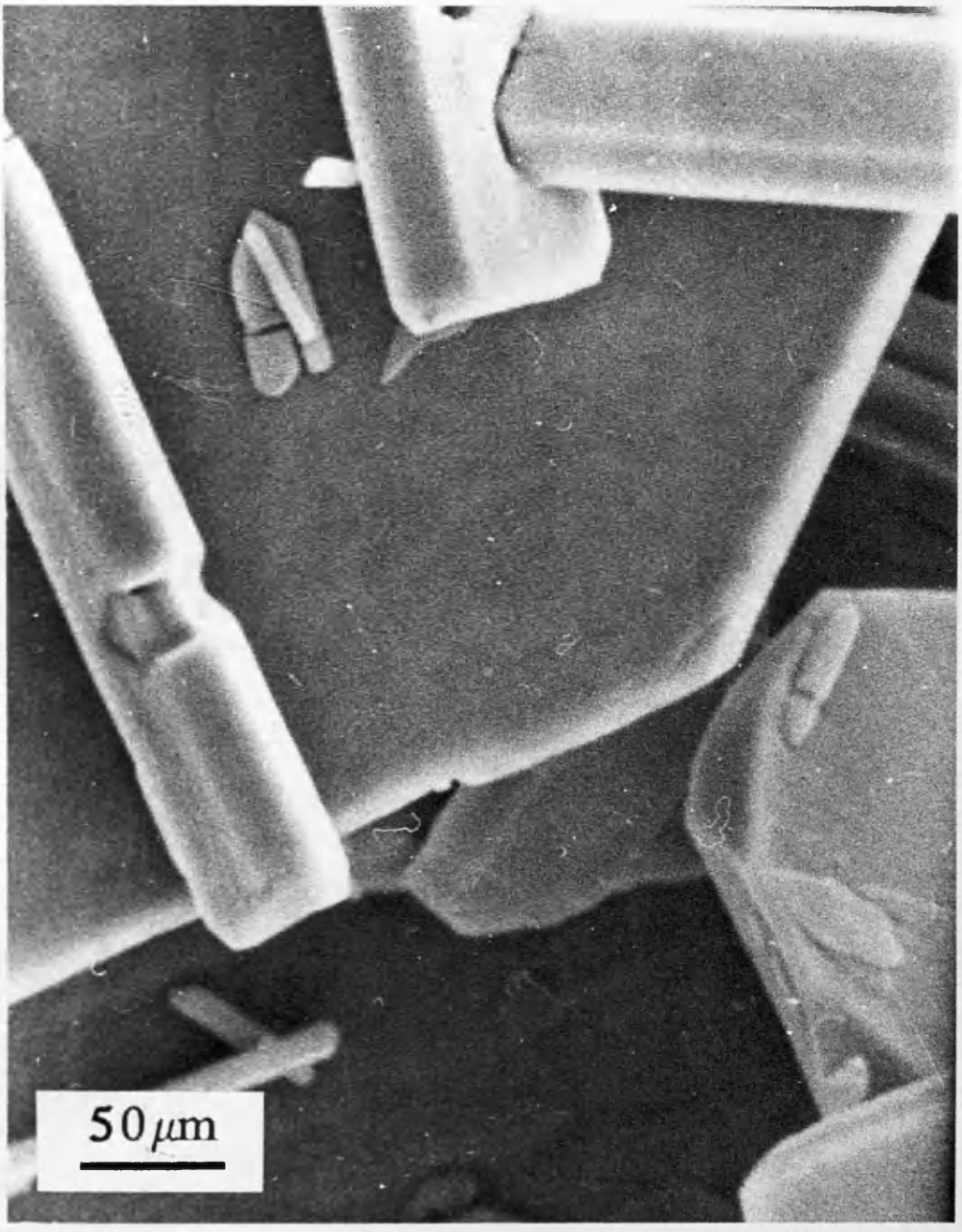

Fig. 3.10: SEM photograph showing that vanadium pentoxide crystals have smooth surfaces.

and pure vanadium pentoxide (the support) were examined by TPR.

i— Vanadium pentoxide

When pure vanadium pentoxide was heated from room temperature to 700°C, the reduction was observed to begin at ca. 450°C (Fig. 3.11). The uptake of hydrogen increased with the temperature rise up to 700°C.

Reported TPR spectra for pure vanadium pentoxide appear to differ from our results. Roozboom et al. (1980) found one single reduction peak at ca. 527°C. At higher temperature Bosch et al. (1984) found two peaks with maximum reduction temperatures of 650 and 690°C. They suggest that the reduction of vanadium pentoxide proceeds as follows:

$$V_2O_5 \longrightarrow 1/3V_6O_{13} \longrightarrow 2VO_2$$

However, it is difficult to compare TPR spectra obtained by different investigators. The experimental conditions reported in the literature differ widely in hydrogen concentration and flow rate as well as sample size and pretreatment.

ii— The catalyst

The TPR of the 1% rhodium supported on vanadium pentoxide catalyst (Fig. 3.12) showed one distinct peak with its maximum reduction temperature at 155°C. The uptake of hydrogen corresponding to this reduction peak was measured to be 0.0365 l/g. However, the amount of hydrogen necessary for the reduction of rhodium ions to their metallic state is far less than that uptake. Since the reduction of one rhodium ion requires one and a half molecules of hydrogen following the reaction:

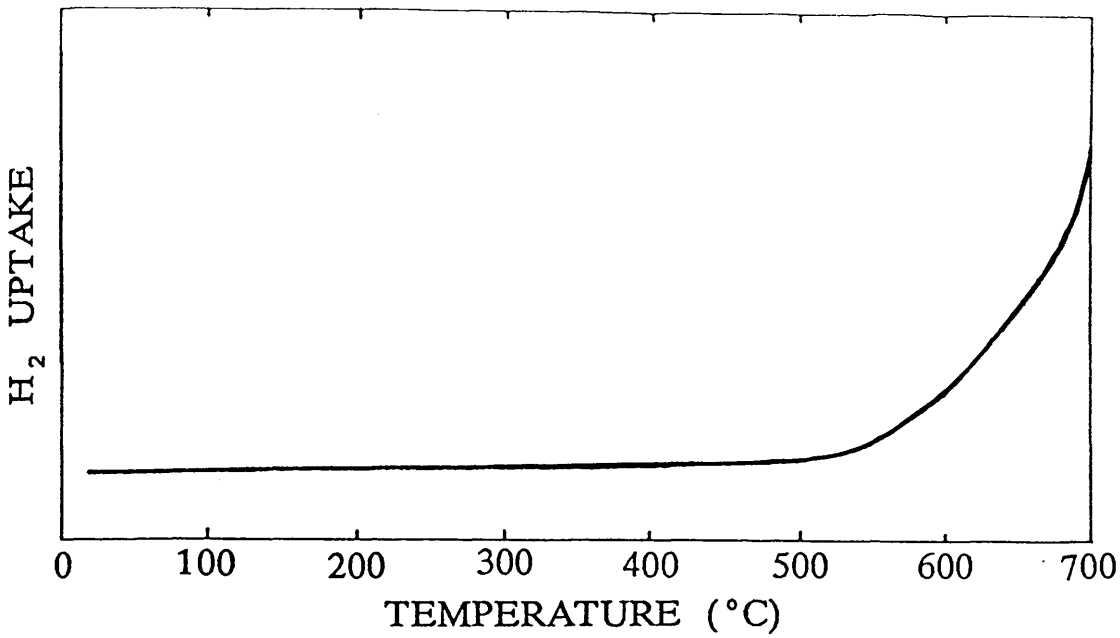

Fig. 3.11: TPR trace for vanadium pentoxide.

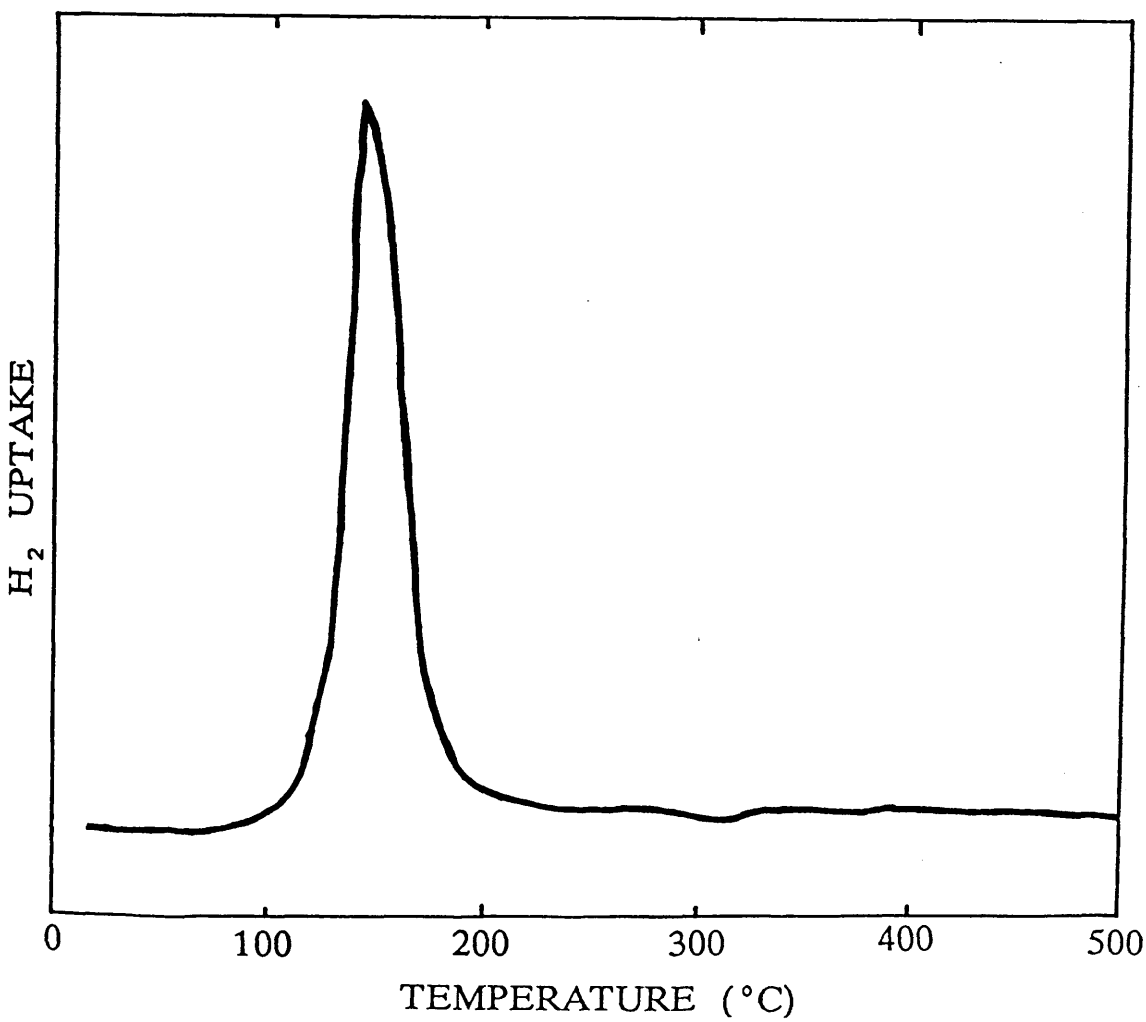

Fig. 3.12: TPR trace for vanadium pentoxide–supported rhodium catalyst.

$$Rh^{3+} + 3/2H_2 \longrightarrow Rh$$

and assuming that the volume of one mole of hydrogen is 22.4 l at standard temperature and pressure, the hydrogen uptake necessary for the reduction of rhodium ions present at the surface of vanadium pentoxide should be 0.00326 l. This suggests that most of the hydrogen uptaken was used for support reduction. The peak would be then attributed to the reduction of rhodium ions to the metallic state and also the reduction of vanadium pentoxide to a lower oxide. The reduction of rhodium ions, supported on non—reducible oxides such as alumina and silica, to the metallic state was found to occur at 167°C when supported on alumina and 178°C when supported on silica (Boumarafi, 1986).

3.3.2.b— Chemisorption of carbon monoxide

Subsequent to the TPR treatment, the catalyst was reduced in situ at 250°C for two hours before the chemisorption of carbon monoxide was carried out. The surface area of the rhodium catalyst supported on vanadium pentoxide was determined from its carbon monoxide uptake and was found to be 2.06m^2/g. This value was used for the calculation of the mean particle diameter using the formula:

$$\frac{S.A.}{w} = \frac{4\pi r^2}{4\pi r^3 \rho/3} = \frac{3}{r\rho}$$

where S.A. is the surface area of the metal and ρ the density of rhodium, which is equal to 12.4g/cc (Weast, 1987). w is the mass of the metal in one gram of catalyst, and r is the mean particle diameter of rhodium particles. The value calculated for the mean particle diameter was r = 1.91nm.

3.3.3– RHODIUM–CATALYSED REDUCTION OF VANADIUM PENTOXIDE

Examination of a catalyst sample used in the TPR experiment in the electron microscope showed that the support was highly reduced to a lower oxide. Therefore a study was undertaken to investigate the causes of the support reduction.

Specimens were prepared for this purpose by reduction of both the catalyst and pure vanadium pentoxide in a stream of hydrogen (50ml/min) for two hours at the selected temperatures of 250, 450 and 600°C.

The specimens thus prepared were characterised by XRD, IR, SEM and TEM.

3.3.3.a– X–ray diffraction

Both the vanadium pentoxide–rhodium supported catalyst and pure vanadium pentoxide were investigated by XRD at the different stages of their reduction.

i– Fresh catalyst

The fresh catalyst was perfectly crystalline and its diffraction pattern was in good agreement with that found for pure vanadium pentoxide (Fig 3.13).

ii– Catalyst reduced at 250°C

When the catalyst was reduced in hydrogen at 250°C, it exhibited an XRD pattern in which the d values corresponded to both vanadium pentoxide and the vanadium oxide V_4O_9 (Theobald et al., 1969). It can be seen from the relative intensities that the

support was predominantly reduced to V_4O_9 (Fig. 3.13). Theobald et al. (1969) indexed the XRD pattern for V_4O_9 on a tetragonal structure, while both Tilley & Hyde (1970), Wilhelmi & Waltersson (1970) and Grymonprez et al. (1977) assumed an orthorhombic structure. The respective lattice parameters are summarised in table 3.1. This assumption enabled Grymonprez et al. (1977) to propose a model for the structure of V_4O_9 based on a superstructure of vanadium pentoxide.

iii— Catalyst reduced at 450°C

The sample obtained after reduction of the catalyst at 450°C showed further reduction of the support. The lattice spacings measured from its XRD pattern were in good agreement with those of vanadium dioxide, VO_2, as reported by Andersson (1954) and Longo & Kierkegaard (1970) (Table 3.2), but disagreed with the values given by Evans & Morse (1955) and Matsuishi (1967) for the same compound.

iv— Catalyst reduced at 600°C

The reduction at 600°C of the catalyst gave a sample which yielded d—spacings that were in good agreement with those measured by Mukherjee (1985) for vanadium monoxide and those listed in the Inorganic Index to the Powder Diffraction File, published by the Joint Committee on Powder Diffraction Standards (Philadelphia, USA), in the file number 1—1293 for the vanadium (III) oxide (Table 3.3). The difference between the two compounds was resolved by SAED, and will be discussed in section 3.3.3.c of this thesis.

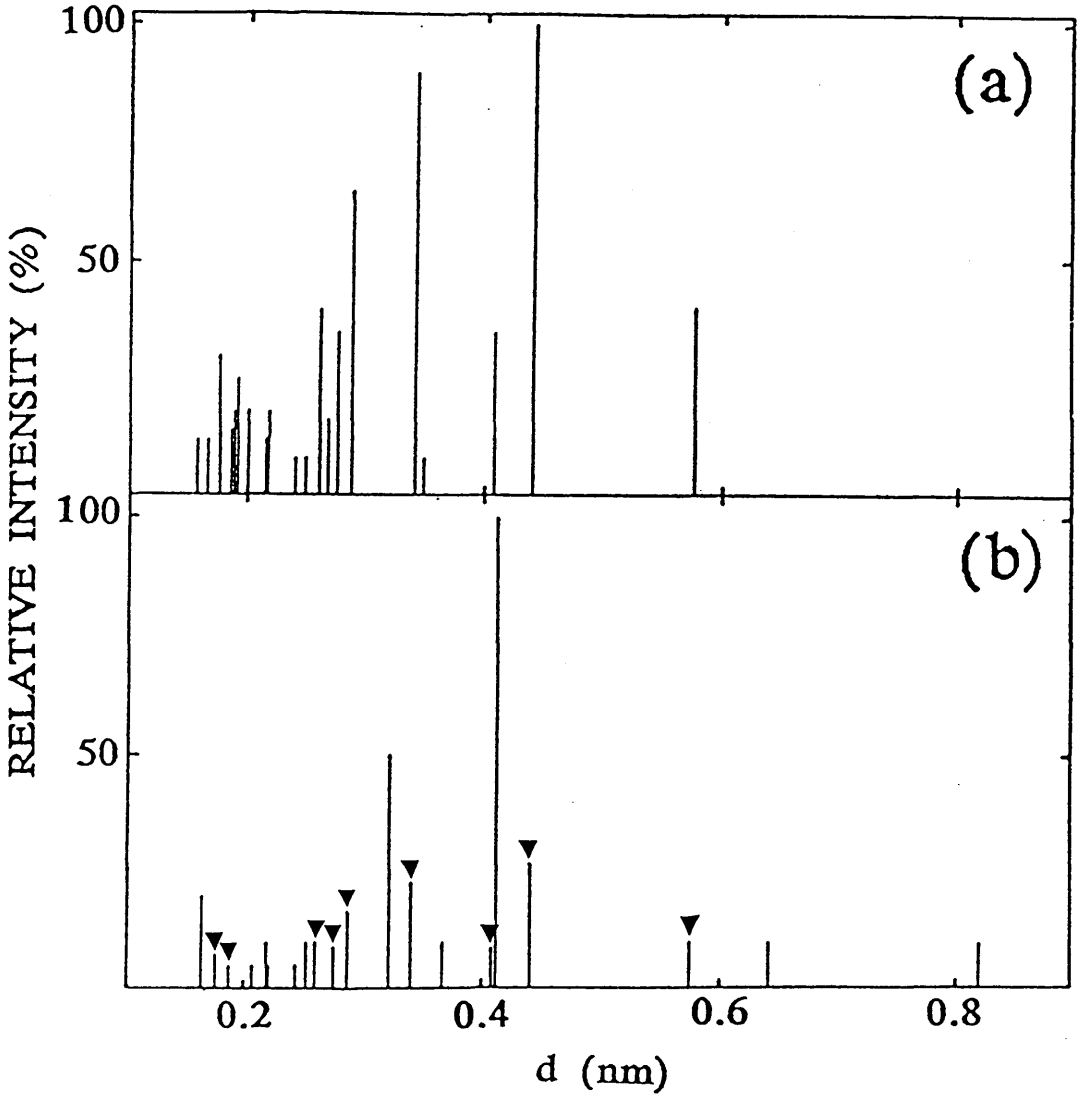

Fig. 3.13: XRD patterns corresponding to (a) vanadium pentoxide for the fresh catalyst, and (b) a mixture of vanadium pentoxide and V_4O_9 (▼) for the catalyst reduced at 250°C.

Table 3.1: Crystallographic data for V_4O_9 according to different authors.

Space group	a (nm)	b (nm)	c (nm)	Reference
$P4_2/mnm$	0.8235		1.032	Theobald et al., 1969
Pnma or $Pn2_1a$	1.7926	0.3631	0.9396	Wilhelmi & Waltersson, 1970
	0.81	1.04	1.61	Tilley & Hyde, 1970
	0.8235	1.032	1.647	Grymonprez et al., 1977

Table 3.2: Lattice spacings generated for the catalyst reduced at 450°C from its XRD pattern.

This work	Andersson (1954)		
d (nm)	d (nm)	I/I_0	hkl
0.9571			
0.3331	0.331	30	$\bar{1}11$
0.3222	0.320	100	011
0.2691	0.268	30	$\bar{1}02$
0.2436	0.2430	40	$\bar{2}02$
	0.2422	60	$\bar{2}11$
	0.2418	30	200
0.2272			
0.2147	0.2139	50	$\bar{2}12$
	0.2131	50	210
0.2034	0.2048	10	$\bar{1}21$
	0.2022	30	012,021
	0.1874	40	$\bar{3}02$
	0.1727	20	$\bar{3}11,\bar{1}22$
0.1660	0.1657	30	$\bar{2}13$
	0.1654	30	$\bar{2}22$
	0.1650	60	220,211
	0.1615	10	$\bar{1}13$
0.1606			
0.1438			
0.1338			

v— Phases obtained at each temperature

The main phases identified by XRD are summarised in table 3.4. It can be seen that the support, vanadium pentoxide, is first reduced to V_4O_9 at 250°C, and then to vanadium dioxide and vanadium monoxide or vanadium sesquioxide at 450 and 600°C, respectively. It is worth mentioning that no V_3O_7 (Waltersson et al., 1974) was found in these samples. However, a weak x—ray line (d = 0.957nm) was present in the XRD pattern of the sample reduced at 450°C which could not be attributed to any of the vanadium oxides listed in the x—ray diffraction file index.

vi— Reduction of pure vanadium pentoxide

When pure vanadium pentoxide was reduced in hydrogen up to 600°C, its XRD pattern showed that no reduction had occurred. This is in contradiction with the TPR result which suggests that vanadium pentoxide starts hydrogen uptake at ca. 450°C. It might be, however, that vanadium pentoxide had been reduced to a certain extent which could not be detected by this technique.

3.3.3.b— Infrared spectroscopy

Fig. 3.14 presents the IR spectra of the rhodium supported on vanadium pentoxide catalyst both fresh and reduced in hydrogen atmosphere at the selected temperatures of 250, 450 and 600°C.

i— Fresh catalyst

The IR spectrum exhibited by the fresh catalyst corresponds to that found in this study for pure vanadium pentoxide, which was in agreement with spectra given in the literature by different authors for

Table 3.3: Lattice spacings, deduced from the XRD pattern, for the catalyst reduced at 600°C.

This work		Mukherjee (1985)		XRD file No.1-1293	
d (nm)	I/I_0	d (nm)	Intensity	d (nm)	I/I_0
0.3663	75	0.3649	Strong	0.365	60
		0.3302	Weak		
0.2715	100	0.2710	Strong	0.270	80
0.2482	90	0.2481	Medium+	0.247	60
		0.2230	Strong	0.232	2
0.2181	50	0.2186	Strong	0.218	20
		0.2092	Strong	0.203	2
0.1828	40	0.1828	Strong	0.183	25
0.1698	90	0.1698	Strong+	0.169	100

Table 3.4: Dependence of support phase composition upon reduction temperature according to XRD patterns.

Reduction temperature (°C)	Phase composition
250	$V_4O_9 + V_2O_5$
450	VO_2
600	VO or V_2O_3

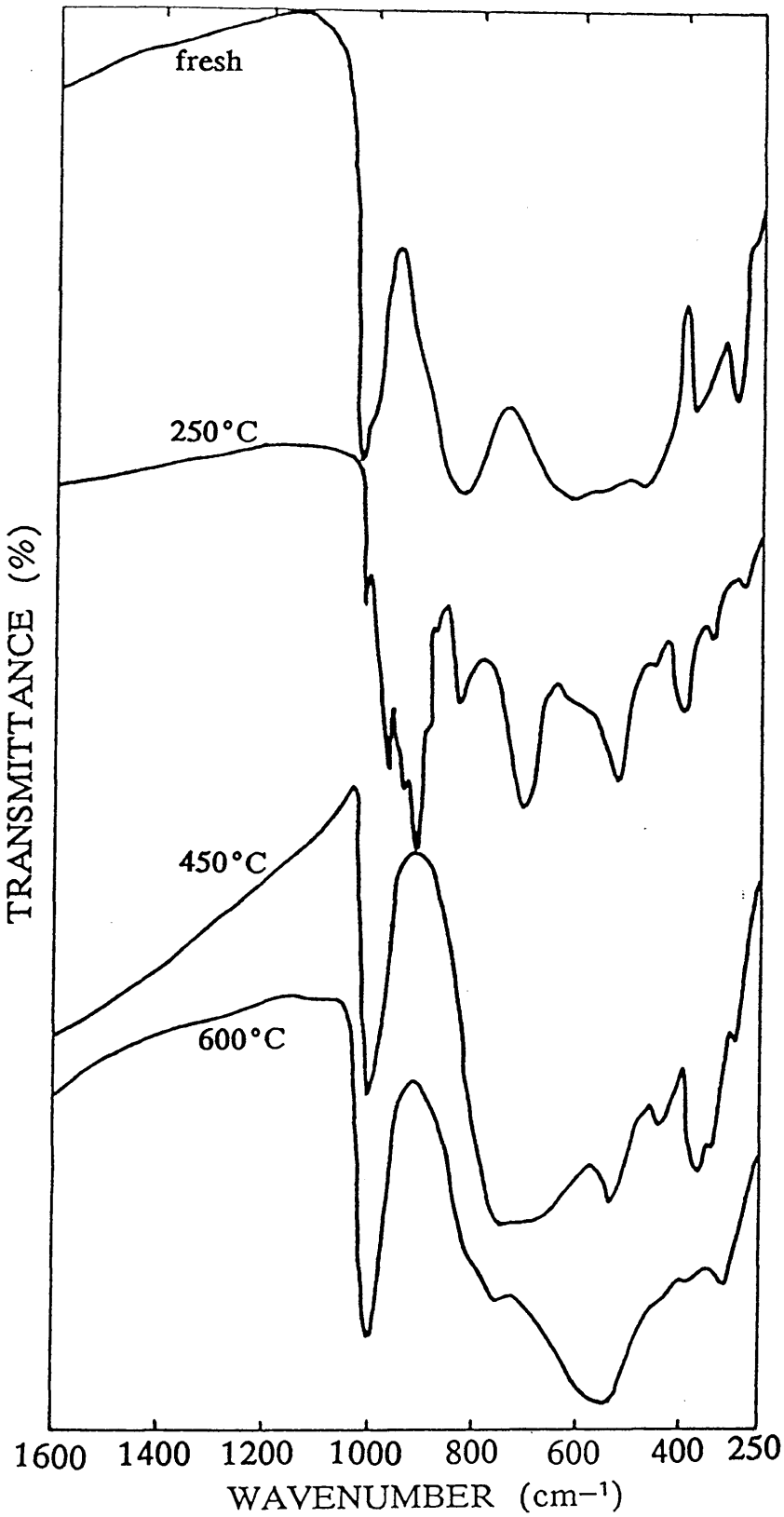

Fig. 3.14: IR spectra of the catalyst fresh and reduced in hydrogen atmosphere at 250, 450 and 600°C.

this compound (Abello et al., 1983; Clauws et al., 1985).

ii— Catalyst reduced at 250°C

When the catalyst had been reduced at 250°C by hydrogen, its spectrum was that of V_4O_9. Typical for this spectrum is the band at 920—930cm^{-1}, which seems to be composed of several sharp peaks. All of the other modes are relevant for V_4O_9 (Theobald, 1978; Clauws, 1980). It can be seen by comparison that there are similarities between the IR spectrum of V_4O_9 and that of vanadium pentoxide. These similarities can be explained by the structural similarities between the two compounds. The greater number of peaks in the spectrum of the catalyst reduced at 250°C can be understood since V_4O_9 has several crystallographically different vanadium and oxygen atoms compared to vanadium pentoxide with three different oxygen atoms and all vanadium atoms the same (Wilhelmi et al., 1971). In addition, the spectrum represents a V_4O_9 compound with which a certain amount of vanadium pentoxide is mixed.

iii— Catalyst reduced at 450°C

After reduction at 450°C, the spectrum developed a strong broad band at 920cm^{-1}. A broad band also seems to appear around 600cm^{-1}. The same IR modes appear to have been observed by Theobald (1978) for vanadium dioxide VO_2(B), even though the spectrum in that case was much less resolved. This spectrum agrees with the spectra obtained by other authors (Kimizuka et al., 1974; Perelyaev et al., 1977). The broad band at 670cm^{-1} has been proposed to be due to V—O—V stretching vibrations, and the peaks around 400—500cm^{-1} to be due to lattice vibrations (Perelyaev et al., 1977). The structure of the V_2O_4 samples investigated by Frederickson & Hausen (1963) and Fabbri & Baraldi (1972) is not

mentioned, but the spectra given are not in agreement with that of monoclinic V_2O_4. IR spectra of VO_2(A) and VO_2(B) have been published (Theobald, 1978).

iv— Catalyst reduced at 600°C

The reduction of the catalyst to 600°C gave an IR spectrum with a sharp large band at 1000cm^{-1} and other bands below 800cm^{-1}.

3.3.3.c— Transmission electron microscopy

The fresh catalyst and samples reduced at 250, 450 and 600°C were characterised by electron diffraction and HREM. The crystals which were investigated showed lattice images and EDP of corresponding phases characterised by XRD and IR at each temperature.

i— Fresh caytalyst

The EDP obtained from fresh catalyst crystals showed rings and/or spots which could be indexed in agreement with the orthorhombic structure of vanadium pentoxide. HREM examination of these crystals showed that the support exposed predominantly the (001) plane, with lattice fringes shown in Fig. 3.15 corresponding to 0.576nm (200) and 0.34nm (110) planes in vanadium pentoxide.

ii— Catalyst reduced at 250°C

The EDP obtained from the catalyst reduced at 250°C showed spotty rings which were difficult to index. The complexity of these

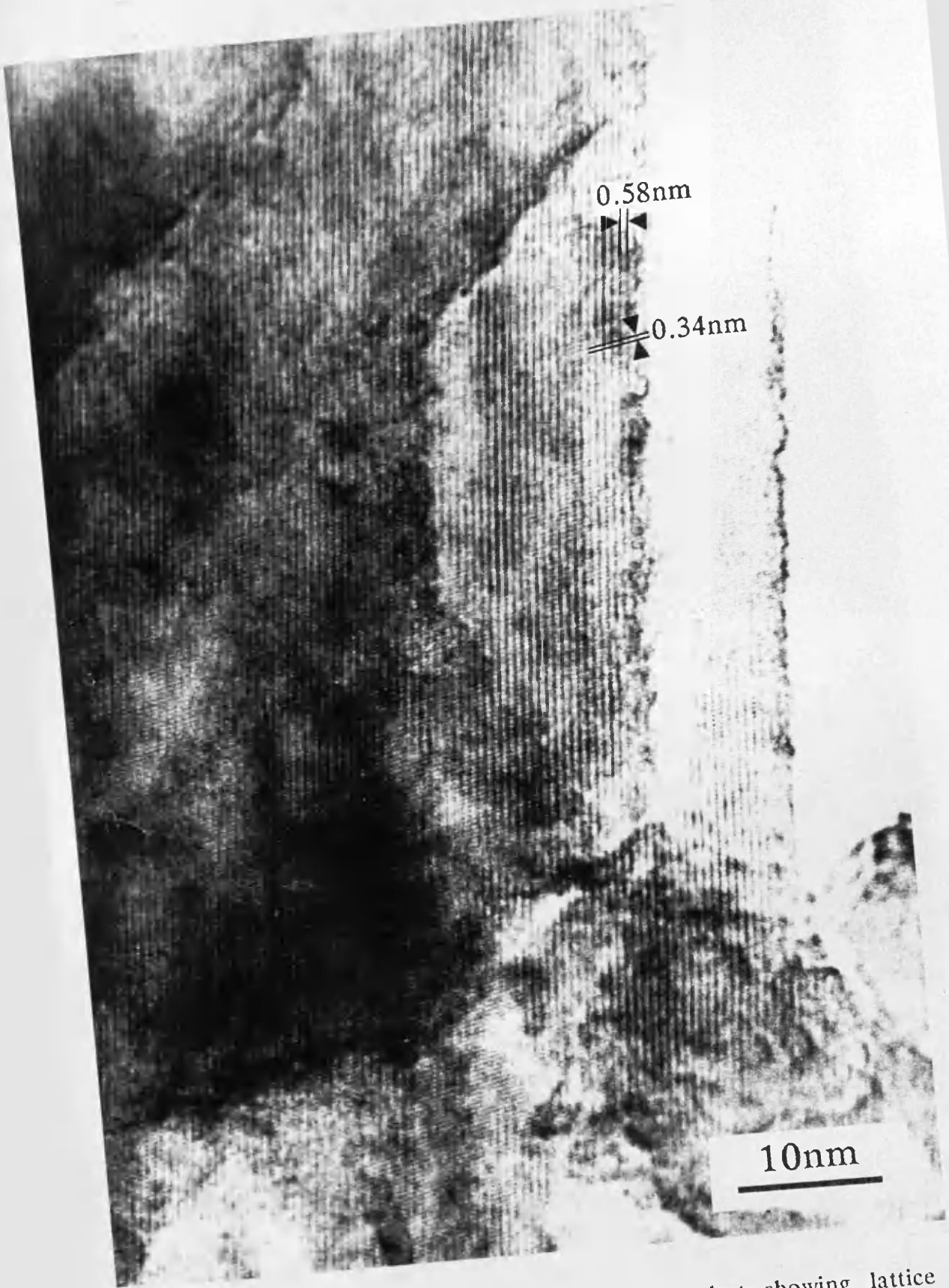

Fig. 3.15: HREM micrograph of the fresh catalyst showing lattice fringes corresponding to vanadium pentoxide.

EDP might be due to the fact that they contained reflections arising from both polycrystalline vanadium pentoxide and V_4O_9.

A SAED pattern from a single crystal is given in Fig. 3.16. The reflections observed in the pattern were in agreement with the crystalline orientation of the crystallographic planes in the tetragonal structure described by Theobald et al. (1969). These reflections could not be indexed in the orthorhombic structure described by Grymonprez et al. (1977).

In this SAED pattern, the electron beam is perpendicular to the (100) plane of the tetragonal structure of V_4O_9. The reflections with lattice spacings of 0.643, 0.516 and 0.412nm correspond to (011), (002) and (020) planes of V_4O_9. The angles measured between the (011) and (002) on one hand and (011) and (020) on the other are: 52° and 38°, respectively. These values are consistent with the values of 51.4° and 38.6°, respectively, which were calculated using the formula (Andrews et al., 1971):

$$\cos\phi = \frac{\frac{1}{a^2}(h_1h_2 + k_1k_2) + \frac{1}{c^2}l_1l_2}{\left[\left\{\frac{1}{a^2}(h_1^2 + k_1^2) + \frac{1}{c^2}l_1^2\right\}\left\{\frac{1}{a^2}(h_2^2 + k_2^2) + \frac{1}{c^2}l_2^2\right\}\right]^{1/2}}$$

where ϕ is the angle between the planes $(h_1k_1l_1)$ and $(h_2k_2l_2)$.

In addition, lattice spacings corresponding to V_4O_9 were commonly observed in this study by TEM. The lattice fringes, shown in Fig. 3.17, with spacings of 0.643 and 0.516nm correspond to (011) and (002) planes of V_4O_9, respectively.

Rhodium particles were observed on the surface of the support for this reduced catalyst, as it can be seen in Fig. 3.18. The particles presented different shapes and sizes. The particle size distribution of the catalyst, measured over about one thousand particles from HREM photographs, is given in the histogram in Fig. 3.19. The arithmetic mean diameter is 4.1nm. This value is higher than that determined from carbon monoxide chemisorption

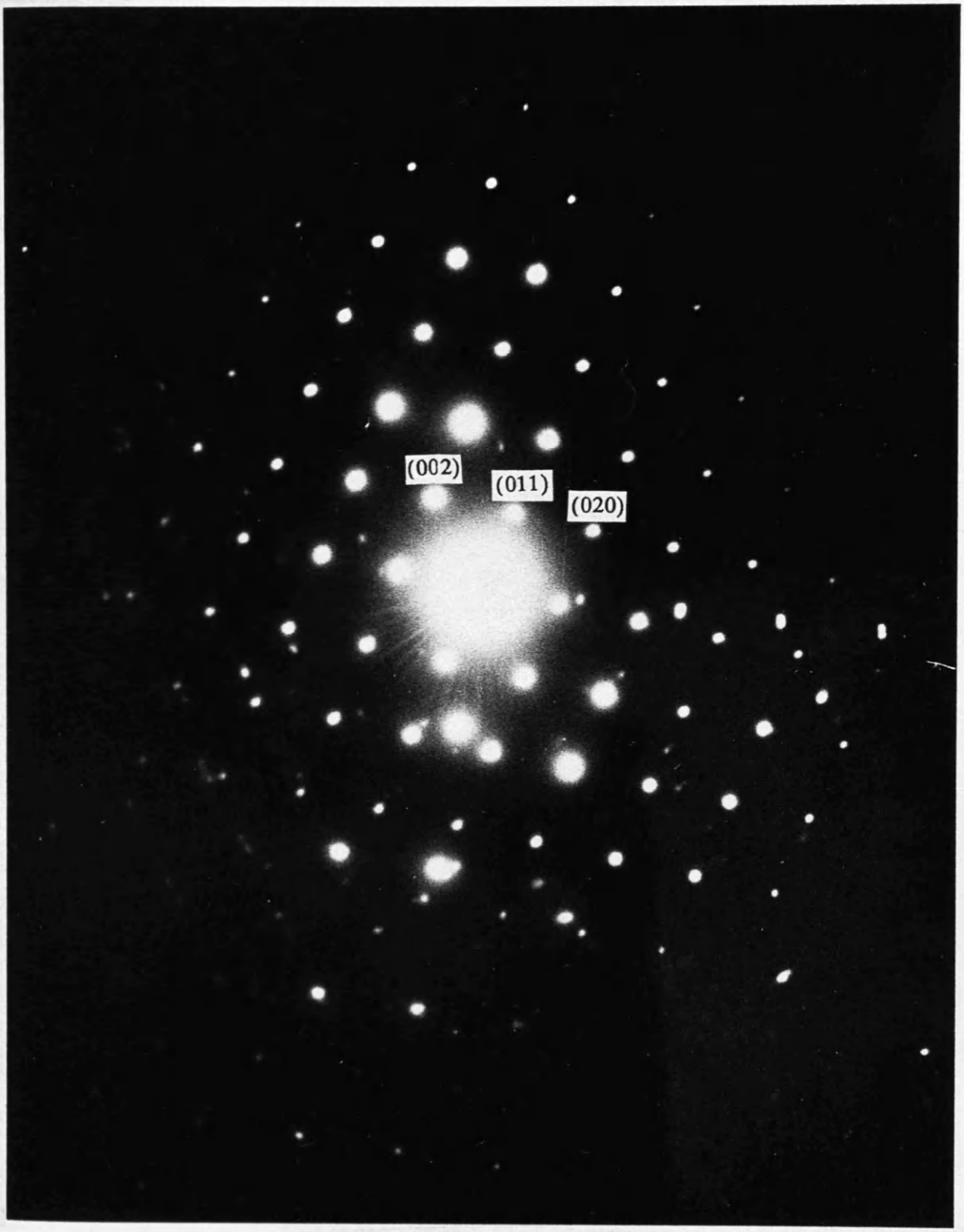

Fig. 3.16: SAED of a single crystal for the catalyst reduced at 250°C.

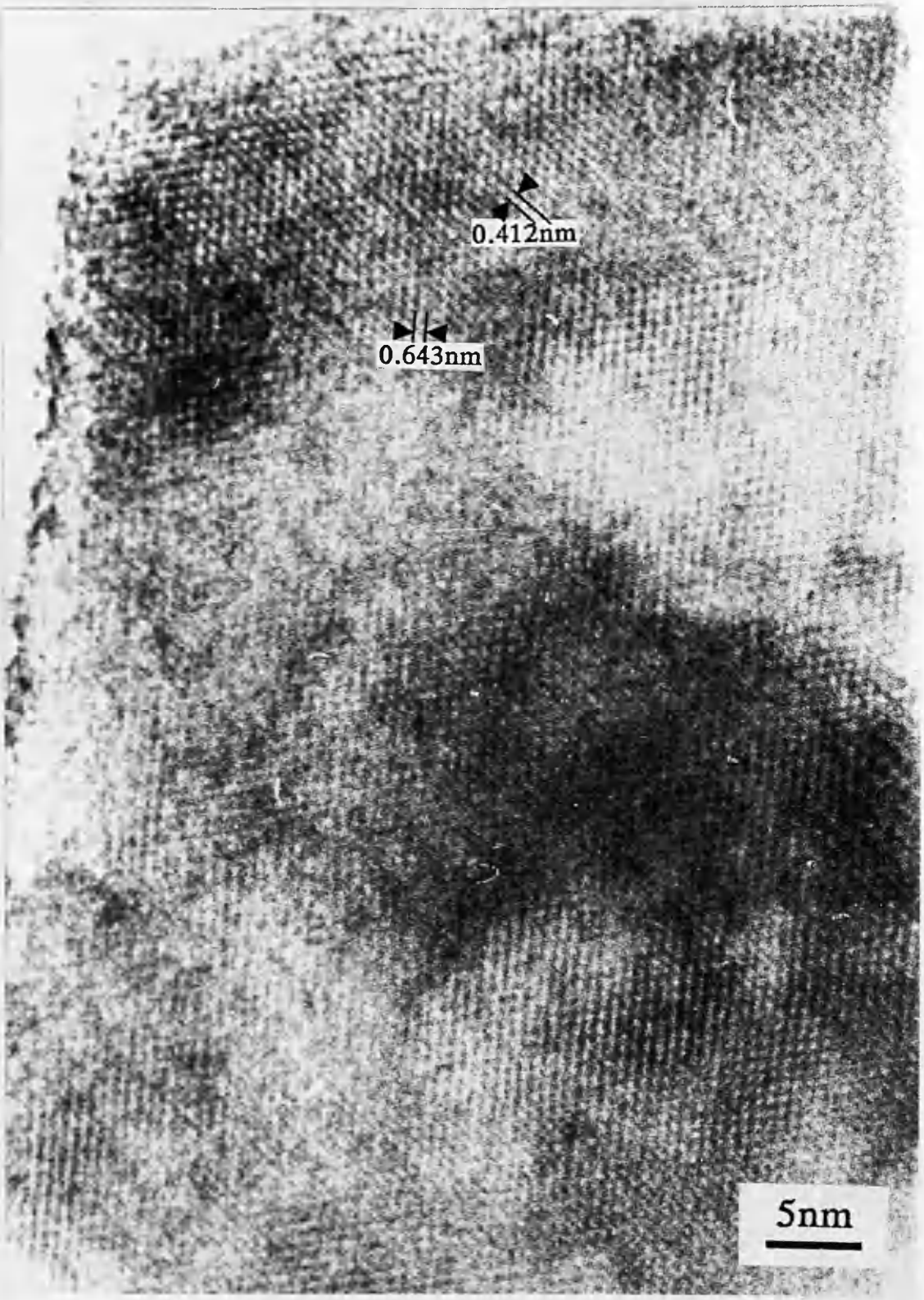

Fig. 3.17: HREM photograph of a crystal from the catalyst reduced at 250°C.

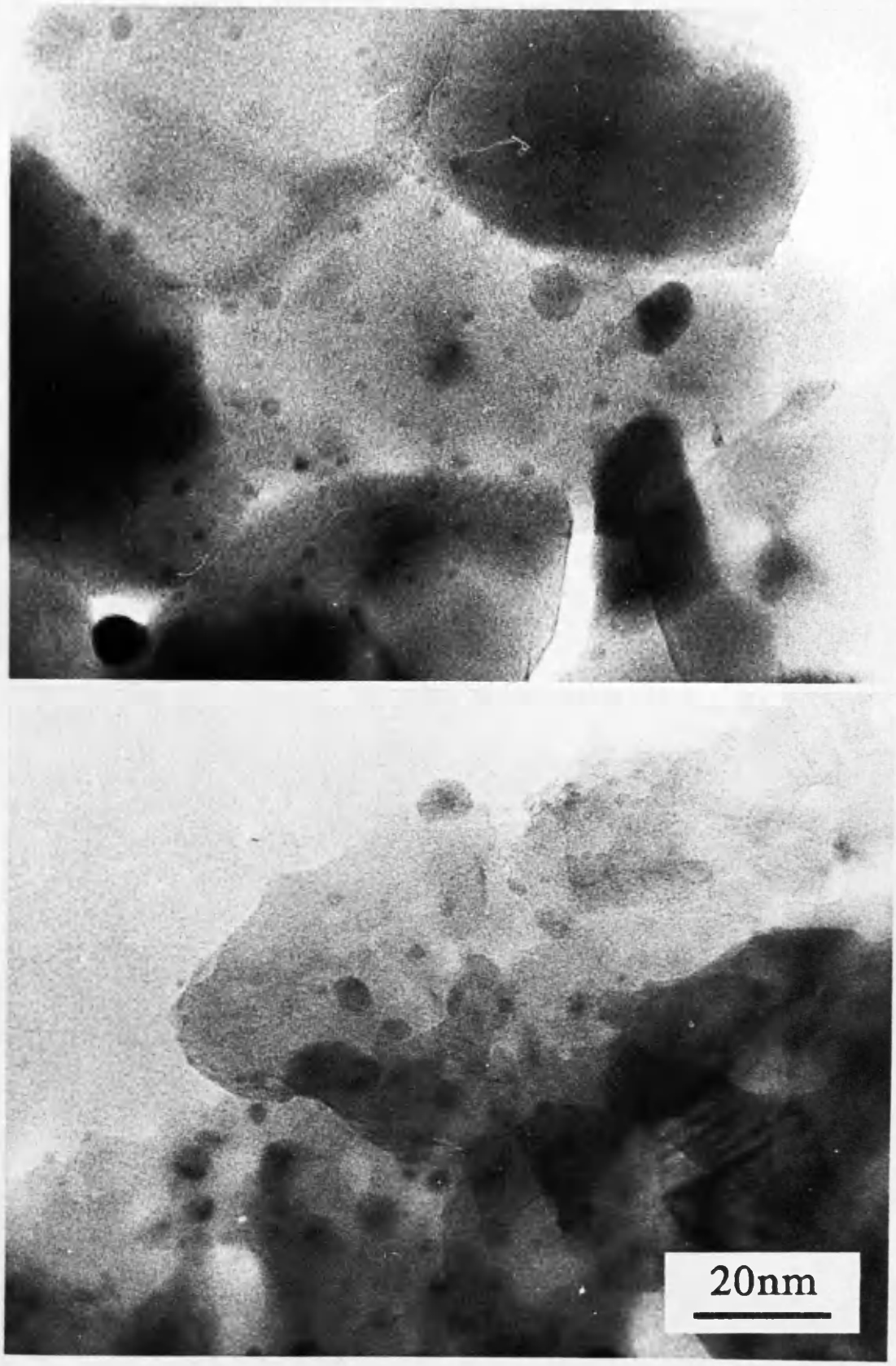

Fig. 3.18: Typical TEM micrographs showing the dispersion of rhodium particles for the catalyst reduced at 250°C.

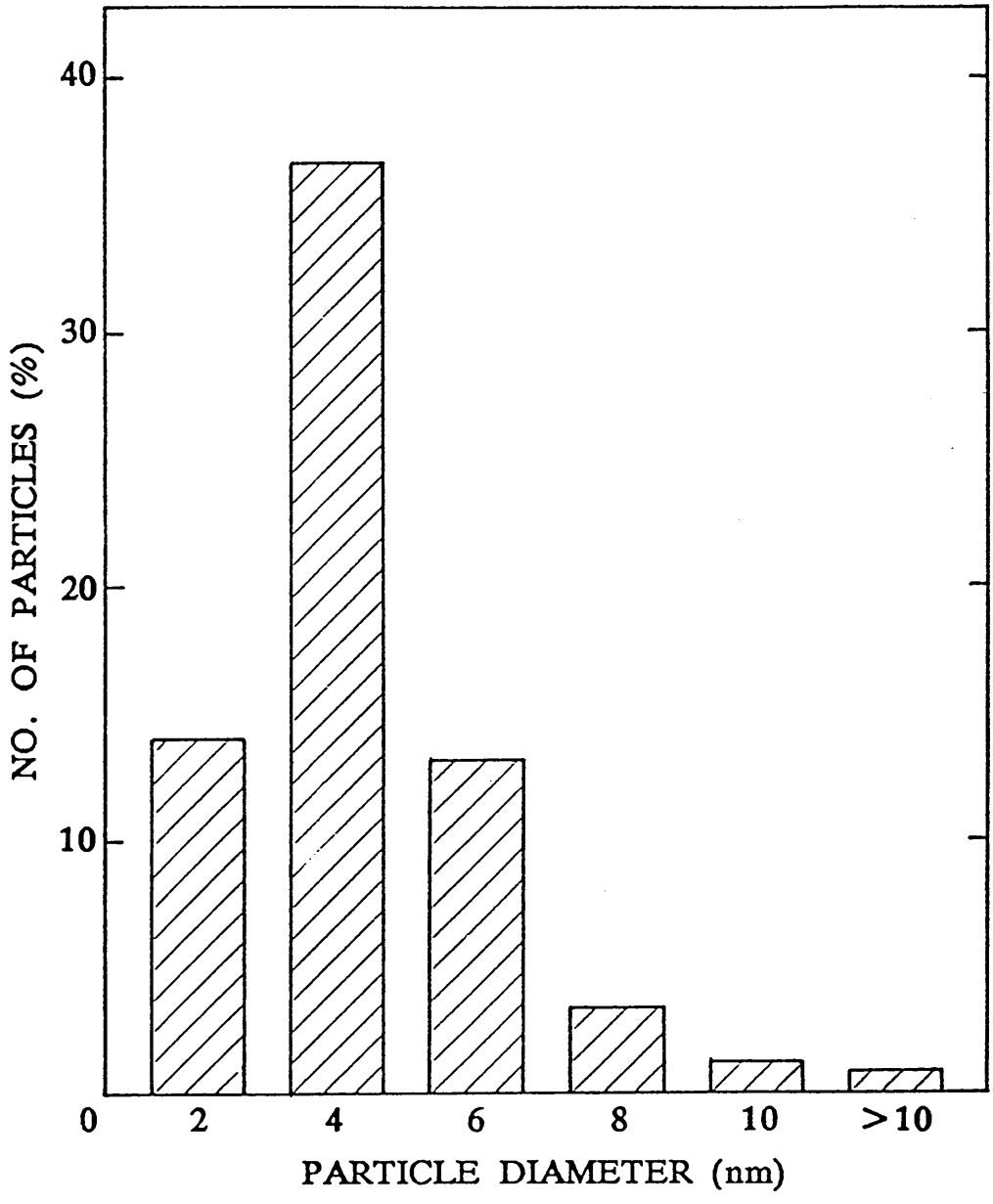

Fig. 3.19: A histogram showing the rhodium particle distribution on the surface of reduced vanadium pentoxide.

experiments.

Fig. 3.20 is another example of rhodium particles detected by HREM on the surface of the reduced vanadium pentoxide support. The two small crystals present in the micrograph show lattice fringes corresponding for one to vanadium pentoxide with the d— value of 0.576nm, and for the other to V_4O_9 with the d— value of 0.643nm.

iii— Catalyst reduced at 450°C

When the catalyst was reduced at 450°C, the crystals yielded an EDP in which the spotty rings (Fig, 3.21) indicated that the crystals of vanadium dioxide, VO_2, dominated the support in this sample. The d— values measured were in good agreement with those deduced from the XRD pattern for the same sample and those given by Andersson (1954) for vanadium dioxide.

SAED patterns of single crystals, like the one represented in Fig. 3.22, showed one strong reflection with the d— values of 0.320nm which corresponds to the (011) plane in the monoclinic structure of vanadium dioxide. This reflection correspond to the most intense peak in the XRD diffraction.

Lattice images corresponding to VO_2 spacings were successfully obtained from the reduced support. The lattice fringes shown in Fig. 3.23 have a spacing of 0.32nm which corresponds to the (100) plane of the structure of vanadium dioxide.

In addition, rhodium particles were observed at the surface of the reduced support. Fig. 2.24 is an example of dispersed rhodium crystallites with different sizes and shapes. The particle size distribution of the catalyst measured from such HREM micrographs is given in the histogram of Fig. 3.25. The arithmetic mean diameter was calculated to be 5.2nm.

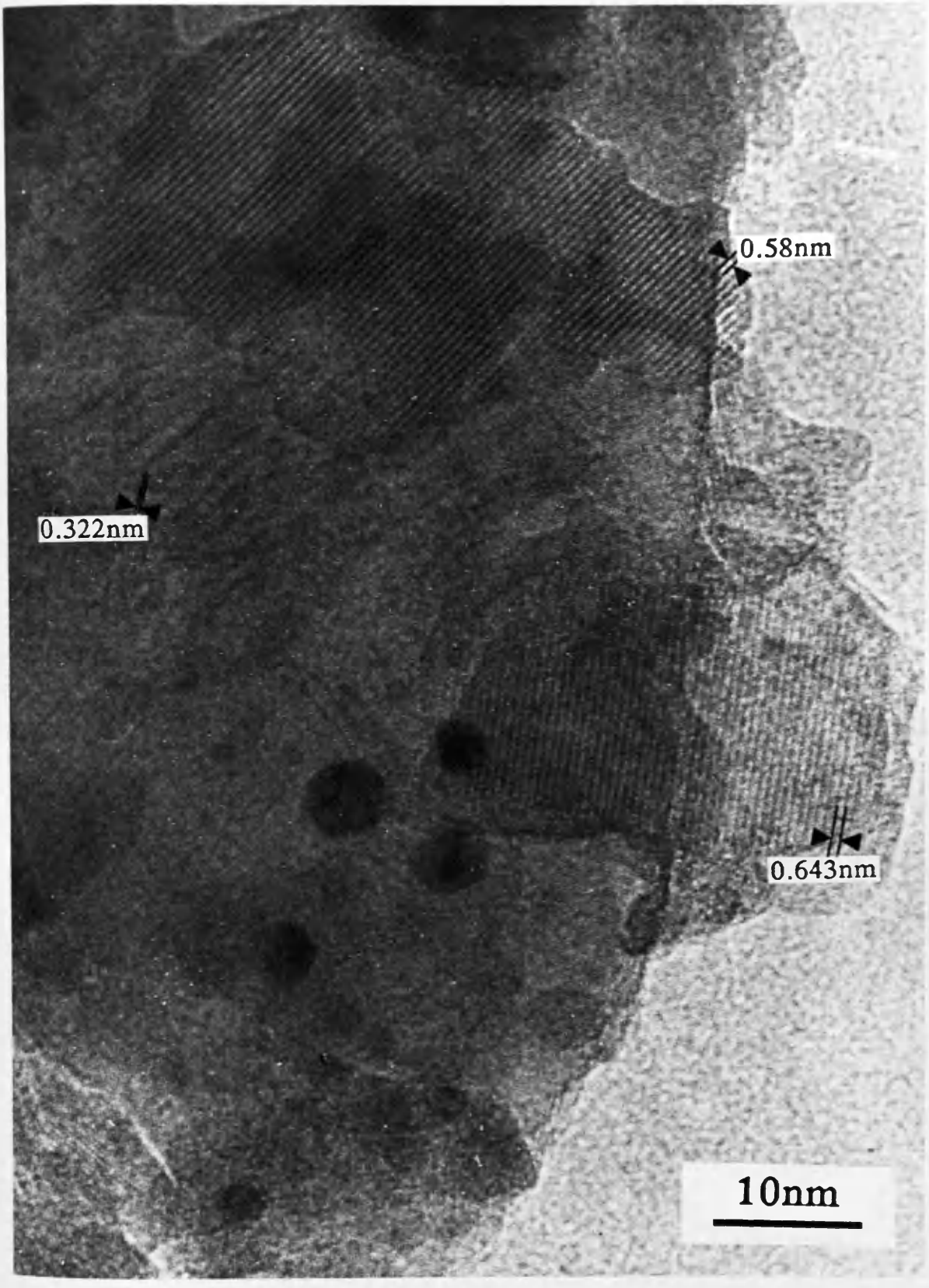

Fig. 3.20: HREM phtograph of the catalyst reduced at 250°C, showing rhodium particles and single crystals corresponding to vanadium pentoxide and V_4O_9.

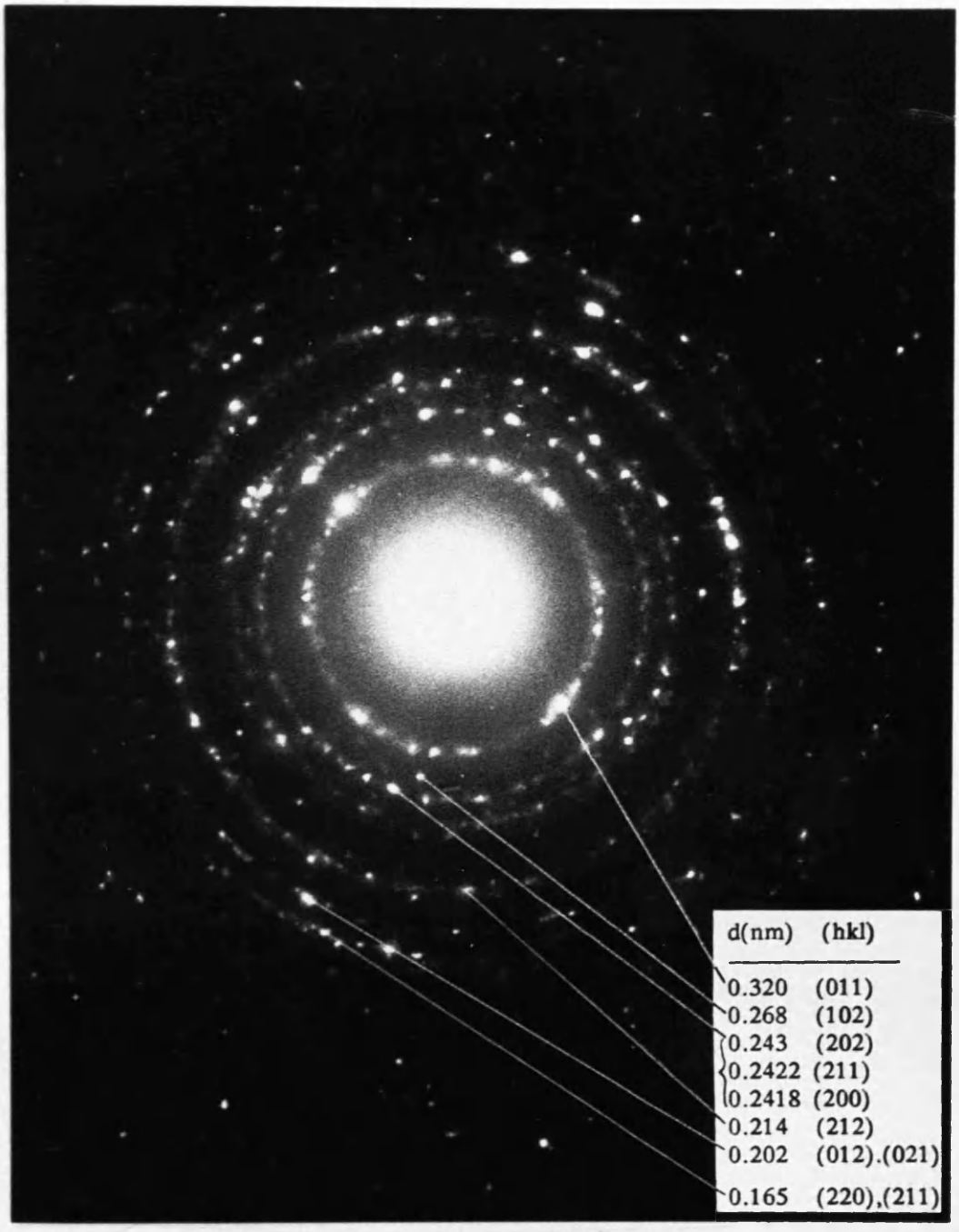

Fig. 3.21: EDP of the catalyst reduced at 450°C.

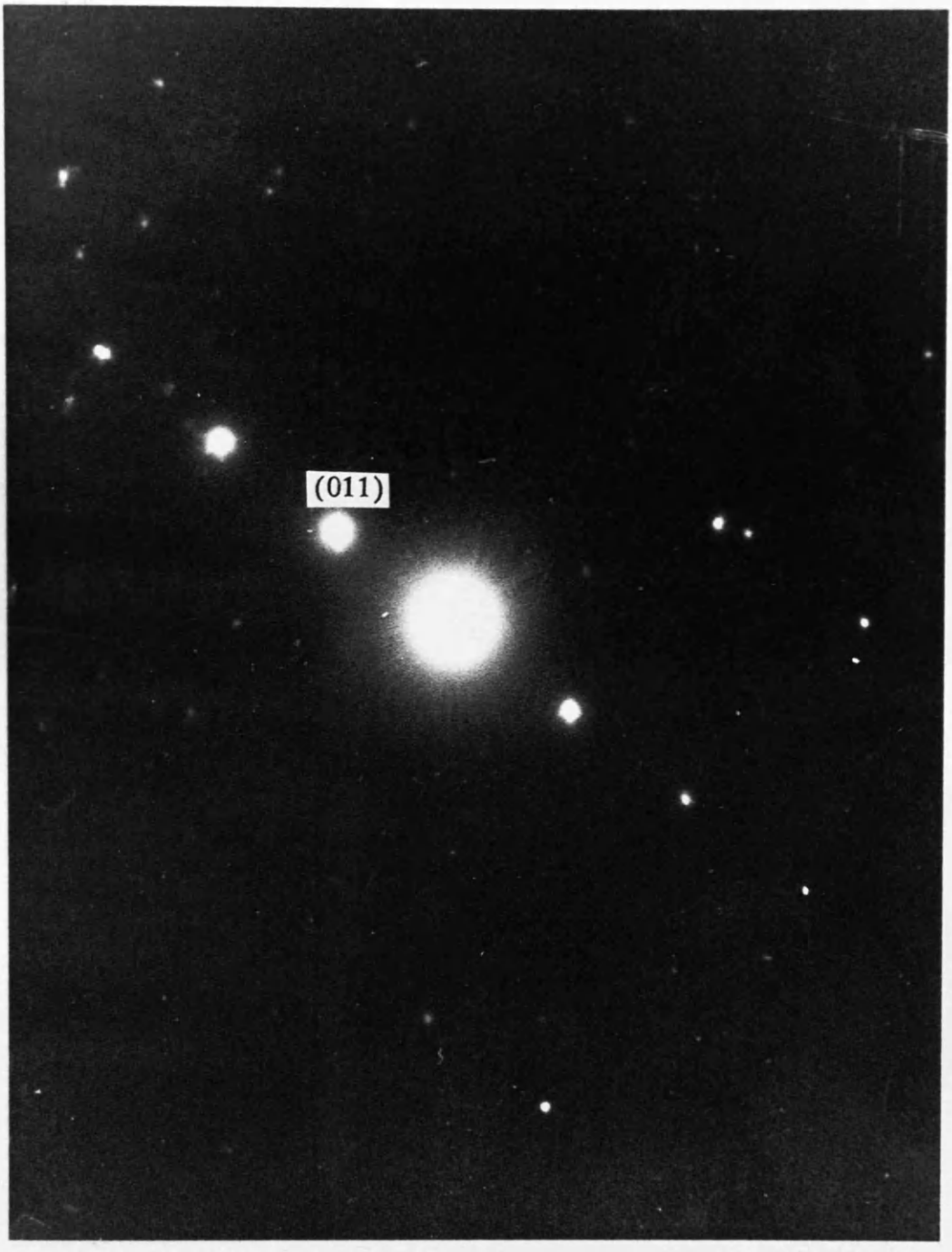

Fig. 3.22: SAED of a single crystal from the catalyst reduced at 450°C.

Fig. 3.23: HREM photograph of a crystal from the catalyst reduced at 450°C.

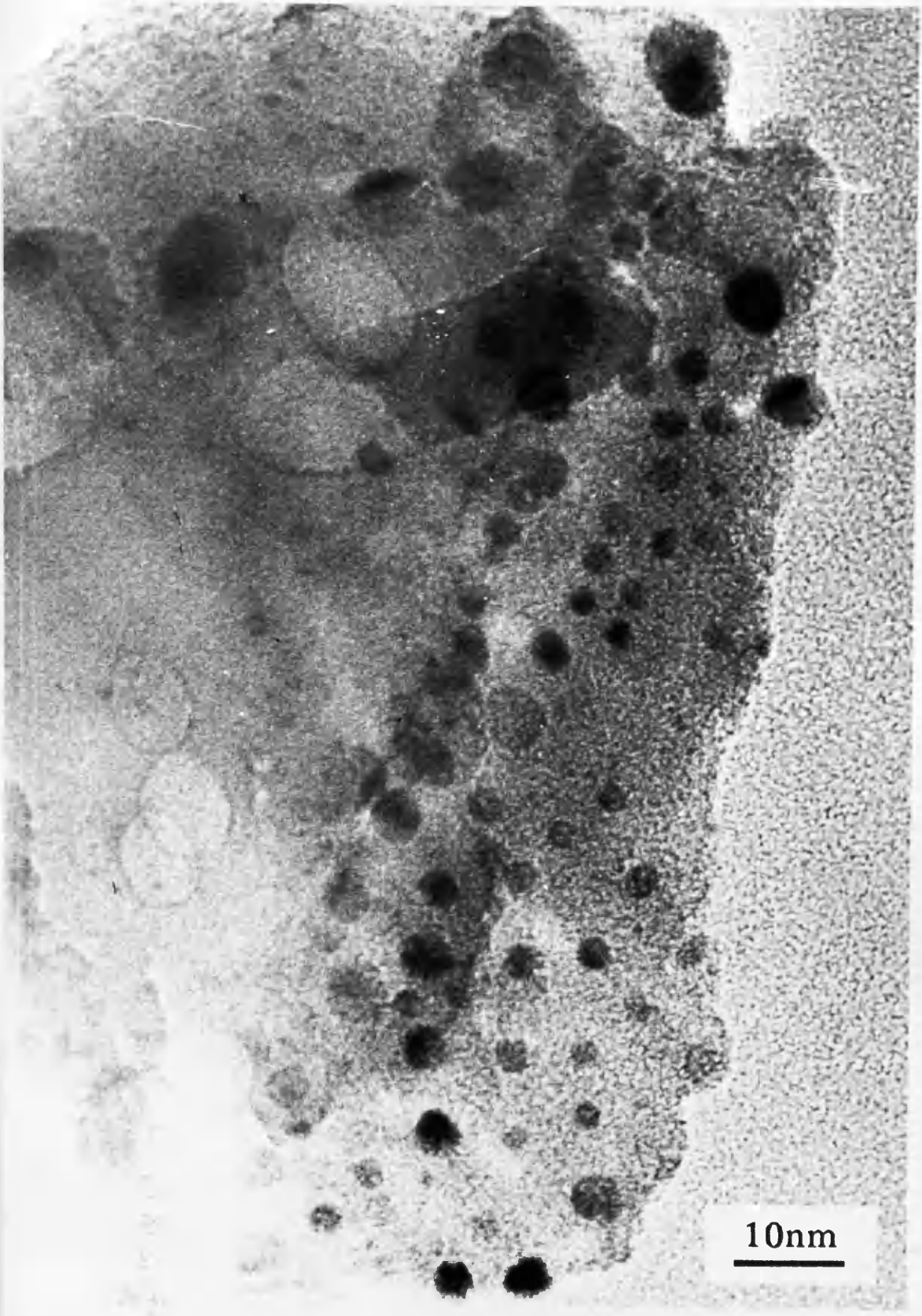

Fig. 3.24: Typical TEM micrograph showing the dispersion of rhodium particles for the catalyst reduced at 450°C.

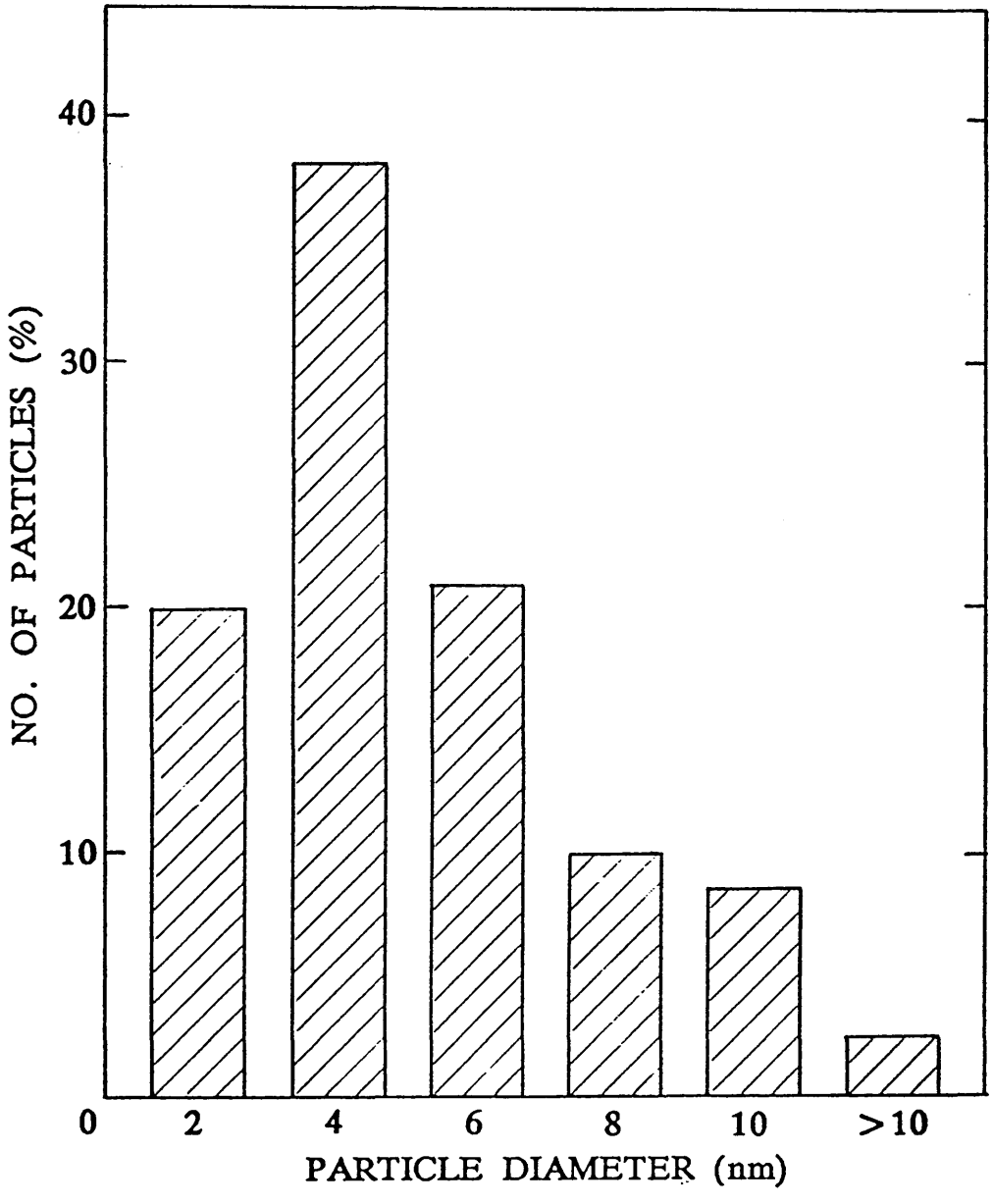

Fig. 3.25: A histogram showing the rhodium particle distribution for the catalyst reduced at 450°C.

iv— Catalyst reduced at 600°C

When the catalyst was reduced at 600°C, the support was further reduced to vanadium monoxide or vanadium sesquioxide as concluded from the XRD studies. However, the indexation of SAED patterns of single crystals (Fig. 3.26) showed that these crystals were not presenting the orientation of vanadium monoxide which has a rock—salt structure as discussed in section 2.3.7.c of the second chapter of this thesis. The reflections present in this SAED pattern can be indexed in the structure of vanadium sesquioxide, as described described in the x—ray diffraction file index. It is apparent that the electron beam was perpendicular to the (100) plane of this compound.

Lattice spacings corresponding to vanadium(III) oxide were commonly observed. The lattice fringes, shown in Fig. 3.27, with a spacing of 0.36nm correspond to the $(\bar{1}02)$ plane of vanadium (III) oxide.

Rhodium particles were successfully observed at the surface of the support in the HREM micrographs as shown in Fig. 3.28. The size distribution of these particles, which is represented in the histogram of Fig. 3.29, indicates that the arithmetic mean diameter is 6.5nm.

v— Size and shape of rhodium particles

It is obvious from the particle size distribution of the catalyst reduced at 250, 450 and 600°C that the thermal treatment of the supported metal catalyst results in an increase of the metal particle size, by sintering or particle coalescence.

The shape of the particles was not easy to define on the catalyst and a spherical shape can be supposed. However, many particles appear to be facetted. The particles present in Fig. 3.30

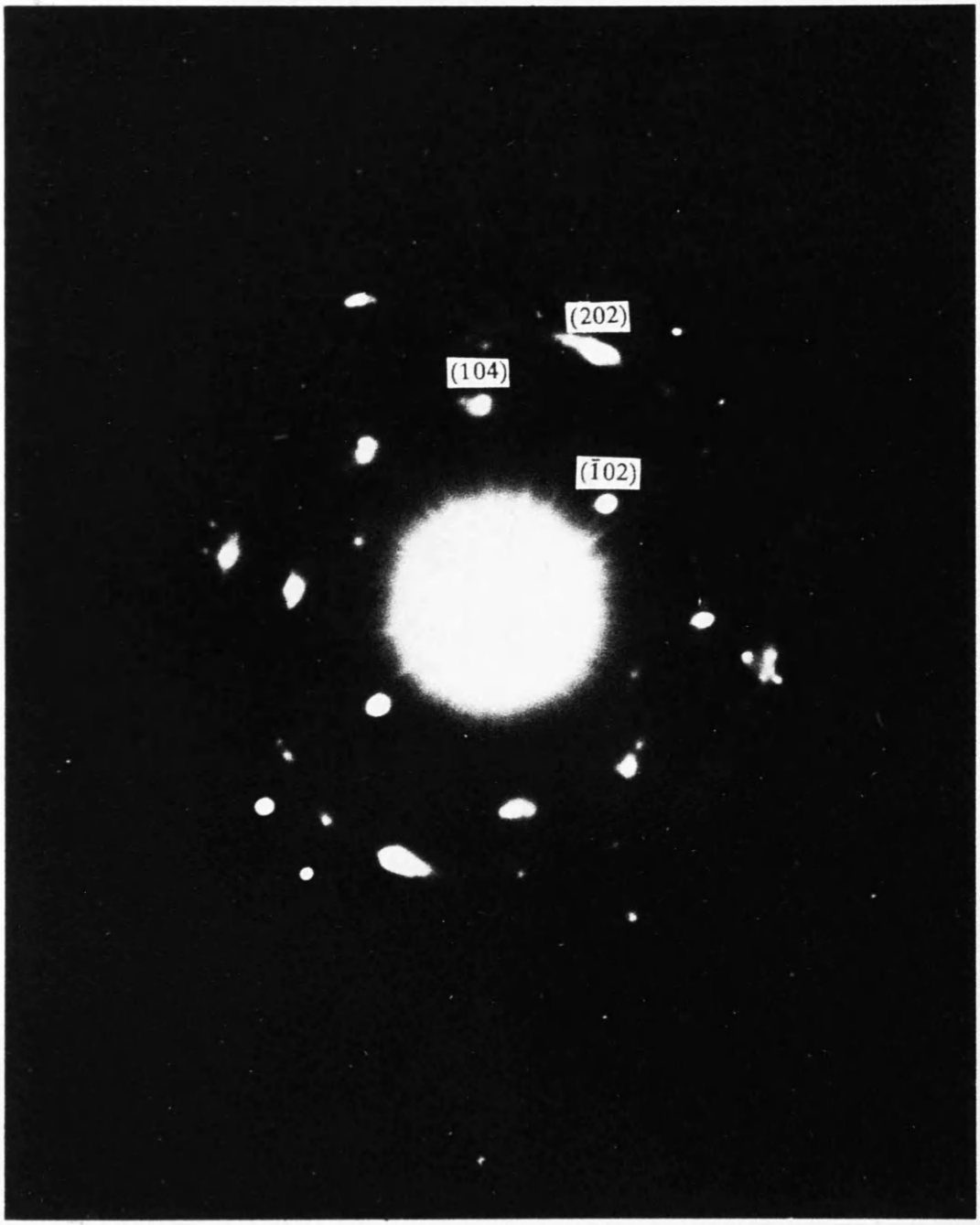

Fig. 3.26: SAED of a single crystal from the catalyst reduced at 600 °C.

Fig. 3.27: HREM micrograph showing lattice fringes corresponding to vanadium sesquioxide.

Fig. 3.28: TEM micrograph showing rhodium particles at the surface of the support for the catalyst reduced at 600°C.

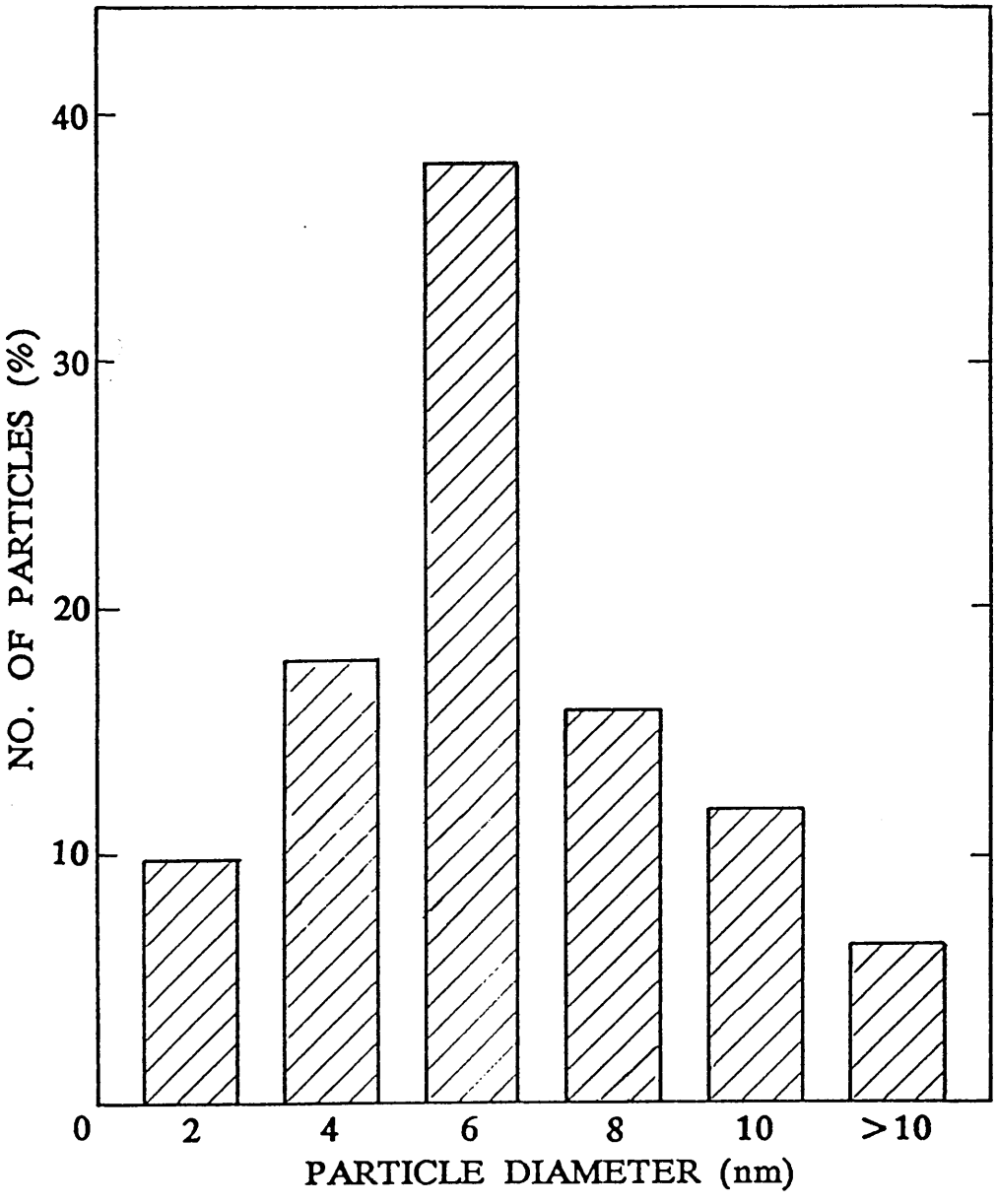

Fig. 3.29: A histogram showing the rhodium particle distribution for the catalyst reduced at 600°C.

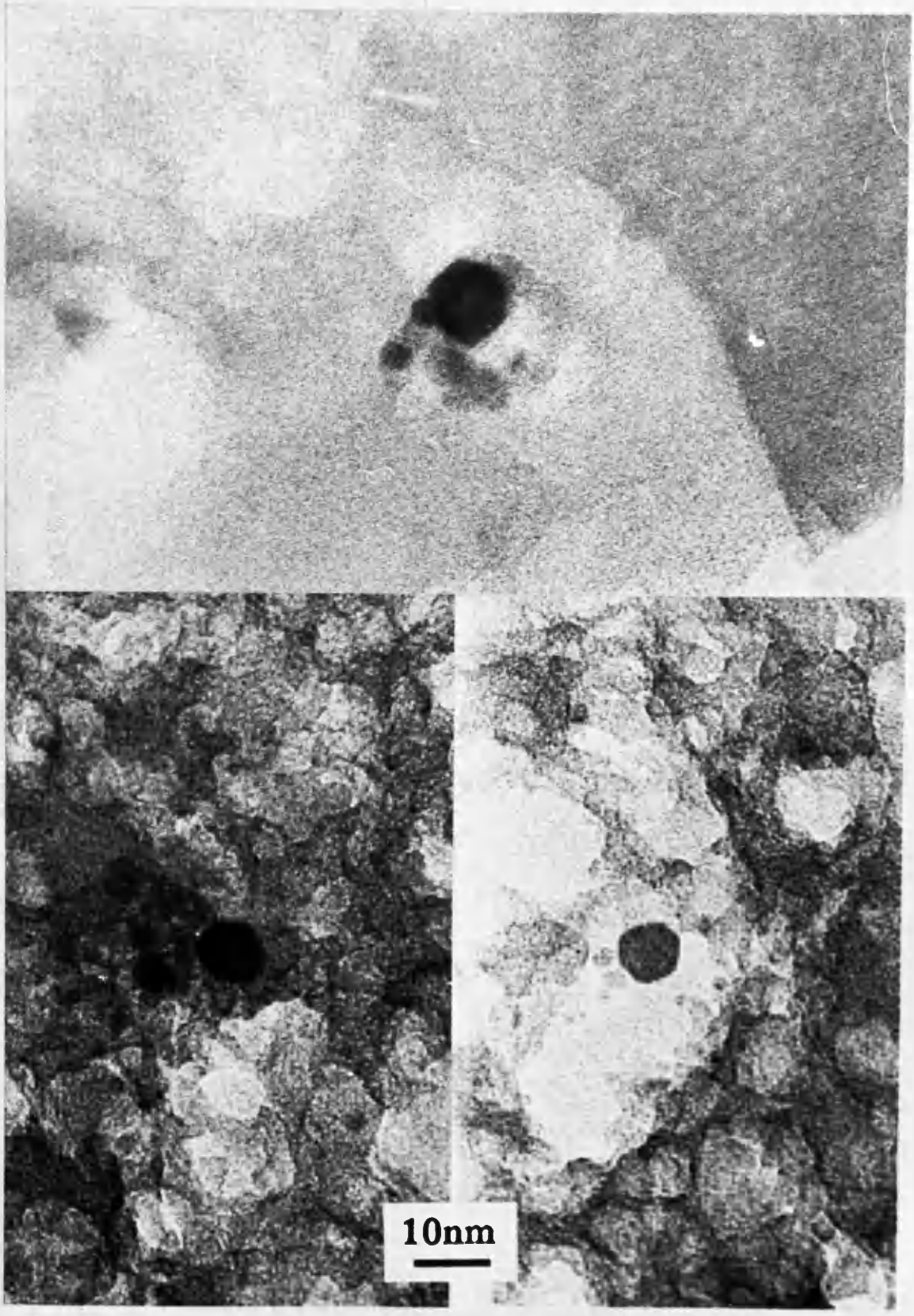

Fig. 3.30: TEM micrograph showing hexagonal–shaped rhodium particles in projection.

present a hexagonal shape in projection. Such facetting, via the formation of atomically dense crystallographic planes, is said to be indicative of the most stable situation (Hoare & Pal, 1971; Fuentes & Figueras, 1980).

vi— Morphological changes during the reduction process

The four micrographs presented in Fig. 3.31 show the fresh catalyst and the progressive reduction of vanadium pentoxide support at 250, 450 and 600°C. It is evident that there is increased mass loss with increasing temperature. In general, the holes produced in the crystals do not appear to be associated with catalyst particles. They may result from initiation of reduction and local atomic rearrangements at active sites in the crystals.

In general it does not appear to be a relationship between the edges of the holes and crystallographic planes of the reduced oxide. Occasionally, exceptions were observed, as shown in Fig. 3.31.b where the edges of the holes seem to be parallel to the lattice fringes.

3.3.3.d— Scanning electron microscopy

Examination of the fresh catalyst in the SEM (Fig. 3.32) revealed that the crystals present the same morphological features as those observed for pure vanadium pentoxide. The catalyst consisted mainly of well formed crystallites of different sizes with smooth surfaces and sharp edges in the crystalline habit of vanadium pentoxide.

The reduction of the catalyst at 250°C resulted in the formation of cracks at its surface (Fig. 3.33). The number of these cracks, as well as their dimensions, increased when the reduction temperature was increased from 250 to 450°C and then to 600°C (Fig. 3.34 and

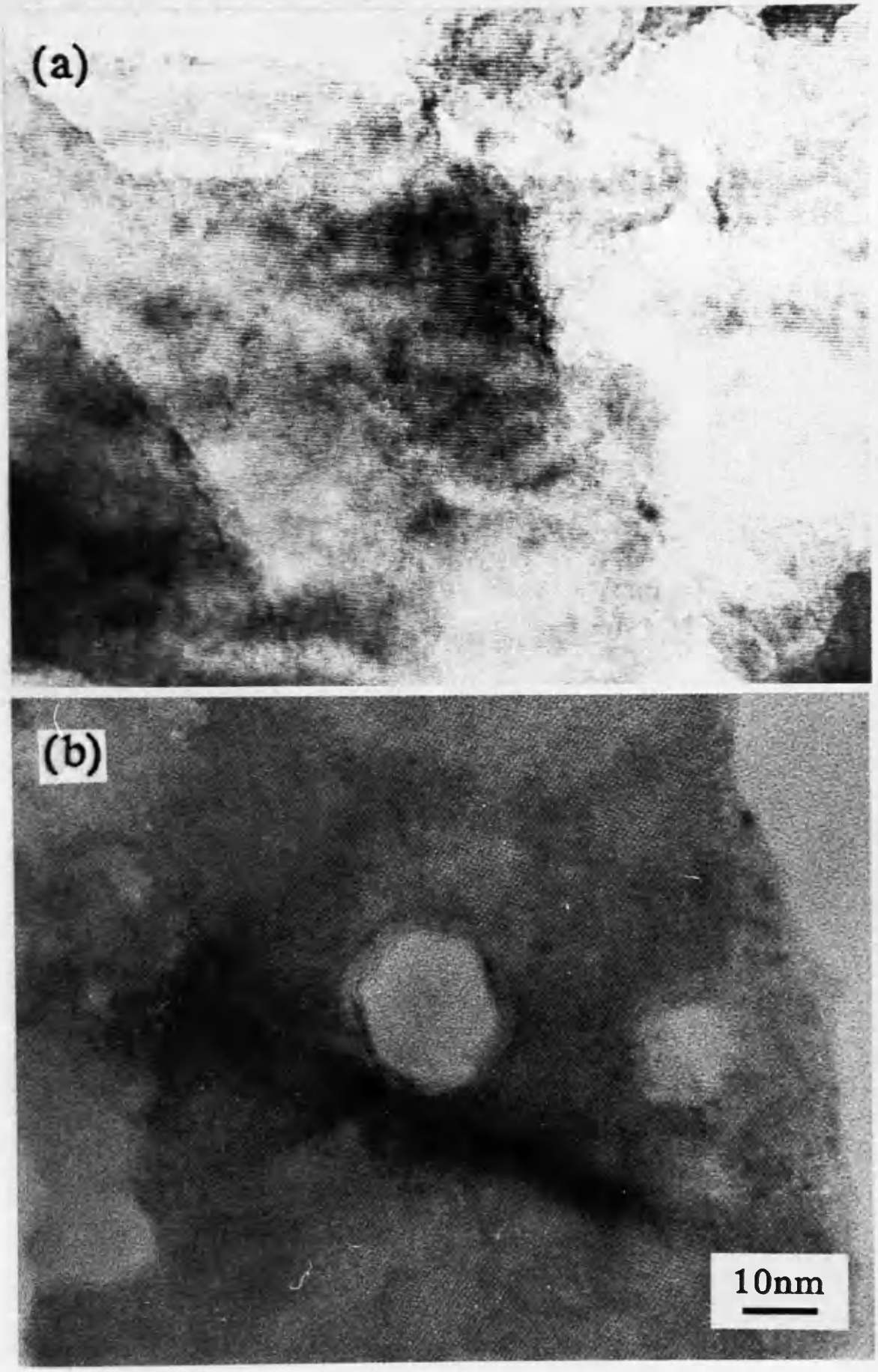
(a)
(b)
10nm

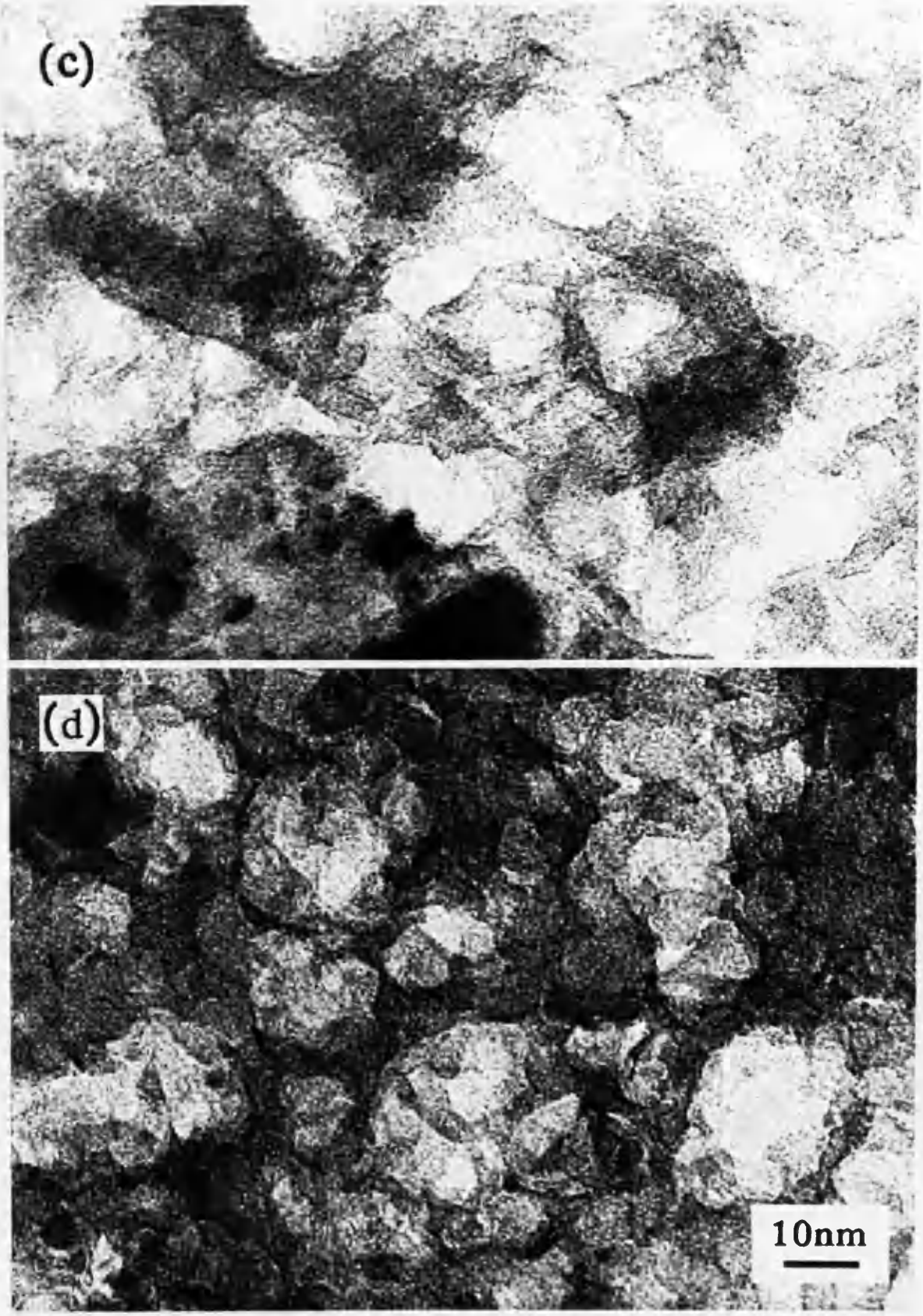

Fig. 3.31: Morphological changes occurring in the support when (a) the fresh catalyst is reduced at (b) 250°C, (c) 450°C and (d) 600°C.

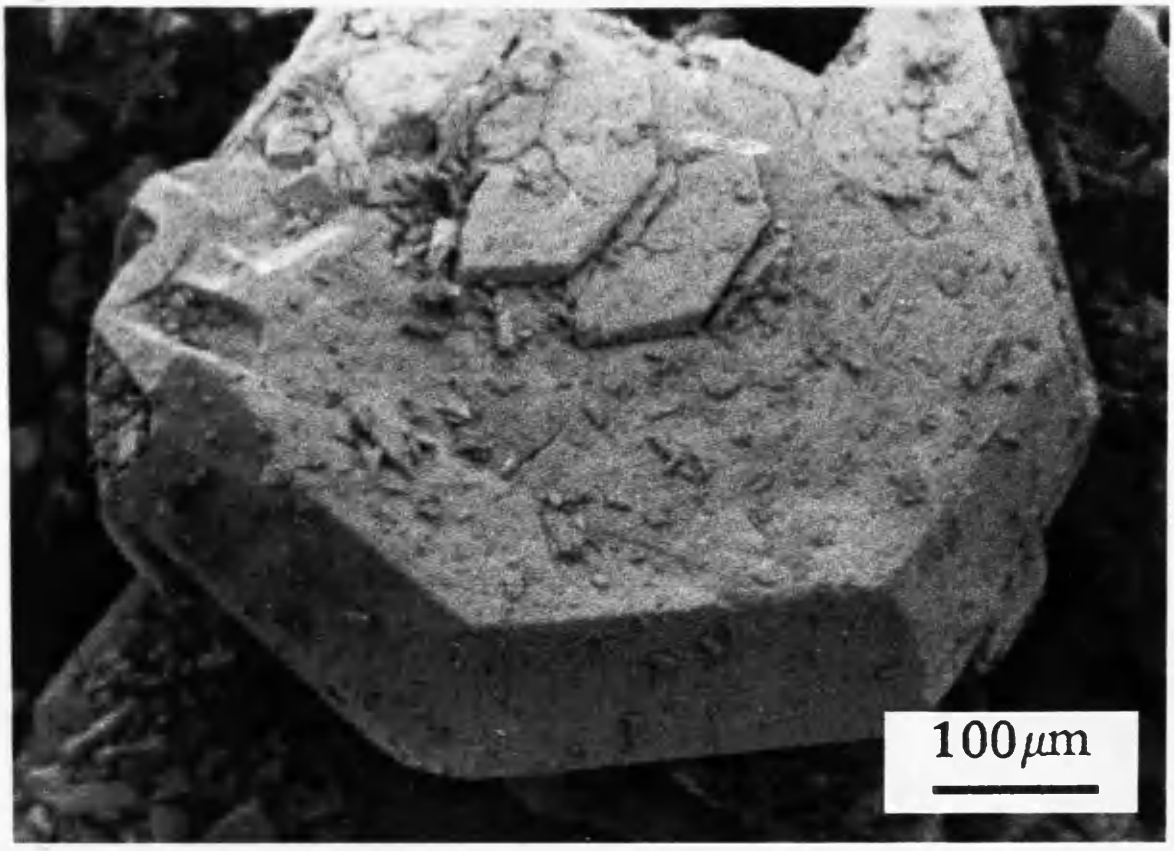

Fig. 3.32: SEM photograph of the fresh catalyst.

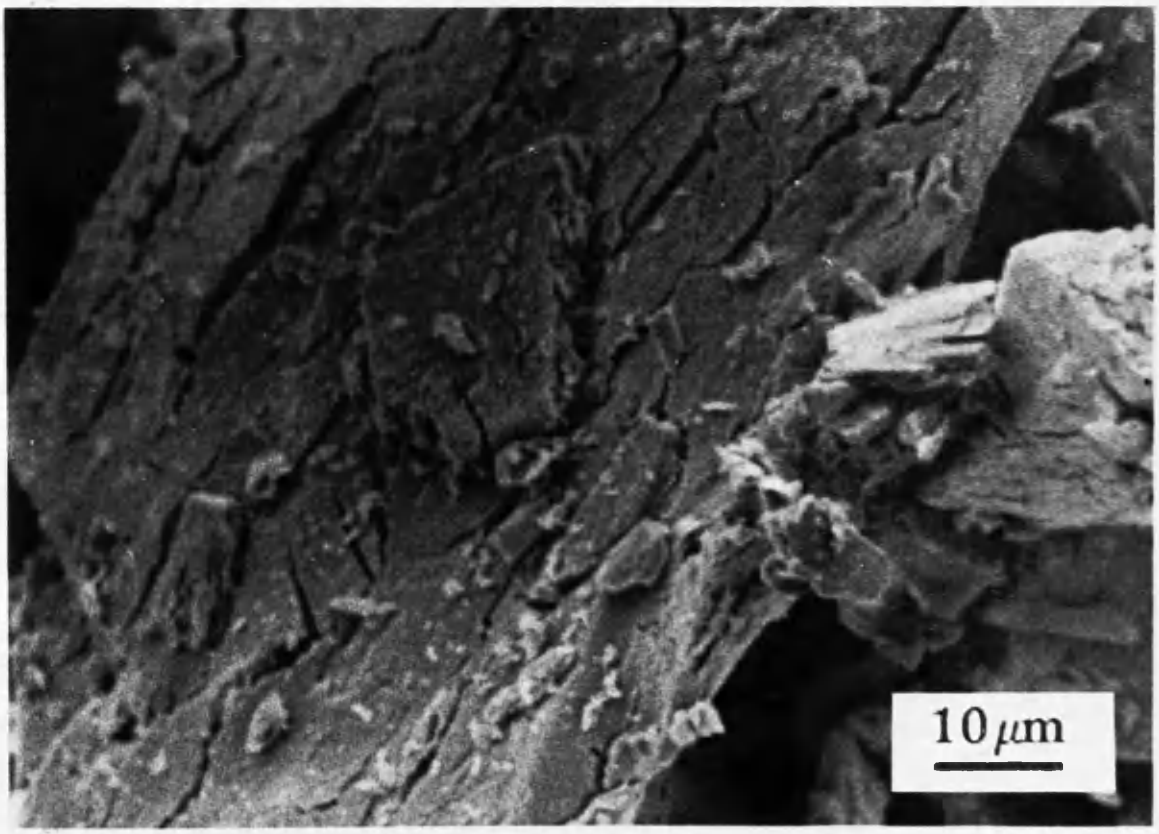

Fig. 3.33: SEM photograph of the catalyst reduced at 250°C.

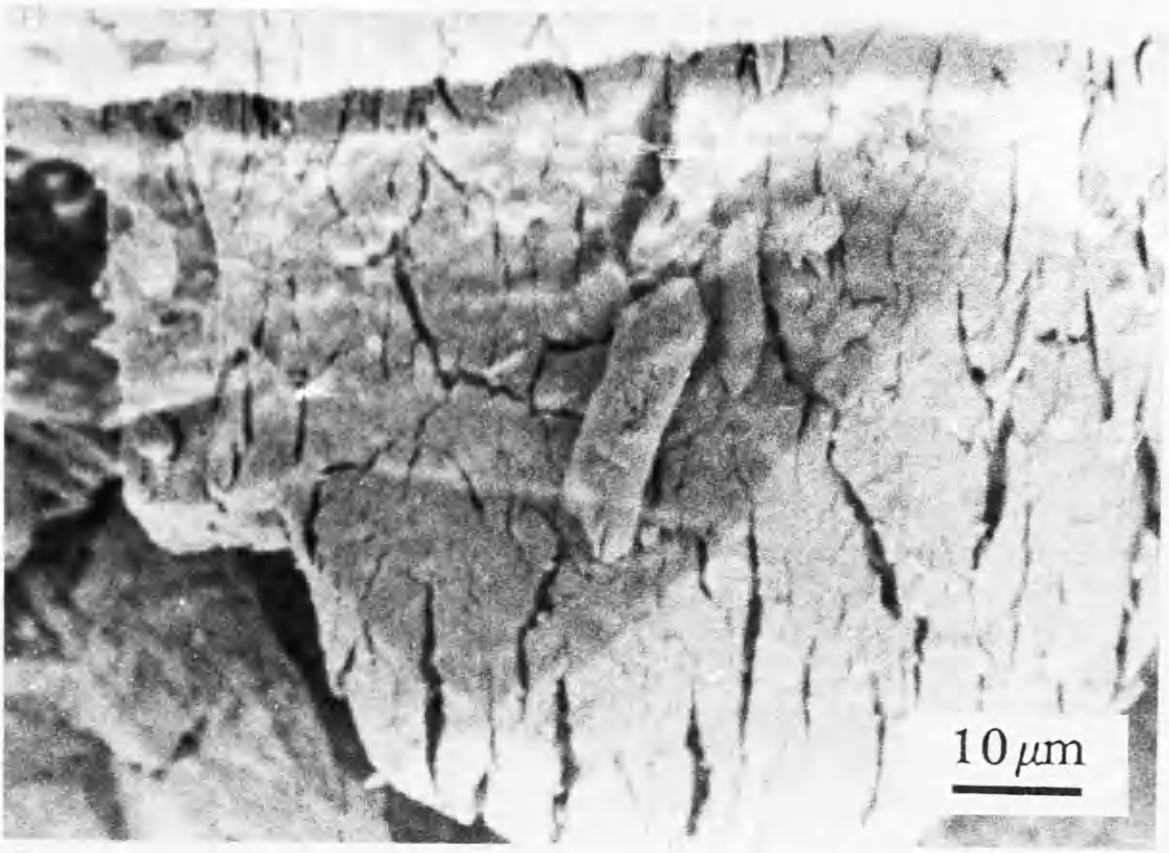

Fig. 3.34: SEM photograph of the catalyst reduced at 450°C.

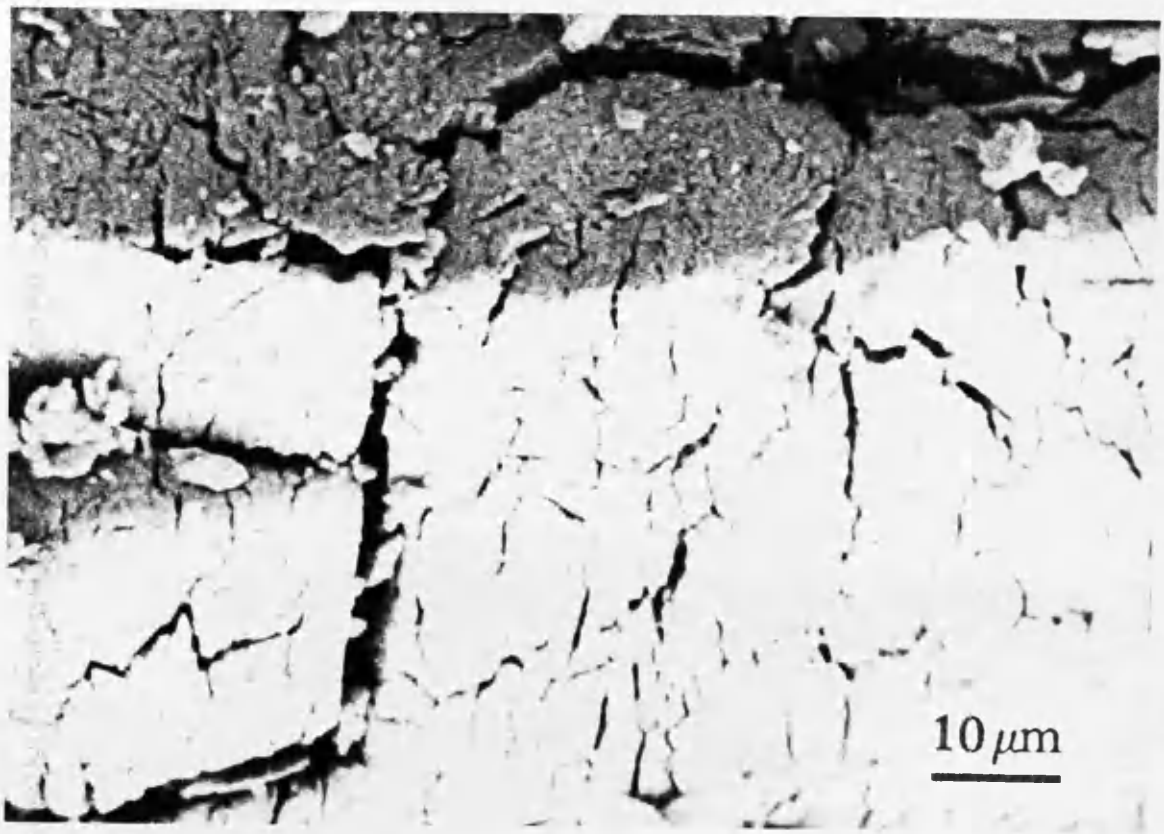

Fig. 3.35: SEM photograph of the catalyst reduced at 600°C.

3.35).

The presence of the cracks could be explained by the mass loss due to the evolution of oxygen from the bulk of the support, vanadium pentoxide, during the reduction process and the structural rearrangement of atoms to form the lower oxides present at each temperature.

The observations by SEM parallel those of the TEM work in that severe shrinkage resulting from mass loss increased with temperature.

However, despite the severe shrinkage, overall the integrity of the original crystalline masses was retained. Fig. 3.37 shows that, even when reduced at 600°C, the catalyst consists of crystallites of sizes comparable to those observed with the same catalyst prior to its reduction (Fig. 3.36).

3.3.3.e— Mechanism of vanadium pentoxide reduction

In the analysis of the above experimental facts, it can be observed that an extremely high catalytic activity in the reduction of vanadium pentoxide is shown by the supported rhodium metal. This catalytic action involves primarily a marked decrease in the temperature, at which the reaction is initiated, by hundreds of degrees.

The reduction by hydrogen of a metal oxide in the solid phase can be thought of as occurring in a number of individual reaction steps. The general scheme of the mechanism of such process has been described by Anderson (1948) who notes three stages:

(a) chemisorption of hydrogen on the surface followed by desorption of water whereby anion vacancies are created.

(b) diffusion of the vacancies from the surface into the bulk.

(c) saturation of the crystal lattice with defects followed by nucleation of the new phase.

Since the gaseous reducing agent, hydrogen, is activated on the

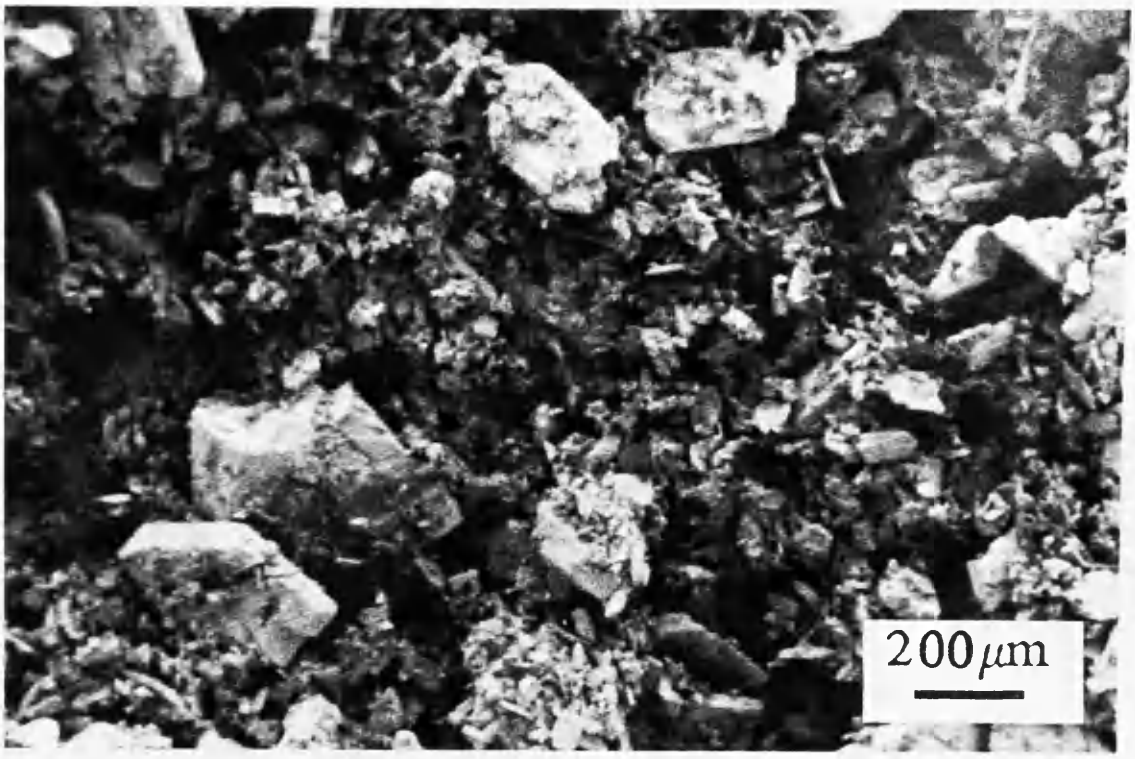

Fig. 3.36: Low magnification SEM phtograph of the fresh catalyst.

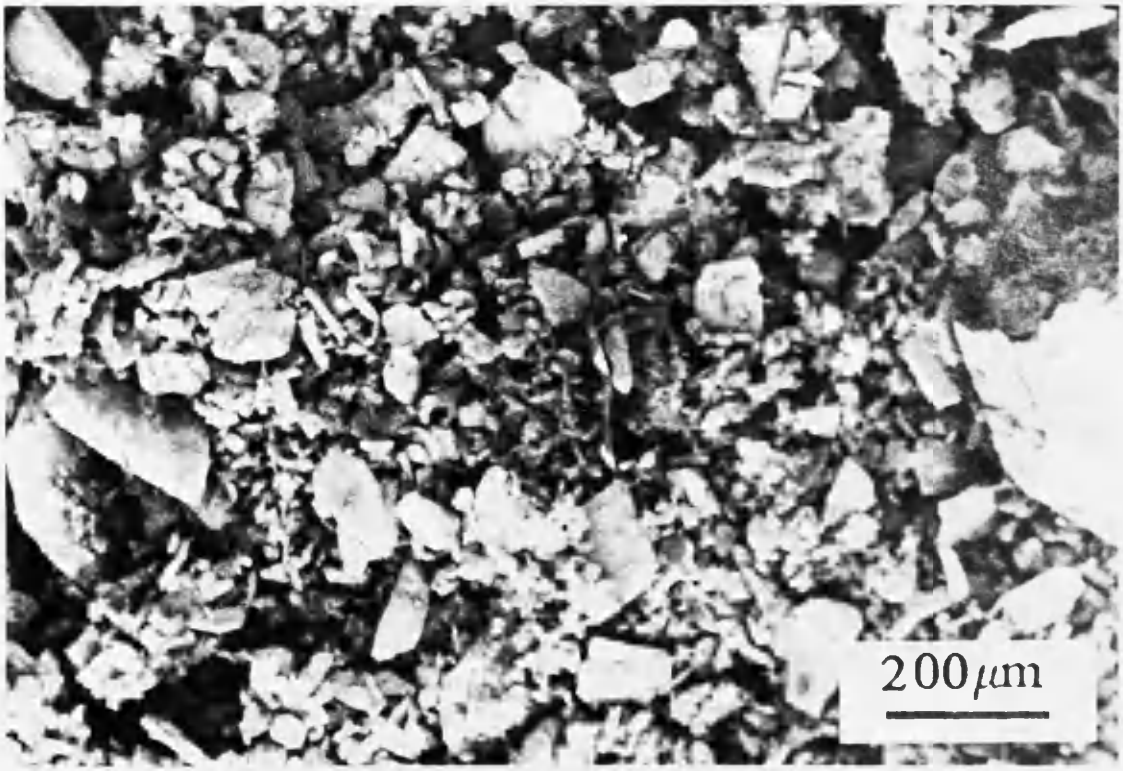

Fig. 3.37: Low magnification SEM phtograph of the catalyst reduced at 600°C.

surface of the supported crystallites, the points of contact between it and the oxide being reduced become centres for the rapid production and growth of nuclei of the new phase. As a result, in the presence of active metallic catalysts there is a sharp decrease in the duration of the induction period and a change in the kinetics of nucleus formation, as observed in the reduction of vanadium pentoxide.

It is widely accepted that the migration of hydrogen atoms from the activating species to the acceptor is the initiating step (Bond & Tripathi, 1976). It is believed that the first hydrogen atoms to arrive from the activator will react as:

$$M^{x+} + O^{2-} + H \longrightarrow M^{(x-1)+} + OH^{-}$$

and that is followed by dehydration to the next lower oxide. It is thus easy to understand how hydrogen atoms can readily lead to an oxide of one lower oxidation state, and why for example, the first product of the catalysed reduction of vanadium pentoxide is V_4O_9 and not vanadium dioxide or vanadium sesquioxide. Provided hydrogen atoms are mobile over and through the lower oxide, its formation can proceed both parallel and normal to the surface.

3.3.3.f— Structural changes occurring through reduction

Vanadium pentoxide structure can be considered to be built of an alternate succession of oxygen atoms planes and vanadium—oxygen atoms planes, as shown in Fig. 3.38.

The passage from vanadium pentoxide to lower vanadium oxides requires the suppression of certain type of oxygen atoms. It has been shown by Gillis (1964) that the removal of all the oxygen atoms indicated by arrows in Fig. 3.38 will lead to the monoclinic structure of V_6O_{13} reported by Aebi (1948), after rearrangement of the ions inside the framework to enable each vanadium ion to be surrounded

only by oxygen ions as the nearest neighbours (Fig. 3.39). The passage from vanadium pentoxide to V_6O_{13} requires thus the suppression of an oxygen plane out of three planes.

It can be supposed that other oxides of vanadium might be formed by similar process. If one plane out of two is removed, $V_{12}O_{22}$ can be obtained and the suppression of all the oxygen planes will lead to vanadium sesquioxide.

The fact that V_4O_9 was observed to grow topotaxially on vanadium pentoxide single crystals together with consideration concerning its growth condition and density (Grymonprez et al., 1977) indicate that V_4O_9 could be a slightly deformed superstructure of vanadium pentoxide.

If one tenth of oxygen atoms are removed from the structure of vanadium pentoxide, in the manner indicated in Fig. 3.40 which is the projection of the structure onto the (001) plane, the unit mesh in this hypothetical superstructure would have one unit vector parallel to the b– axis and of length 2b = 0.7126nm. The second unit vector would have a length of 0.6024nm and would include an angle of 17° with a; the angle between the two unit vectors in this model would, consequently, be 107°. Fig. 3.41 shows the projection of this superstructure onto the (100) plane. The unit vector in the third direction would be 4c = 1.748nm.

The difference between the characteristics of this superstructure and those of V_4O_9 are small and can easily be explained by minor distortions. A driving force for this distortions seems to be a repulsive action between the oxygen vacancies.

Other models are possible in which the oxygen vacancies are located on other sites but with the same arrangement. Because it has been shown that the vanadyl oxygen atoms are the most reactive, it was preferred to remove them periodically.

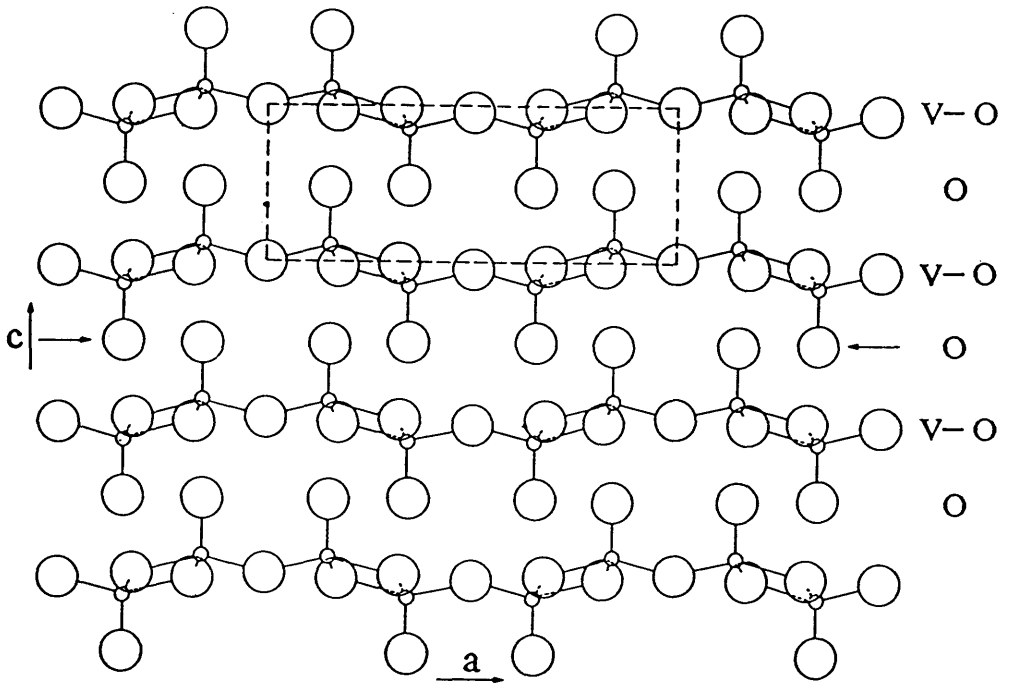

Fig. 3.38: Projection of vanadium pentoxide structure onto the (010) plane.

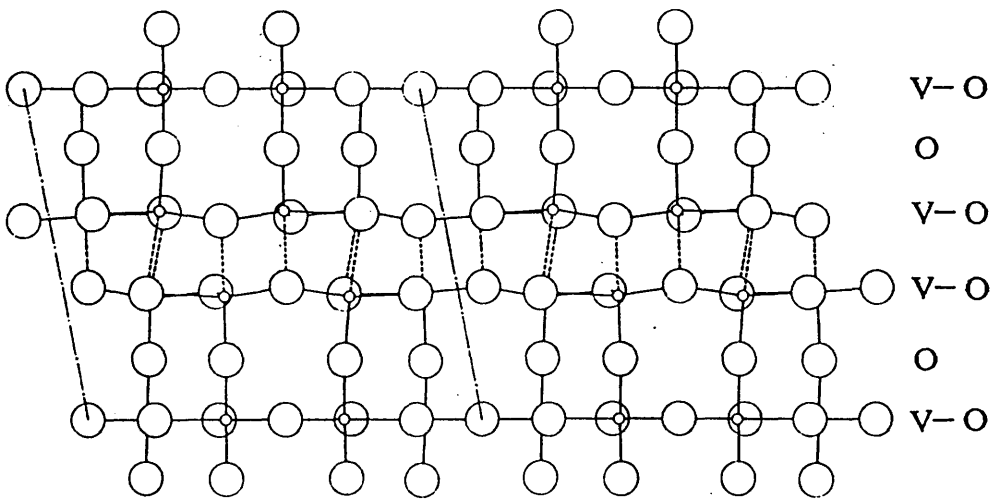

Fig. 3.39: Projection of V_6O_{13} structure onto the (010) plane.

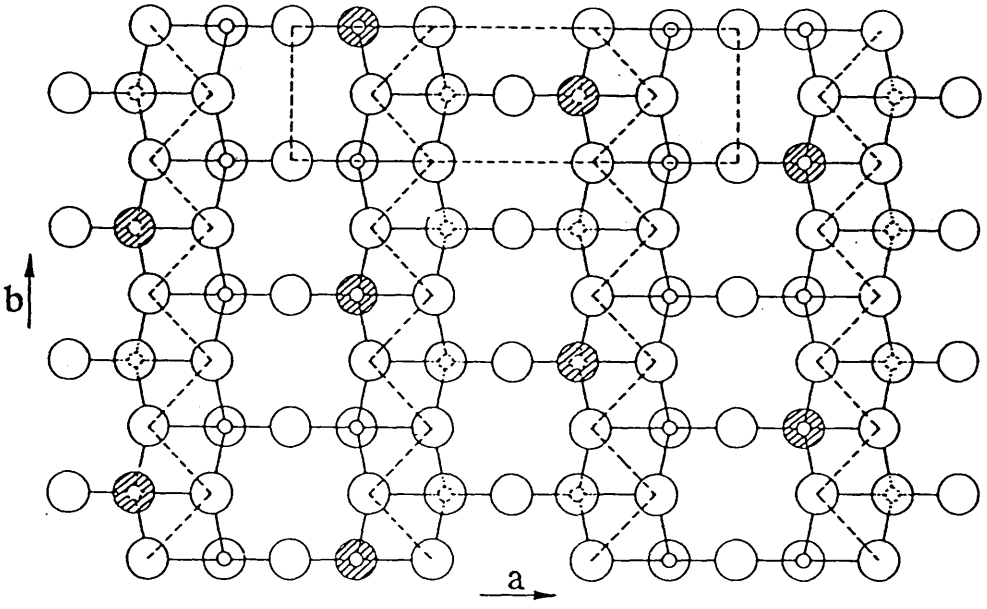

Fig. 3.40: Projection of vanadium pentoxide structure onto the (001) plane showing V_4O_9 as a superstructure of vanadium pentoxide when one tenth of the oxygen atoms are removed.

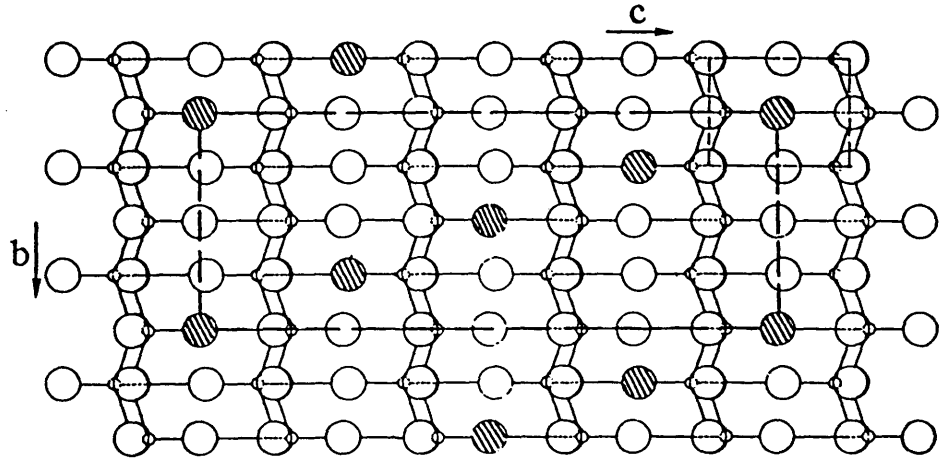

Fig. 3.41: Projection of the superstructure onto the (100)plane.

3.3.4– BUTANE HYDROGENOLYSIS

The hydrogenolysis of n– butane was used as a test reaction for the characterisation of the activity and selectivity of the rhodium catalyst supported on vanadium pentoxide. Alumina support material loaded with the same amount of rhodium was prepared by similar method and tested in the butane hydrogenolysis reaction.

3.3.4.a– Rhodium supported on vanadium pentoxide

i– Preliminary test

First it must be shown that there is no reaction on the support. A blank on the support was negative: there is no hydrogenolysis of butane on the vanadium pentoxide support material alone, at least within the range of temperatures studied here (between 200 and 300°C). Thus it can be affirmed that in the case of the 1% rhodium supported on vanadium pentoxide catalyst, hydrogenolysis of carbon– carbon bonds in butane does not take place in the absence of the metal.

ii– Variation of activity with time

The mixture, hydrogen and butane, was passed over the catalyst at 220°C and the conversion rate as well as selectivities for the three products of the reaction were monitored during the working time. Fig. 3.42 shows the variation of the conversion rate of butane, into the three products of the hydrogenolysis reaction, with working time.

At the start the conversion rate changed very quickly. This could be attributed to the temperature variation induced by the fact that the reaction is exothermic. The steady state was reached after about five hours, and the curve obtained after that time could be

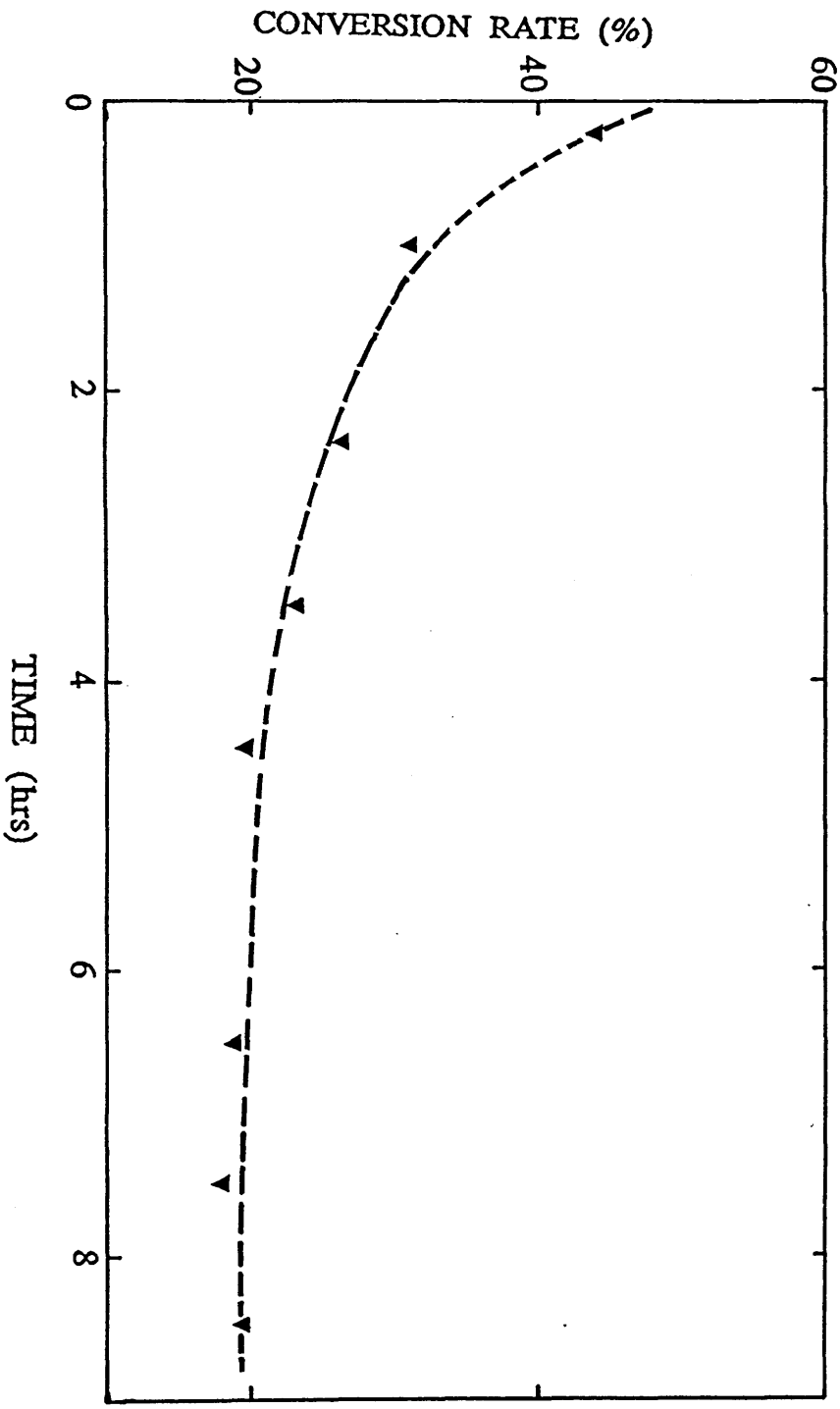

Fig. 3.42: Variation of butane conversion rate with working time.

considered to be a straight line. The extrapolation of this linear portion of the curve to time zero permits calculation of the initial activity and selectivities of the catalyst at the chosen temperature. At this temperature it was found that about 19% of the butane was initially converted into the three products of the hydrogenolysis reaction, namely: methane, ethane and propane. The initial rate of the reaction was calculated and its value is 0.118mol/h.g of rhodium.

The selectivities for methane and propane increased in the course of the time, while that of ethane decreased. After the steady state was reached, the selectivity for the three products of butane hydrogenolysis leveled out, giving initial values of 0.16, 0.63 and 0.86 for methane, ethane and propane, respectively.

iii— Influence of the temperature

The hydrogenolysis of butane was carried out at different temperatures. At each temperature, the reaction was allowed to proceed until the steady state was reached. The steady state was then maintained for a length of time sufficient to trace with a satisfactory precision the straight line giving the conversion rate versus the time. The temperature was then modified and another straight line was obtained.

The curve obtained was in the form of steps as shown in Fig. 3.43. At the end of the day, all the parameters were set back to the initial conditions and the catalyst was maintained under hydrogen overnight.

Activity and selectivity

The initial conversion rates of butane and the selectivities for methane, ethane and propane were determined from the curves in form of steps obtained by varying the temperature between 210 and

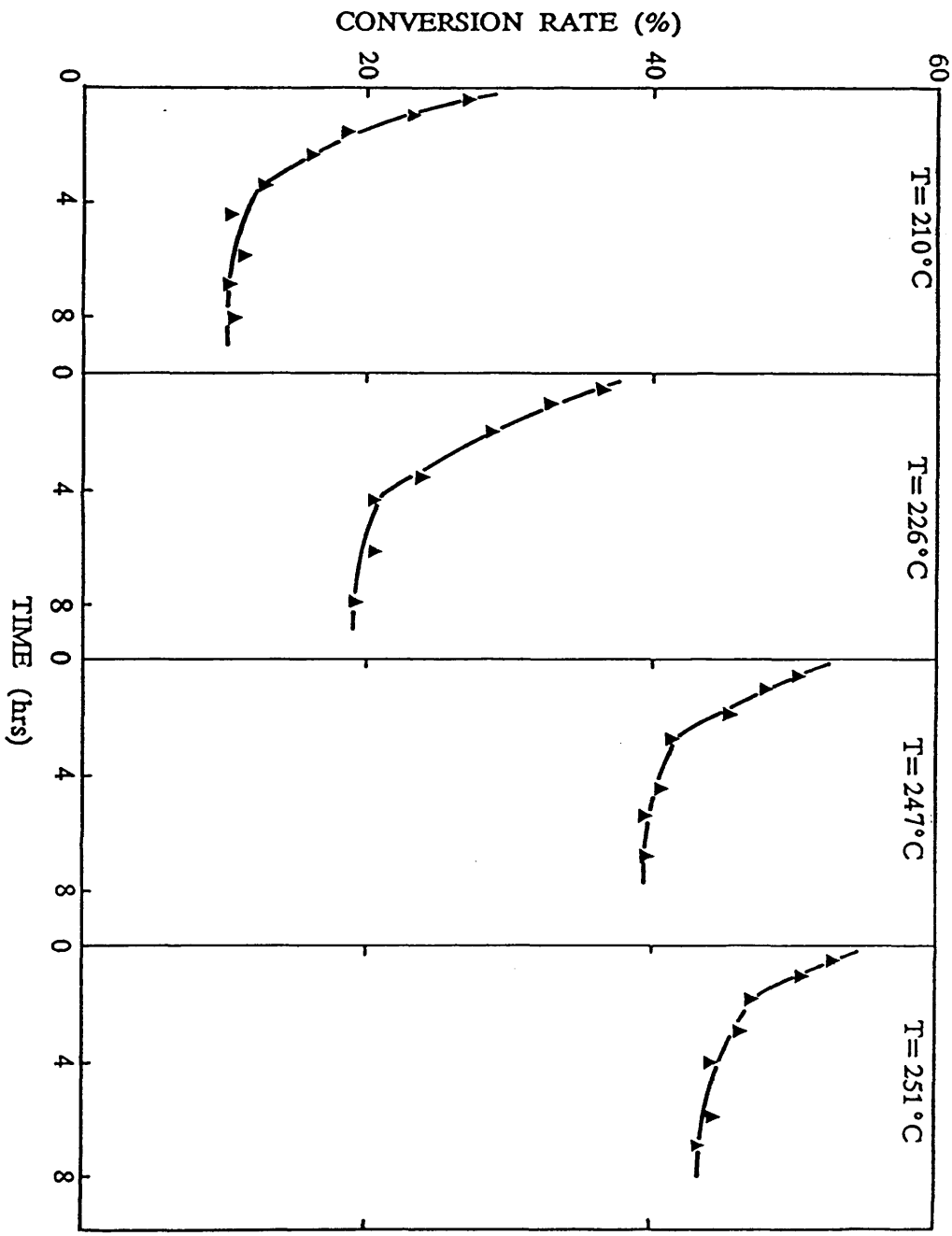

Fig. 3.43: Conversion rate variation with time at different temperatures.

251 °C and extrapolating the linear portions of each step to the time zero. The product distribution variation with temperature is listed in table 3.3 and the variation of the initial conversion rate with temperature is illustrated in Fig. 3.44.

The treatment of the results is very complex because the reaction gives methane, ethane and propane by hydrogenolysis. In addition, ethane and methane may come from the secondary hydrogenolysis of the products formed initially.

The ratio $C_3/C_1 = \alpha$ must be equal to three if only a single hydrogenolysis occurs, in other words, if the resultant fragments from the rupture of butane desorb without further cracking. Experimentally, it was found that α was inferior to three for conversion rates different from zero, but as shown in Fig. 3.45, α approached three when the conversion rate approached zero. It can thus be affirmed that for the catalyst studied, only a single hydrogenolysis takes place. The values of α which are inferior to three might be due to successive hydrogenolysis reactions of small amounts of the primary products of the reaction which are ethane and propane.

These reactions were taken into account in the determination of the initial rates of the rupture of central and terminal bonds in butane, using the relations determined by Leclercq (1976) which give the selectivity for one or the other of the two bonds.

Selectivities for the rupture of terminal and central bonds are listed in table 3.3 together with temperatures and conversion rates, and their variation with temperature is also shown in Fig. 3.44.

It appears from these data that at 210°C, the hydrogenolysis occurred almost on a single bond, which is the terminal one. When the temperature was raised, the selectivity for the rupture of the terminal bond decreased in favor of that of the central bond for which the selectivity increased. At high temperature (251 °C), both bonds break down at the surface of the catalyst with equal chances.

The variation of selectivities with conversion rates (Fig 3.46)

Table 3.5: Distribution of the products obtained from butane hydrogenolysis on vanadium pentoxide— supported rhodium catalyst at different temperatures.

T (°C)	τ	r	S_1	S_2	S_3	S_{ter}	S_{int}
210	0.108	0.064	0.949	0.133	0.928	0.94	0.06
226	0.196	0.116	0.777	0.486	0.750	0.76	0.24
247	0.392	0.231	0.556	1.031	0.461	0.51	0.49
251	0.430	0.254	0.555	1.062	0.440	0.50	0.50

τ: Initial conversion rate.
r: Reaction rate in mol/h.g of rhodium.
S_i (i=1 to 3): Selectivity for the reaction product C_i.
S_{int}: Selectivity for internal bond rupture in percent.
S_{ter}: Selectivity for terminal bond rupture in percent.

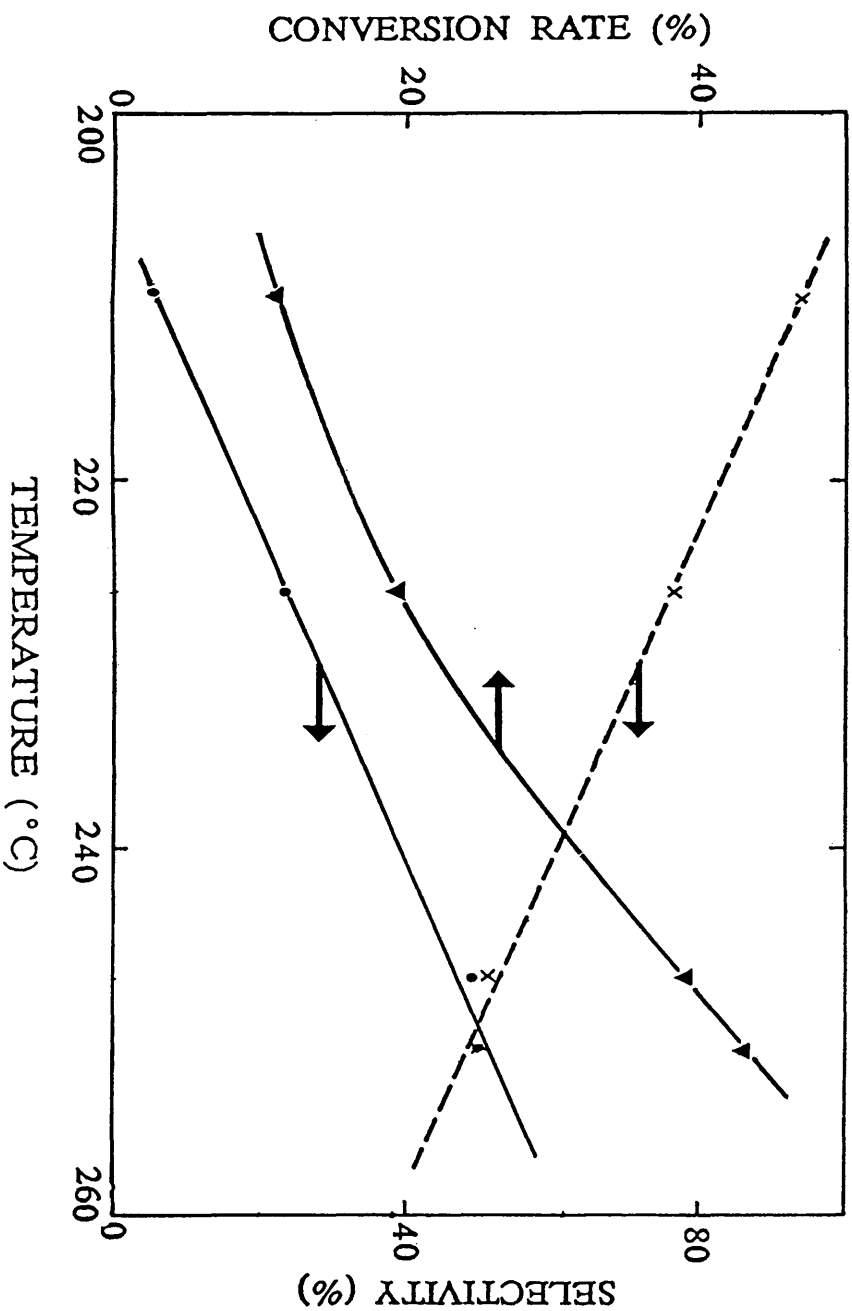

Fig. 3.44: Variation of conversion rate (▼) and selectivities for terminal (×) and internal (•) bond ruptures in butane with temperature.

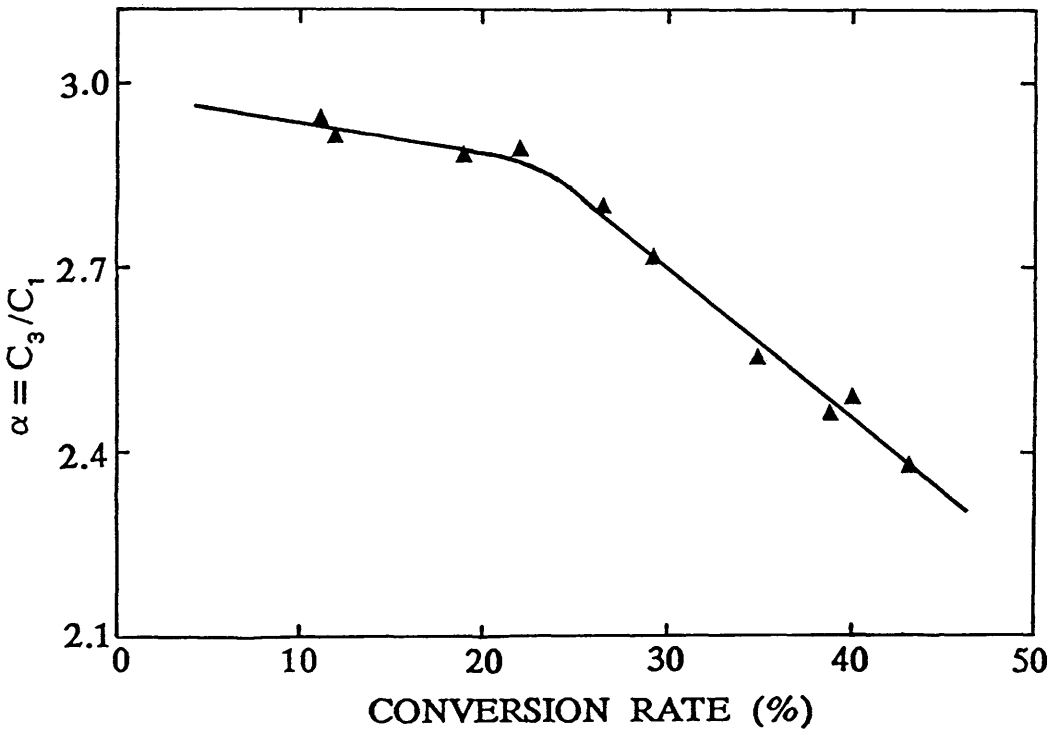

Fig. 3.45: Variation of $\alpha = C_3/C_1$ with the rate of conversion of butane.

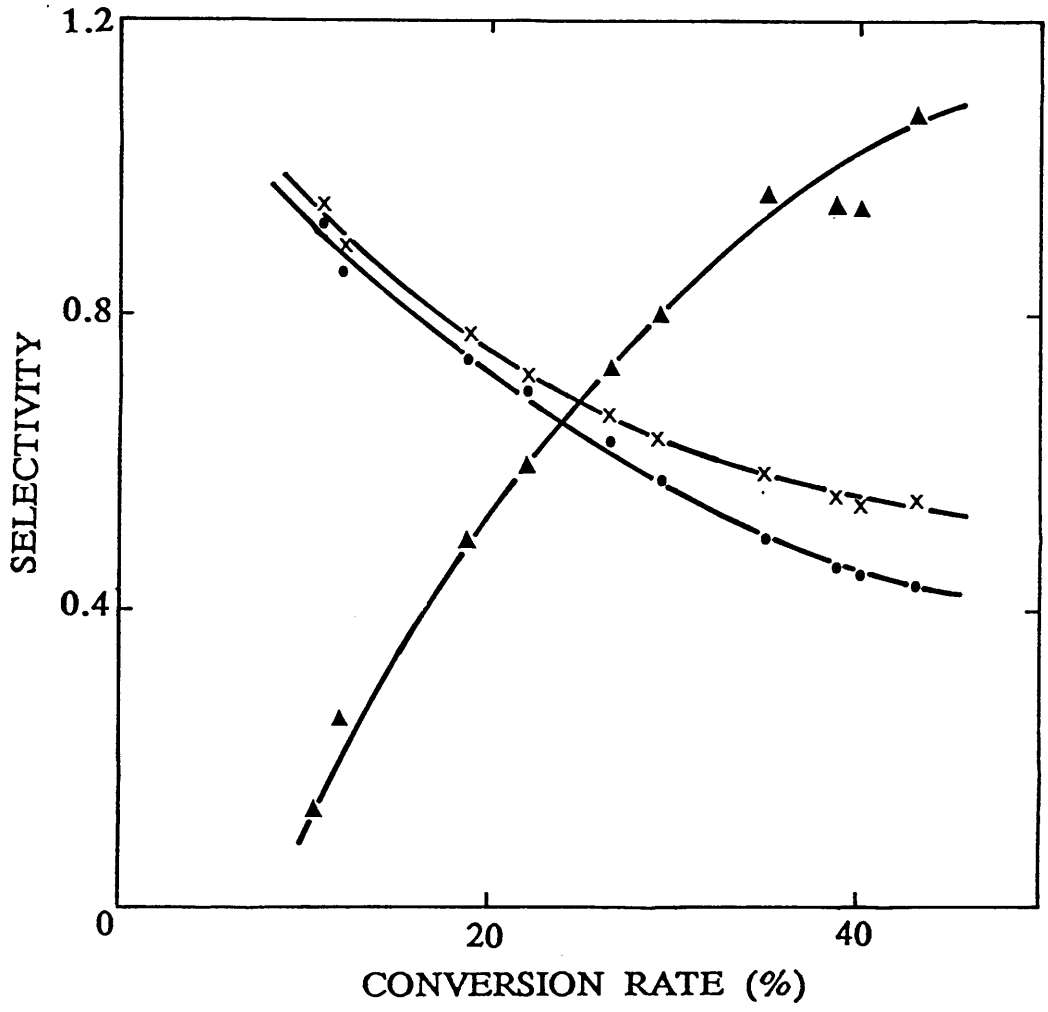

Fig. 3.46: Variation of selectivities for methane (×), ethane (•) and propane (▲) with the conversion rate for vanadium pentoxide–supported rhodium catalyst.

indicated that no consecutive reaction of propane and ethane to create still smaller alkanes occurred. In this single hydrogenolysis process the rupture of the central bond seem to be favoured to the terminal one. As the conversion rate increased, the selectivity for ethane increased at the expense of that for propane and methane, but at high conversion rates (more than 35%) all selectivities leveled out.

Activation energy

The temperature was changed in order to measure the apparent activation energy (E) by maintaining the partial pressures of both hydrogen and butane constant using the expression:

$$r = A.p_{H_2}^{a}.p_{C_4}^{b}.\exp(-\frac{E}{RT})$$

where r is the reaction rate, A is a constant, $p(H_2)$ and $p(C_4)$ are the partial pressures of hydrogen and butane, respectively.

The equation was changed into a linear form with respect to the parameters by taking the logarithm and the best estimate of the parameter E was obtained by linear regression analysis.

The activation energy for the butane hydrogenolysis, over the vanadium pentoxide— supported rhodium catalyst, was determined from the trace in Fig. 3.47. Its value is 71 kJ/mol with a correlation coefficient of the least squares plot exceeding 0.99968.

iv— Variation of selectivities with temperature

The product distribution corresponding to the primary cracking of the butane was examined by extrapolating curves of selectivities against conversion rates to zero conversion. The data are plotted as

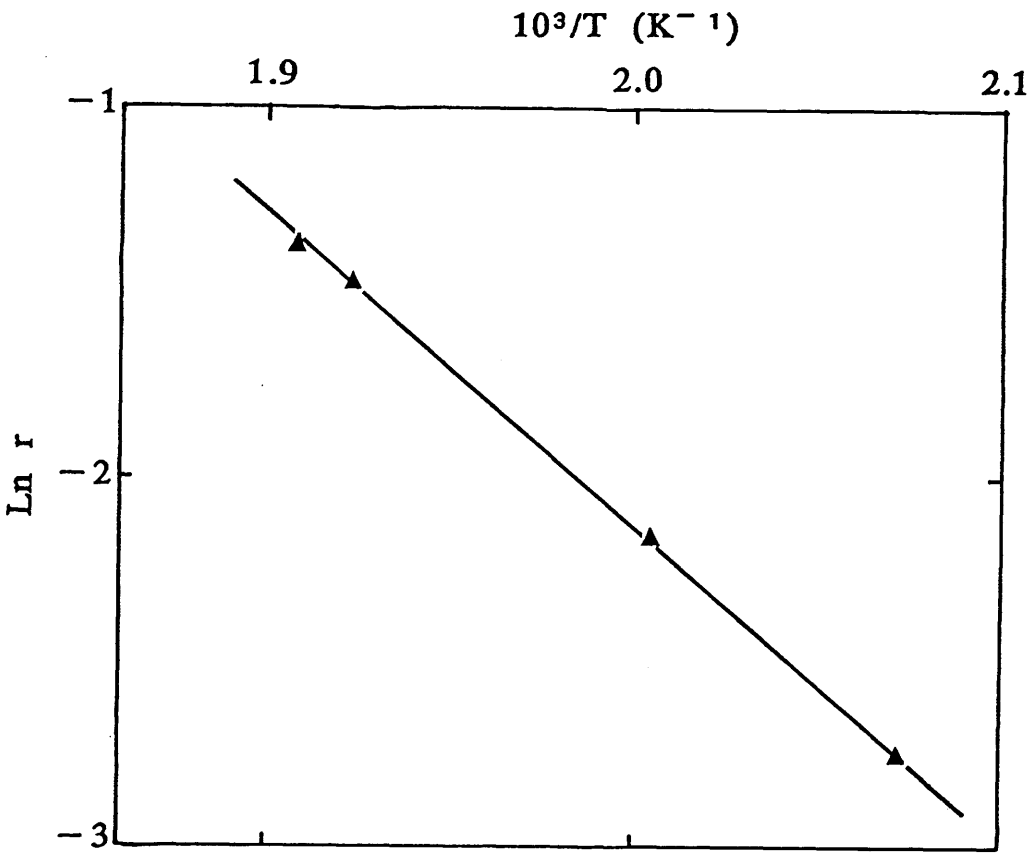

Fig. 3.47: Curve giving the activation energy for butane hydrogenolysis on vanadium pentoxide— supported rhodium catalyst

a function of temperature in Fig. 3.48.

The selectivities for all compounds obtained by hydrogenolysis of butane were strongly dependent upon temperature. At lower temperatures, selectivities for propane and methane approached unity and that for ethane was very small. In this case one of the adsorbed iC_4 species must have ruptured, and the resultant fragments desorbed without further cracking. At higher temperatures there was an increase in the amount of ethane formed. At the same time, the amounts of methane and propane decreased.

This result shows that we are dealing with a single hydrogenolysis, because otherwise the amount of methane would have increased as the initially formed C_3 fragments would have cracked again before desorbing and forming, in this way, one molecule of ethane and two of methane. In addition, when the temperature increased the rupture of the central bond was favored. At high temperatures (above 240°C) the selectivities seem to level out.

3.3.4.b— Rhodium supported on alumina

i— Influence of the temperature

The rhodium supported on alumina catalyst was reduced in situ at 250°C overnight (16 hours approximately) before a mixture of hydrogen and butane (6:1) was passed over it. The curve obtained by modifying the temperature, between 169 and 203°C, in the hydrogenolysis of butane was in form of steps. The initial rates of conversion of butane were obtained by extrapolating the linear portions of each step to the time zero.

The variation of the conversion rate of butane with temperature is illustrated in Fig. 3.49 and the product distribution variation with temperature is listed in table 3.4.

It was found in this experiment that the ratio α was inferior to

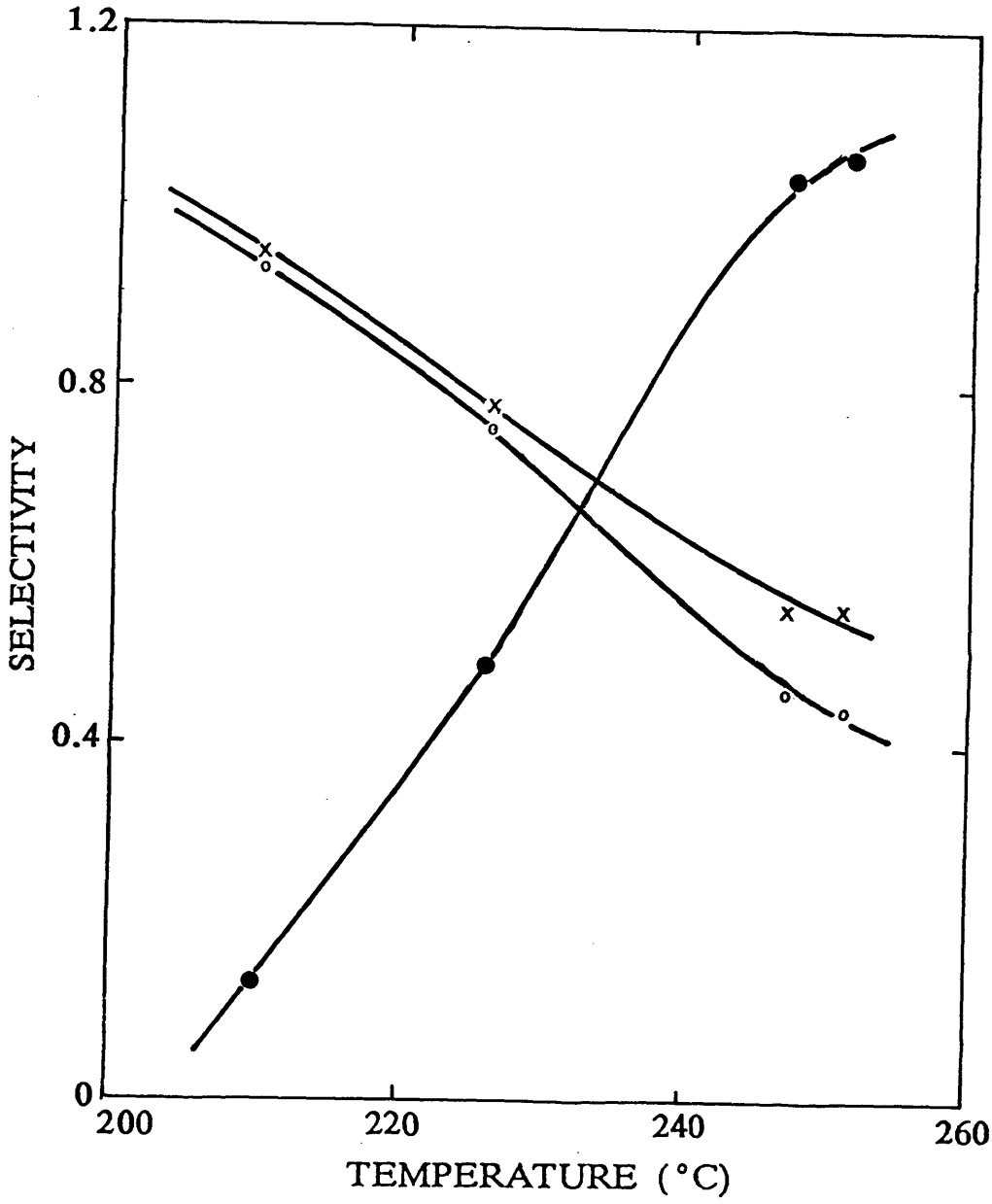

Fig. 3.48: Variation of selectivities for methane (x), ethane (●) and propane (o) with temperature.

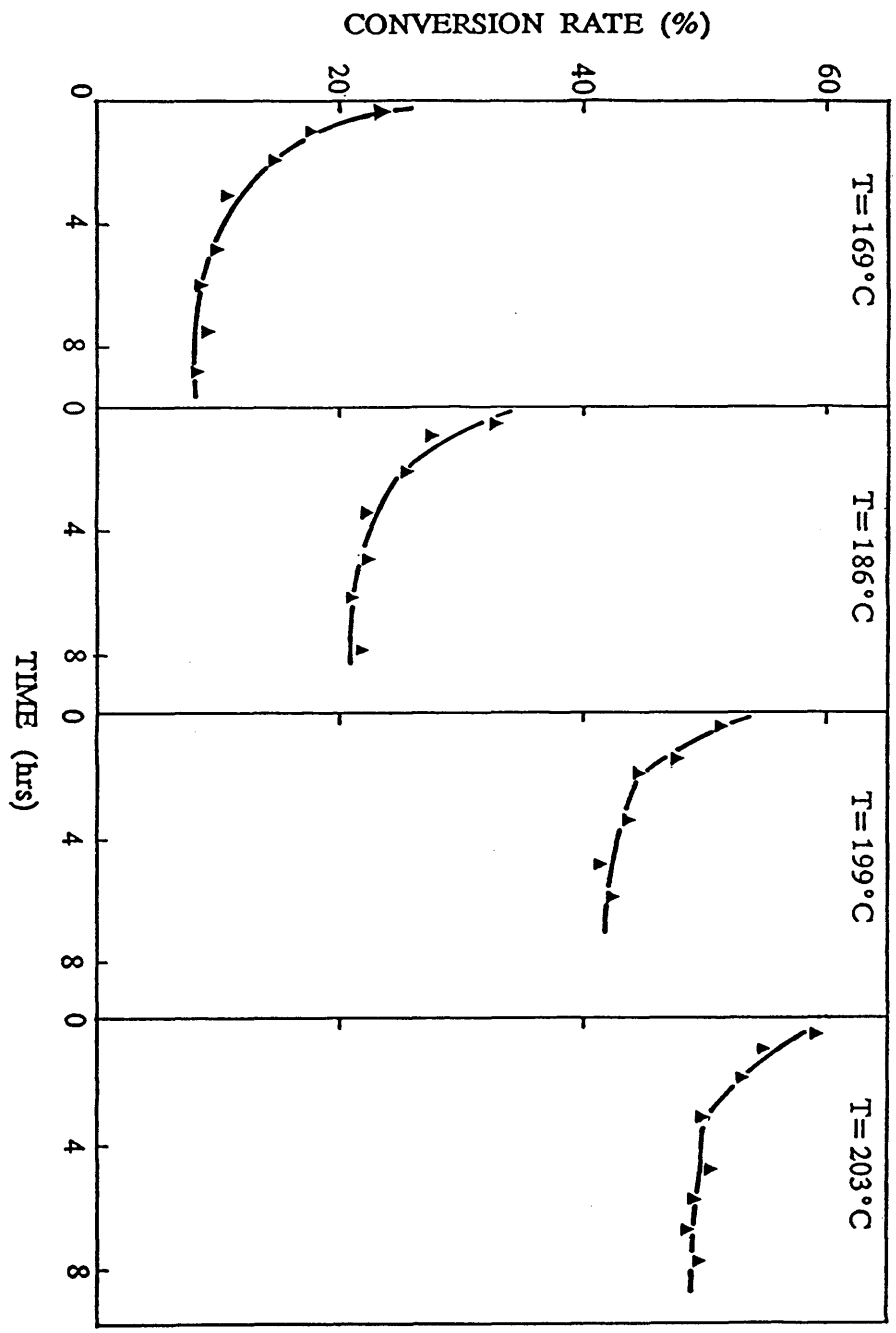

Fig. 3.49: Conversion rate variation with time at different temperatures.

Table 3.6: Distribution of the products obtained from butane hydrogenolysis on γ-alumina-supported rhodium catalyst at different temperatures.

T (°C)	τ	r	S_1	S_2	S_3	S_{ter}	S_{int}
169	0.093	0.055	0.630	0.754	0.621	0.63	0.37
186	0.212	0.125	0.448	1.163	0.409	0.43	0.57
199	0.423	0.249	0.294	1.592	0.174	0.23	0.77
203	0.487	0.287	0.263	1.693	0.117	0.19	0.81

τ: Initial conversion rate.
r: Reaction rate in mol/h.g of rhodium.
S_i (i=1 to 3): Selectivity for the reaction product C_i.
S_{int}: Selectivity for internal bond rupture in percent.
S_{ter}: Selectivity for terminal bond rupture in percent.

three. However, as shown in Fig. 3.50 its value approached three for low conversion rates (less than 25%). For higher conversion rates the value of α was far from the value three. This means that for low conversion rates only single hydrogenolysis occurred, unlike high values of conversion rate for which multiple hydrogenolysis seem to have taken place.

The product distribution corresponding to the cracking of the butane was examined by extrapolating curves of selectivities against conversion rates to zero conversion. The data are plotted as a function of conversion rate in Fig. 3.51.

The selectivities for all compound obtained by hydrogenolysis of butane were strongly dependent upon temperature. At low temperature (169°C), selectivities for methane, ethane and propane were comparable. When the temperature was raised, the amount of ethane formed increased and at the same time, the amounts of methane and propane decreased. Below 186°C, the rate of decrease of the selectivities for methane and ethane were the same. This shows that we are dealing with a single hydrogenolysis. Above that temperature, the rate of decrease in the selectivity for ethane was higher than that for methane, this is probably an indication for a multiple hydrogenolysis. The initially formed C_3 fragments might have cracked again before desorbing and forming, in this way, one molecule of ethane and two of methane.

The selectivities and rates for the rupture of the terminal and the central bonds are listed in table 3.4 following the method used by Leclercq (1976). This values indicate that at 169°C, more than 60% of the bonds ruptured were terminal. When the temperature was increased, the rupture of the central bond was favoured. At high temperature (203°C), 80% of the bonds ruptured in the butane hydrogenolysis reaction were central.

The activation energy for the hydrogenolysis of butane over the 1% rhodium supported on γ-alumina catalyst was determined from

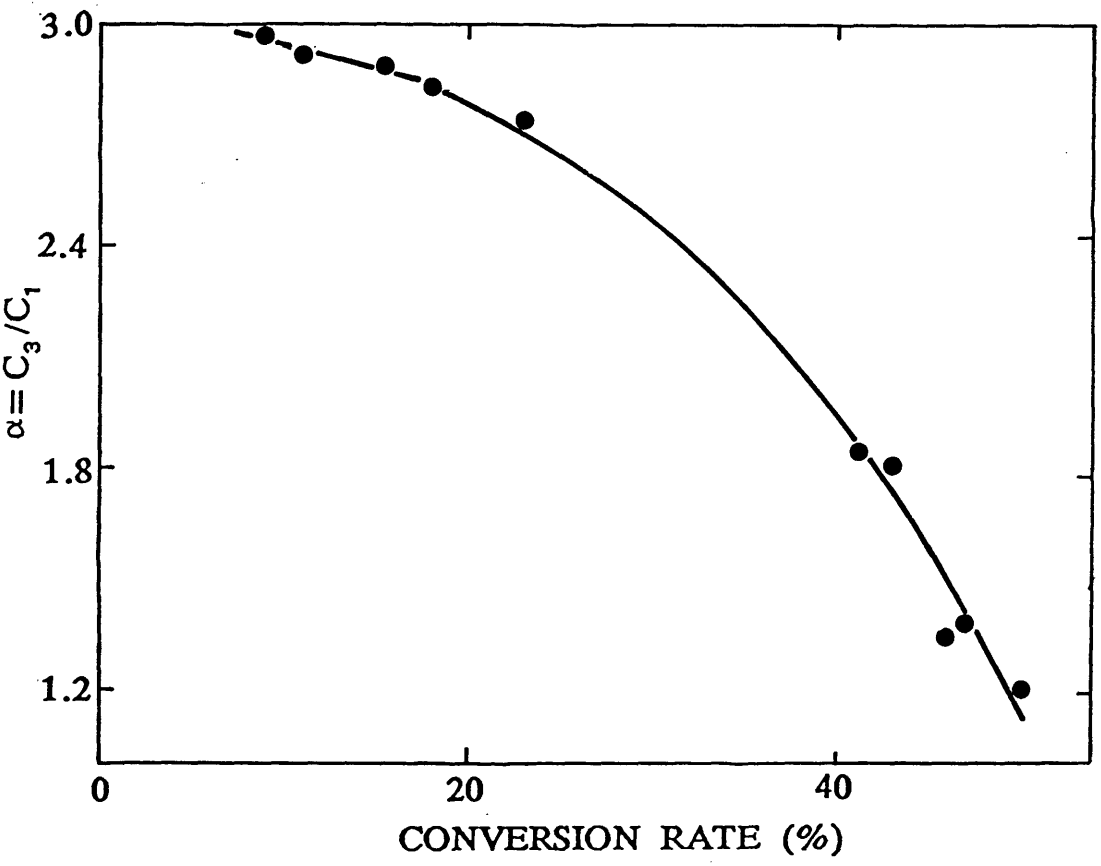

Fig. 3.50: Variation of $\alpha = C_3/C_1$ with the conversion rate.

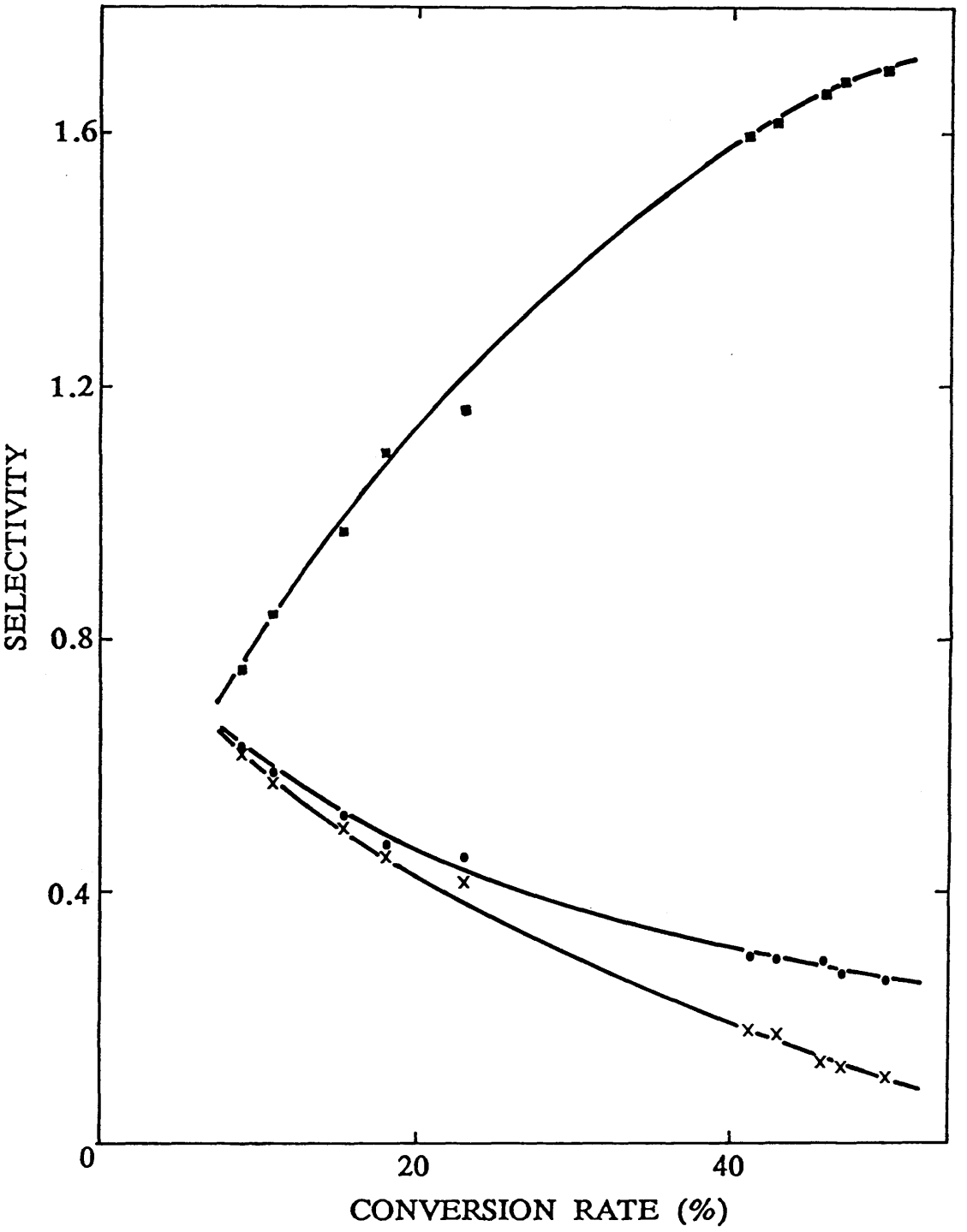

Fig. 3.51: Variation of selectivities for methane (•), ethane (■) and propane (x) with the conversion rate for γ– alumina– supported rhodium catalyst.

the trace in Fig. 3.52. Its value of 86.53kJ/mol was determined from the slope of the least square plot with a correlation coefficient of 0.9992.

3.3.4.c— Comparison between the two catalysts

Rhodium supported on both vanadium pentoxide and alumina proved to be an active catalyst in the hydrogenolysis of butane. However, it has been shown that it was more active when supported on alumina than on vanadium pentoxide. Rhodium supported on vanadium pentoxide gave the same activity than when supported on alumina but at temperatures approximately 40°C higher. This difference in activity might be explained by the fact that alumina exposed a much higher surface area ($140 m^2/g$) than vanadium pentoxide ($6 m^2/g$). This might have resulted in a better dispersion of rhodium crystallites at the surface of alumina.

Except at high conversion rates where the alumina—supported catalyst showed some multiple hydrogenolysis, only single hydrogenolysis occurred with both catalysts.

The variation of the selectivities for the terminal and central bonds with the conversion rate is shown diagrammatically in Fig. 3.53. This variation show the same trend for both catalysts: when the conversion rate increased the selectivity for the central bond increased on the expense of that for the terminal bond which decreased.

When rhodium was supported on vanadium pentoxide, only the terminal bond ruptured at low conversion rates (around 10%). When higher conversion rates were obtained the amount of terminal bonds ruptured decreased to constitute 50% at conversion rates around 40%.

With γ-alumina as support, at low conversion rate (10%) about 50% of the bonds ruptured were central. At higher conversion rates the breaking of the central bond was favored and constituted more than 80% at conversion rates of about 50%.

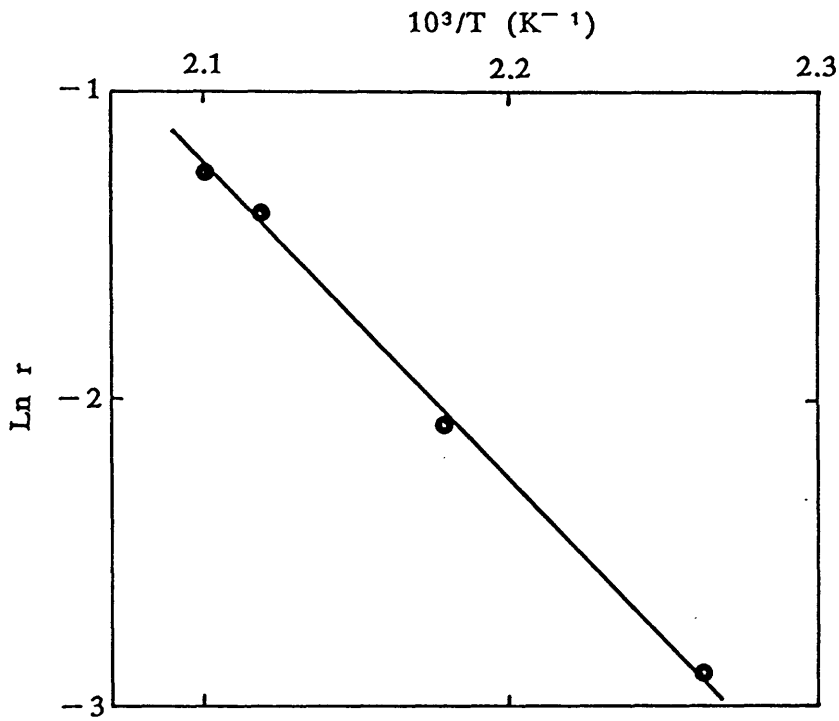

Fig. 3.52: Curve giving the activation energy for butane hydrogenolysis on γ- alumina- supported rhodium catalyst.

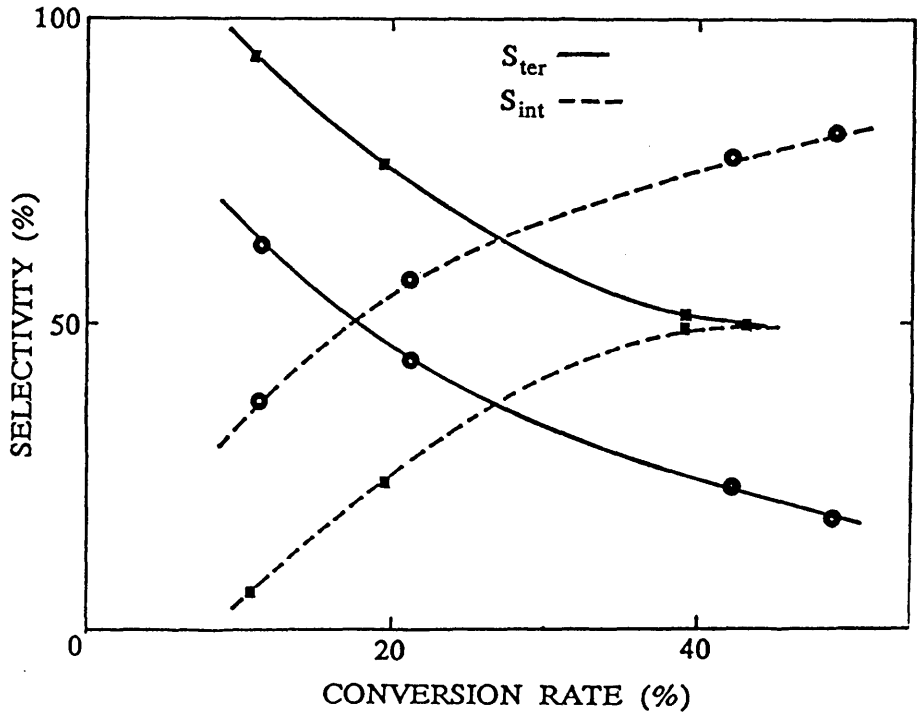

Fig. 3.53: Variation of selectivities for the rupture of terminal (S_{ter}) and internal (S_{int}) bonds in butane, for vanadium pentoxide- (■) and γ - alumina- (◉) supported rhodium catalyst with temperature.

CHAPTER FOUR

CONCLUSION

*** 4.1 ***

THERMAL DECOMPOSITION OF AMMONIUM METAVANADATE

The thermal decomposition of AMV is the method most used for the preparation of vanadium pentoxide. This decomposition is rather a complex process and its nature depends upon various factors. Furthermore, results obtained by various investigators are often contradictory.

The stoichiometry of the various stages involved in the thermal decomposition of AMV in air have been determined by thermal analyses and the parent AMV as well as products obtained at different temperatures have been characterised by their IR spectra, XRD data, and SEM and TEM examinations.

4.1.1– THERMAL ANALYSES

The production of vanadium pentoxide from AMV involves a series of chemical reactions. The decomposition commenced at 150°C with simultaneous loss of ammonia and water, in the ratio 2:1, through an endothermic process encompassing the first and second stages of the decomposition leading to ABV and AHV at 190 and 230°C, respectively.

The third and final stage of the decomposition involves an exothermic reaction and brings the weight loss to 22.1% leading to vanadium pentoxide. The exothermic process is probably a combination of two processes, the removal of ammonia and water (endothermic), and a more pronounced exothermic effect due either to crystal lattice rearrangement to form vanadium pentoxide or to the catalytic decomposition of ammonia on the surface of freshly formed

vanadium pentoxide.

4.1.2– STRUCTURAL CHANGES

Both XRD and IR as well as TEM showed that when AMV was heated up to 140°C, it retained its structure. Up to 230°C, the samples were identified as being AHV and finally pure vanadium pentoxide constituted the specimens heated at 320 and 400°C.

The structural changes involved in the decomposition of AMV are considerable. In AMV, as in potassium metavanadate, two of the four oxygen atoms tetrahedrally surrounding each vanadium atom are involved in linking the tetrahedra together, while the other two oxygen atoms are not shared.

AHV is isostructural with potassium hexavanadate and cesium hexavanadate whose structure has been shown to consist of layers of distorted VO_5 square pyramids linked together by sharing corners and edges, with the cations occupying positions between the layers, in irregular 12–fold coordination.

The structure of vanadium pentoxide is formed of square pyramids linked into layers through oxygen atoms. The next nearest oxygen neighbour is in the adjacent layer at a long distance forming a very weak bond and can be regarded as forming a very distorted octahedron. These VO_6 octahedra form a three–dimensional framework structure.

The structure is thus changing from a chain structure to a layered one through another layered structure.

The structural changes have shown up, to some extent at least, in the IR spectra at various stages of the decomposition. Notably, the ammonium ion bands persisted through the first and second stages of the decomposition, although their intensity decreased. However, they disappeared through the third stage showing the removal of the last traces of ammonium ion from a basically vanadium pentoxide

structure.

The ABV which has been seen as an intermediate from the thermal analyses results, has not been, however, detected as a stable intermediate, on cooling to room temperature, in the present XRD, IR and TEM studies. Efforts to prepare it at a lower temperature and shorter calcination times have failed and gave only AHV product.

HREM examination of the specimens provided structural details of the corresponding phases as characterised by XRD and IR at each temperature. All the samples were subject to electron beam radiation damage. AMV was less stable than both AHV and vanadium pentoxide therefore the minimum dose technique was used for its high resolution imaging. It was evident from single—crystal SAED patterns and HREM images that vanadium pentoxide crystals expose the (001) planes due to their lamellar structure.

The (001) planes are known to contain the vanadyl groups which play an important role as adsorption and reaction sites for many catalytic reactions such as oxidation and ammoxidation.

4.1.3— MORPHOLOGY OF THE CRYSTALS

SEM of the samples revealed morphological similarities between all these specimens. A wide range of well—formed crystals with smooth surfaces and sharp edges were observed. These morphological similarities suggest that no recrystallisation has occurred during the course of the thermal decomposition.

4.1.4— CONCLUSION

Overall, the studies show that the structure and the morphology of the parent material, decomposition intermediate and final product of the thermal decomposition of AMV are closely related. The

decomposition involves scission of the V—O bonds in the AMV structure accompanied by simultaneous evolution of gaseous ammonia and water with subsequent rearrangement by small atomic movements to form AHV. Further decomposition to vanadium pentoxide follows a similar process.

*** 4.2 ***

VANADIUM PENTOXIDE–SUPPORTED RHODIUM CATALYST

4.2.1— INTERNAL STRUCTURE OF VANADIUM PENTOXIDE

The internal structure of vanadium pentoxide crystals produced from the thermal decomposition of AMV in air was investigated by HREM in conjunction with SEM and gas adsorption studies. A comparison was made between two different ways of preparing specimens for HREM examination, namely, ultrasonic dispersion and thin sectioning.

Examination of intact crystals dispersed ultrasonically showed preferential exposure of the (001) planes which are of importance in catalysis. However, due to thickness differences and radiation damage, the HREM images can be misinterpreted and some features can be mistaken for pores in these crystals. After examination of thin sectioned crystals in the electron microscope, it is concluded that vanadium pentoxide is non—porous, in agreement with krypton gas adsorption and SEM studies. HREM images obtained from these crystals showed extensive crystalline regions in which the structural integrity remained intact.

The increased stability of thin sectioned material in the electron microscope, compared to ultrasonic dispersed crystals, might be due to increased thickness and/or encapsulation by embedding medium.

4.2.2— RHODIUM—CATALYSED REDUCTION OF VANADIUM PENTOXIDE

It is well established that certain metal oxides are reduced more

readily by hydrogen when precious metals are present, due to hydrogen spillover. The effect of reduction temperature on both a vanadium pentoxide—supported rhodium catalyst and the vanadium pentoxide support itself was investigated using XRD, IR, TPR, SEM and TEM.

According to the TPR curves obtained, the maximum reduction temperature of the catalyst was at 155°C. The uptake of hydrogen measured for the single peak present in the trace corresponds to the reduction of rhodium ions to the metallic state, as well as the partial reduction of vanadium pentoxide. As expected, this peak was absent from the TPR trace of pure vanadium pentoxide which showed that the reduction of vanadium pentoxide begins at ca. 450°C and that the uptake of hydrogen increases when the temperature is raised up to 700°C.

IR and XRD studies showed that the presence of rhodium caused a decrease in the temperature required for onset of reduction. Reduction of the metal—loaded catalyst showed that the support was first reduced largely to V_4O_9 at 250°C and then to vanadium dioxide (VO_2) and vanadium monoxide or vanadium sesquioxide at 450 and 600°C, respectively. In contrast, when vanadium pentoxide itself was treated up to 600°C, IR and XRD techniques indicated that no reduction had occurred within detectable limits.

SEM showed that the smooth surfaces of the fresh catalyst have been altered, due probably to oxygen evolution from the bulk of the support during reduction and crystalline rearrangements. HREM examination of the specimens provided structural details of the corresponding phases as characterised by IR and XRD. SAED was used to resolve the difference between vanadium monoxide and vanadium sesquioxide for the specimen reduced at 600°C. The reflections obtained in SAED were indexed in agreement with vanadium sesquioxide structure.

After reduction, rhodium particles were observed on the surface

of the support. It was obvious from particle size distribution histograms determined from TEM images that the thermal treatment of the supported–metal catalyst resulted in an increase of the metal particle size.

4.2.3– BUTANE HYDROGENOLYSIS

The action of the rhodium catalyst supported on vanadium pentoxide was studied in the hydrogenolysis of butane, a reaction for which rhodium metal is known to be among the most active catalysts, using a continuous flow fixed–bed apparatus at atmospheric pressure.

An alumina–supported rhodium catalyst was prepared and tested under the same conditions as the vanadium pentoxide–supported catalyst.

Metallic rhodium supported on both supports proved to be active in the hydrogenolysis of butane. However, the catalyst was more active when it was supported on γ-alumina than on vanadium pentoxide. This better activity might be attributed to a better distribution of rhodium particles at the surface of γ-alumina due to its higher surface area ($140 m^2/g$), compared to that of vanadium pentoxide ($6 m^2/g$).

Except at high conversion rates where the alumina–supported catalyst showed some multiple hydrogenolysis, only single hydrogenolysis, with better selectivity for central bond rupture, occurred with both catalysts.

REFERENCES

Titles are abbreviated based on a standard of the international Organisation for standardisation and the Chemical Abstract Service Source Index.

Abbe, E. (1873). *Arch. Mikrosk. Anat. Entwicklungsmech.*, 9, 413

Abello, L., Husson, E., Repelin, Y. & Lucazeau, G. (1983). *Spectrochim. Acta*, A39, 641

Acres, G.J.K., Bird, A.J., Jenkins, J.W. & King, F. (1981). *Catalysis 'Spec. Period. Rep.'* (Kemball, C. & Dowden, D.A., Eds), London: R. Soc. Chem., Vol. 4, p. 1

Aebi, F. (1948). *Helv. Chim. Acta*, 31, 8

Agar, A.W. (1960). *Br. J. Appl. Phys.*, 11, 185

Agar, A.W. (1965). in "*Techniques for electron microscopy*" (Kay, D.H., Ed.) 2nd Edn, Oxford: Blackwell, p. 1

Ahmed, H. (1971). *Electron Microsc. Anal.* (Nixon, W.C., Ed.), London: Inst. Phys., Conf. Ser. No. 10, p. 30

Allpress, J.G., Hewat, E.A., Moodie, A.F. & Sanders, J.V. (1972). *Acta Crystallogr.*, A28, 528

Anderson, J.R. (1973). *Adv. Catal.*, 23, 1

Anderson, J.R. (1975). *Structure of metallic catalysts*. London: Academic

Anderson, J.S. (1948). *Discuss. Faraday Soc.*, 4, 163

Anderson, J.S. (1974). In "*Defects and transport in oxides*" (Seltzer, M.S. & Jaffee, R.I., Eds), New York: Plenum, p. 30

Andersson, A. (1981). *J. Catal.*, 69, 465

Andersson, A. (1982a). *J. Catal.*, 76, 144

Andersson, A. (1982b). *J. Solid State Chem.*, 42, 263

Andersson, A. (1985). In "*Adsorption and catalysis on oxide surf—*

aces" (Che, M. & Bond, G.C., Eds), Amsterdam: Elsevier, p. 381

Andersson, A., Bovin, J—O. & Walter, P. (1986). *J. Catal.*, **98**, 204

Andersson, A. & Lundin, S.T. (1979). *J. Catal.*, **58**, 383

Andersson, A. & Lundin, S.T. (1980). *J. Catal.*, **65**, 9

Andersson, G. (1954). *Acta Chem. Scand.*, **8**, 1599

Andrews, K.W., Dyson, D.J. & Keown, S.R. (1971). *Interpretation of electron diffraction patterns*, London: Hilger & Watt.

Angell, C.L. & Schaffer, P.C. (1965). *J. Phys. Chem.*, **69**, 3463

Ardenne, M. von (1944). *Kolloid—Z.*, **108**, 195

Bachmann, H.G., Ahmed, F.R. & Barnes, W.H. (1961). *Z. Krist—allogr.*, **115**, 110

Bachmann, H.G. & Barnes, W.H. (1961). *Z. Kristallogr.*, **115**, 215

Bahl, M.K., Tsai, S.C. & Chung, Y.W. (1980). *Phys. Rev.*, **B21**, 1344

Baird, T. (1982). *Catalysis 'Spec. Period. Rep.'* (Bond, G.C & Webb, G., Eds), London: R. Soc. Chem., Vol. **5**, p. 172

Baird, T. (1984). *Electron Microsc. Anal., 1983* (Doig, P., Ed.), London: Inst. Phys., Conf. Ser. No. **68**, p. 239

Baker, R.T.K., Prestridge, E.B. & Garten R.L. (1979). *J. Catal.*, **56**, 390

Banus, M.D. & Reed, T.B. (1970). In "*Chemistry of extended defects in non—metallic solids*" (Eyring, L. & O'Keeffe, M., Eds), Amsterdam: North— Holland, p. 488

BASF: Badische Anilin und Sodafabrik A.G. (1968), *Fr. Demande*, 541,62

Batley, G.E., Ekstrom, A. & Johnson, D.A. (1974). *J. Catal.*, **34**, 368

Batson, P.E., Chen, C.H. & Silcox, J. (1976). *Proc. 34th Annu. Meet. Electron Microsc. Soc. Am.* (Bailey, G.W., Ed.). Baton Rouge: Claitor, p. 534

Beeston, B.E.P. (1972). in "*Practical methods in electron microscopy*" (Glauert, A.M., Ed.), Amsterdam: North–Holland, Vol. 1, p. 192

Belomestnykh, I.P., Bogdanova, O.K. & Shakhnovich, G.V. (1976). *U.S.S.R. Pat. Doc.*, 522,851

Beltran, J. & Guillem, C. (1957). *An. R. Soc. Esp. Fis. Quim.*, B53, 223 and 735

Benesi, H.A. (1967). *J. Catal.*, 8, 368

Beorchia, A. & Bonhomme, P. (1974). *Optik (Stuttgart)*, 39, 437

Bernard, J.R., Turlier, P. & Bousquet, J. (1977). *Ger. Offen*, 2,628,958

Berzelius, J.J. (1832). *Philos. Mag. [2]*, 11, 7

Bhaskarannair, C.S., Ghosh, A.K., Basu, A.N. & Lahiri, A. (1974). *Indian Pat.*, 131,076

Bhatnagar, I.K., Chakrabarty, D.K. & Biswas, A.B. (1972). *Indian J. Chem.*, 10, 1025

Bhattacharyya, S.K. & Mahanti, P. (1971). *J. Catal.*, 20, 10

Bielanski, A. & Inglot, A. (1974). *Bull. Acad. Pol. Sci., Ser. Sci. Chim.*, 22, 773 and 785

Bielanski, A. & Inglot, A. (1977). *React. Kinet. Catal. Lett.*, 6, 63

Blejean, C., Boutry, C. & Montarnal, R. (1970). *C.R. Acad. Sci. Paris*, C270, 257

Block, S. (1960). *Nature (London)*, 186, 540

Bolton, A.P. & Lanewala, M.A. (1970). *J. Catal.*, 18, 154

Bond, G.C. (1975). In "*The physical basis of heterogeneous catalysis*" (Drauglis, E. & Jaffee, R.I., Eds), New York: Plenum, p. 53

Bond, G.C. (1982). In "*Metal support and metal additive effects in catalysis*" (Imelik, B., Naccache, C., Condurier, G., Praliaud, H., Meriaudeau, P., Gallezot, P., Martin, G.A. & Vedrine, G.C., Eds). Amsterdam: Elsevier, p. 1

Bond, G.C. & Burch, R. (1983). *Catalysis 'Spec. Period. Rep.'*

(Bond, G.C & Webb, G., Eds), London: R. Soc. Chem., Vol. 6, p. 27

Bond, G.C. & Konig, P. (1982). *J. Catal.*, **77**, 309

Bond, G.C., Rajaram, R.R. & Burch, R. (1986). *J. Phys. Chem.*, **90**, 4877

Bond, G.C., Sermon, P.A. & Tripathi, J.B.P. (1973). *Ind. Chim. Belg.*, **38**, 506

Bond, G.C. & Tripathi, J.B.P. (1976). *J. Chem. Soc., Faraday Trans. 1*, **72**, 933

Bond, G.C. & Yide, X. (1984). *J. Chem. Soc., Faraday Trans. 1*, **80**, 969 and 3103

Borries, B. von & Ruska, E. (1939). *Z. Wiss. Mikrosk. Mikrosk. Tech.*, **56**, 314

Bosch, H., Kip, B.J., Ommen, J.G. van & Gellings, P.J. (1984). *J. Chem. Soc., Faraday Trans. 1*, **80**, 2479

Botto, I.L., Baran, E.J. & Aymonino, P.J. (1976). *Monatsh. Chem.*, **107**, 1127

Boudart, M. (1969). *Adv. Catal.*, **20**, 153

Boudart, M. & Ptak, L.D. (1970). *J. Catal.*, **16**, 90

Boumarafi, B. (1986). *M.Sc. Thesis*, Glasgow Univ.

Bovin, J—O., Wallenberg, L.R. & Smith, D.J. (1985). *Electron Microsc. Anal.* (Tatlock, G.J., Ed.), London: Inst. Phys., Conf. Ser. No. **78**, p. 481

Bradley, D.E. (1954). *Br. J. Appl. Phys.*, **5**, 65

Broglie, L. de (1924). *Philos. Mag.*, **47**, 446

Brown, L.M., Ed. (1987). *Electron Microsc. Anal.*, London: Inst. Phys., Conf. Ser. No. **90**, Chapt. 7

Brown, M.E, Dollimore, D. & Galwey, A.K. (1980). *Compr. Chem. Kinet.* (Bamford, C.H. & Tipper, C.F.H., Eds.), Amsterdam: Elsevier, Vol. 22, p. 1

Brown, M.E., Glasser, L. & Stewart, B.V. (1973). *Prog. Vac.*

Microbalance Tech. (Bevan, S.C., Gregg, S.G. & Parkyns, N.D., Eds.), London: Heyden, Vol. 2, p. 125

Brown, M.E., Glasser, L. & Stewart, B.V. (1974). *J. Therm. Anal.*, 6, 529

Brown, M.E., Glasser, L. & Stewart, B.V. (1975). *J. Therm. Anal.*, 7, 125

Brown, M.E. & Stewart, B.V. (1970). *J. Therm. Anal.*, 2, 287

Bursill, L.A., Lin, P.J., Smith, D.J. & Grey, I.E. (1985). *Electron Microsc. Anal.* (Tatlock, G.J., Ed.), London: Inst. Phys., Conf. Ser. No. 78, p. 463

Burton, E.F., Hillier, J. & Prebus, A. (1939). *Phys. Rev.*, 56, 1171

Burton, E.F., Sennett, R.S. & Ellis, S.G. (1947). *Nature (London)*, 160, 565

Burton, J.J. & Garten, R.L. (1977). In *"Advanced materials in catalysis"* (Burton, J.J. & Garten, R.L., Eds.), London: Academic, p. 1

Busch, H. (1926). *Ann. Phys. (Leipzig)*, 81, 974

Busch, H. (1927). *Arch. Elektrotech. (Berlin)*, 18, 583

Buseck, P.R., Ed. (1985). *High-resolution electron microscopy, Proc. Arizona State Univ. Centen. Symp. High-Resolut. Electron Microsc., Ultramicroscopy*, 18(1-4).

Bystrom, A., Wilhelmi, K.A. & Brotzen, O. (1950). *Acta Chem. Scand.*, 4, 1119

Calvo, C. (1954). *Ph.D. Thesis*, Rutgers Univ.

Carter, J.L., Cusumano, J.A. & Sinfelt, J.H. (1971). *J. Catal.*, 20, 223

Chen, B-H. & White, J.M. (1982). *J. Phys. Chem.*, 86, 3534

Chien, S-H., Shelimov, B.N., Resasco, D.E., Lee, E.H. & Haller, G.L. (1982). *J. Catal.*, 77, 301

Christmann, H.F. & Teel, P.H. (1974). *U.S. Pat.*, 3,843,745

Cimino, A., Boudart, M. & Taylor, H.S. (1954). *J. Phys. Chem.*,

58, 786

Clauws, P. (1980). *Verh. K. Acad. Wet. Lett. Schone Kunsten Belg., Kl. Wet.*, 42, 159

Clauws, P., Broeckx, J. & Vennik, J. (1985). *Phys. Status Solidi*, B131, 459

Clauws, P. & Vennik, J. (1976). *Phys. Status Solidi*, B76, 707

Conferences: *Int. Congr.*, 4— yearly, latest 11th, Kyoto 1986; *Eur. Congr.*, 4— yearly in between, latest 9th, York, 1988; *Annu. and Bienn. Natl. Meet.*, e.g. EMSA (USA), EMAG (UK) etc...

Cosslett, V.E. (1951). *Practical electron microscopy*, London: Butterworth

Cosslett, V.E. (1967). *J. Electron Microsc.*, 16, 51

Cosslett, V.E. (1981). *Contemp. Phys.*, 22, 3 and 147

Cosslett, V.E. (1987). *Adv. Opt. Electron Microsc.* (Barer, R. & Cosslett, V.E., Eds), London: Academic, Vol. 10, p. 215

Cosslett, V.E., Camps, R.A., Saxton, W.O., Smith, D.J., Nixon, W.C., Ahmed, H., Catto, C.J.D., Cleaver, J.R.A., Smith, K.C.A., Timbs, A.E., Turner, P.W. & Ross, P.M. (1979). *Nature (London)*, 281, 49

Cowley, J.M. (1975). *Diffraction physics*, Amsterdam: North—Holland

Cowley, J.M. (1979). in "*Introduction to analytical electron microscopy*" (Hren, J.J., Goldstein, J.I. & Joy, D.C., Eds), New York: Plenum, p. 1

Cowley, J.M. & Moodie, A.F. (1957). *Acta Crystallogr.*, 10, 609

Crewe, A.V., Eggenberger, D.N., Wall, J. & Welter, L.M. (1968). *Rev. Sci. Instrum.*, 39, 576

Crewe, A.V., Langmore, J.P. & Isaacson, M.S. (1975). In "*Physical aspects of electron microscopy and microbeam analysis*" (Siegel, B.M. & Beaman, D.R., Eds), New York: Wiley, p. 47

Csencsits, R. & Gronsky, R. (1987). *Ultramicroscopy*, 23, 421

Dadyburjor, D.B., Jewur, S.S. & Ruckenstein, E. (1979). *Catal.*

Rev.— Sci. Eng., 19, 293

Dahmen, U., Kim, M.G., & Searcy, A.W. (1987). *Ultramicroscopy*, 23, 365

D'Alessandro, A.F. & Farkas, A. (1956). *J. Colloid. Sci.*, 11, 653

Dalmon, J.A. & Martin, G.A. (1980). *J. Catal.*, 66, 214

Davisson, C. & Germer, L.H. (1927). *Phys. Rev.*, 30, 705

DeCanio, S.J., Apple, T.M. & Dybowski, C.R. (1983). *J. Phys. Chem.*, 87, 194

Delannay, F., Ed. (1984). *Characterisation of heterogeneous catalysts,* New York: Dekker

Deschanvres, A. & Nouet, G. (1967). *C.R. Acad. Sci. Paris*, C264, 2041

Deschanvres, A., Nouet, G. & Raveau, B. (1965). *C.R. Acad. Sci. Paris*, C261, 3144

Dowden, D.A. (1978). *Catalysis 'Spec. Period. Rep.'* (Kemball, C. & Dowden, D.A., Eds.), London: R. Soc. Chem., Vol. 2, p. 1

Dowie, R.S., Whan, D.A. & Kemball, C. (1972). *J. Chem. Soc., Faraday Trans. 1*, 68, 2150

Dubois, P. & Breton, P. (1938). *C.R. Acad. Sci. Paris*, 206, 1969

Duval, C. (1953). *Inorganic thermogravimetric analysis*, Amsterdam: Elsevier, p. 170

Duval, C. & Morette, A. (1950). *Anal. Chim. Acta*, 4, 490

Edington, J.W. (1974). *The operation and calibration of the electron microscope*, London: MacMillan

Edington, J.W. (1975). *Electron diffraction in the electron microscope*, London: MacMillan

Eisenhandler, C.B. & Siegel, B.M. (1966). *J. Appl. Phys.*, 37, 1613

Ellestad, O.H. & Naccache, C. (1981). In "*Prespectives in catalysis*" (Larssson, R., Ed.), Lund: C.W.K. Gleerup, p. 95

English, C.A. & Venables, J.A. (1971). *Electron Microsc. Anal.*

(Nixon, W.C., Ed.), London: Inst. Phys., Conf. Ser. No. 10, p. 40

English, C.A. & Venables, J.A. (1972). *Electron microsc., Proc. 5th Eur. Congr.* (W.C. Nixon, Ed.), London: Inst. Phys., Conf. Ser. No. 14, p. 172

Enjalbert, R. & Galy, J. (1986). *Acta Crystallogr.*, C42, 1467

Ennos, A.E. (1953). *Br. J. Appl. Phys.*, 4, 101

Erdey, L., Gal, S. & Liptay, G. (1964). *Talanta*, 11, 913

Erickson, H.P. (1973). *Adv. Opt. Electron Microsc.* (Barer, R. & Cosslett, V.E., Eds), London: Academic, Vol. 5, p. 163

Essen, C.G. van (1979). in "*Electron microscopy and microanalysis of crystalline materials*" (Belk, J.A., Ed.), London: Appl. Sci., p. 99

Evans Jr., H.T. (1960). *Z. Kristallogr.*, 114, 257

Evans Jr., H.T. & Block, S. (1966). *Inorg. Chem.*, 5, 1808

Evans Jr., H.T. & Mrose, M.E. (1955). *Am. Mineral.*, 40, 861

Evans Jr., H.T. & Mrose, M.E. (1958). *Acta Crystallogr.*, 11, 56

Everhart, T.E. (1960). *J. Appl. Phys.*, 31, 1483

Everhart, T.E. & Hayes, T.L. (1972). *Sci. Am.*, 226, 55

Evnin, A.B., Rabo, J.A. & Kasai, P.H. (1973). *J. Catal.*, 30, 109

Fabbri, G. & Baraldi, P. (1972). *Anal. Chem.*, 44, 1325

Fedorov, P.I., Akulkina, L.M. & Razgon, E.S. (1967). *Russ. J. Inorg. Chem.*, 12, 98

Fejes, P.L. (1977). *Acta Crystallogr.*, A33, 109

Flynn, P.C, Wanke, S.E. & Turner, P.S. (1974). *J. Catal.*, 33, 233

Foger, K. (1984). In "*Catalysis — Science and technology*" (Anderson, J.R. & Boudart, M., Eds), Berlin: Springer—Verlag, Vol. 6, p. 227

Foger, K. & Anderson, J.R. (1979). *J. Catal.*, 59, 325

Forni, L. & Giraldi, G. (1976). *J. Catal.*, **41**, 338

Frank, J. (1973). *Optik (Stuttgart)*, **38**, 519

Frederickson Jr., L.D. & Hausen, D.M. (1963). *Anal. Chem.*, **35**, 818

Freeman, L.A., Howie, A. & Treacy, M.M.J. (1977). *J. Microsc. (Oxford)*, **111**, 165

Fryer, J.R. (1978). *Acta Crystallogr.*, A34, 603

Fryer, J.R. (1979). *The chemical applications of transmission electron microscopy*, London: Academic

Fryer, J.R. (1983). *Mol. Cryst. Liq. Cryst.*, **96**, 275

Fryer, J.R., Cleaver, J.R.A. & Smith, D.J. (1980). *Electron Microsc. Anal.* (Mulvey, T., Ed.), London: Inst. Phys., Conf. Ser. No. **52**, p. 287

Fryer, J.R. & Holland, F. (1984). *Proc. R. Soc. London,* A393, 353

Fryer, J.R. & Smith, D.J. (1984). *J. Microsc. (Oxford)*, **141**, 3

Fuentes, S. & Figueras, F. (1980). *J. Catal.*, **61**, 443

Fujiyoshi, Y., Kobayashi, T., Ishizuka, K., Uyeda, N., Ishida, Y. & Harada, Y. (1980). *Ultramicroscopy*, **5**, 459

Fung, S.C. (1982). *J. Catal.*, **76**, 225

Galbraith, S.T., Baird, T. & Fryer, J.R. (1979). *Acta Crystallogr.*, **A35**, 197

Gallezot, P. (1979). *Catal. Rev.—Sci. Eng.*, **20**, 121

Galwey, A.K. (1975). *Int. Rev. Sci.: Inorg. Chem., Ser. 2* (Roberts, L.E.J., Ed.), London: Butterworth, Vol. **10**, p. 147

Gasior, M., Grzybowska, B., Haber, J., Machej, T. & Ziolkowski, J. (1979). *J. Catal.*, **58**, 15

Gasior, M. & Machej, T. (1983). *J. Catal.*, **83**, 472

Geiss, R.H. (1979). in "*Introduction to analytical electron microscopy*" (Hren, J.J., Goldstein, J.I. & Joy, D.C., Eds), New York: Plenum, p. 43

Gellings, P.J. (1985). *Catalysis 'Spec. Period. Rep.'* (Bond, G.C & Webb, G., Eds), London: R. Soc. Chem., Vol. 7, p. 105

Gerland, B.W. (1877). *Chem. News*, 36, 29 and 271

Germain, J.– E. & Perez, R. (1972). *Bull. Soc. Chim. Fr.*, 2042

Gevers, R. (1978). in "*Diffraction and imaging techniques in material science*" (Amelincks, S., Gevers, R. & Landuyt, J. van, Eds), Amsterdam: North– Holland, Vol. 1, p. 9

Giancard, B., Guido, P., Girodano, D.A. & Romano, C. (1976). *U.S. Pat.*, 3,981,912

Gillis, E. (1964). *C.R. Acad. Sci. Paris*, 258, 4765

Gilson, T.R., Bizri, O.F. & Cheetham, N. (1973). *J. Chem. Soc. Dalton Trans.*, 291

Gjonnes, J. (1976). In "*Developments in electron microscopy and analysis*" (Venables, J.A., Ed.), London: Academic, p. 369

Gleaser, R.M. (1975). in "*Physical aspects of electron microscopy and microbeam analysis*" (Siegel, B.M. & Beeman, D.R., Ed.), New York: Wiley, p. 205

Goodman, P., Ed. (1981). *Fifty Years of Electron Diffraction*, Dordrecht: Reidel

Goodman, P. & Moodie, A.F. (1974). *Acta Crystallogr.*, A30, 280

Goodenough, J.B. (1971). *Prog. Solid State Chem.* (Reiss, H., Ed.), Oxford: Pergamon, Vol. 5, p. 145

Grabowski, R., Grzybowska, B., Haber, J. & Sloczynski, J. (1975). *React. Kinet. Catal. Lett.*, 2, 81

Grivet, P. (1972). *Electron Optics*, 2nd Edn., Oxford: Pergamon

Grymonprez, G., Fiermans, L. & Vennik, J. (1977). *Acta Cryst– allogr.*, A33, 834

Guczi, L., Matusek, K., Sarkany, A. & Tetenyi, P. (1979). *Bull. Soc. Chim. Belg.*, 88, 497

Haine, M.E. & Cosslett, V.E. (1961). *The electron microscope*, London: Spon

Haine, M.E. & Mulvey, T. (1954). *J. Sci. Instrum.*, **31**, 326

Hakomori, S. (1929). *J. Chem. Soc. Jpn.*, **50**, 231

Hall, C.E. (1966). *Introduction to Electron Microscopy*, 2nd Edn, New York: McGraw–Hill

Hall, C.E. & Hines, R.L. (1970). *Philos. Mag.*, **21**, 1175

Hanic, F. (1958). *Chem. Svesti*, **12**, 579

Hanszen, K.J. (1971). *Adv. Opt. Electron Microsc.* (Barer, R. & Cosslett, V.E., Eds), London: Academic, Vol. **4**, p. 1

Harada, Y. & Watanabe, E. (1978). *JEOL News*, **16E**, 5

Hart, R.G. & Yoshiyama, J.M. (1975). *J. Ultrastruct. Res.*, **51**, 40

Hartman, R.S., Hartman, R.E, Alsberg, H. & Nathan, R. (1974). *Electron microsc., Proc. 26th Int. Congr.* (Sanders, J.V. & Goodchild, D.J., Eds), Canberra: Aust. Acad. Sci., Vol. **2**, p. 674

Hawkes, P.A. (1972). *Electron Optics and Electron Microscopy*, London: Taylor & Francis

Hawkes, P.A. (1980). *Adv. Electron. Electron Phys., Suppl. 13A: Applied Charged Particle Optics* (Septier, A., Ed.), New York: Academic, p. 45

Hawkes, P.A., Ed. (1985). *The beginnings of electron microscopy*, New York: Academic

Heidenreich, R.D. (1964). *Fundamentals of transmission electron microscopy*, New York: Wiley–Interscience

Heinrich, K.F.J. (1975). *Adv. Opt. Electron Microsc.* (Barer, R. & Cosslett, V.E., Eds), London: Academic, Vol. **6**, p. 275

Hermann, J.M., Disdier, J. & Pichat, P. (1982). In "*Metal support and metal additive effects in catalysis*" (Imelik, B., Naccache, C., Condurier, G., Praliaud, H., Meriaudeau, P., Gallezot, P., Martin, G.A. & Vedrine, G.C., Eds). Amsterdam: Elsevier, p. 27

Hillier, J. (1946). *J. Appl. Phys.*, **17**, 411

Hillier, J. (1948). *J. Appl. Phys.*, **19**, 226

Hillier, J. & Ramberg, E.G. (1947). *J. Appl. Phys.*, **18**, 48

Hillier, J. & Vance, A.W. (1941). *Proc. Inst. Radio Eng., Aust.*, **29**, 167

Hillier, J. & Vance, A.W. (1945). *Electron optics and the electron microscope*, New York: Wiley

Hines, R.L. (1984). *Adv. Opt. Electron Microsc.* (Barer, R. & Cosslett, V.E., Eds), London: Academic, Vol. 9, p. 180

Hirsch, P.B., Howie, A., Nicholson, R.B., Pashley, D.W. & Whelan, M.J. (1965). in "*Electron microscopy of thin crystals*", London: Butterworth

Hoare, M.R. & Pal, P. (1971). *Adv. Phys.*, 20, 161

Hobbs, L.W. (1979). in "*Introduction to analytical electron microscopy*" (Hren, J.J., Goldstein, J.I. & Joy, D.C., Eds), New York: Plenum, p. 437

Hobbs, L.W. (1984). in "*Quantitative electron microscopy*" (Chapman, J.N. & Craven, A.J., Eds), Edinburgh: Scott. Univ. Summer School Phys., p. 399

Hobbs, L.W. (1987). *Ultramicroscopy*, **23**, 339

Holland, F. (1984). *Ph.D. Thesis*, Glasgow Univ.

Holland, F., Fryer, J.R. & Baird, T. (1983). *Electron Microsc. Anal.* (Doig, P., Ed.), London: Inst. Phys., Conf. Ser. No. **68**, p. 19

Horiuchi, S., Saeki, M., Matsui, Y. & Nagata, F. (1975). *Acta Crystallogr.*, A31, 660

Horne, R.W. & Markham, R. (1973). in "*Practical methods in electron microscopy*" (Glauert, A.M., Ed.), Amsterdam: North–Holland, Vol. 1, p. 325

Howie, A. (1980). In "*Characterisation of catalysts*" (Thomas, J.M. & Lambert, R.M., Eds). Chichester: Wiley, p.89

Humphreys, C.J. (1979). *Rep. Prog. Phys., London: Inst. Phys.*, Vol. 42, p. 1825

Hutchison, J.L. (1978). *Chem. Scr.*, 14, 181

Hutchison, J.L. (1982). *Ultramicroscopy*, 9, 191

Hutchison, J.L. & Briscoe, N.A. (1985). *Ultramicroscopy*, 18, 435

Iijima, S. (1977). *Optik (Stuttgart)*, 48, 193

Iijima, S. (1986). *Electron Microsc., Proc. 11th Int. Congr.* (Imura, T., Maruse, S. & Suzuki, T., Eds), Tokyo: Jpn. Soc. Electron Microsc., Vol. 2, p. 1437

Il'Chenko, N.I. (1972). *Russ. Chem. Rev.*, 41, 47

Il'Chenko, N.I., Pyatnitskii, Yu.I., Golodets, G.I. & Roiter, V.A. (1970). *Katal. Katal.*, 6, 31; *C.A.*, 74: 130838t

Il'Chenko, N.I. & Yuza, V.A. (1966). *Katal. Katal.*, 2, 118; *C.A.*, 66: 59222q

Imelik, B., Naccache, C., Condurier, G., Praliaud, H., Meriaudeau, P., Gallezot, P., Martin, G.A. & Vedrine, G.C., Eds (1982). *Metal support and metal additive effects in catalysis*, Amsterdam: Elsevier

Jones, W. (1975). *Surf. Defect. Prop. Solids 'Spec. Period. Rep.'* (Roberts, M.W. & Thomas, T.M., Eds.), London: R. Soc. Chem., Vol. 5, p. 65

Kang, Z.C., Eyring, L. & Smith, D.J. (1987). *Ultramicroscopy*, 22, 71

Kao, C.C., Tsai, S.C., Bahl, M.K., Chung, Y.W. & Lo, W.J. (1980). *Surf. Sci.*, 95, 1

Kato, H., Hosimiya, H. & Nakazima, S. (1939). *J. Chem. Soc. Jpn.*, 60, 1115

Kelmers, A.D. (1961a). *J. Inorg. Nucl. Chem.*, 17, 168

Kelmers, A.D. (1961b). *J. Inorg. Nucl. Chem.*, 21, 45

Kempling, J.C. & Anderson, R.B. (1970). *Ind. Eng. Chem. Process Des. Develop.*, 9, 116

Kempling, J.C. & Anderson, R.B. (1972). *Ind. Eng. Chem. Process Des. Develop.*, 11, 146

Kenney, C.N. (1980). *Catalysis 'Spec. Period. Rep.'* (Kemball, C. & Dowden, D.A., Eds), London: R. Soc. Chem., Vol. 3, p. 123

Keown, S.R. (1974). in "*Modern physical techniques in materials*

techn ology" (Mulvey, T. & Webster, R.K., Eds), London: Oxford Univ. Press, p. 94

Kera, Y. & Hirota, K. (1969). *J. Phys. Chem.*, **73**, 3973

Kera, Y., Tertani, S. & Hirota, K. (1967). *Bull. Chem. Soc. Jpn.*, **40**, 2458

Kerr, G.T. (1969). *J. Catal.*, 15, 200

Kerr, R.O. (1966). *U.S. Pat.*, 3,255,212

Ketelaar, J.A.A. (1936). *Nature (London)*, **137**, 316

Khoobiar, S.J. (1964). *J. Phys. Chem.*, **68**, 411

Kikuchi, F. & Morita, Y. (1969). *J. Catal.*, **15**, 217

Kimizuka, N., Ishii, M., Kawada, I, Saeki, M. & Nakahira, M. (1974). *J. Solid State Chem.*, 9, 69

Knoll, M. & Ruska, E. (1932). *Ann. Phys. (Leipzig)*, **12**, 607

Kochloefl, K. & Bazant, V. (1968). *J. Catal.*, **10**, 140

Kofstad, P. (1972). *Nonstoichiometry, diffusion and electrical conductivity in binary oxides*, New York: Wiley, p. 175

Kosuge, K. (1967). *J. Phys. Chem. Solids*, **28**, 1613

Kuo, I.A.M. & Glaeser, R.M. (1975). *Ultramicroscopy*, **1**, 53

Kuzuya, M., Hibino, M. & Maruse, S. (1984). *Ultramicroscopy*, **15**, 233

Lachartre, M. (1924). *Bull. Soc. Chim. Fr.*, **35**, 321

Lamure, J. & Colin, G. (1964). *C.R. Acad. Sci. Paris*, **258**, 6433

Lazarev, A.N. (1972). *Vibrational spectra and structure of silicates*, New York: Consultant Bur.

Leclercq, L. (1976). *ès—Sci. Phys. Dr. Thesis*, Poitiers Univ.

Leclercq, G., Charcosset, H., Maurel, R., Betizeau, C., Bolivar, C., Frety, R., Jaunay, D., Mendez, H. & Tournayan, L. (1979). *Bull. Soc. Chim. Belg.*, 88, 577

Leclercq, G., Leclercq, L. & Maurel, R. (1979). *Bull. Soc. Chim. Belg.*, 88, 599

Leclercq, G., Romero, T., Pietrzyk, S., Grimblot, J. & Leclercq, L. (1984). *J. Mol. Catal.*, **25**, 67

Levanto, U. (1969). *Acta Polytech. Scand., Chem. Technol. Metall. Ser.*, 82, 8

Logan, S.K. & Kemball, C. (1960). *Trans. Faraday Soc.*, **56**, 144

Longo, J.M. & Kierkegaard, P. (1970). *Acta Chem. Scand.*, **24**, 420

Luft, N.W. (1955). *Ind. Chem.*, **31**, 502

Lukesh, J.S. (1950). *Acta Crystallogr.*, 3, 476

Lynch, D.F. & O'Keefe, M.A. (1972). *Acta Crystallogr.*, **A28**, 536

Machatschki, F. (1936). *Naturwissenschaften*, **24**, 742

Machiels, C.J. & Anderson, R.B. (1979). *J. Catal.*, **58**, 253, 260 and 268

McKinley, W.A. & Feshbach, H. (1948). *Phys. Rev.*, **74**, 1759

McMullan, D. (1953). *Proc. Inst. Elect. Engnrs. (London)*, **B100**, 245

Magnan, C., Ed. (1961). *Traité de microscopie electronique*, Paris: Hermann

Magneli, A. & Blomberg, B. (1951). *Acta Chem. Scand.*, **5**, 585

Makin, M.J. (1978). *Electron Microsc., Proc. 9th Int. Congr.* (Sturgess, J.M., Ed.), Toronto: Microsc. Soc. Can., Vol. 3, p. 330

Marks, L.D. & Howie, A. (1979). *Nature (London)*, **282**, 196

Marks, L.D. & Smith, D.J. (1983). *J. Microsc. (Oxford)*, **130**, 249

Martin, M., Schmidt, W. & Scharfe, G. (1976). *Ger. Offen*, 2,453,232

Matsuishi, N. (1967). *Jpn. J. Appl. Phys.*, **6**, 1060

Matsumoto, H., Saito, Y. & Yoneda, Y. (1970). *J. Catal.*, **19**, 101

Matsumoto, H., Saito, Y. & Yoneda, Y. (1971). *J. Catal.*, 22, 182

Mattes, R. (1971). *Z. Anorg. Allgem. Chem.*, 382, 163

Matyi, R.J., Schwartz, L.H. & Butt, J.B. (1987). *Catal. Rev.–Sci. Eng.*, 29, 41

Maurel, R. & Leclercq, G. (1971). *Bull. Soc. Chim. Fr.*, 1234

Menter, J.W. (1956). *Proc. R. Soc. London*, A236, 119

Meriaudeau, P., Ellestad, O.H., Dufaux, M. & Naccache, C. (1982). *J. Catal.*, 75, 243

Miller, F.A. & Wilkins, C.H. (1952). *Anal. Chem.*, 24, 1253

Millward, G.R. (1980). *J. Catal.*, 64, 381

Misell, D.L. (1973). *Adv. Electron. Electron Phys.* (Marton, L., Ed.), New York: Academic, Vol. 32, p. 63

Miyamoto, A., Hattori, A. & Murakami, Y. (1983). *J. Solid State Chem.*, 47, 373

Miyamoto, A., Yamazaki, Y., Inomata, M. & Murakami, Y. (1981). *J. Phys. Chem.*, 85, 2366

Moodie, A.F. & Warble, C.E. (1974). *Electron microsc., Proc. 8th Int. Congr.* (Sanders, J.V. & Goodchild, D.J., Eds), Canberra: Aust. Acad. Sci., Vol. 1, p. 230

Morette, A. (1958). in "*Nouveau traité de chimie minérale*" (Pascal, P., Ed.), Paris: Masson, Vol. 12, p. 49

Mori, K., Miyamoto, A. & Murakami, Y. (1985). *J. Phys. Chem.*, 89, 4265

Moss, R.L. (1981). *Catalysis 'Spec. Period. Rep.'* (Kemball, C. & Dowden, D.A., Eds.), London: R. Chem. Soc., Vol. 4, p. 31

Mukherjee, A. (1985). *J. Less–Common Metals*, 107, 89

Mulvey, T. (1967). *Proc. Roy. Microsc. Soc.*, 2, 201

Murakami, Y., Ando, H. & Niwa, M. (1981). *J. Catal.*, 67, 472

Murata, Y., Fryer, J.R. & Baird, T. (1976). *J. Microsc. (Oxford)*, 108, 261

Nakamura, M., Yamada, M. & Amano, A. (1975). *J. Catal.*, 39, 125

Natl. Bur. Stand. (U.S.). (1958). *Circ. 539*, 8, 66

Niwa, M. & Murakami, Y. (1982). *J. Catal.*, 76, 9

Norbald, J.A. (1875). *Bull. Soc. Chim. Fr. [2]*, 23, 64

Oatley, C.W. (1972). *The scanning electron microscope*, Cambridge: Cambridge Univ. Press

Oatley, C.W., Nixon, W.C. & Pease, R.F.W. (1965). *Adv. Electron. Electron Phys.* (Marton, L., Ed.), New York: Academic, Vol. 21, p. 181

Oikawa, et al (1970). *Ultramicroscopy*, 4, 181

Ono, I., Iikuni, T. & Mizoguchi, J. (1972). *Jpn. Kokai (Pat. Doc.)*, 72 14,204

Paal, Z. & Tetenyi, P. (1977). *Nature (London)*, 267, 234

Paal, Z. & Tetenyi, P. (1979). *React. Kinet. Catal. Lett.*, 12, 131

Park, H. (1972). *Bull. Chem. Soc. Jpn.*, 45, 2753

Patrina, I.B. & Ioffe, V.A. (1964). *Sov. Phys. Solid State*, 6, 2227

Pease, R.F.W. (1971). *Proc. 4th Annu. Scanning Electron Microsc. Symp.* (Johari, O. & Corvin, I., Eds), Chicago: I.I.T. Res. Inst., p. 11

Perelyaev, V.A., Miller, V.I., Perelyaeva, L.A., Grebenshchikova, N.E., Shveikin, G.P. & Chirkov, A.K. (1977). *Russ. J. Inorg. Chem.*, 22, 1267

Phillips, R. (1960). *Br. J. Appl. Phys.*, 11, 504

Pincus, H.J. (1978). *Adv. Opt. Electron Microsc.* (Cosslett, V.E. & Barer, R., Eds), London: Academic, Vol. 7, p. 17

Poole, J.B. le (1947). *Philips Tech. Rev.*, 9, 33

Poppa, H. & Heinemann, K. (1980). *Optik (Stuttgart)*, 56, 183

Porter, A.B. (1906). *Proc. Philos. Mag.*, 11, 154

Power Jr., P.C. & Pincus, H.J. (1974). *Science (Washington D.C.)*, 186, 234

Prestridge, E.B. & Yates, D.C.J. (1971). *Nature (London)*, 234, 345

Pyatnitskii, Yu.I. & Golodets, G.I. (1975). *React. Kinet. Catal. Lett.*, 2, 143

Rabo, J.A., Pickert, P.E., Stamires, D.N. & Boyle, J.E. (1961). *Actes 2nd Congr. Int. Catal., Paris 1960,* Paris: Technip, Vol. 2, p. 2055

Reid, N. (1974). in "*Practical methods in electron microscopy*" (Glauert, A.M., Ed.), Amsterdam: North—Holland, Vol. 3, p. 211

Reimer, L. (1976). *Proc. 9th Annu. Scanning Electron Microsc. Symp.* (Johari, O. & Corvin, I., Eds), Chicago: I.I.T. Res. Inst., Vol. 1, p. 1

Reuter, B. & Jaskowsky, J. (1967). *Inorg. Synth.*, 9, 80

Reynolds, G.T. (1968). *Adv. Opt. Electron Microsc.* (Barer, R. & Cosslett, V.E., Eds), London: Academic, Vol. 2, p. 1

Roiter, V.A. & Yuza, V.A. (1962). *Kinet. Katal.*, 3, 343

Roozboom, F., Mittelmeyer—Hazeleger, M.C., Moulijn, J.A., Medema, J., Beer, V.H.J. de & Gellings, P.J. (1980). *J. Phys. Chem.*, 84, 1783

Roscoe, H.E. (1870). *Proc. R. Soc. London*, 18, 37 and 316

Ruckenstein, E. & Chu, Y.F. (1979). *J. Catal.*, 59, 109

Ruska, E. (1934). *Z. Phys.*, 87, 580

Ruska, E. (1980). *Microsc. Acta, Suppl. 5: The early development of electron lenses and electron microscopy* (Mulvey, T., Transl.), Stuttgart: Hirzel

Sancier, K.M. (1971). *J. Catal.*, 23, 298

Sanders, J.V. (1985). In "*Catalysis — Science and technology*" (Anderson, J.R. & Boudart, M., Eds), Berlin: Springer—Verlag, Vol. 7, p. 51

Sas, T.M., Novozhilov, V.A., Velikodnyi, Yu.A., Bulychev, V.N., Suvorov, V.V. & Sorokin, V.E. (1978). *Russ. J. Inorg. Chem.*, 23,

1805

Sata, T. & Ito, Y. (1968). *Kogyo Kagaku Zasshi*, 71, 647; *C.A.*, 69: 90305e

Sata, T., Komoda, E. & Ito, Y. (1968). *Kogyo Kagaku Zasshi*, 71, 643; *C.A.*, 69: 48875r

Satava, S. (1959). *Collect. Czech. Chem. Commun.*, 24, 2172

Scherzer, O. (1949). *J. Appl. Phys.*, 20, 20

Schonberg, N. (1954). *Acta Chem. Scand.*, 8, 221

Scott, K.F. & Phillips, C.S.G. (1980). *J. Chem. Soc., Faraday Trans. I*, 76, 683

Sefstrom, N.G. (1831). *Ann. Chim. Phys. [2]*, 46, 105

Seitz, F. & Koehler, J.S. (1956). *Solid state Phys.*, 2, 305

Selim, S.A., Philip, Ch.A. & Mikhail, R.Sh. (1980). *Thermochim. Acta*, 36, 287

Seoane, J.L., Boutry, P. & Montarnal, R. (1980). *J. Catal.*, 63, 182 and 191

Sermon, P.A. & Bond, G.C. (1973). *Catal. Rev.*, 8, 211

Sesbes, T.A. (1955). *Rev. Fac. Sci. Univ. Istanbul*, 20C, 272

Sexton, B.A., Hughes, A.E. & Foger, K. (1982). *J. Catal.*, 77, 85

Shaprinskaya, T.M., Korneichuk, G.P. & Stasevich, V.P. (1970). *Kinet. Katal.*, 11, 139

Sharma, R., Barry, J. & Eyring, L. (1987). *Ultramicroscopy*, 23, 453

Sharma, R.K., Rai, K.N. & Srivastava, R.D. (1980). *J. Catal.*, 63, 271

Shidlovskii, A.A. (1960). *Izv. Vyss. Uchebn. Zaved., Khim. Khim. Tekhnol.*, 3, 405; *C.A.*, 54: 21974d

Simard, G.L., Steger, J.F., Arnott, R.J. & Siegel, L.A. (1955). *Ind. Eng. Chem.*, 47, 1424

Simon, R. (1970). *J. Appl. Phys.*, **41**, 4632

Sinfelt, J.H. (1970). *Catal. Rev.*, **3**, 175

Sinfelt, J.H. (1972). *J. Catal.*, **27**, 468

Sinfelt, J.H. (1973). *Adv. Catal.*, **3**, 91

Sinfelt, J.H. & Cusumano, J.A. (1977). In "*Advanced materials in catalysis*" (Burton, J.J. & Garten, R.L, Eds). London: Academic, p. 1

Sinfelt, J.H. & Taylor, W.F. (1968). *Trans. Faraday Soc.*, **64**, 3086

Sinfelt, J.H. & Yates, D.J.C. (1967). *J. Catal.*, **8**, 82

Smith, D.J. (1985). *Electron Microsc. Anal.* (Tatlock, G.J., Ed.), London: Inst. Phys., Conf. Ser. No. **78**, p. 311

Smith, D.J. (1986). *Electron Microsc., Proc. 11th Int. Congr.* (Imura, T., Maruse, S. & Suzuki, T., Eds), Tokyo: Jpn. Soc. Electron Microsc., Vol. 2, p. 929

Smith, D.J., Camps, R.A., Freeman, L.A., Hill, R., Nixon, W.C. & Smith, K.C.A. (1983a). *J. Microsc. (Oxford)*, **130**, 127

Smith, D.J., Camps, R.A., O'Keefe, M.A., Saxton, W.O. & Wood, G.J. (1985). *Ultramicroscopy*, **18**, 63

Smith, D.J., McCartney, M.R. & Bursill, L.A. (1987), *Ultramicroscopy*, **23**, 299

Smith, D.J., White, D., Baird, T. & Fryer, J.R. (1983b). *J. Catal.*, **81**, 107

Spence, J.C.H. (1980). *Experimental high-resolution electron microscopy*, Oxford: Clarendon

Stefani, G. & Fontana, P. (1976). *Ger. Offen*, 2,505,844

Stukanovskaya, N.A, Svintsova, L.G., Yuza, V.A., Korneichuk, G.P. & Roiter, V.A. (1970). *Katal. Katal.*, **6**, 18; *C.A.*, **74**: 130839u

Stukanovskaya, N.A, Yuza, V.A., Svintsova, L.G., Duchinskaya, V.I. & Roiter, V.A. (1968). *Dokl. Akad. Nauk. SSSR*, **180**, 1169; *C.A.*, **69**: 70790f

Subba Rao, V.V. & Mulay, V.N. (1970). *Indian J. Chem.*, 8, 750

Synecek, V. & Hanic, F. (1954). *Czech. J. Phys.*, **4**, 120

Taniguchi, M. & Ingraham, T.R. (1964). *Can. J. Chem.*, **42**, 2467

Tarama, K., Teranishi, S. & Miyazaki, T. (1952). *J. Chem. Soc. Jpn.*, **55**, 68

Tarama, K., Yoshida, S. & Tamura, N. (1965). *Proc. 3rd Int. Congr. Catal., Amsterdam 1964* (Sachtler, W.M.H., Schuit, G.C.A. & Zwietering, P., Eds), Amsterdam: North–Holland, Vol. 1, p. 282

Tashiro, T. (1931). *J. Chem. Soc. Jpn.*, **52**, 727

Tauster, S.J. & Fung, S.C. (1978). *J. Catal.*, **55**, 29

Tauster, S.J. & Fung, S.C. & Garten, R.L. (1978). *J. Am. Chem. Soc.*, **100**, 170

Theobald, F. (1978). *Rev. Roum. Chim.*, **23**, 887

Theobald, F., Cabala, R. & Bernard, J. (1969). *C.R. Acad. Sci. Paris*, **C269**, 1209

Thomas, J.M. & Lambert, R.M., Eds (1980). *Characterisation of catalysts*, Chichester: Wiley

Thomson, G.P. & Reid, A. (1927). *Nature (London)*, **119**, 890

Thon, F. & Siegel, B.M. (1970). *Ber. Bunsenges. Phys. Chem.*, **74**, 1116

Tilley, R.J.D. & Hyde, B.G. (1970). *J. Phys. Chem. Solids*, **31**, 1613

Trau, J. (1962). *Rocz. Chem.*, **36**, 1365

Trau, J. (1966). *Zesz. Nauk. Politech. Krakow*, **21**, 113; *C.A.*, **58**: 12156b

Treacy, M.M.J. & Howie, A. (1980). *J. Catal.*, **63**, 265

Treacy, M.M.J., Howie, A. & Wilson, C.J. (1978). *Philos. Mag.*, **A38**, 569

Tri, T.M., Massardier, J., Gallezot, P. & Imelik, B. (1981). *Proc. 7th Int. Congr. Catal., Tokyo 1980* (Seiyama, T. & Tanabe, K., Eds), Amsterdam: Elsevier, Part A, p. 266

Urban, K. (1979). *Phys. Status Solidi*, **A56**, 157

Urbanek, A. & Trela, M. (1980). *Catal. Rev.—Sci. Eng.*, **21**, 73

Uyeda, N., Kubayashi, T., Ishizuka, K. & Fujiyoshi, Y. (1980). *Nature (London)*, **285**, 95

Uytterhoeven, J.B., Christer, L.G. & Hall, W.K. (1965). *J. Phys. Chem.*, **69**, 2117

Wadsley, A.D. (1955). *Acta Crystallogr.*, **8**, 695

Wadsley, A.D. (1957). *Acta Crystallogr.*, **10**, 261

Wainwright, M.S. & Foster, N.R. (1979). *Catal. Rev.—Sci. Eng.*, 19, 211

Waltersson, K., Forslund, B., Wilhelmi, K.—A., Andersson, S. & Galy, J. (1974). *Acta Crystallogr.*, **B30**, 2644

Watson, J.H.L., Cardell, R.R. & Heller, W. (1962). *J. Phys. Chem.*, **66**, 1757

Watt, I.M. (1985). *The principles and practice of electron microscopy*, Cambridge: Cambridge Univ. Press

Weast, R.C., Ed. (1987). *CRC handbook of chemistry and physics*, 68th Edn, Boca Raton: C.R.C.

Wells, O.C. (1974). *Scanning electron microscopy*, New York: McGraw—Hill

Westman, S. & Nordmark, C. (1960). *Acta Chem. Scand.*, **14**, 465

Whelan, M.J. (1978). in "*Diffraction and imaging techniques in material science*" (Amelincks, S., Gevers, R. & Landuyt, J. van, Eds), Amsterdam: North—Holland, Vol. **1**, p. 43

White, D. (1982). *Ph.D. Thesis*, Glasgow Univ.

White, D., Hutchison, J.L. & Ramdas, S. (1987). *Electron Microsc. Anal.* (Brown, L.M., Ed.), London: Inst. Phys., Conf. Ser. No. **90**, p. 249

Wilhelmi, K.—A. & Waltersson, K. (1970). *Acta Chem. scand.*, 24, 3409

Wilhelmi, K.—A., Waltersson, K. & Kihlborg, L. (1971). *Acta Chem.*

Scand., **25**, 2675

Williams, R.C. & Fisher, H.W. (1970). *J. Mol. Biol.*, **52**, 121

Wischnitzer, S. (1981). *Introduction to electron microscopy*, 3nd Edn, New York: Pergamon

Wolf, R.J. & Joy, D.C. (1971). *Electron Mcrosc. Anal.* (Nixon, W.C., Ed.), London: Inst. Phys., Conf. Ser. No. **10**, p. 34

Wong, T.C., Brown, L.F., Haller, G.L. & Kemball, C. (1981). *J. Chem. Soc., Faraday Trans. 1*, **77**, 519

Yacaman, M.J. (1984). *Appl. Catal.*, **13**, 1

Yacaman, M.J. & Ocana, Z.T. (1977). *Phys. Status Solidi*, A42, 571

Yang, C.Y., Heinemann, K., Yacaman, M.J. & Poppa, H. (1979). *Thin Solid Films*, **58**, 163

Yao, H.C. & Shelef, M. (1979). *J. Catal.*, **56**, 12

Yonezawa, A., Nakagawa, S. & Suzuki, M. (1977). *Proc. 35th Annu. Meet. Electron Microsc. Soc. Am.* (Bailey, G.W., Ed.). Baton Rouge: Claitor, p. 62

Zenith, J., Contreras, J.L., Dominguez, J.M. & Yacaman, M.J. (1980). *J. Microsc. Spectrosc. Electron*, **5**, 291

Zurkova, L. & Ulicka, L. (1985). *Thermochim. Acta*, **85**, 111

Zworykin, V.K., Morton, G.A., Ramberg, E.G., Hillier, J. & Vance, E.W. (1945). *Electron optics and the electron microscope*, New York: Wiley